3. SITE 1223[1]

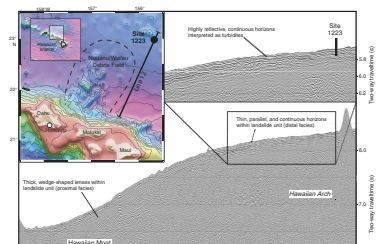Shipboard Scientific Party[2]

PRELIMINARY RESULTS

Introduction and Objectives

Recent studies have shown that the collapse of large volcanoes as a result of gravitational instability plays an important role in shaping volcanic environments. Detailed offshore bathymetric surveys of the Hawaiian Ridge (Moore et al., 1994), Reunion Island (Lenat et al., 1989), and the Canary Islands (Masson et al., 2002; Carracedo, 1999) reveal extremely large landslides. In the case of Hawaii, one of the Nuuanu Landslides caused by the collapse of Koolau Volcano on Oahu extends to 200 km from the island. In the Canary Islands, the debris extends to 30 km. Landslides on both island chains might have generated huge tsunamis (Moore, 1964; Moore and Moore, 1988; Moore et al., 1989). Herrero-Bervera et al. (2002) estimated the age of Nuuanu Landslides at 2.1–1.8 Ma. However, the size, the age, and the number of Nuuanu Landslides are still in question. Site 1223 is ~300 km from Oahu, ~100 km to the northeast of the presently defined Nuuanu Wailau debris field (Fig. F1). The objective of drilling at Site 1223 is to address the above questions.

Major Results

A number of important results were obtained for Hole 1223A. One of the objectives of coring at this site was to determine if the Nuuanu Landslide occurred as a single or as a multistage event as indicated by the number of turbidites recovered. Several unconsolidated volcaniclastic turbidites of varying thickness were recovered in the first two cores from Hole 1223A. Eight of these were >10 cm thick at 1, 3, and 4 meters below seafloor (mbsf) for Unit 1, and 5.2, 6, 6.9, 7.3, and 7.9 mbsf for Unit 2. Many were <1 cm thick. Paleomagnetic data indicate that all but

F1. Site 1223 and Nuuanu Landslide locations, p. 54.

the uppermost turbidite have an age between 1.77 and 1.95 Ma. The top turbidite has an estimated age between 0.78 and 1.77 Ma.

A surprising discovery was the recovery of the two crystal vitric tuff layers. Preliminary geochemical analyses indicate these tuffs are geochemically similar to Hawaiian tholeiitic basalts. The olivines in the vitric tuff are fresh. Kink banding and fibrous structures were observed in some olivines. The fibrous structure may have been caused by crystallization of hematite. The kink banding and fibrous structures indicate that the source for these olivines may be mantle derived under shear stress.

Another important result is the identification of wairakite in the vitric tuff. Wairakite is stable at a temperature range from 200° to 300°C. This suggests that considerable heat was involved when the crystal vitric tuff was deposited. Tentative interpretations for the origin of crystal vitric tuffs are given in "Interpretation of Tuffs," p. 27, in "Lithology."

Overview of Cores

The water depth at Site 1223 was 4245.8 m. We took two advanced piston corer (APC) and four extended core barrel (XCB) cores. We cored 41 m and recovered 23.54 m of core (57.4% recovery), with 12.7 m cored and 10.87 m recovered (85.6% recovery) with the APC and 28.3 m cored and 12.67 m recovered (44.8% recovery) with the XCB. After two APC cores, we switched to XCB coring. The use of the XCB system at these shallow depths and the long time needed for coring was unexpected as was the presence of lithified volcanic rocks. Core 200-1223A-5X was advanced only 1.0 m when it was recovered because of indications of jamming. Core 200-1223A-6X was advanced 8.0 m to a depth of 41.0 mbsf when it was recovered because of the time on site expiring.

Lithology

We have identified 14 distinct lithologic units (Fig. F2). Unit 1 (0–5.11 mbsf) contains yellowish brown clay and volcaniclastic turbidites. Unit 2 (5.11–7.32 mbsf) consists of volcaniclastic turbidites only. Unit 3 (7.32–7.90 mbsf) is a thin layer of dark-brown clay. Unit 4 (7.90–10.78 mbsf) is unconsolidated black sand. Unit 5 (12.70–15.06 mbsf) is a crystal vitric tuff. Unit 6 (15.06–15.29 mbsf) is bioturbated claystone. Unit 7 (15.29–16.10 mbsf) is volcaniclastic sandy siltstone. Unit 8 (22.30–22.80 mbsf) is volcaniclastic silty claystone with carbonate granules. Unit 9 (22.80–22.91 mbsf) is volcaniclastic claystone. Unit 10 (22.91–24.92 mbsf) is volcaniclastic silty claystone. Unit 11 is vitric tuff. Subunit 11A (32.00–33.00 mbsf) is altered vitric tuff, highly disturbed by drilling. Subunit 11B (33.00–36.99 mbsf) is palagonitized crystal vitric tuff. Unit 12 (36.99–37.47) is volcaniclastic silty claystone with anhydrite vugs. Unit 13 (37.47–38.31 mbsf) is volcaniclastic silty claystone. Unit 14 (38.31–38.70 mbsf) is volcaniclastic clayey siltstone. Coring gaps of several meters exist between some of the cores, so additional units may exist or those identified may be thicker by several meters.

Volcanic material is present throughout the stratigraphic column. Although we identified 14 distinct lithologic units, they may be grouped into three main types of lithologies: (1) unconsolidated clay and volcanic sediments, (2) weakly consolidated claystones and siltstones, and (3) crystal vitric tuffs. The turbidites are concentrated in the upper 12.7 m of the core. The tuffs have a volcanic fraction that ranges from 45% to 100%. The main constituents are (in order of increasing abundance)

F2. Lithologic units and stratigraphy of cores, p. 55.
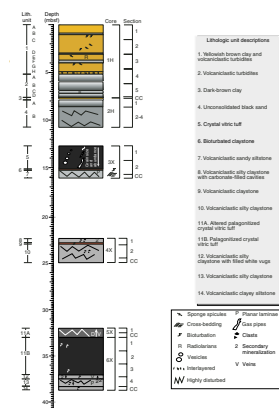
glassy shards, vitric fragments, olivine phenocrysts and clasts, plagioclase, palagonitized glass, lithic fragments, and clinopyroxene clasts. A MgO-rich olivine and Ca-rich plagioclase composition indicates equilibrium with mafic magmas. The mudstones and siltstones are found both in the middle and the bottom of the sections cored; they have high contents of clay, indicating detrital sources, and they have a low but variable volcanic fraction (~1%–25%). The silty claystone at the bottom of the palagonitized crystal vitric tuff (Subunit 11B) is characterized by the presence of relatively large (up to 3.5 mm) vugs filled by anhydrite, a mineral associated with hydrothermally altered basic rocks. The vitric tuffs were found just below the sand and at the top and in the middle of the mudstones and siltstones cored. The "nonvolcanic" fraction is composed of claystone clasts, micritic clasts, and, more rarely, radiolarians (generally <1%).

Whole-rock inductively coupled plasma–atomic emission spectroscopy (ICP-AES) analyses were conducted on the two vitric tuffs, as well as several of the siltstones and claystones. The tuff's major components are SiO_2 (47.6–49.6 wt%), TiO_2 (~2 wt%), Al_2O_3 (11.3–11.9 wt%), Fe_2O_3 (11.3–12.7 wt%), MgO (12.4–15.8 wt%), CaO (6.74–7.17 wt%), Na_2O (2.19–3.07 wt%), K_2O (0.47–0.83 wt%), and P_2O_3 (0.16–0.23 wt%). Its trace elements are Ba (50–70 ppm), Sr (22–330 ppm), Y (~20 ppm), Zr (~120 ppm), and Ni (~430–580 ppm). The high MgO concentrations are not surprising because of the high percentage of olivine present. Siltstones and claystones show similar values as those from the above tuffs. The geochemistries of whole-rock crystal vitric tuff, siltstone, and claystone were compared with the basalt glass geochemistry of mid-ocean-ridge basalt (MORB), Kilauea tholeiitic basalt, Haleakala alkali basalt, North Arch alkali basalt, and Koolau tholeiitic basalt. The crystal vitric tuff, siltstones, and claystones have the most in common, geochemically, with the Hawaiian tholeiitic lavas. There are some ambiguities in the measurements and samples, however, because the tuff contains clay minerals that may affect the chemical compositions.

Several of the claystones and siltstones contain effervescing white vugs. X-ray diffraction (XRD) analysis of the filling from Sample 200-1223A-6X-4, 0–20 cm, gave a complex spectrum. The majority of the material in the vugs is anhydrite and a Ca sulfate. Additional components include paragonite, wairakite, and analcime, with pumpellyite of varying compositions as a minor component. Grains from two intervals in the turbidite were analyzed by XRD (200-1223A-1H-5, 94–95 cm and 114–115 cm). The upper interval has brown grains with dominant XRD peaks at wavelengths consistent with phillipsite. In addition, some of the smaller peaks have spectra consistent with clay minerals, mainly smectite and illite and minor plagioclase. Therefore, the composition of the material analyzed is mainly phillipsite with clay minerals and minor plagioclase. The lower interval has white granules that give sharp XRD peaks at wavelengths consistent with calcite and some lower-amplitude peaks interpreted to be plagioclase.

Wairakite was originally found in hot springs in the geothermal fields of Wairakei in New Zealand and of Onikobe in Japan (Miyashiro, 1973). It has also been found in hydrothermal areas in the Mariana Trough (Natland and Hekinian, 1982). Wairakite is stable at a temperature range from 200° to 300°C. This suggests that considerable heat was involved when the crystal vitric tuff was deposited sometime thereafter.

Some of the olivine clasts in the tuffaceous layers show kink banding. Many mantle rocks such as lherzolites and dunites show kink

banding in olivine crystals. Also, tectonized peridotites often show such microstructures (e.g., Ishii et al., 1992). The kink bands are formed where shear is applied to the olivine crystal as shown by Kirby's deformation experiment (Kirby, 1983). Dislocations by shear stress in the olivine crystals generate the kink bands. Another interesting feature is the mass of fibrous lines identified in the olivine crystals. Iron oxide crystallization may be the cause of this structure. The presence of kink bands and fibrous structures indicates that olivine crystals in the crystal vitric tuffs may have been subjected to tectonic deformation.

Other Observations

We measured bulk density using gamma ray attenuation (GRA), magnetic susceptibility, natural gamma ray (NGR), and compressional velocity (V_P) on whole-core sections with the multisensor track (MST). Moisture and density and V_P were also measured on selected individual samples. The yellowish brown clay in Core 200-1223A-1H has 83% porosity and a V_P of 1.5 km/s. GRA density values from 0 to 10 mbsf gradually increase downhole from 1.2 to 2.2 g/cm³. The GRA densities agree with the bulk densities of the individual measurements, except for Core 200-1223A-3X, where GRA densities of the vitric tuff average 1.8 g/cm³ but bulk densities are slightly higher. Corresponding V_P values for the vitric tuff in Core 200-1223A-3X average ~3.3 km/s. Bulk density, grain density, and V_P for the siltstone in Core 200-1223A-4X are 1.6–2.0 g/cm³, 2.8 g/cm³, and 1.8–3.3 km/s, respectively. The vitric tuff in Core 200-1223A-6X has a 2.1-g/cm³ bulk density, a 2.6-g/cm³ grain density, and a 4.0-km/s V_P. Grain densities of vitric tuff in Core 200-1223A-6X are lower than those in Core 3X because of the higher levels of alteration in Core 6X. The V_P of the crystal vitric tuffs in Unit 5 (just below sand) and Unit 11 are ~3 and ~4 km/s, respectively. However, the bulk densities for both are similar, at ~2.2 g/cm³. The V_P for the upper crystal vitric tuff deviates from the generally expected compressional velocity-density relationship (e.g., Johnston and Christensen, 1997), possibly because of the weak consolidation of Unit 5. V_P and density increase with depth within the turbidites of Units 1 and 2, and the gradients can be associated with the graded bedding in the turbidites. Using this velocity and density increase with depth, we can identify the presence of the turbidite layers.

The magnetostratigraphy for Hole 1223A appears to record all the major chrons and subchrons from Chron C1n (the Brunhes Chron; 0.0–0.780 Ma) through Chron 2r (1.95–2.581 Ma). The Brunhes normal polarity interval spans only the top 14 cm of Core 200-1223A-1H, which is thinner than expected by ~1 m based on prior piston coring in the vicinity. Thus, we may not have recovered the very upper meter or so of the sedimentary section, or sedimentation rates may vary locally. The top and base of the normal polarity interval interpreted as Subchron C1r.1n (Jaramillo Subchron; 0.99–1.07 Ma) are at 0.79 and 1.23 mbsf, respectively. The top and base of the normal polarity interval interpreted as Chron C2n (the Olduvai Chron; 1.77–1.95 Ma) are at 2.02 and ~7 mbsf, respectively. All core recovered below ~7 mbsf appears to be of reversed polarity, which is interpreted to be the upper part of Chron C2r, possibly with the entire interval lying within Subchron C2r.1r (1.95–2.14 Ma).

Microbiological analyses from Site 1223 were conducted on sediments and tuffs. Most probable number (MPN) series were prepared

from all samples in order to determine the concentration of sulfate-reducing as well as fermentative bacteria. From Site 1223, twenty-five distinct microbial colonies could be isolated to pure cultures and could be further characterized as facultatively anaerobic organisms forming stable cell aggregates under appropriate conditions.

Conclusions

One of the objectives of coring at this site was to try to determine if the Nuuanu Landslide occurred as a single or as a multistage event by inference from the number of turbidites recovered. Several unconsolidated volcaniclastic turbidites of varying thickness were recovered. Paleomagnetic data indicate that all but the uppermost turbidite have an age between 1.77 and 1.95 Ma; the top turbidite has an estimated age between 0.78 and 1.77 Ma. A surprising discovery was the recovery of the two crystal vitric tuff layers. Preliminary geochemical analyses indicate these tuffs are tholeiitic basalts that have geochemical similarities to Hawaiian tholeiites; olivine accumulations have preferentially enriched the MgO content of the bulk ICP-AES analyses. However, there remain some other possibilities for the sources of crystal vitric tuffs, such as a part of the Hawaiian Arch or a nearby seamount. The genesis of crystal vitric tuffs can be complicated. Questions arise about why they are indurated so close to the seafloor; why they are so glassy; why they are so rich in fresh olivine; why they include kink banding and fibrous structures in the olivine crystals; and why they were warm when emplaced.

Preliminary results are summarized below:

1. We recovered several lithologic units that were transported to the site, most likely by a number of distinct landslide events. The origin of the deposits, as indicated by petrographic inspection and geochemistry, is the Hawaiian Islands. Furthermore, the age of the transported units is coeval with the age estimate for the Nuuanu Landslides. The turbidites associated with the landslides were also identified by physical properties changes.
2. Two pyroclastic events similar to the 1980 Mount Saint Helens' eruption but an order of magnitude larger occurred on Koolau at ~2 Ma. They may correlate with the collapse of the flank of the volcano and the formation of the Nuuanu debris field.
3. The thickness of turbidites and pyroclastic material corresponding to the Nuuanu age (1.8–2.4 Ma) is >38 m at Site 1223, over 300 km from Oahu. We did not core to the bottom of this Nuuanu-related sequence; thus, the related deposits may be thicker and additional landslide events may have occurred.

BACKGROUND AND OBJECTIVES

Background

Hawaiian volcanoes are enormous edifices that frequently experience slope failure, generating landslides, debris flows, and turbidity currents. The collapses of Hawaiian volcanoes have generated some of the largest landslides on Earth, and large tsunamis have likely accompanied them (Moore, 1964; Moore and Moore, 1988; Moore et al., 1989, 1994). Deposits from dozens of major landslides, some with lengths of 200 km

and volumes >1000 m³, have been recognized along the Hawaiian Ridge (Fig. F1) (Moore et al., 1994). Large landslides have also been recognized on the flanks of other ocean volcanoes such as those at Reunion Island (Lenat et al., 1989) and the Canary Islands (Carracedo, 1999; Masson et al., 2002).

The island of Oahu is the source for the giant Nuuanu Landslide, which broke away from the northeast flank of Koolau Volcano. This giant landslide is described as a debris avalanche by Moore et al. (1994) and undoubtedly generated turbidity currents that extend many hundreds of kilometers from the islands (Rees et al., 1993) as observed for other Hawaiian landslides (e.g., Moore et al., 1989; Garcia and Hull, 1994). Massive blocks from this slide are found as far as 230 km away from Oahu (e.g., Moore et al., 1989; Naka et al., 2000). The largest block in the debris field is the Tuscaloosa Seamount, which is ~30 km long, 17 km wide, and at least 2 km tall. The debris avalanche deposit is spread over a 23,000 km² area (Normark et al., 1993; Naka et al., 2000) and has distal portions that extend up the Hawaiian Arch. In order to reach the upper portion of the arch (the target site for drilling), the landslide would have had to traverse the deep moat on the northeast side of Oahu and travel uphill for over 100 km.

Sampling the debris avalanche deposit by gravity and piston cores has proven difficult because a carapace of younger debris (turbidites and associated deposits) overlies the deposit. The thickness and depositional history of the debris avalanche, therefore, are poorly known. Estimates of the thickness of the distal portion of the debris avalanche deposit vary from 1 to 100 m, but for planning purposes we had assumed that the thickness was <10 m (Rees et al., 1993). The age of the landslide was poorly constrained; it apparently occurred near the end or after the formation of the Koolau Volcano, which has surface flows that are 1.8–2.6 Ma based on K-Ar dating by Doell and Dalrymple (1973).

Scientific Objectives

There are many questions about the Nuuanu debris avalanche that may be addressed by drilling at Site 1223 (Fig. F1). First, is the method of emplacement of the Nuuanu debris avalanche a single catastrophic event, or does it consist of multiple collapses? As mentioned above, the timing of the giant Nuuanu debris avalanche is unknown; however, paleomagnetic and biostratigraphic data may help to constrain its age. Second, determining the thickness of the landslide deposit at the distal end and providing ground truth for the seismic data will aid in estimating the volume of the debris avalanche deposit. Finally, studying the debris avalanche deposits from Nuuanu will help to gain an insight into potential hazards related to giant landslides on the flanks of ocean island volcanoes.

OPERATIONS

The *JOIDES Resolution* arrived in port at Pier 1A in the Honolulu Harbor with the first line ashore at 0752 hr on 16 December 2001, marking the end of Leg 199 and the start of Leg 200 (all times are reported in local ship time, which is Universal Time Coordinated [UTC] – 10 hr in Honolulu and at Site 1223). Scientists, Ocean Drilling Program (ODP) technical staff, and the Transocean Sedco Forex crew for Leg 200 began boarding the ship on the morning of 17 December. The port call ex-

tended slightly over 4 days, with the limiting factor being the required inspections that were conducted by the American Bureau of Shipping. We still managed to depart over a day ahead of the time allotted for the Leg 200 port call. With the last line from port clearing at 1404 hr on 20 December, the *JOIDES Resolution* was under way to Site 1223 (Scientific Prospectus Site NU-1) (see Table **T4**, p. 170, in the "Site 1224" chapter for an operations synopsis).

Transit to Site 1223

After clearing the harbor under the pilot's instructions at 1418 hr on 20 December, the vessel traveled through the Honolulu channel, passed within a couple of nautical miles (nmi) of Diamond Head, and proceeded into the open ocean. Vessel motion became moderate with a 2-ft heave, a 2° pitch, and 1° to 3° rolls as a result of 15-kt winds and 6-ft seas with 8- to 10-ft swells off the starboard bow. The 170-nmi voyage to Site 1223 required 17.0 hr at an average speed of 10.0 kt.

Site 1223

We started lowering thrusters at 0718 on December 21, switching to dynamic positioning mode at Site 1223 at 0730 hr. The drilling crew immediately began assembling the bottom-hole assembly (BHA), which consisted of a refurbished 11⁷/₁₆-in APC/XCB rotary bit (type OC1293 with C7 inserts), a bit sub, a seal bore drill collar, a landing saver sub, a modified top sub, a modified head sub, a nonmagnetic drill collar, five 8¼-in drill collars, a tapered drill collar, six 5½-in joints of drill pipe, and one crossover sub. The BHA length was 136.1 m with a weight of 34,751 lb. The coring tools included the Tensor orientation package with the APC monel barrel that was to be run on every second core.

All thrusters were secure by 0740 hr; hydrophones were down by 0810 hr; and the beacon was away by 0850 hr. After the vessel settled on location, the water depth was determined to be 4255.4 meters below rig floor (mbrf) from the corrected depth of the precision depth recorder referenced to the dual elevator stool on the rig floor (see the **"Explanatory Notes"** chapter).

Hole 1223A

In preparation for shooting the first core, we first tagged the seafloor with the bit, which gave a depth of ~4247 mbrf. To ensure recovery of the mudline, we raised the bit to 4244 mbrf before shooting the first core. Hole 1223A was spudded with the APC at 2030 hr on 21 December at a depth, indicated by recovery, of 4235.1 m below sea level (mbsl), or 4245.8 mbrf. The APC was fired but did not bleed off immediately, indicating stiff sediments and an incomplete stroke of the APC piston. The stiff interval was likely caused by light-colored calcite granules overlain by black sand present in the bottom of the 7.79 m of core recovered. The second APC also had incomplete stroke with poor bleed-off of pressure. The core liner came back with a mixture of water and unconsolidated black sand.

We switched to the XCB coring system at 0030 hr on December 22. The use of the XCB system at these shallow depths and the long time needed for coring were unexpected as was the presence of lithified volcanic rocks, including a dark-colored vitric tuff that was recovered in

Core 200-1223A-3X and below. Core 200-1223A-5X was advanced only 1.0 m when it was recovered because there were indications of jamming. Core 200-1223A-6X was advanced 8.0 m to a depth of 41.0 mbsf when it was recovered because the time on site had expired.

Overall, we cored 41 m and recovered 23.54 m of core (57.4% recovery), with 12.7 m cored and 10.87 m recovered (85.6% recovery) with the APC and 28.3 m cored and 12.67 m recovered (44.8% recovery) with the XCB (Tables T1, T2). The drill bit cleared the rig floor at 0130 hr on 23 December, and we departed for Site 1224.

LITHOLOGY

Unit Descriptions

In Hole 1223A, we cored a 41.0-m interval and recovered 23.5 m of core that ranges in age from Pliocene to recent and consists primarily of unconsolidated sediments, weakly consolidated claystones and siltstones, and crystal vitric tuffs (Fig. F2; Table T3). The recovered sequence is divided into 14 units on the basis of lithology, induration, and alteration. Several units (1, 2, 4, and 11) are divided into subunits (A, B, C, etc.) (Fig. F2). Sediments and units that are labeled "volcaniclastic" contain >30% volcanic material and do not refer to the environment or method of deposition.

In the following, ages are inferred from magnetic stratigraphy (see "Paleomagnetism," p. 34). The uppermost part of the lithologic sequence consists of alternating layers of clay and normally graded volcaniclastic fine sands and muds. At least eight separate turbidites were identified as part of the top unconsolidated units. A massive dark-brown 0.58-m-thick layer of clay (Unit 3) underlies the turbidite layers. Under this clay is unconsolidated black sand (Unit 4) (another possible turbidite). Although a significant amount of the sand was lost during the coring process as a result of its coarse and unconsolidated nature, 2.88 m was recovered. We estimate that ~2 m of material was not recovered from this interval, and it is likely that most of the coring gap is part of this unconsolidated black sand.

An indurated crystal vitric tuff (Unit 5) lies beneath the unconsolidated black sand. This unit marks the top of a series of volcanic and volcaniclastic units that continue to at least 38.7 of the 41 mbsf and is one of two vitric tuff layers recovered. The two crystal vitric tuffs (Unit 5 and Subunit 11B) are separated by almost 17 m. Both are very fine to medium grained and have olivine, glassy shards, vitric fragments, and lithic fragments. Vesicles are common in the glass shards of both tuffs, but the lower tuff is significantly more altered. Below both tuffs are a series of very fine grained, weakly indurated volcaniclastic claystone and siltstone units. A few units are bioturbated, one heavily (~80%), and the rare laminae are commonly indistinct. White effervescing granules are present in several of these units. Fine-grained crystals, altered coarse grains, and glass fragments are found throughout the units.

Unit 1

Interval: 200-1223A-1H-1, 0 cm, to 1H-4, 67 cm
Depth: 0–5.11 mbsf
Thickness: 5.11 m

Age: 0–1.88 Ma
Lithology: yellowish brown clay and volcaniclastic turbidites

Unit 1 contains alternating layers of clay of pelagic origin (Subunits 1A, 1C, 1E, and 1G) and normally graded volcaniclastic sand, silt, and clay turbidites (Subunits 1B, 1D, 1F, and 1H). At least four turbidite sequences are present with a minimum thickness of 10 cm (Fig. F3) (Subunits 1B, 1D, 1F, and 1H). Numerous small turbidite deposits may be present as laminae within the clay and larger turbidite sequences (Fig. F4). Alternatively, some of these may represent the parallel laminae portion of a Bouma sequence, division D (Bouma, 1962), and may be part of the next turbidite below. Bioturbation and burrows are present below three of the four turbidites. Sponge spicules are common in both the clay and turbidite layers. Subunit 1B includes ~30 cm of alternating beds and laminae of clay and volcaniclastic grains that may represent additional smaller turbidites or division D in the Bouma sequence.

Unit 2

Interval: 200-1223A-1H-4, 67 cm, to 1H-CC, 9 cm
Depth: 5.11–7.32 mbsf
Thickness: 2.21 m
Age: 1.88–1.96 Ma
Lithology: volcaniclastic turbidites

Unit 2 includes several turbidites directly overlying one another. The sharp basal contacts indicate that erosion of the turbidite below has occurred (Fig. F5). At least four turbidites are represented in this unit, and each is labeled as individual subunits in Figure F2. Additional smaller beds may also be turbidites.
Although each of the turbidite sequences includes layers of fine black sand grading upward to silt and clay, all four large turbidites are composed primarily of very fine sand. Beds of granules made of calcite (identified by XRD) are located at the bottom of Subunit 2C (Fig. F5). Rare radiolarians are present in these layers.

Unit 3

Interval: 200-1223A-1H-CC, 9 cm, to 2H-1, 20 cm
Depth: 7.32–7.90 mbsf
Thickness: 0.58 m
Age: 1.96–1.97 Ma
Lithology: dark-brown clay

Unit 3 is a 0.58-m-thick massive dark-brown clay layer (Fig. F6).

Unit 4

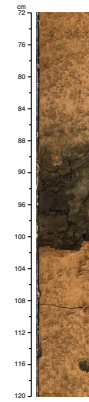Interval: 200-1223A-2H-1, 20 cm, to 2H-4, 90 cm
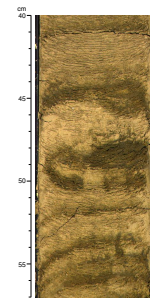Depth: 7.90–10.78 mbsf
Thickness: 2.88 m
Age: 1.97–2.04 Ma
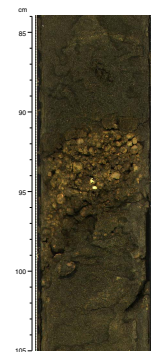Lithology: unconsolidated black sand

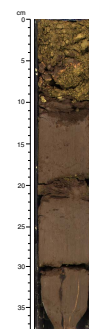**F3.** Volcaniclastic turbidite with clay above and below, p. 56.

F4. Multiple thin turbidite layers in a Bouma sequence, p. 57.

F5. A turbidite directly overlying another turbidite, p. 58.

F6. Dark-brown clay underlying a coarse turbidite, p. 59.

Unit 4 is divided into two subunits, 4A and 4B. Subunit 4A is the upper 0.75 m of Unit 4 and consists of fining-upward black sand (Fig. F7). Subunit 4B (2.13 m) is unconsolidated fine black sand, made of the same material, but highly disturbed during drilling. Coarse fresh glass is abundant throughout this unit. Approximately 40% of the volume of this unit may have been lost during recovery of Core 200-1223A-2H.

Unit 5

Interval: 200-1223A-3X-1, 0 cm, to 3X-2, 86 cm
Depth: 12.70–15.06 mbsf
Thickness: 2.36 m
Age: 2.08–2.14 Ma
Lithology: crystal vitric tuff

Unit 5 is an angular to subrounded clast-supported lithified very fine to medium-grained crystal vitric tuff in a brown clayey matrix (Fig. F8). The grain size increases with depth from medium to coarse. Section 200-1223A-3X-1 is predominantly medium-grained sand. This normally graded tuff also contains radiolarians in the clay matrix and structures currently interpreted to be gas pipes (Fig. F9). The length and width of the pipes increase toward the middle of Unit 5 and then decrease above and below.

Petrographic observations indicate an equigranular texture. Abundances of olivine, glassy shards, and vitric fragments decrease from the top toward the bottom of the unit (13%–6%, 20%–10%, and 16%–10%, respectively). The proportion of lithic fragments, however, increases downward from 8% to 20%; grain size also increases downward.

Glassy shards have a thin rim of clay in the top of the unit, but the glass in the lower half of the unit is missing this rim. Lithic fragments have subophitic to intergranular textures with plagioclase, clinopyroxene, olivine, and Fe-Ti oxides. There are two types of vitric fragments, one that has black to brown glass and the other with pale-brown glass. Both have spherulitic plagioclase and rare euhedral phenocrysts of olivine and plagioclase. They are cemented in a brown clayey matrix that ranges from 20% to 40% in volume. Many vesicles and cavities (5%–7%) are filled with zeolites. Chlorite grains are rare (<1%).

Unit 6

Interval: 200-1223A-3X-2, 86–109 cm
Depth: 15.06–15.29 mbsf
Thickness: 0.23 m
Age: 2.14–2.15 Ma
Lithology: bioturbated claystone

An erosional surface separates this unit into two parts. The upper part is a 4-cm-thick massive and heavily bioturbated (~80%) interval, and the lower part is a 19-cm-thick intermittently laminated interval with minor bioturbation (~5%) (Fig. F10). Sharp contacts are present at the top and bottom. The fine-grained, dark-gray, <0.5-cm-thick top and bottom contacts are horizontal and parallel with their adjacent units. The thin laminae below the inclined erosional surface are <0.5 cm thick with cross-bedding (101 cm) (Fig. F10). Both the clay matrix and the burrow fillings contain glass, olivine, and plagioclase. The burrows range from 0.1 to 1.0
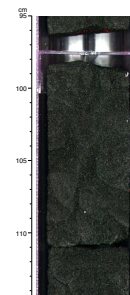
F7. Contact between clay and underlying black sand, p. 60.
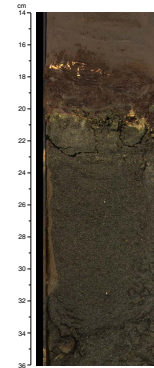
F8. Upper portion of Unit 5 crystal vitric tuff, p. 61.

F9. Possible gas pipes in crystal vitric tuff, p. 62.

cm in diameter and from 0.5 to 2 cm in length; they are not oriented; and ~10% are curved.

Unit 7

Interval: 200-1223A-3X-2, 109 cm, to 3X-CC, 40 cm
Depth: 15.29–16.10 mbsf
Thickness: 0.81 m
Age: 2.14–>2.15 Ma
Lithology: volcaniclastic sandy siltstone

In Unit 7, layers of sand-sized grains consisting of clay are interlayered with volcaniclastic silt (Fig. F11). The sediments are weakly indurated clast-supported sandy siltstone with poorly oriented silt particles. Coherent clumps of clay-sized particles are well rounded and between ~0.06 and 2 mm in size. The silt is angular to subrounded. Cross-bedding and planar laminations are present in the larger pieces that have not been significantly disturbed by drilling. The laminations may be due to concentrations of clay clumps in parallel, linear orientation. This unit was highly disturbed by drilling and broken into biscuits surrounded by slurry. Components of the 0.2-mm (fine sand) fraction are ~5% olivine, ~2% plagioclase, >10%–20% glass shards, ~10% vitric fragments, and >10% lithic fragments.

Unit 8

Interval: 200-1223A-4X-1, 0 cm, to 4X-4, 50 cm
Depth: 22.30–22.80 mbsf
Thickness: 0.50 m
Age: late Pliocene
Lithology: volcaniclastic silty claystone with carbonate-filled cavities

Overall, the volcaniclastic silty claystone fines upward with an intermediate layer containing <0.5-cm subangular to subrounded cavities filled with white material, some of which effervesce (Fig. F12). Cavities decrease in size and abundance with depth. The shape of the cavities changes from round to elongated in the upper part of the unit to almost entirely elongated in the lower portion. Based on macroscopic observations, crystals increase in size and abundance with depth (~30%–40% crystals in the lower section and ~15%–30% at the top). The unit is disturbed by drilling and is "biscuited." A sharp erosional contact with a rip-up clast >1 cm in size marks the lower boundary of this unit (Fig. F13).

Unit 9

Interval: 200-1223A-4X-1, 50–61 cm
Depth: 22.80–22.91 mbsf
Thickness: 0.11 m
Age: late Pliocene
Lithology: volcaniclastic claystone

Unit 9 is a massive weakly indurated, well-sorted, matrix-supported claystone with ~1% fine sand sized crystals. A few burrows are present.

F10. Sharp contact between bioturbated claystone and crystal vitric tuff, p. 63.
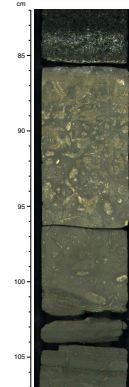
F11. Weakly indurated volcaniclastic sandy siltstone, p. 64.
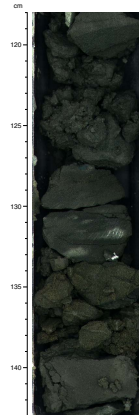
F12. Volcaniclastic silty claystone with carbonate granules, p. 65.

Their diameters are all <0.5 cm, with most <0.2 cm. Observations of thin sections show that some cavities are partially filled with zeolites, possibly phillipsite. A sharp erosional contact in a dark layer marks the top of this unit. Another dark 0.5-cm-thick layer marks the gradational base of the unit (Fig. F14).
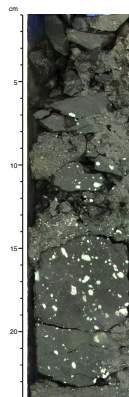
Unit 10

Interval: 200-1223A-4X-1, 61 cm, to 4X-CC, 37 cm
Depth: 22.91–24.92 mbsf
Thickness: 2.01 m
Age: late Pliocene
Lithology: volcaniclastic silty claystone

Unit 10 is a moderately well sorted silty claystone with small amounts of fine-grained crystals (7%–10%) and glass (~2%). Although most of the unit is massive, a few minor laminations are present (Fig. F15). Coarse lithic clasts are scattered throughout the unit. An area (10 cm thick) of granule and pebble breccia is present in the middle of the unit (Fig. F16). One large (>5 cm) clast is located near the top of the unit. The percentage of crystals and the size of crystal grains increase significantly with depth. Glass shards are fresh, angular, and range in size from fine sand to silt. Crystals are rounded to subrounded.

Subunit 11A

Interval: 200-1223A-5X-1, 0 cm, to 5X-CC, 39 cm
Depth: 32.0–33.0 mbsf
Thickness: 1.0 m
Age: late Pliocene
Lithology: altered palagonitized crystal vitric tuff

Unit 11 is divided into two subunits, 11A and 11B. The components are similar for the two subunits, but Subunit 11A is more altered and was highly disturbed by drilling. Subunit 11A is a matrix-supported medium- to very coarse grained palagonitized crystal vitric tuff (Fig. F17). The main constituents are glassy shards altered to palagonite (26%), vitric (8%) and lithic (4%) fragments, and olivine (~7%), with minor amounts of plagioclase (1%). Rounded cavities that resemble vesicles increase in size and abundance upward. The glassy shards appear to have experienced two types of alteration. The glass first altered to palagonite, and then the palagonite altered to chlorite and clay. Alteration of the glass decreases with depth.

Subunit 11B

Interval: 200-1223A-6X-1, 0 cm, to 6X-3, 105 cm
Depth: 33.0–36.99 mbsf
Thickness: 3.99 m
Age: late Pliocene
Lithology: palagonitized crystal vitric tuff

Subunit 11B is a lithified, altered, very fine to fine-grained palagonitized vitric tuff with subangular to subrounded volcanic fragments in a brown clayey matrix (Fig. F18). The main constituents are glassy

F13. Rip-up clast in volcaniclastic silty claystone, p. 66,
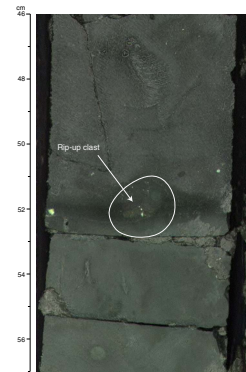
F14. Volcaniclastic claystone with an upper sharp contact and a basal gradational layer, p. 67.
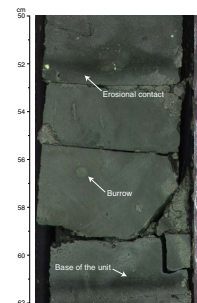
F15. Volcaniclastic silty claystone, p. 68.
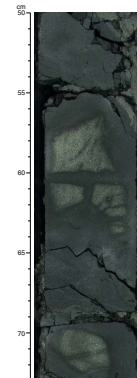
shards, lithic fragments, vitric shards, olivine, and plagioclase. Grain size decreases with depth from fine to very fine. For the entire subunit, glassy shard content increases (30%–80%), whereas spherulitic glassy abundance (10.5%–6.5%) decreases with depth. Palagonitization of the glassy shards is more complete with depth. The lithic fragment content is low (~5%) and constant. Some vesicles and cavities (~5%–7%) in glass shards are filled with material identified as zeolites. The main difference between Unit 11 and Unit 5 is based on the alteration extent of glass: the glass is highly palagonitized in Unit 11, whereas it is less altered in Unit 5. Almost all of the glass in Subunit 11B is either replaced by or has rims of palagonite (see "Alteration," p. 21).

Unit 12

Interval: 200-1223A-6X-3, 105 cm, to 6X-4, 8 cm
Depth: 36.99–37.47 mbsf
Thickness: 0.48 m
Age: late Pliocene
Lithology: volcaniclastic silty claystone with filled white vugs

A sharp contact marks the top of Unit 12. It is a weakly indurated, matrix-supported massive silty claystone with irregular to spherical cavities (<0.1–0.4 cm) filled with white material that effervesces vigorously and leaves a white platy residue (Fig. F19). Preliminary electron microprobe analyses indicate that this material is anhydrite. XRD analysis shows that the surrounding claystone contains paragonite, wairakite, kaolinite, and illite (see "X-Ray Diffraction Analyses," p. 19). Large angular clasts (~1 cm) at the base of the unit are very soft and can be easily scratched with a fingernail. The clasts increase in abundance with depth.

Unit 13

Interval: 200-1223A-6X-4, 8–89 cm
Depth: 37.47–38.31 mbsf
Thickness: 0.84 m
Age: late Pliocene
Lithology: volcaniclastic silty claystone

Unit 13 is a weakly indurated, matrix-supported clayey siltstone. It contains <7% angular to subrounded lithic clasts (average size = 0.3 mm) in the lower half of the unit (Fig. F20). It has a higher percentage of silt than the bottom of Unit 12. There are two distinct intervals with anhydrite and/or calcite fillings; some are in cavities, and some are more vein-like. Two zones (~5–6 cm) of highly disturbed material (drill slurry) between drilling biscuits contain broken pieces of similar white material that probably originally was veins (Fig. F21). Faint planar laminations are present in the lower part of the unit. Small claystone clasts, <0.1 to 0.5 cm in size, with darker angular to subrounded edges (sometimes oval shaped), form ~5% of the unit. The unit is more massive toward the bottom. The regions with the laminations and lithic clasts are less disturbed than other parts of the unit (Fig. F22).

Unit 14

Interval: 200-1223A-6X-CC, 0–39 cm

F16. Granule and pebble breccia, p. 69.
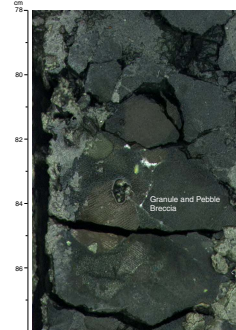
F17. Altered palagonitized crystal vitric tuff, p. 70.

F18. Palagonitized crystal vitric tuff, p. 71.

F19. Volcaniclastic silty claystone with anhydrite-filled vugs, p. 72.
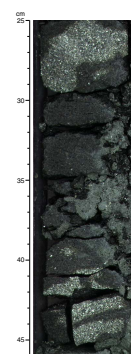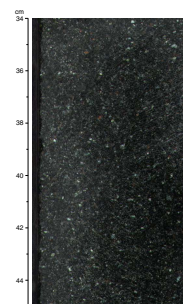
Depth: 38.31–38.70 mbsf
Thickness: 0.39 m
Age: late Pliocene
Lithology: volcaniclastic clayey siltstone

Unit 14 is a weakly indurated, matrix-supported clayey siltstone (Fig. F23). A few coarse clasts (<1%; 2 mm) in the siltstone are very soft and easily scratched with a fingernail. Angular to subrounded clasts measuring ~1 cm × 0.5 cm are present at the base (Fig. F23).

Petrography

The rocks recovered in Hole 1223A have three main lithologies, all of which have volcanic components varying from ~1% to >99% in volume. The three unit types are (1) barely consolidated to unconsolidated sediments, (2) weakly consolidated claystones and siltstones, and (3) crystal vitric tuffs.

The weakly consolidated to unconsolidated sands have a volcanic fraction close to 99% in volume and, therefore, can be called volcaniclastic sand or volcaniclastic ash. The main constituents are (in order of abundance) fresh glassy shards, olivine, vitric fragments, plagioclase, lithic fragments, palagonitized glass, and clinopyroxene. In a few cases, radiolarians (<1% in volume) are found.

The claystones and siltstones have a "nonvolcanic" fraction (60%–99%) composed mainly of clay minerals and, more subordinately, of carbonate/anhydrite granules. The main difference between these two groups of rocks is the silty fraction, which is represented by volcanic material—less than ~20% in volume in claystone and generally between 20% and 30% in volume in siltstones. Alteration products such as zeolites, anhydrite, and chlorite are relatively common and found in vesicles; they are concentrated in vugs or associated with glass shards. The volcanic fraction is represented by small olivine and plagioclase clasts together with glassy shards, which are altered to palagonite in varying amounts.

The indurated crystal vitric tuffs are composed of >50% (in volume) volcanic material, mostly as clasts of minerals and lithic/vitric fragments. The relative abundance of the volcanic material is variable, but the overall distribution is (in order of abundance) glass shards (fresh to altered), lithic and vitric fragments, olivine, plagioclase, and clinopyroxene clasts. The clayey matrix ranges from 15% to 50% in volume (in all but one case it is <40%). Relatively common authigenic minerals are zeolite (from 1% to 15% in volume; generally <10%), chlorite (from 1% to 10%; generally <5%), Fe oxyhydroxides (5%–20%), and sulfide minerals (<1%).

A more detailed petrographic description for each lithology is presented below, with a special emphasis on the crystal vitric tuffaceous layers. More information on the alteration products can be found in "Alteration," p. 21. Table T4 represents a general review of the most important petrographic features of the different units of Site 1223. A detailed table for each individual thin section is available in "Site 1223 Thin Sections," p. 20.

Unconsolidated Sediments

The unconsolidated sediments in the nine thin sections examined (18, 19, 27, 28, 29, 30, 31, 32, and 33) are either volcaniclastic sand lay-

ers or the coarse fraction of a turbidite sequence. Volcaniclastic sand (>60% volcanic material) is designated volcanic ash when it consists of particles <2 mm in diameter (Mazzullo et al., 1988). The volcanic ash layers of Unit 1 and the black volcanic ash of Unit 4 are normally graded (from 0.1 to 0.3 mm), with an average size of ~0.2 mm (Fig. F24). The most common components in these ash layers (Fig. F25) are
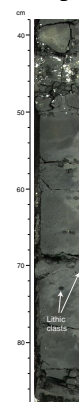
1. Subangular unaltered pale-yellow glassy shards (from 34% to 56% in volume). They range in size between 0.3 and 0.2 mm; in some cases they are relatively vesicular.
2. Black to dark-brown subrounded to subangular vitric fragments (18%–21% in volume). Vitric fragments are distinguished from glassy shards in the unconsolidated sediments by their darker color, which is related to the presence of microlites. The average size of the fragments is <2 mm. Rare plagioclase crystallites are present.
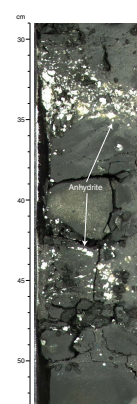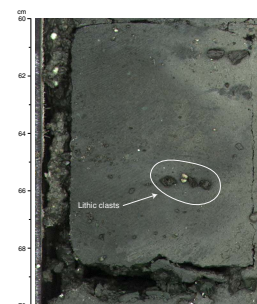3. Lithic fragments (2%–4% in volume) that have clinopyroxene, opaques, and possibly olivine in an intergranular relationship with plagioclase. The average size of the lithic fragments is <0.2 mm.
4. Olivine clasts (14%–18% in volume) that have a 2V of ~90°, reflecting high MgO contents with a chrysolitic (Fo_{80-90}) composition. Olivine, occasionally found within glassy shards, has an average size of 0.2 mm. It is anhedral to subangular and equant.
5. Subhedral plagioclase (6%–14% in volume) that is columnar with an average size of 0.2 mm.
6. Palagonite (1%–8% in volume) that is a common alteration product of glass; it is distinguishable from fresh glass by its darker color (orange to dark orange). In the unconsolidated sediments, palagonite is generally not associated with fresh glass but is present as discrete subrounded clasts <0.2 mm in size.
7. Anhedral pale-yellow clinopyroxene (1%–4% in volume) that on average is <0.2 mm.

Associated with this paragenesis, claystone and carbonate clasts are found in the volcaniclastic sand from the turbidite sequence (Unit 2) (Fig. F26). The claystone clasts (~50% in volume) range from 0.1 to 4 mm, with an average size of 1.8 mm, and are subangular to spherical in shape. In some cases these clasts have a relatively high percentage of carbonate inside. The carbonate clasts (~5% in volume) are made up of calcite (micrite) and range in size from 0.3 to 3.5 mm, with an average size of 0.6 mm (Fig. F26).

Claystones and Siltstones

Nine thin sections from Site 1223 were examined (6, 8, 10, 11, 13, 16, 17, 21, and 23). The silty to sandy fraction of these sediments is represented by volcanic material; other components are claystone and carbonate (micritic) granules. The most common volcanic material in silty claystones is represented by anhedral to subhedral relatively fresh olivine clasts with a size of <0.15 mm and euhedral to anhedral plagioclase grains generally <0.1 mm in size. The maximum extinction angle measured in plagioclase is 35°, which implies labradoritic or more Ca-rich compositions. Volcanic material is more abundant in coarser lithologies, such as sandy siltstones. In this case the maximum size of the vol-

F23. Weakly indurated matrix-supported clayey siltstone, p. 76.
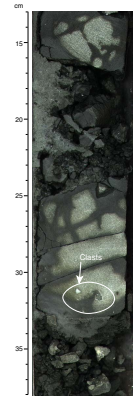
T4. Important petrographic features of the different units, Site 1223, p. 143.

F24. Sandy fraction of the turbidite levels, p. 77.
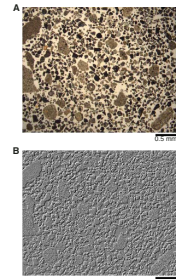
F25. Sandy fraction of turbidite layers, p. 78.
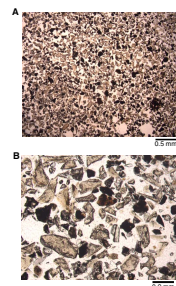
canic material ranges from ~0.7 (olivine clasts) to ~0.3 mm (glassy shards). The most abundant are

1. Glassy shards (<2% in volume) that are pale yellow when fresh and dark orange when they have altered to palagonite. The glass is generally found as subrounded to subangular fragments <0.3 mm in size.
2. Black to dark-brown vitric fragments (~5%–7% in volume) distinguishable from the glassy shards by their darker-colored glass and the presence of spherulitic plagioclase. Coarser-grained vitric fragments grade into lithic fragments.
3. Lithic fragments (~2%–7% in volume) that are subrounded to subangular in shape and <0.4 mm in size. They have intergranular texture with plagioclase and clinopyroxene and sometimes opaques and olivine.
4. Olivine clasts (~5%–8% in volume). The 2V of ~90° indicates high MgO content and chrysolitic (Fo_{80-90}) composition. Olivine is relatively fresh and, in some cases, highly fractured.
5. Plagioclase crystals (~2%–3% in volume) that have an average size of <0.2 mm and are anhedral to subhedral with equant to columnar habit. Plagioclase has a $2V\alpha < 80°$, indicating Ca-rich composition, close to bytownite.

The silty claystones (Units 12 and 13), below the lower tuffaceous layer, have 2% to 20% vugs (Fig. F27). The size of the vugs across the sections range from 0.4 to 1.7 mm, but with a maximum diameter of 3.5 mm. They are spherical to subrounded and are filled by a mineral that is white in hand specimen and colorless in thin section. This mineral has a columnar to hexagonal shape (Fig. F28), parallel extinction, high birefringence, three pronounced cleavage directions, and uniaxial negative character. Preliminary electron microprobe analysis on shore shows that Ca and S are present, indicating that the mineral is a calcium sulfate, either gypsum or anhydrite. Shipboard XRD patterns display peaks of anhydrite (see "X-Ray Diffraction Analyses," p. 19).

Crystal Vitric Tuffs

Two tuffaceous layers were examined in the nine thin sections examined from Cores 200-1223A-3X (Unit 5) and 5X–6X (Subunits 11A and 11B). A brief petrographic description of these layers is presented below.

Core 200-1223A-3X (Unit 5) (Thin Sections 1, 3, 4, and 5)

This tuff is medium to very coarse grained, with a maximum grain size of <2.2 mm and an average size of <1.1 mm (Fig. F29). The texture is equigranular. The main constituents are

1. Olivine (~5%–13% in volume). These crystals are anhedral to subhedral and equant. The high 2V (~90°) suggests they have high MgO contents and chrysolitic composition. Olivine is present mainly in the clayey matrix as broken clasts (average size = 0.4–0.6 mm). More rarely, the olivines are enclosed in glassy shards and are anhedral to euhedral (Fig. F30). A few olivine clasts have kink bands (Fig. F31).
2. Plagioclase (<1% in volume). Plagioclase has a $2V\alpha > 80°$, which indicates bytownitic to labradoritic composition. The crystals

F26. Claystone with volcanic sand in a turbidite, p. 79.
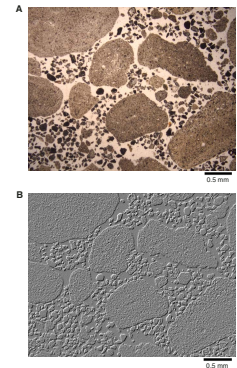
F27. Anhydrite-filled vug in volcaniclastic silty claystone, p. 80.
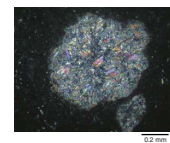
F28. Columnar and hexagonal habit of anhydrite in vugs, p. 81.
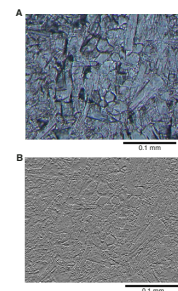
F29. Crystal vitric tuff, p. 82.

F30. Skeletal and euhedral olivine in shards in crystal vitric tuff, p. 83.
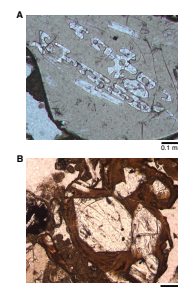
are anhedral to subhedral and have a columnar to equant habit. They are between 0.1 and 0.3 mm in size.

3. Clinopyroxene (rare; <1% in volume). An augitic composition is estimated for the clinopyroxenes based on the $2V\gamma$ (~60°) and the color and birefringence. It is found as fresh euhedral to anhedral twinned crystals in glassy shards as well as in the clayey matrix (Fig. **F32**).

4. Glassy shards (~10%–25% in volume). These shards are pale yellow and generally fresh. In some cases, the glass is bordered with a thin rim of brown clay. The size of the subangular to subrounded shards ranges from 0.3 to 1 mm, with a maximum size of 2 mm (Fig. **F33**). Euhedral to subhedral crystals of olivine and/or plagioclase are relatively common. The glass shards range from highly vesicular to vesicle free (Fig. **F33**).

5. Vitric fragments (~5%–16% in volume). These fragments generally have spherulitic plagioclase and dendritic Fe-Ti oxides and a basaltic composition based on preliminary microprobe analyses (S. Sherman, unpubl. data). (Fig. **F34**). There are also a few euhedral olivine and plagioclase phenocrysts present. The size of the vitric fragments ranges from 0.4 to 1 mm, and their shape is subrounded to subangular.

6. Lithic fragments (~8%–20% in volume). These fragments have a basaltic composition and intergranular, intersertal, and/or subophitic textures (Fig. **F35**). The main constituents of the lithic fragments are bytownite, augite, chrysolite, opaque minerals, and glass, with pigeonite present in some of the fragments. There are some relatively large olivine phenocrysts present. The lithic fragments (size = 0.4–1.1 mm) are subrounded to subangular.

All of the above components are cemented in a brown matrix made up of clay minerals and Fe oxyhydroxides that range from 20% to 40% in volume. The olivine, glassy shard, and vitric fragment content decrease downward in the unit (~13%–6%, ~20%–10%, and ~16%–10% in volume, respectively). The proportion of lithic fragments, however, increases downward (8%–20% in volume); grain size also increases downward. Lithic and vitric fragments are interpreted to be different portions of pillows and/or lava flows. Vitric fragments represent the outer glassy quenched rim of pillows, whereas lithic fragments are pillows or flow interiors that cooled more slowly. Many vesicles and cavities (~5%–7% in volume) are filled with zeolites. Rounded grains of chlorite are rare (<1%); in some cases, chlorite replaces all or part of the glassy shards.

Core 200-1223A-5X (Subunit 11A) (Thin Sections 2 and 22)

This tuff is very fine to medium grained, with a maximum grain size of <1.6 mm and an average size <1.0 mm. The texture is equigranular. The main constituents are

1. Olivine (~3% in volume) that is generally found as altered anhedral clasts with chrysolitic composition ($2V\gamma = 90°$).
2. Plagioclase (<2% in volume) that is subhedral to anhedral, with a degree of alteration ranging from incipient to strong. The combination of the high $2V\gamma$ (~90°) and the maximum extinction angle measured, ~35°, suggest bytownitic to labradoritic composition (An_{65-85}).

F31. Kink banding in an olivine clast in crystal vitric tuff, p. 84.
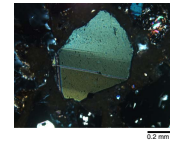
F32. Euhedral clinopyroxene in crystal vitric tuff, p. 85.
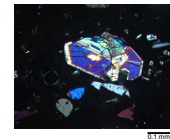
F33. Vesicle-free, highly vesicular pale-yellow glass shards, p. 86.
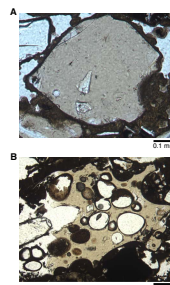
F34. Plagioclase spherulites in vitric fragments, p. 87.
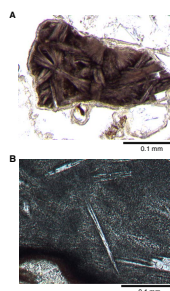
F35. Lithic fragment in crystal vitric tuff, p. 88.
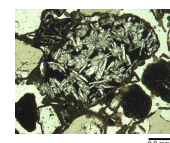
3. Glassy shards (~26% in volume) that are almost completely altered. They generally have an "atoll-like" structure (Fig. F36), with an interior composed of chlorite and clay minerals and an outer rim of palagonite. The altered glassy shards range from highly vesicular to almost bubble free (Figs. F37, F38). In some cases the vesicles are partially filled, and occasionally they host euhedral to subhedral plagioclase and olivine crystals up to 0.9 mm in size.
4. Lithic fragments (~4% in volume) that have a basaltic composition with intergranular and intersertal textures. The lithic fragments are composed of bytownite, augite, chrysolite, and opaque minerals, with or without glass. Their size ranges from 0.6 to 1 mm, and their shape is subrounded.
5. Vitric fragments (~8% in volume) that have spherulitic plagioclase and dendritic Fe-Ti oxides; in some fragments, euhedral olivine and plagioclase phenocrysts are present. Preliminary microprobe analyses of the glass matrix in the lithic fragments show tholeiitic basalt composition (S. Sherman, unpubl. data).

All of the components are cemented in a brown clayey matrix (~45% in volume). Vesicles and cavities (~20%–25% in volume) are filled by zeolites and chlorite. As in Core 200-1223A-3X, chlorite is present both as alteration of glass and as discrete granules.

Core 200-1223A-6X (Subunit 11B) (Thin Sections 14, 15, and 20)

This tuff is very fine to fine grained, with a maximum grain size <1.5 mm, and the average grain size is <0.6 mm (Fig. F39). The texture is equigranular. The main constituents are

1. Olivine crystals (~7%–10% in volume) that are anhedral to rarely euhedral and have an equant to prismatic habit (Fig. F40). Olivine is fresh and its high $2V\gamma$ (= 90°) suggests a chrysolitic composition. The average size is ~0.4 mm.
2. Plagioclase (rare; <1% in volume). The high $2V\gamma$ (>80°) and maximum extinction angle measured, ~40°, suggest bytownitic to labradoritic composition. The average size is <0.3 mm.
3. Glassy shards (30%–80% in volume) that are mostly altered to palagonite, although a small percentage retain fresh glass in the cores. In some cases, glassy shards contain euhedral to anhedral olivine and/or plagioclase crystals. The glass is slightly to highly vesicular (Fig. F41).
4. Lithic fragments (~2%–6% in volume). These fragments have a basaltic composition and intergranular, intersertal, and/or subophitic textures. They are subrounded and their size ranges from 0.4 to 0.7 mm.
5. Vitric fragments (~7%–11% in volume). They have basaltic compositions, with spherulitic plagioclase and dendritic Fe-Ti oxides; in some fragments, euhedral olivine and plagioclase phenocrysts are present. Their size ranges from 0.4 to 0.7 mm.

All of these components are cemented in a brown clayey matrix whose abundance ranges from 30% to 40% in volume. The grain size decreases toward the bottom of the unit. Glassy shard content increases, whereas vitric fragment content decreases toward the bottom of the unit (~30%–80% and ~10.5%–6.5% in volume, respectively); the lithic fragment percentage is always low (<5% in volume). As in the Unit 5 tuffs,

F36. Altered glassy shard in crystal vitric tuff, p. 89.

F37. Vesicular, vesicle-free altered glass in altered palagonitized crystal vitric tuff, p. 90.
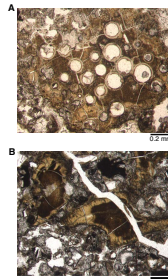
F38. Palagonitized glass altered to chlorite, p. 91.

F39. Partially palagonitized glass shards in crystal vitric tuff, p. 92.
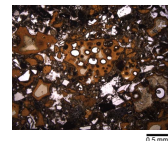
F40. Anhedral and subhedral olivine in the palagonitized crystal vitric tuff, p. 93.
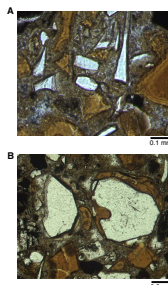
the lithic and vitric fragments can be considered to have formed from different portions of pillows and/or lava flows. Vesicles and cavities (~5%–7% in volume) are sometimes filled with zeolites. Rare rounded grains of chlorite (<1% in volume) also are present.

Summary

The essential features of the tuffaceous layers can be summarized as follows:

1. There are high percentages of olivine, glassy shards, and lithic and vitric fragments in both upper and lower tuffaceous units; most of these components are plausibly related to different portions of pillow lavas that cooled at different rates. The textures of the vitric and lithic fragments, however, do not always reflect "typical" cooling units of pillow basalts.
2. MgO-rich olivine and CaO-rich plagioclase compositions found in both the layers indicate equilibrium with mafic melts.
3. Olivine, plagioclase, and clinopyroxene crystals are fresh in Unit 5 and Subunit 11B. Only Subunit 11A has altered olivines, plagioclases, and clinopyroxenes.
4. There is a high percentage of clayey matrix (~30%–50% in volume) in both layers.
5. The mineral paragenesis of the lithic fragments is typical of tholeiitic basalts (presence of pigeonite).
6. The glassy shards are generally fresh or bordered by a thin brown clayey rim in Unit 5 (Core 200-1223A-3X), but they are almost totally altered to palagonite in Subunits 11A (Core 200-1223A-5X) and 11B (Core 200-1223A-6X).
7. The Subunit 11A tuff (Core 200-1223A-5X) has the highest percentage of zeolites (~15%) and clay minerals (~10%). There is a higher percentage of zeolites in Subunit 11B (Core 200-1223A-6X) (~6% in volume) than in Unit 5 (Core 200-1223A-3X) (~1%).
8. The crystal vitric tuffs (Unit 5 and Subunit 11B) are anomalously lithified considering their shallow level of emplacement, although samples of Unit 5 disintegrated upon heating to 100°C in an oven.
9. The presence of low-grade metamorphic minerals (e.g., paragonite, anhydrite, and wairakite) indicates relatively high temperatures (150°–350°C) (see "Alteration," p. 21).

X-Ray Diffraction Analyses

XRD analyses of granules, vein fillings, and veinlets were performed to determine the presence and composition of major and minor phases in order to gain a more thorough understanding of possible secondary mineralization. Material from the following were analyzed by X-ray diffraction (Table T5): (1) yellow and brown granules recovered from Unit 2 in the coarse-grained layer of the turbidite (Fig. F42), (2) an inclusion in Subunit 11B, the palagonitized crystal vitric tuff (Fig. F43), and (3) both vein and vug filling material from Unit 12 (Fig. F44).

Brown and Yellowish Granules in Unit 2

Two types of granules in the Unit 2 turbidite were analyzed by XRD. The brown granules (Sample 200-1223A-1H-5, 94–95 cm) have a com-

F41. Skeletal olivine in a palagonitized glass shard and glass shard with palagonite rim, p. 94.
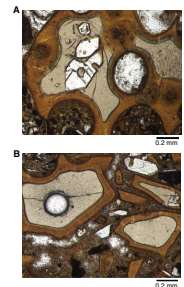
T5. XRD analyses results for samples, Site 1223, p. 144.

F42. XRD patterns for brown and yellowish granules, p. 95.
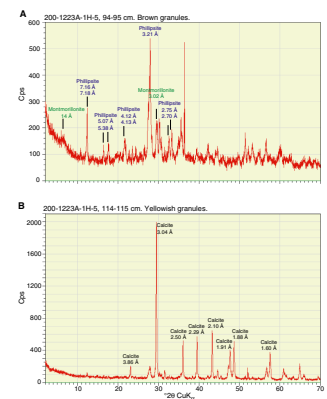
F43. XRD pattern for an inclusion in the lower crystal vitric tuff, p. 96.
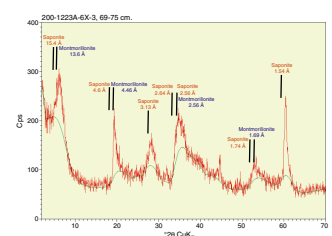
plex XRD pattern. The main peaks correspond to phillipsite (zeolite) with minor peaks that match the clay minerals (montmorillonite). Peaks for plagioclase are present at 3.20, 2.51, and 2.46 Å, but are not labeled on Figure **F42A.** Based on the XRD analyses, the yellowish granules (Sample 200-1223A-1H-5, 114–115 cm) have a simple spectrum that corresponds to calcite plus some low-intensity peaks that match plagioclase (Fig. **F42B**).

Inclusion in the Lower Palagonitized Crystal Vitric Tuff (Subunit 11B)

The palagonitized crystal vitric tuff (Subunit 11B) has a fine-grained inclusion (interval 200-1223A-6H-3, 69–75 cm) that has a greenish rim and a white core. The white and green materials were separated and sampled for XRD analyses (Fig. **F43**). Both XRD analyses have similar patterns. Major peaks, at 13.6, 4.46, 2.56, and 1.69 Å, are characteristic of montmorillonite, whereas peaks at 15.4, 4.6, 3.13, 2.64, 1.74, and 1.54 Å indicate the presence of saponite. The identified peaks are listed in Table **T6.**

White Vug Filling in the Volcaniclastic Silty Claystone (Unit 12)

XRD analyses were conducted on material sampled from thin veins (Samples 200-1223A-6X-3, 117–118 cm) and white filled vugs (Samples 200-1223A-6X-3, 129–130 cm, and 6X-4, 0–20 and 34–35 cm) in the volcaniclastic silty claystone of Unit 12 located directly below the palagonitized crystal vitric tuff. Apparently, both vug fillings and a portion of their surroundings were incorporated in the XRD samples. Thus both of the samples have complex but similar d-spacing patterns indicating the presence of several minerals (Fig. **F44**).

The upper part of Unit 12 (Sample 200-1223A-6X-3, 117–118 cm) has many thin white veins. XRD patterns of this sample have some small peaks that are distinctive from the white vug filling material. These peaks are identified as zeolite-group minerals such as phillipsite, thomsonite, and natrolite (natrolite not shown) (Fig. **F44B**) (Miyashiro, 1973).

The characteristics and interpretation of these patterns are as follows:

1. The highest peak, located at 9.67 Å, is seen among many mica-group minerals but is lower than the typical 10-Å peak for muscovite or illite. Other smaller peaks that are characteristic of mica-group minerals are also present. The micaceous mineral that best matches this pattern, particularly the principal peak at 9.67 Å, is paragonite, the Na analog of muscovite.
2. The second highest peak is located at 5.56 Å. The mineral wairakite has a principal peak at this position. There is an additional peak at 3.39 Å, which may be related to wairakite.
3. The peaks located at 3.87, 3.47, 2.18, and 2.07 Å correspond to the mineral anhydrite. This was verified by postcruise electron microprobe analysis (J. Natland, pers. comm., 2002). The identified peak positions for these analyses are listed in Table **T6.** The minerals pumpellyite, kaolinite, and montmorillonite may be present in accessory amounts. Overall, the main component in the vugs is anhydrite. It sits in a matrix of claystone in which clay minerals are largely transformed to paragonite and fine

F44. XRD patterns for a white vug filling and white veinlets, p. 97.
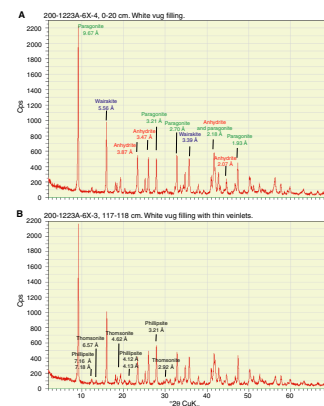
T6. Principal wavelengths and corresponding °2θ of mineral peaks identified, p. 145.

veins of wairakite. Accessory minerals are kaolinite, montmorillonite, and possibly pumpellyite.

Alteration

Introduction

Postdepositional mineralogical transformation of sedimentary material is usually described either as diagenesis or as metamorphism, depending on the conditions and the degree of the transformation with respect to pressure and temperature. Because the two terms encompass all combinations of temperature and pressure affecting crustal rocks, there should be no need for others. However, the word "alteration" has come to be applied to chemical and mineralogical transformations of igneous rock of the ocean crust that take place in response to interactions with seawater at low pressure, where there is still sufficient porosity in the rocks to allow ready flow of hydrous fluids through them. The engine of fluid flux is temperature, whether it is provided by proximity to igneous intrusions at, for example, a ridge axis or seamount or it is derived from the subsequent cooling of any part of the oceanic lithosphere. Alteration at high temperature is commonly described as hydrothermal alteration; alteration that occurs near the ambient temperature of bottom water is low-temperature alteration. High- and low-temperature alteration are often linked through a continuum of processes that occur during particular regimes of hydrologic flow. The agent of mineralogical transformation in either case is the driven fluid, originally seawater, which both dissolves soluble constituents of the rocks and deposits those constituents with which it is saturated. Dissolution and deposition depend on the conditions of the fluid, especially temperature, oxidation state, fugacities of H_2O and CO_2, alkalinity, and the degree of acidity. It is also usual to include among alteration mineral assemblages those materials that now line or fill original void spaces such as fractures or vesicles in addition to the replacement products of primary phases. Alteration in the marine realm is not the same as weathering, which takes place on land mainly in response to the flow of groundwater.

The volcaniclastic sediments and rocks recovered in Hole 1223A provide a special case of alteration. Although the agent of transformation appears to have been heated seawater and seawater likely flowed through the rock as well, chemical and mineralogical changes that led to induration were accomplished far from the usual sources of heat in the ocean crust and virtually at the seafloor. The effects of alteration were also extremely restricted, occurring in the two lithified crystal vitric tuffs, each only a few meters thick. Indeed, the induration is one of the most important consequences of the alteration. However, there were additional contact metamorphic effects in subjacent sediment, although the effects did not extend very far. Most of the rest of the sedimentary section has experienced an incipient diagenesis that produced partial lithification. Even this is surprising in view of the insignificant thickness of sediment above them. The terms alteration, contact metamorphism, and diagenesis thus have specific meanings in the context of the short sedimentary section cored in Hole 1223A, and it is important to bear in mind their distinctions in considering the descriptions that now follow.

Protoliths and Lithologies

There are four main protoliths to the partially and largely transformed sediments and rocks of Hole 1223A. These are

Pelagic, a combination of red or brown clay and the tests of siliceous microorganisms, mainly radiolarians;
Detrital, clays and lithic volcanic materials derived from the long-term weathering and erosion on land;
Subaerial volcaniclastic, volcanic glass, associated minerals, and lithic fragments that reached the ocean either during or after volcanic eruptions on the islands; and
Submarine volcaniclastic, also volcanic glass, associated minerals, and lithic fragments, but which erupted directly underwater.

Hole 1223A is below the calcium carbonate compensation depth; thus, the seafloor received no pelagic calcareous material in the history represented by the cores. However, there are minor amounts of other biogenic material such as sponge spicules and traces of authigenic material and metamorphosed basalt in some of the sediments.

These protoliths are combined in different proportions in the lithologies recovered in Hole 1223A. No sediment or rock appears to be without at least some fraction of all four components, including radiolarians. This is because all of the volcaniclastic material traveled across the seafloor in some kind of density flow and entrained pelagic material as it flowed. Some mixing also resulted locally from bioturbation. The pelagic protolith is most important in the upper 7 m of the section, lending the soft sediment a distinctive brownish hue. Several meters of unconsolidated lithic-vitric sand underlies this and overlies Unit 5.

Unit 5 is an indurated crystal vitric tuff composed mainly of sandsized submarine volcanogenic glass shards, associated igneous minerals (olivine, plagioclase, and clinopyroxene in decreasing order of abundance), and angular lithic grains set in a finer-grained matrix. The mystery of this rock is that it is well indurated, or cemented, even though it lies beneath a minimal thickness of surficial sediment. The usual pattern of lithification during burial diagenesis has not occurred here. To accomplish the same induration in similar materials simply by burial normally requires hundreds of meters of overburden, as attested by many holes drilled in the western Pacific Ocean and elsewhere (e.g., Hussong, Uyeda, et al., 1982; Taylor, Fujioka, et al., 1990).

Along the basal contact with the crystal vitric tuff of Unit 11, the underlying silty claystone (Unit 12) is partially recrystallized for a thickness of some 40 cm. It contains narrow veins lined with a mineral that is either wairakite or analcime, and vugs or cavities that are completely filled with white secondary minerals, including anhydrite. The cause of the induration of the deeper vitric tuff is no less mysterious than that of the upper one because it is covered with only 32 m of sediment and rock.

Alteration Petrography

Alteration is easier to identify in thin sections than it is to define macroscopically. Chiefly it occurs when some primary material such as volcanic glass becomes something else, such as clays and iron oxyhydroxides. It is essential to recognize what the material was originally, by

its shape, textural relationship with other substances, or the presence of relict phases, before inferring that it has become something else.

The two indurated vitric tuffs qualify as altered because in both tuffs much of the fine-grained matrix that originally contained sand-sized vitric, lithic, and mineral fragments has been replaced by clay minerals and zeolites. The clays and zeolites are the principal agents in the cementation of the rocks. In the lower tuff, nearly 90% of the original sand-sized glass has been replaced by palagonite. Palagonite is an unusual secondary substance to encounter in shallowly buried volcanogenic sediments. It usually replaces basaltic volcanic glass that is found in hyaloclastites and aquagene tuffs, which combine lobes of pillow lava with hyaloclastitic breccia carapaces (e.g., Peacock, 1926; Carlisle, 1963; Bonatti, 1965). It can also form during the flow of low-temperature groundwater through vitric tuff (Hay and Iijima, 1968) and more rapidly in tuffaceous materials under hydrothermal conditions, between 50° and 200°C (Hoppe, 1940; Surdam, 1973; Furnes, 1975). It involves a fairly extensive change in the composition of the original glass, a complementary formation of zeolites, and a reduction in density. Peacock (1926) described two types of palagonite. Both are orange or reddish brown. Gel palagonite is isotropic in cross-polarized light. Fibro-palagonite contains smectites with distinctive birefringence. Peacock considered the gel palagonite to be a mineraloid; it has a distinctive appearance but lacks obvious crystallographic attributes. In the Icelandic tuffs he studied, gel palagonite formed first and, so Peacock believed, at a higher temperature than fibro-palagonite. Icelandic tuffs that were transformed mainly to gel palagonite tend to be well indurated and break with a conchoidal fracture. Peacock (1926) also noted the common presence of spherical structures in palagonite consisting in many cases of bundles of needles radiating from a common center. These he termed spherulites. This term was later used to describe radiating needles of plagioclase formed from the melt at very high cooling rates in experiments on basalt that are observed near the rims of rapidly quenched submarine pillow basalt (e.g., Kirkpatrick, 1979).

Most of these attributes of palagonite can be seen in the thin sections of Subunit 11B. Figure F45 depicts palagonite in Sample 200-1223A-6X-3 (Piece 1C, 86–89 cm) taken 3.64 m from the top of the tuff and 1.35 m above its base. In this sample, matrix material accounts for 40% of the mode. It is largely inchoate, but most of it is colored the same amber red as coherent palagonitized glass shards, and it contains small broken bits of unaltered igneous silicate minerals, chiefly olivine and lesser plagioclase. A good deal of it is also clay, and radiolarians can be seen here and there; thus, it must include some fraction of pelagic material even if that material is now transformed to other substances.

The proportion of definable glass and palagonitized glass shards averages 38.1% as determined by 1000-point counts for each of the three thin sections. The proportion of glass exclusive of the matrix is 64.6%, and of this 91% is palagonitized (Fig. F45A). The small proportion of unaltered glass in the shards is always enclosed in a rim of palagonite ~0.1 mm thick (Fig. F45B). The rims are separated from the glass by sharp boundaries. Their nearly uniform thickness shows that they formed after deposition, after all movement and fracturing of glass in the tuff had ceased. Crystals of olivine are unaltered in both palagonitized glass shards and the matrix throughout most of the lower tuff (Fig. F45A, F45B, F45C). Near the top of this tuff, however, olivine is almost entirely replaced by fairly strongly birefringent clear clays.

F45. Palagonitic basaltic glass shards in vitric tuff, p. 98.
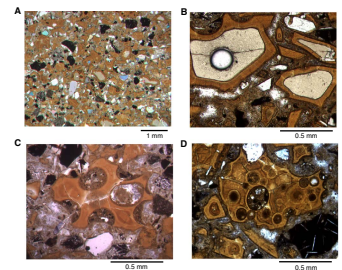
Many former glass shards are vesicular, with large bubbles forming as much as 50% of the fragments. Two examples shown in Figure F45C and F45D are completely palagonitized. Original palagonite rims appear to be intact and are present on all vesicle rims, whether they are open to the external matrix material or not. Darker islets of palagonite between the vesicles may be relics of original fresh glass interiors, as in Figure F45A and F45B. The palagonite shard depicted in Figure F45A has two types of spherical structure, both of which are circular in the plane of the section. These spherical structures are open vesicles that are filled with matrix material and rimmed zones of darker radiating fibers (Peacock, 1926). These probably are radiating bundles of plagioclase fibers that grew at high cooling rates as the glass was quenched and well before the palagonite formed. They now have sharply defined rims of palagonite, as if the bundles of plagioclase fibers served as impermeable barriers to the fluids that otherwise reconstituted the glass. Figure F45D also shows a lithic grain with small acicular plagioclases at the lower right. The grain is completely untouched by palagonitization, as are all of the darker lithic grains in Figure F45A and F45B. The alteration process thus affected only the glass.

Alteration is more extensive near the top of the lower tuff in Subunit 11A. Once glassy interiors surrounded by palagonite rims are now altered to green clays (Fig. F46A), and some of the palagonite rims themselves have also been replaced by green clays (Fig. F46B). Large void spaces between palagonite grains are now lined with rosettes of zeolite (Fig. F46C, F46D, F46E, F46F). There are at least three zeolites. One is fibrous, perhaps natrolite. The second has a columnar shape with flat terminations resembling thomsonite. The most abundant zeolite has pyramidal terminations on individual crystals; therefore, it is probably phillipsite. A second stage of alteration, or at least a more continued alteration, thus appears to have followed the formation of palagonite in the upper part of this tuff.

The upper indurated tuff in Unit 5 is unlike the tuff in Unit 11 in that it has almost no palagonite, although it is cemented by clay minerals and zeolites and almost all of its original glass is still fresh. Most glass shards are still quite fresh, as is olivine. The grains simply are cemented by a dull greenish brown clay mineral of globular habit (Fig. F47A, F47B, F47C). Some vesicles and voids are lined with radiating zeolite rosettes that are probably phillipsite (Fig. F47D).

An unusual aspect of some olivine grains may be related to alteration. In several thin sections of the vitric tuffs, fractured grains of the mineral are intricately decorated with exsolved reddish iron oxides (Fig. F48). In some grains, this is so extensive that transmitted light is almost entirely occluded. In other grains, the decoration is present as closely spaced swirls or fine lines (Fig. F48A, F48C, F48D, F48E, F48F). In still other grains, the cross-sectional pattern is that of cuspate stacks that alternate between being concave upward and downward (Fig. F48C, F48D, F48E, F48F). The birefringent olivine between the stacks is highlighted by different amounts of a faint oxidative stain, with boundaries present precisely where the stacks change from concave upward to concave downward. Extinction is uniform throughout, so these are not kink bands, although there are olivine grains in the thin sections with kink-banding subgrains (Fig. F48B).

The cuspate arrangement of these swirls resembles that revealed in olivine grains in deformed cumulate dunite xenoliths from Hualalai Volcano, Hawaii, using a procedure described by Kirby and Green (1980). They produced the identical pattern by heating thin sections in

F46. Alteration in altered palagonitized crystal vitric tuff, p. 99.
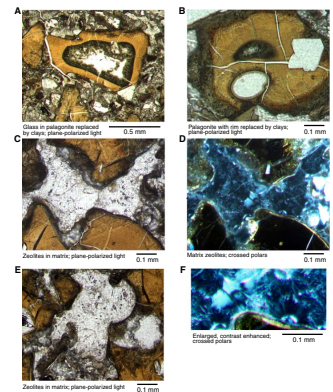
F47. Cementation and alteration in the upper vitric tuff, p. 100.
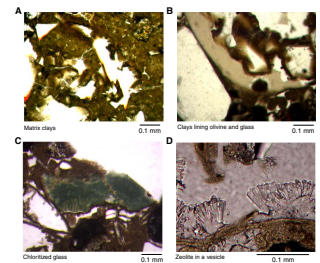
F48. Deformed and decorated olivine crystals in the upper crystal vitric tuff, p. 101.
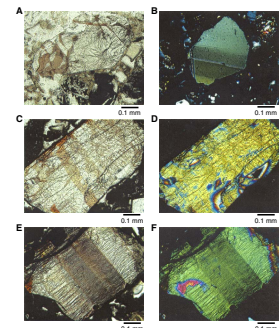
an oxygen-rich environment. This was done in order to reveal the intricate patterns of dislocation in the deformed olivine crystals that otherwise would not be evident during routine petrographic examination. The dislocations are manifestations of stresses acting on the dunite in the deep crust or upper mantle beneath the volcano. In the vitric tuffs of Hole 1223A, nature evidently supplied a similarly oxidizing and warm environment with the same result on deformed olivine grains. Most of the olivine in the tuffs is phenocrystic, thus it is not deformed. The scattered grains of olivine with the decorated patterns revealed by oxidative heating are scavenged bits of deformed dunite that, like the Hualalai xenoliths, came from the deep lower crust or upper mantle. The decorated patterns show up only because of the general alteration experienced by the surrounding tuffs.

Adjacent Sediments

The basal contact of the upper tuff (Unit 5) with the sediments is marked by a narrow lighter zone about 1 cm wide in the tuff itself. The underlying sediment is compact, bioturbated, and lighter in color for some 30 cm more than siltstones and mudstones farther away.

The contact of the lower tuff (Subunit 11B) with the underlying sediments of lithologic Unit 12 is marked by a fairly high concentration of subspherical white patches that appear to be cavity or vug fillings. Narrow irregular veinlets filled with white material link the cavities, crossing the core diagonally every few millimeters (Fig. F49A, F49B, F49C). The veins and filled cavities are set in a moderately indurated light-brown fine-grained matrix. X-ray diffractograms show that if this matrix once contained clay minerals, it has them no longer. In thin section, the veinlets are lined with two minerals, one with moderate birefringence that is present in sprays and the other with very low birefringence that is present in blocks (Fig. F50A, F50B). From X-ray diffractograms, the latter is either wairakite or analcime, both of which have almost indistinguishable powder diffraction patterns. A similar blocky mineral fills many circular relict tests of radiolarians (Figs. F49H, F50C, F50D, F50E). The white infilling in the patches (Fig. F49D, F50E) is a bladed biaxial negative mineral that has intermediate to high birefringence, parallel extinction, and three prominent orthogonal cleavage directions; these features match the orthorhombic sulfate mineral anhydrite. Some grains have pseudohexagonal cross sections (Fig. F49E; embossed image). Several anhydrite peaks are present in the diffractogram of this material shown in Figure F44A. The same diffractogram produced peaks for a multimineral assemblage including paragonite, wairakite/analcime, and possibly pumpellyite; these were evidently incorporated from the claystone directly surrounding the assemblage. The mineral with low birefringence in the vein fillings likely is wairakite or analcime, and pumpellyite may be the other. The matrix surrounding the white patches is very fine grained, with tiny relict grains of pyroxene and titanomagnetite. Much of this matrix is recrystallized to very tiny crystals having low birefringence, probably paragonite; some of them have square cross sections (Fig. F49G). Some tiny voids also contain tiny stellate intergrowths of sharply pointed crystals, perhaps cristobalite (Fig. F49I).

The material beneath the lower Subunit 11B tuff is recrystallized, and its mineralogy suggests a contact facies equivalent to the prehnite-pumpellyite facies of regional metamorphism (e.g., Miyashiro, 1973). Wairakite is present in some hydrothermal assemblages and is stable at

F49. Indurated claystone at the basal contact of the lower vitric tuff, p. 102.
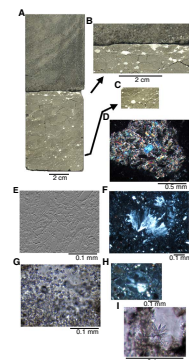
F50. Vein and radiolarian fillings in recrystallized claystone, p. 103.
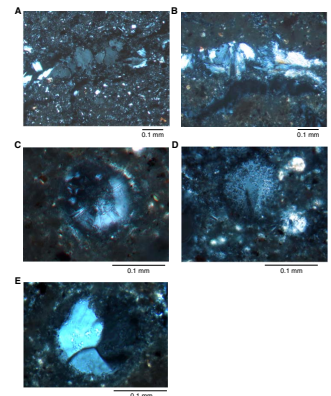
temperatures of perhaps 150° to 250°C (Liou, 1971; Seki, 1973; Tomasson and Kristmannsdóttir, 1972; Elders et al., 1979; Kristmannsdóttir, 1976). Paragonite, the sodic equivalent of muscovite, is an unusual mineral to find at a recrystallized contact, but its identification is based on both X-ray diffractograms and optical properties. It is usually found in regionally metamorphosed metaluminous rocks of the greenschist or blueschist facies associated with andalusite or kyanite (Deer et al., 1992). It is also known to replace chlorite in hydrothermally altered basalts in the stockwork beneath high-temperature sulfide mounds on the Mid-Atlantic Ridge (Honnorez et al., 1998). These basalts lie ~100 m below the seafloor just beneath breccias veined with anhydrite, pyrite, and quartz. Temperatures determined from oxygen isotope analyses of quartz associated with the paragonite and fluid inclusion studies of the anhydrite range from 212° to 390°C (Alt and Teagle, 1998; Petersen et al., 1998; Teagle et al., 1998).

About 50 cm below the contact with the tuff, the contact zone gives way to a darker, less consolidated greenish gray silty claystone (Unit 13). This material was recovered as drilling biscuits that are zones of coherent and undisturbed core, each several centimeters thick but separated by narrower zones of highly disturbed sediment and distorted by rotation of the core barrel during the coring process. The biscuits themselves are laminated to slightly cross-bedded, with small rip-up clasts of fine-grained claystone. Two of the intervening disturbed zones contain broken bits of a white secondary mineral resembling that of the white patches near the contact with the tuff. X-ray diffractograms revealed a similar mineralogy. Whether these were originally circular patches, veins, or both is unknown. Their presence in softer claystones does establish that contact effects persisted, but diminished, with distance from the base of the tuff.

Interpretation of Alteration

Alteration and cementation in the lower tuff (Subunit 11B) and the transformations in sediments at its lower contact probably occurred at an elevated temperature of at least 150°–250°C. This is consistent with prehnite-pumpellyite to zeolite metamorphic conditions and the presences of wairakite or analcime described above. This may have been a retrograde sequence. The formation of palagonite and its associated zeolites in the lower tuff was probably synchronous with the formation of these secondary minerals. Paragonite and anhydrite in underlying sedimentary rocks, however, may well have formed at significantly higher temperatures, based on comparison to the Trans-Atlantic Geotraverse (TAG) hydrothermal stockwork.

The formation of palagonite was not isochemical. In this case, it involved loss of CaO and Sr and addition of K_2O, Na_2O, and Ba to the bulk compositions of the rocks (see "Geochemistry," p. 30). These exchanges required substantial flow of fluids derived from seawater through the porous tuffs. The presence of the Na-mica, paragonite, also suggests that some of the fluids were saline brines (cf., Honnorez et al., 1998). The alteration differed from that at the TAG hydrothermal mound, however, because it was exclusively oxidative in character. There is no sulfide mineralization at Site 1223. Alteration at high temperature under oxidative conditions had surprisingly little affect on olivine, except for those grains containing deformation dislocations that become loci for exsolution possibly of iron oxides. In contrast, un-

der nonoxidative hydrothermal conditions, olivine is usually completely transformed to clays and other secondary minerals.

The sources of heat for the alteration and contact metamorphism may have been either distant or local. If local, they were presumably produced by igneous activity, either intrusion or extrusion, that has not yet been documented for this part of the Hawaiian Arch. Neither lava fields nor fissures associated with such hypothetical volcanism are evident in the smoothly sedimented crest of the arch near Site 1223 that has been seismically profiled, although the site is downslope from a small seamount. The nearest known young volcanism on the arch occurred at the North Arch volcanic field, some 200 km to the northwest. There, lavas and tuffs are alkalic olivine basalts, basanites, and olivine nephelinites (Dixon et al., 1997), unlike the tholeiitic precursors to the indurated tuffs and other sedimentary rocks of Hole 1223A. Similar volcanism near the drill site thus would only coincidentally have driven hydrothermal fluids through the sediments that we cored.

The distant alternative is that the tuffs themselves were pyroclastic in origin and were deposited containing some heat. Nevertheless, the amount of heat in a few meters of such materials is unlikely to have driven fluid flow for very long, at least if the deposit was small. On the other hand, a widespread blanket of hot material deposited suddenly might have acted abruptly as a compressive load on uncompacted surface sediments, and, where sufficiently thick, as a permeability barrier to fluids mobilized by sudden compaction. The fluids were forced to flow laterally and may have sustained high temperatures at the base of the tuff for some time. The result is that the most concentrated effects of alteration and contact metamorphism are present at the base. A similar effect was postulated for the pattern of fluid flow at the top of the basaltic basement that lies beneath ~100 m of volcaniclastic turbidites in the eastern Mariana Trough at DSDP Site 456 (Natland and Hékinian, 1982). There, greenschist-facies hydrothermal conditions were reached in the basalts, and both wairakite and cristobalite formed in the sediments at the contact.

This hypothesis provides a mechanism for directing fluid flow and thus concentrating the most pronounced alteration effects in the tuff beds themselves, rather than in adjacent sediments. This probably would not have been the case if hydrothermal flow was directed along vertical fissures associated with local igneous action. Admittedly, the geometry of fluid flow in variably permeable sediments is difficult to extrapolate over long distances from the vantage of a single hole.

At Site 1223, the two tuffs experienced alteration that was different either in type or in degree. The upper tuff is not palagonitized, although it is cemented by clay minerals and zeolites, and almost all of its original glass is still fresh. The essential difference was probably temperature—lower for the upper tuff—although the upper tuff may have experienced less fluid flow as well. Lower temperature and reduced fluid flow may mean the same thing—less heat was available to drive fluids, whether or not it was derived locally or from a more distant source.

Interpretation of Tuffs

We consider two origins for the crystal vitric tuffs—a Hawaiian Islands source and a local source. If the source of the tuffs was local, they were presumably produced by igneous activity, either intrusion or extrusion, that has not yet been documented for this part of the Hawaiian Arch. Neither lava fields nor fissures associated with such hypothetical

volcanism are evident in seismic data of the smoothly sedimented crest of the arch near Site 1223, but no high-resolution bathymetry data have been taken of the surrounding area. The nearest known young volcanism on the arch occurred at the North Arch volcanic field, some 200 km to the northwest. There, lavas and tuffs are alkalic olivine basalts, basanites, and olivine nephelinites (Dixon et al., 1997), which are very unlike the tholeiitic precursors to the indurated tuffs and other sedimentary rocks of Hole 1223A. Similar volcanism near the drill site, thus, would only have coincidentally driven hydrothermal fluids through the sediments that we cored.

A possible scenario for the Hawaiian Islands source hypothesis is that a very large eruption of primitive Hawaiian tholeiite occurred when a deep magma reservoir was breached by the catastrophic failure of the flank of a volcano, similar to the 1980 eruption of Mount Saint Helens (Fig. F51) (Moore and Albee, 1981). This may have occurred on Oahu when the northeast flank of Koolau Volcano collapsed, producing the giant Nuuanu debris avalanche. Sudden decompression caused pressure release, vesiculation, and expansion of the magma. The magma erupted as a directed blast and passed over the collapsing blocks now strewn on the seafloor as a submarine pyroclastic debris flow that reached over the Hawaiian Arch. In this scenario, if the material reached the area of Site 1223 (300 km away) quickly enough in a bottom-hugging density flow, it may have retained enough heat to cause the alteration and induration of the two crystal vitric tuffs. Water surrounding a hot pyroclastic flow may become vaporized, creating a water vapor barrier around the flow that helps to insulate the flow and prevent mixing (Kato et al. 1971; Yamazaki et al., 1973).

Subaerial pyroclastic flows have observed velocities ranging from 14 km/hr (Tsuya, 1930) to 230 km/hr (Moore and Melson, 1969) and travel great distances (>100 km) moving over and around obstacles (surmount >600 m) (Fisher and Schmincke, 1984). Their ability to move has been attributed to several factors, namely exsolution of gas from glassy particles, gas being released when particles are broken, and the heating of the medium causing thermal expansion (e.g., Sparks, 1979). The gas reduces the friction between particles allowing the flow to travel faster. In addition to moving at tremendous speeds, pyroclastic flows are very good at retaining heat. Boyd (1961) calculated that cold air has a minimal effect on a hot pyroclastic flow. Therefore, a hot pyroclastic flow may remain at almost magmatic temperatures during transport and even after deposition.

The above applies to subaerial pyroclastic eruptions; subaqueous pyroclastic flows are less well understood. A massive coarse-grained subaqueous pyroclastic flow deposit >4.5 m thick and extending as far as 250 km from its source was recovered in the Grenada Basin, Lesser Antilles. Carey and Sigurdsson (1980) interpreted the deposit to be a debris flow that originated when a hot subaerially erupted pyroclastic flow entered the ocean. The debris flow incorporated pelagic sediment and seawater, decreasing internal friction and giving the flow great mobility and the ability to suspend large fragments. Thermal remanent magnetism of a similar deposit (Pliocene–Miocene in age) was interpreted by Kato et al. (1971) to have been deposited at temperatures ~500°C.

Both the whole-rock ICP-AES analyses and the preliminary electron microprobe analyses of individual glass fragments within both crystal vitric tuffs (Unit 5 and Subunit 11B) support a Hawaiian Islands source. Unlike the whole-rock ICP-AES analyses, the effects of olivine accumulation and alteration do not complicate the glass geochemistry. There-

F51. Schematic drawing of a landslide and the resulting directed blast eruption, p. 104.
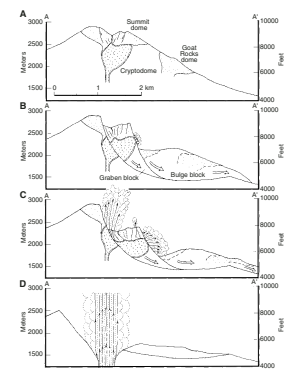
fore, it is easier to compare the glass geochemistry from the tuffs with the geochemistry from other potential sources (i.e., Hawaiian Islands and North Arch volcanic field). The glass geochemistry suggests that the tuffs have tholeiitic basalt compositions and are similar to Hawaiian tholeiitic basalts.

Futhermore, the glasses in both tuffs have low S concentrations (majority <300 ppm) (S. Sherman, unpubl. data). Sulfur concentrations can be used to estimate depths of eruption (e.g., Moore and Fabbi, 1971; Dixon et al., 1991). Low S concentrations (<200 ppm) are indicative of significant degassing and predominantly result from subaerial eruptions. Deep submarine glasses with low S contents were recovered from Puna Ridge, which is a submarine extension of Kilauea Volcano. The low S abundances for these glasses were attributed to mixing between lavas that had degassed at or near the subaerial surface with the rift lavas that were erupted underwater (Clague et al., 1995). Therefore, the low S concentrations in the glasses in the tuffs suggest that they were erupted subaerially or at least mixed with subaerial lavas. A subaerial eruption supports a Hawaiian rather than a North Arch source for the tuffs. Not only is the North Arch volcanic field submarine, the majority of the glasses from the North Arch volcanic field have S contents >300 ppm (Dixon et al., 1997). It may be difficult to imagine the source for the tuffs from Site 1223 as one of the Hawaiian Islands, but the geochemical evidence indicates it is the most likely option.

BIOSTRATIGRAPHY[3]

Because the focus of Leg 200 was on basement drilling, we did not have a paleontologist on board. Bob Goll, from ODP-TAMU (Texas A&M University), examined sediment samples for radiolarians and wrote a first draft of the following report. In addition, John Firth, also from ODP-TAMU, examined several samples for calcareous nannofossils, but the samples were found to be barren.

A total of six samples were investigated for radiolarians: 200-1223A-1H-1, 72–74 cm; 1H-3, 125–127 cm; 1H-CC, 19–21 cm; 1H-CC, 29–31 cm; 6X-4, 17–19 cm; and 6X-CC, 15–17 cm. Of these, only three samples (200-1223A-1H-1, 72–74 cm; 1H-CC, 29–31 cm; and 6X-4, 17–19 cm) contain radiolarians. Sample 200-1223A-1H-1, 72–74 cm, contains common opal-CT replacement pseudomorphs of radiolarians that cannot be identified taxonomically, and the sample cannot be dated on the basis of these occurrences.

Mixed preservation states characterize the remaining two samples, where moderately preserved specimens are present in association with opal-CT forms. Specimens in the original opal-A silica phase are rare but sufficient to provide a general age. The Eocene species, *Eusyringium fistuligerum,* was observed in Sample 200-1223A-1H-CC, 29–31 cm. This sample is from the dark-brown clay (lithologic Unit 3) that overlies the bulk of those deposits thought to be related to the Nuuanu Landslide.

The presence of numerous specimens of *Phormocystis striata exquisita* and one specimen of *Phormocystis striata striata* in Sample 200-1223A-6X-4, 17–19 cm, is regarded as reliable evidence to support the assignment of this fauna to the *Buryella clinata* Zone as indicated by Sanfilippo et al. (1985). This sample comes from lithologic Unit 13, which is near the base of the cored interval.

Both samples have radiolarians that indicate an early Eocene age. Without consideration for reworking, this age is in conflict with the age

constraint from the geochemistry of the tuffs which indicates that the vitric tuffs have an age no older than ~3 Ma (i.e., no older than the volcanics from which the Site 1223 deposits were derived, which the geochemistry indicates is from one of the Hawaiian Islands). Similarly, the magnetostratigraphy indicates that the sediments above the dark-brown clay of lithologic Unit 3 were deposited during Chrons C2n to C1n, with all underlying sediments, including those samples with identifiable radiolarians, falling within a dominantly reversed polarity zone interpreted to be Chron 2r (1.950–2.581 Ma).

Reworking of radiolarians would, however, be expected in landslide-related deposits, though less so in the dark-brown clay of Unit 3 if it is a pelagic clay. The depositional environment for the clay is not known at this time, and the unit is thin enough that bioturbation could have resulted in reworking of sediments from below and above, with both being either turbidites or landslide units where reworked radiolarians could occur. Reworking may also be suggested by the lack of radiolarians in the second sample analyzed from lithologic Unit 3 (Sample 200-1223A-1H-CC, 19–21 cm), which is only 10 cm above that which contains early Eocene radiolarians. Sporadic occurrences of these microfossils and the mixed, generally poor, preservation states support the interpretation of reworking. We consider that reworking is likely and that the early Eocene age is not representative of the age of the units.

GEOCHEMISTRY

Samples selected for ICP-AES analysis from the cores of Hole 1223A included four from the crystal vitric tuff of Unit 5, five from the palagonitized crystal vitric tuff of Unit 11, and seven siltstones and claystones from Units 8, 10, 13, and 14. All major oxides and the trace elements Ba, Sr, Y, Zr, Ni, V, Cr, and Sc were measured. Iron is reported as Fe_2O_3 (Table T7). Loss on ignition (LOI) is mainly a measure of volatile $(H_2O + CO_2)$ loss on heating of the sample to 1000°C, but it also includes some addition of oxygen resulting from oxidation of iron. The analyses shed light on the diagenesis and the alteration of the sedimentary rocks and crystal vitric tuffs, the possible contribution of detrital clays to the sedimentary rock bulk compositions, and the provenance of the sedimentary rocks and the crystal vitric tuffs. These topics are discussed below.

T7. ICP-AES analyses, Hole 1223A, p. 146.

Diagenesis and Alteration vs. a Detrital Component

Observations on cores, smear slides, and thin sections indicate a basaltic provenance for most of the rocks and sediments recovered from Hole 1223A. Basaltic glass, both fresh and altered, is ubiquitous, and it is accompanied by varying proportions of olivine, pyroxenes, and plagioclase as separate grains or fragments. Many olivine crystals include tiny Cr spinel. The abundance of olivine and Cr spinel in the bulk rock analyzed is the cause of the high MgO, Ni, and Cr contents (Table T7). There are also lithic fragments that individually combine these several minerals together with titanomagnetite. Much of the matrix of tuffs, siltstones, and claystones is very fine clay minerals. Whether clay minerals are detrital, authigenic, or both is important to establish. The tuff matrix has a great deal of authigenic clay and several zeolites. These are the principal cementing minerals of the upper tuff of Unit 5, in which most glass is still fresh. Clays and zeolites also cement the dominantly

palagonitized glass in the lower tuff of Unit 11. Much of the clay in the siltstones and claystones appears to be detrital, as discussed below.

Both subaerial tropical weathering and submarine authigenesis produce the high K_2O clay minerals smectite, illite, or mixed-layer smectite-illite. Because clay minerals are hydrous, high LOI in our samples is an indication of clay content. The correlation between K_2O and LOI contents among our samples (Fig. **F52**) indicates a high proportion of potassic clay minerals. Therefore, K_2O should not be used as a geochemical discriminant to establish provenance.

The bulk compositions of samples from Hole 1223A are proportionately aluminous compared with other basaltic protoliths. A ternary diagram of CaO-Al_2O_3-K_2O (Fig. **F53A**) shows that the sample compositions are shifted toward the compositions of aluminous subaerial clay minerals such as illite, montmorillonite, and kaolinite. This shift toward the clay field is a consequence of lower CaO rather than higher Al_2O_3 (Table **T7**). The effect of the K_2O increase during alteration, even though substantial (Fig. **F52**), is proportionately small compared with the variation in Al_2O_3, and thus only produces a minor shift toward the K_2O axis in this ternary plot.

Analyses of glass-palagonite pairs from DSDP Hole 504B by Noack et al. (1983) suggest that palagonitization produces a similar relative effect to that of addition of detrital clays (Fig. **F53A**). However, when the same comparisons are made using total iron as $Fe_2O_3^T$, Al_2O_3, and MgO on a ternary MAF diagram (Fig. **F53B**), the addition of clays and formation of palagonite have opposing results. Samples of Hole 1223A, circled as Group 2 in Figure **F53,** likely contain a significantly higher proportion of detrital clay than those circled as Group 1. Both groups are displaced away from MORB glasses and tholeiitic basalt glasses from Kilauea Volcano, Hawaii, toward Al_2O_3 in Figure **F53A.** None of the samples are displaced away from Hawaiian glasses toward marine secondary clays (Fig. **F53B**). Thus, the claystones, siltstones, and the vitric tuffs have at least some detrital, but not marine, secondary clay. If palagonitization in the lower tuff caused the glass to become enriched in Fe_2O_3 and MgO with respect to Al_2O_3, then the effect was more than compensated by the presence of detrital clays in the samples.

Therefore, to a first order, the analyzed samples from Hole 1223A are composed of components of basaltic rock diluted to varying extents by aluminous detrital clays. Such clays were produced by subaerial tropical weathering and carried by streams to offshore regions. Emergent Hawaiian volcanoes are the only potential sources for such material in the vicinity.

The overall effects of this dilution on bulk compositions are as follows. A higher fraction of detrital clays in the samples would produce lower CaO, TiO_2, P_2O_5, MnO, and Sr in the analyses. Typical illite, montmorillonite, and kaolinite in tropical soils have very little or none of these components. On an anhydrous basis, addition of such clays to a volcaniclastic component would slightly increase SiO_2 and MgO and slightly lower V, Sc, and Fe_2O_3. It would cause higher K_2O and Ba, which tend to be leached from basalts by subaerial tropical weathering and thus are carried away in solution and in clays. All of these effects are apparent in correlative trends of these constituents to one another in our data. The only anomalous oxide is Na_2O, which is present only in minor amounts in tropical detrital clays. It would be relatively diluted in samples with a high proportion of such clays. Where the CaO content is low, for example, the Na_2O contents would be low as well and have a

F52. LOI vs. K_2O for vitric tuffs, p. 105.
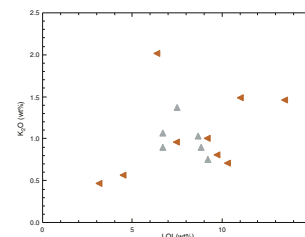
F53. Ternary diagrams showing effects of addition of detrital and authigenic clays to basaltic volcaniclastic material, p. 106.
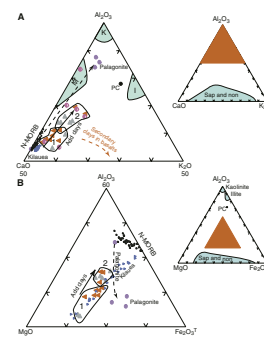
positive correlation. However, all samples analyzed from Hole 1223A have high Na_2O contents that are anticorrelated with CaO. Analyzed samples that have a large detrital clay component have more Na_2O than samples with a small clay component. In some samples, especially the tuffs, this may be related to the abundance of sodic zeolites (e.g., analcime) in vesicles, cavities, and other void spaces. High Na_2O would therefore be an authigenic effect. Another possibility is that sea salt, especially in the porous claystones and siltstones, caused the elevated Na_2O concentrations. After several days of desiccation in the core laboratory, salt crystals formed on the sawed surfaces of some of these rocks.

Two very closely spaced samples (200-1223A-4X-2, 53–56 and 56–58 cm) have slightly higher SiO_2 and P_2O_5 than any of the others. This may be the result of a higher proportion of radiolarian-bearing pelagic clay in these samples. The radiolarians would cause the SiO_2 enrichment, whereas a high proportion of icthyoliths (fish teeth) in the pelagic clay would provide the elevated P_2O_5 concentrations. The lower SiO_2 and P_2O_5 contents in the other tuffs, siltstones, and claystones indicate that pelagic clay is a smaller component and that it is more likely that their clay component is detrital.

The effects of palagonitization on the bulk composition of the lower tuff seem to have been fairly small, whereas in some subaerial settings, it causes wholesale reconstitution of the composition of glassy tuffs (e.g., Hay and Iijima, 1968). The chemistry of the lower tuff is similar to that of the upper tuff, the siltstones, and the claystones. The main effect of the palagonitization is that the lower tuffs have higher LOI and are reddish brown rather than greenish gray. This conclusion may need revision, or at least it will become better understood when actual compositions of glass pairs and palagonite can be determined on the samples and additional literature sources are investigated. However, for now, we can say that several samples of both tuffs and the claystones and siltstones circled as Group 1 in Figure F53 have comparatively low proportions of detrital clay and fairly minimal effects of alteration. Thus, these samples are the most useful for comparison with potential igneous sources in order to determine the provenance of their volcaniclastic components.

Provenance

Provenance is an important issue because of the possibility that the volcaniclastic rocks at Site 1223 are related to the Nuuanu Landslide, which originated by the collapse of a major portion of the island of Oahu. An island provenance would be a prerequisite if this was indeed the case. However, the problem with an island provenance is that heat seemed to be required to explain the induration of the two tuffs so near the seafloor. A local provenance for the tuffs, perhaps a nearby seamount, would be consistent with this hypothesis. Accordingly, we compared bulk compositions of samples from Hole 1223A with Hawaiian basalts, with lavas of the North Arch volcanic field some 300 km to the northwest, and with both normal and enriched mid-ocean-ridge basalts (N-MORB and E-MORB). Our initial petrographic interpretation was that the olivine-bearing glass shards in the tuffs resembled types of Hawaiian tholeiite, but the issue still remained whether tholeiites might have erupted recently along the Hawaiian Arch and thus provided a local source for the tuffs essentially identical to the islands.

The presence of a significant component of aluminous detrital clay, produced by subaerial erosion and confirmed by chemical analyses, clarifies these questions. The source of the aluminous component in all of the sediments and tuffs was clearly the islands, making it unlikely that a separate local source provided the volcanic glass shards and associated minerals and lithic fragments. But can the chemical analyses tell us which type of Hawaiian basalt contributed to the sedimentary materials? Tholeiitic basalt is the most voluminous type of Hawaiian lava (e.g., Macdonald and Katsura, 1964; Clague and Dalrymple, 1987). However, alkalic olivine basalts, basanites, and olivine nephelinites erupt during both the earliest and latest stages of Hawaiian volcanism, and it is possible that these contributed volcaniclastic materials to the sedimentary succession at Site 1223.

Figure F54 shows the similarity of analyzed samples from Hole 1223A to Hawaiian tholeiite represented by basalt glasses from Kilauea Volcano and its undersea extension, Puna Ridge (Clague et al., 1995). The diagrams also show strong differences between our samples (as well as Kilauea tholeiites) and Hawaiian alkalic olivine basalts, basanites, and olivine nephelinites from three localities—the North Arch volcanic field (Dixon et al., 1997), the Honolulu Volcanic Series of Oahu (Jackson and Wright, 1970; Clague and Frey, 1982), and the Hana Volcanic Series of Haleakala Volcano, Maui (Chen et al., 1991). Data are also plotted for a representative suite of abyssal tholeiites from the East Pacific Rise (Fig. F54C, F54D) (J. Natland, Y. Niu, and P. Castillo, unpubl. data). This suite includes a wide range of primitive and differentiated abyssal tholeiites (N-MORB).

Because we compare bulk sediment compositions to compositions of glasses from Kilauea and the East Pacific Rise, the effects of abundant olivine in Site 1223 samples need to be taken into account. Olivine forms 9–13 wt% of the mode of the vitric tuffs. If its composition is about Fo_{85}, the effect of subtracting 13 wt% of olivine from the bulk composition of a tuff with 10.5 wt% Al_2O_3, 47.5 wt% SiO_2, and 11 wt% iron as Fe_2O_3 is shown by the arrows in Figure F54A and F54B. This is approximately the composition of Group 1 tuff in Figure F53 with the lower amount of detrital clay component. The tips of the arrows in Figure F54A and F54B are approximately that of an aphyric basalt or basalt glass still very closely resembling the composition of Kilauea tholeiite. It differs greatly from the compositions of Hawaiian alkalic basaltic lavas and MORB.

In Figure F54C and F54D, compositions of samples from Hole 1223A are additionally compared with E-MORB glasses, using a compilation drawn from the literature, and with eight analyses of magnesian tholeiites and tholeiitic picrites from Koolau Volcano (Frey et al., 1994). E-MORBs resemble N-MORBs, except they are slightly more aluminous. Most of the Koolau lavas can be distinguished from Kilauea lavas by their slightly higher SiO_2 and lower iron (as Fe_2O_3) contents. On these diagrams, the effects of addition of detrital clays and authigenesis make it difficult to ascertain which Hawaiian volcano is the more likely source for the samples from Hole 1223A.

Figure F55 and Table T7 provide additional information about the provenance of samples from Hole 1223A. Data from N-MORB, E-MORB, Kilauea-Puna Ridge, and Koolau Volcano are plotted for comparison. Again, samples from Hole 1223A resemble Hawaiian tholeiites rather than N-MORB or E-MORB. Several of the tuffs from Hole 1223A, including those falling in Group 1 in Figure F53, have higher SiO_2, lower Ba,

F54. Major oxide discriminant diagrams, p. 107.
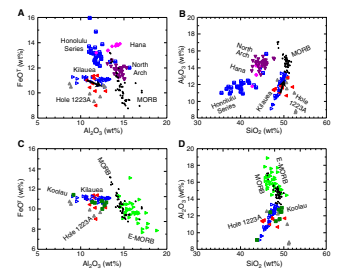
F55. Comparison of Hole 1223A with Kilauea-Puna Ridge and Koolau tholeiites, p. 108.
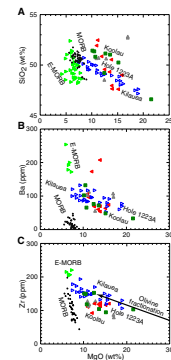
and lower Zr than Kilauea glasses at given MgO content (Fig. F55A, F55B, F55C). For these elements, they more closely resemble Koolau Volcano. SiO_2 and Ba concentrations reflect the presence of some detrital clay, but in two samples Ba clearly is too high. However, this comparison holds for those samples with the least amount of clay and highest CaO contents. In addition, Zr is an element that is usually unaffected by alteration. It is also usually precisely and consistently measured from one laboratory to the next. The measurements should give a relatively accurate estimation of its original concentration in volcanic glass and lithic fragments in the sediments and tuffs, diluted by up to 13 wt% with olivine and only small amounts of clay in several of the tuffs. The effect of subtraction of olivine (with ~45 wt% MgO and no Zr) is shown by the arrow in Figure F55C. Addition or subtraction of olivine cannot direct residual liquid compositions from Koolau into the field of Kilauea tholeiites. Dilution by clays in samples of Hole 1223A will draw compositions nearly toward the origin (no Zr; <1 wt% MgO), but in several samples this effect is minimal. The diagram thus suggests a Koolau provenance for the vitric tuffs. The higher SiO_2 and lower Ba and $Fe_2O_3{}^T$ (Fig. F54C) of the same samples support this contention.

These data are not definitive. Preliminary electron microprobe data of glasses from the upper vitric tuff show chemistry similar to Koolau Volcano (S. Sherman, unpubl. data). The high MgO content in the bulk analyses is due to the accumulation of olivine and is not due to high MgO in the glass (preliminary microprobe analyses have MgO contents between 6 and 8 wt%). The evaluation here, however, suggests that certain trace elements, including Ba and Zr, should also be measured on glasses in the final provenance evaluation.

PALEOMAGNETISM

We used progressive alternating-field (AF) demagnetization of split-core sections and discrete samples along with rock magnetic experiments to characterize the paleomagnetic signal and resolve the magnetization components recorded in the recovered core. The component interpreted to record the magnetization at or near the time of deposition was then used to construct a magnetostratigraphy for Hole 1223A.

All split-core and discrete samples have a sizable drilling overprint, which is characterized by a steep downward direction and by a radial-horizontal component that points toward the center of the core. In the ODP core orientation system, the latter results in a strong bias in the declinations toward 0°. Initial natural remanent magnetization (NRM) measurements are thus characterized by inclinations >+60° and declinations of ~0°. In general, <30-mT AF demagnetization removes the drilling overprint but also reduces the magnetization by ~90%. Along the periphery of the core, the drilling overprint can be more demagnetization resistant, sometimes requiring AF demagnetization of up to 60 mT, particularly in the vitric tuff units. Small biases may thus persist in some of the split-core measurements for which AF demagnetization generally did not exceed 50 mT.

Following removal of the drilling overprint and excluding intervals disturbed by drilling, the sediments above 7 mbsf have stable remanent magnetizations that provide a record of the geomagnetic field at or near the time of deposition. Though more difficult to resolve, the underlying units similarly have stable remanent magnetizations, but the acquisition mechanism may be more complex than a depositional remanent

magnetization (DRM) or postdepositional remanent magnetization (pDRM). Given the porous, permeable nature of the vitric tuff units and their degree of alteration (see "Alteration," p. 21, in "Lithology"), some subsequent thermal or chemical remagnetization cannot be precluded.

The magnetostratigraphy provides age constraints that can be used to test hypotheses about the origin of the lithologic units. For example, are the volcaniclastic turbidites in Unit 2, the unconsolidated black sand in Unit 4, the vitric tuffs in Units 5 and 11, and/or other units co-eval with previously dated landslide events? Alternatively, if the origin of the lithologic units can be established independently, then ages for each unit provided by the magnetostratigraphy will be the primary constraint on the age of depositional (landslide?) events. At this point, the ages provided by the magnetostratigraphy indicate that Units 2 through 14 are >1.8 Ma and <2.6 Ma. Thus all are roughly coeval with the range of ages for the Nuuanu Landslide, which is interpreted to have occurred between 1.95 and 2.15 Ma by Herrero-Bervera et al. (2002).

Split-Core and Whole-Core Samples

Measurements

We made 28,062 remanent magnetization measurements along the archive-half sections from Hole 1223A. Measurements were made every 1 cm before and after AF demagnetization. All sections were progressively demagnetized in steps of 1–5 mT up to peak fields of between 50 and 70 mT. The high peak fields were necessary to resolve the characteristic remanent magnetization (ChRM) direction and allowed us to complete principal component analysis (PCA) on each interval measured along a section. Magnetic susceptibility was measured on whole-core sections every 2.5 cm (Fig. F56). Both remanence and susceptibility data for these sections are available from the ODP Janus database.

Analysis and Results

For interpretation of the data, we extracted the split-core results from the ODP Janus database and removed all measurements made within 5 cm of the section ends, as these measurements are biased by edge effects. We then removed all measurements made in regions disturbed by drilling or where there were gaps, such as those caused by removal of whole-round samples. The disturbed intervals and gaps used are given in Table T8. The resulting cleaned data set contains 22,843 measurements made at 1455 intervals along the archive halves (Table T9).

Prior to demagnetization, the inclinations display a very strong tendency for directions that point steeply downward and to the north; the inclinations are positive and typically >60° over the entire cored interval, indicating the presence of a steep downward-directed drilling overprint (Fig. F56). Also, the declinations are biased toward 0°, which for azimuthally unoriented cores (as are all the Leg 200 cores) indicates the presence of a radial overprint. The overprint is radially inward for the APC and XCB cores from Hole 1223A. Both radial and vertical overprints are observed during most ODP legs and are artifacts of the drilling process.

The overprint is similar, though not identical, to applying an isothermal remanent magnetization (IRM) of roughly 5–25 mT to the core. Thus, the intensity measured prior to demagnetization is a good proxy

F56. Inclination, declination, and intensity prior to AF demagnetization, p. 109.
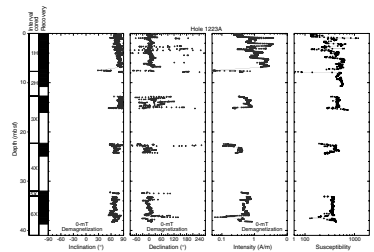
T8. Drilling-disturbed intervals and gaps, p. 147.

T9. Paleomagnetic data from archive-half sections, Hole 1223A, p. 148.

for concentration of magnetic minerals (mainly magnetite and titano-magnetite), as is the susceptibility, with both giving similar relative variations downhole (Fig. F56). The median intensity is 6.09×10^{-1} A/m prior to demagnetization but is reduced to 2.61×10^{-2} A/m after 20-mT demagnetization. Thus, over 90% of the magnetization of the samples is generally removed in order to remove most or all of the drilling overprint.

Orthogonal vector demagnetization plots illustrate that a ChRM direction can be isolated for most of the cored interval following removal of the drilling overprint by AF demagnetization of 10–30 mT (Fig. F57). For sediments and rocks from Cores 200-1223A-2H through 6X, the drilling overprint is more resistant to demagnetization, requiring demagnetization up to 50 mT to remove most or all of the overprint (Fig. F58). After the drilling overprint has been removed, the measured intervals generally display linear demagnetization paths that trend toward the origin or nearly to the origin. It is this magnetization component that is considered the ChRM, particularly the highest coercivity component following >30-mT demagnetization. In some cases the ChRM is not resolved, although the change in direction during demagnetization can often be used to infer the magnetic polarity of the interval. In the latter case, the directions obtained during progressive demagnetization tend to lie along a great circle path on a stereonet, with the beginning of the path representative of the drilling overprint and the directions after each demagnetization step trending closer and closer to the ChRM direction and possibly reaching it as shown in Figure F58.

In the vector demagnetization diagrams, the systematic offset from the origin of the linear demagnetization paths, such as is apparent by the decay of the declination in Figure F57, may be caused by a sensor for one axis of the magnetometer being slightly more noisy than the others, by small magnetic fields existing in the sensor region, or by real magnetization components that are unremoved by AF demagnetization. In some cases, the magnetization of the interval has been reduced to near the noise level of the magnetometer, but generally this is not the case. Furthermore, the offset is consistent over many measurements rather than being random noise. Given that many of the demagnetization paths trend to the origin, we think it is most likely that any consistent magnetization direction measured for an interval following AF demagnetization is related to unremoved components of magnetization in that interval.

In order to estimate the ChRM, we conducted PCA (Kirschvink, 1980) on the data using a program that iteratively searches for the demagnetization steps that minimized the size of the maximum angular deviation (MAD) angle, which is a measure of how well the vector demagnetization data fit a line. MAD values <10° are typically considered to provide lines that fit the observations well. The program requires at least four demagnetization steps be used, never uses steps lower than a user-defined value, does not require that the best-fit PCA line pass through the origin of the plot (the "free" option of standard PCA), and generally favors high-coercivity components over low-coercivity components in samples with multicomponent magnetizations. Because the drilling overprint persisted beyond 20-mT demagnetization in some of the intervals, particularly in the vitric tuffs though less so in the soft sediments, we only used results from 30-mT or higher demagnetization for Core 200-1223A-1H and from 40-mT or higher demagnetization for the other cores in the PCA. For comparison, the program also computes a Fisherian mean of the highest three or four demagnetization steps for

F57. AF demagnetization results, 200-1223A-1H-1, 65 cm, p. 110
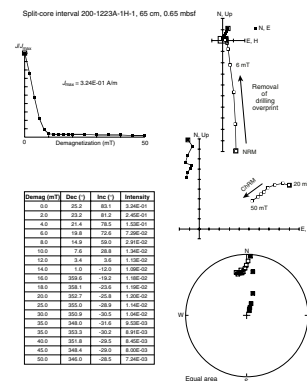
F58. AF demagnetization results, 200-1223A-6X-3, 90 cm, p. 111.
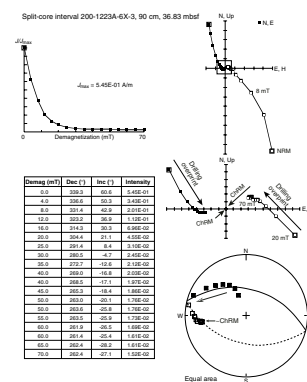
each interval. This is referred to as the stable endpoint direction. Typically, only the highest three demagnetization steps are used in the average, unless the mean of these three directions has a precision parameter <200 (a measure of dispersion), in which case the fourth highest demagnetization step is included. In cases where the precision parameter is <200, the program will first search for outliers and remove them if they lie >10° from the mean. Both the PCA and stable endpoint directions for all 1455 intervals are given in Table **T10.** Comparison of the stable endpoint with the PCA direction can be useful for indicating where unremoved or partially unremoved magnetization components exist or where progressive demagnetization has been ineffective in revealing linear demagnetization paths. To assist with this comparison, we have computed the angular distance between the two directions and included it in Table **T10.**

Comparison of inclinations obtained from the methods show good agreement for most of the upper 7 m of the section (Fig. **F59**). The agreement is an indication that AF demagnetization has been successful in removing overprints and that a single component of magnetization remains. The mean inclination of this direction in the normal and reversed polarity intervals is consistent with the inclination expected for a geocentric axial dipole, which is 40.3° for normal polarity rocks and –40.3° for reversed polarity rocks at Site 1223 (Fig. **F59**). Thus, the ChRM provides a record of the magnetic field direction at the time the sediments were being deposited (a DRM) or shortly thereafter (a pDRM). Because AF demagnetization did not fully resolve the ChRM in some intervals below 7 mbsf, the PCA and stable endpoint directions sometimes do not coincide. In such cases, we think the stable endpoint direction will generally be closer to the true ChRM direction because it is an average of the directions from the highest demagnetization steps.

Discrete Samples

Measurements

We measured the NRM of 25 discrete samples before and after AF demagnetization (Table **T11**). Of these, 11 samples (~7 cm³ volume) were collected from sediments from Cores 200-1223A-1H and 2H and the other 14 are from two 1-cm-thick intervals in the lowest vitric tuff—3 samples are from interval 200-1223A-6X-1, 55–56 cm, and 11 samples are from interval 200-1223A-6X-2, 90 cm. The samples from the vitric tuff were cut into small pieces with volumes <1 cm³. The pieces were taken from different parts of 1-cm-thick slices of the working half to assess how the drilling overprint varied with location.

Following demagnetization, we conducted ARM and IRM experiments (see **"Paleomagnetism,"** p. 17, in the "Explanatory Notes" chapter) on the 11 sediment samples and on 8 of the vitric tuff samples (Tables **T12, T13**).

Analysis and Results

PCA and stable endpoint analyses of the NRM were conducted in the manner described above for the split cores, with results given in Table **T14.** The discrete samples were demagnetized in more steps and at higher peak fields, which allows the ChRM to be analyzed in more detail. Orthogonal vector demagnetization plots for sediments from Core 200-1223A-1H show the samples have two components, the low-

T10. PCA results from paleomagnetic data, Hole 1223A, p. 149.

F59. Magnetostratigraphy and inclinations from split cores and discrete samples, p. 112.
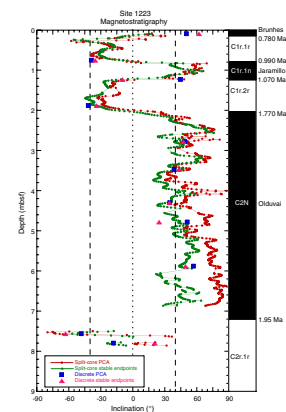
T11. Paleomagnetic data from discrete samples, Hole 1223A, p. 150.

T12. ARM data from discrete samples, Hole 1223A, p. 151.

T13. IRM data from discrete samples, Hole 1223A, p. 152.

T14. PCA results from paleomagnetic data from discrete samples, Hole 1223A, p. 153.

coercivity drilling overprint, which is removed after 10- to 20-mT demagnetization, and the ChRM (Figs. F60, F61). The discrete sample directions agree well with what was obtained from split-core measurements, and the inclinations agree with the expected geocentric axial dipole inclination at Site 1223.

The few samples taken from the lowest vitric tuff unit illustrate that the ChRM can also be resolved by detailed demagnetization of samples taken from near the center of the core (Fig. F62), where typically 10- to 20-mT demagnetization removes the drilling overprint. Samples from near the periphery, however, are more severely affected by the drilling overprint and often require demagnetization up to 55–60 mT to remove the overprint. By 60-mT demagnetization, only a few percent of the initial NRM remains, making it more difficult to accurately estimate the direction of the remaining ChRM. This would explain the difficulty we had resolving the ChRM in some intervals from the split-core measurements (e.g., compare Fig. F62 to Fig. F58).

Although we have not had time to thoroughly evaluate the magnetic mineralogy that carries the remanent signal, the AF demagnetization behavior, IRM acquisition (Fig. F63), backfield IRM results, and volcanogenic lithology together provide strong circumstantial evidence that magnetite or titanomagnetite is the main magnetic carrier. A higher-coercivity mineral, perhaps hematite, could also be present as evidenced by a small component of the ChRM that remains after AF demagnetization of 80 mT and after applying a saturation IRM of 1 T and then demagnetizing the sample up to 80 mT.

Magnetostratigraphy

The magnetic inclination derived from the ChRM is used as the indicator of polarity, where positive inclinations indicate normal polarity and negative inclinations indicate reversed polarity. Because the cores are azimuthally unoriented, we do not use the declination as it does not provide direct evidence of polarity, although it could be used to indicate relative declination changes. Because coring gaps of several meters are present within the cored interval and because the lithologic section contains units that indicate discontinuous sedimentation, such as the turbidites, some polarity intervals may not have been recovered or may be missing. No independent age constraints are currently available, so we have based the correlation of the polarity intervals with polarity chrons upon the assumption that the top of the lithologic sequence was 0 Ma. In addition, seismic data and previous piston coring in the area indicate that the sediments are likely to be a few million years old (Naka et al., 2000; Herrero-Bervera et al., 2002).

With the above constraints and caveats, the magnetostratigraphic record from Hole 1223A (Figs. F59, F64; Table T15) appears to contain all the major chrons and subchrons from Chron C1n (the Brunhes Chron; 0.0–0.780 Ma) through Chron 2r (1.950–2.581 Ma). Possibly Subchron C2r.1n (2.140–2.150 Ma), which falls within Chron C2r, is recorded in the bioturbated clay (lithologic Unit 6) near the base of Section 200-1223A-3X-2. The interval from the core catcher of Core 200-1223A-1H to the bottom of Core 200-1223A-6X is otherwise reversely magnetized and is interpreted to lie within Chron C2r.

Uncertainty in the polarity of the bioturbated clay unit (Unit 6) in Section 200-1223-3X-2 results from an ambiguity in the orthogonal demagnetization diagrams from split-core measurements. After removal of the drilling overprint, a linear demagnetization path indicative of a

F60. AF demagnetization results, 200-1223A-1H-2, 38 cm, p. 113.
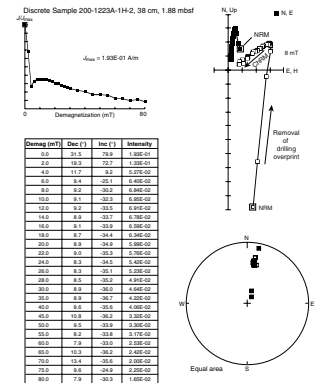
F61. AF demagnetization results, 200-1223A-1H-3, 47 cm, p. 114.
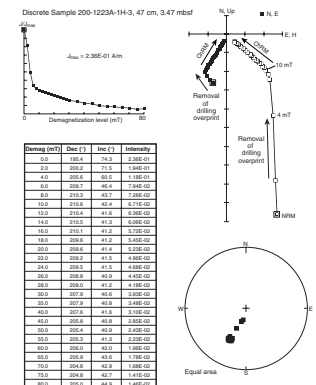
F62. Orthogonal vector demagnetization plots, p. 115.
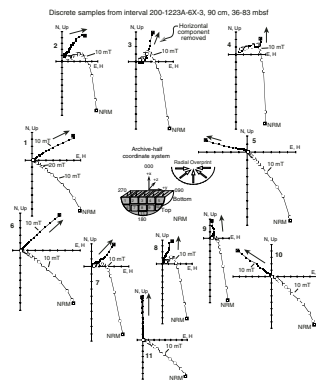
T15. Magnetostratigraphy, Site 1223, p. 154.

normal polarity interval is apparent, but the demagnetization path decays toward a shallow inclination, which with further demagnetization could be reversed polarity rather than the origin of the plot. As discussed above, there are multiple reasons why such behavior may occur, one of which is that there is an unremoved reversed polarity component. Discrete samples have been collected from this interval and will be measured postcruise in a less noisy magnetic environment, which should help resolve the ambiguity.

A notable anomaly in the magnetostratigraphy is the thinness of the upper normal polarity interval, which spans only the top 14 cm of Core 200-1223A-1H. This is thinner than expected by ~1 m based on prior piston coring in the vicinity (Herrero-Bervera et al., 2002). Furthermore, there is a distinct possibility that the BHA was slightly below the mudline when Core 200-1223A-1H was shot. The resulting recovery of <9.5 m (a full core) was taken to indicate that the mudline had been recovered. Partial recovery could have been caused instead by the cutting shoe encountering the turbidite in Unit 2, the base of which contained granules. The core was deformed through the base of the turbidite, indicating the piston corer did cut through the unit with difficulty. Additionally, penetration of the cutting shoe is often inhibited in sandy units, as was also the case for Core 200-1223A-2H. Thus, we may not have recovered the very upper meter or so of the sedimentary section or sedimentation rates may vary locally.

Ages and Sedimentation Rates

Given the magnetostratigraphic record, ages for the lithologic units and their boundaries can be estimated by interpolation between the observed reversals (Table **T16**). Linear interpolation implies constant sedimentation between the reversals, which is likely a poor assumption given the nature of the lithologic section. It does, however, give ages consistent with stratigraphic superposition and the magnetostratigraphic record. Thus, we provide ages based on linear interpolation, but the reader should be aware of the limitations of this simplistic age model.

Similarly, average sedimentation rates are calculated between reversals (Table **T15**). Coring gaps between cores and other intervals of poor recovery or suspect recovery, such as inferred here for the top of Chron C1n, may cause some inaccuracies in these estimates. Most of the reversals, however, occur within Core 200-1223A-1H, in which coring gaps are not an issue but hiatuses or erosional events may remain problematic. The average sedimentation rates are, of course, poor estimates of the true sedimentation rates for turbidites and landslide deposits.

MICROBIOLOGY

Microbiology Objectives for Both Sites

Leg 200 was the first ODP cruise to carry out onboard microbial examinations of water, sediment, and rock samples. Classical cultivation approaches as well as fluorescent in situ hybridization (FISH), different fluorescent staining techniques, and shore-based investigations like deoxyribonucleic acid (DNA)-related analyses, biolipid marker analyses, and various microscopic methods such as electron microscopy (transmission electron microscopy [TEM], environmental scanning electron

F63. IRM acquisition results for two vitric tuff subsamples, p. 116.
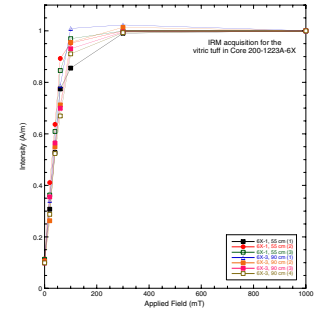
F64. Magnetostratigraphy, inclination, and declination from PCA and stable endpoints, p. 117.
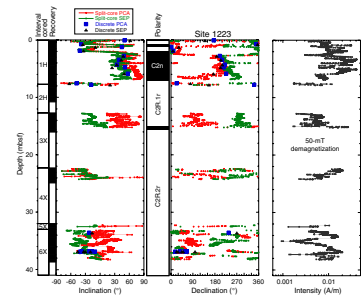
T16. Ages of lithologic units, Hole 1223A, p. 155.

microscopy [ESEM], and field emission scanning electron microscopy [FE-SEM]) were used.

The microbiology objectives for Leg 200 included

1. Determining the amount of total cell counts and active bacteria, in both pore waters and attached to the solid phase (so-called "biofilm" communities) within deep marine sediments and the associated volcanic rocks by nucleic acid staining techniques and FISH;
2. Conducting cultivation studies with various solid and liquid media under both aerobic and anaerobic conditions including most probable number (MPN) determinations for sulfate-reducing and fermentative bacteria;
3. Comprehensive sampling of both sediments and rock material for postcruise DNA extraction and further elucidation of the microbial diversity by DNA analysis and for assessing proxies of bacterial activity within the deep biosphere by electron microscopy; and
4. A detailed determination of bacterial lipids as diagnostic tools for particular groups of both eubacterial and archaeal life.

The general goal of the microbiological investigations conducted during Leg 200 was to obtain insights into the mutual interdependent relations between the microbial communities and the geochemical processes within the sedimentary, igneous, and volcanic environments.

Results at Site 1223

Samples were taken for both cultivation and cultivation-independent approaches. Magnetostratigraphic measurements of the first core indicated that during recovery a significant amount of presumably loose sediment was displaced as the APC penetrated into the sediment. The sample from 0 mbsf might therefore be more accurately defined as near surface. From a water depth of 4235.1 m, two near-surface samples were taken from the uncontaminated center part of the core. After removing a thin layer (0.5 cm) of sediment from the section's end, samples were taken from the very upper part and from 5 cm deep in the core under sterile conditions using autoclaved spatulas. The sediment was classified as yellowish brown clay with volcaniclastic turbidites (Fig. F65). The next samples came from distinct layers of black sands at depths of 0.95 and 7.90 mbsf, respectively (Fig. F66). Additional sediment samples, classified as volcaniclastic turbidites, were taken at depths of 5.95 and 6 mbsf (Fig. F67). In order to determine distinctive microbial communities at various depths and within different volcaniclastic layers, a sample of volcaniclastic silt claystone was taken from a depth of 23.94 mbsf (Fig. F68). Further samples were taken in order to compare the microbial communities of the two different tuff layers embedded in volcaniclastic silty claystone from a depth of 32.24 mbsf (classified as altered vitric tuff) and 37.33 mbsf (described as palagonitized crystal vitric tuff) (Figs. F69, F70).

For a comparative determination of total cell counts within the sediments from Hole 1223A, the green fluorescent nucleic acid stains SYTO 9 and SYBR Green I and the red fluorescent stain SYTO 62 were successfully combined with the commonly used DNA stain, 4′,6-diamidino-2′-phenylindole-dihydrochloride (DAPI). The detection limit was calculated to be 1×10^4 cells per gram of wet sediment. Bacteria were present

F65. Uppermost yellowish brown clay, p. 118.

F66. Black sand layers, p. 119.
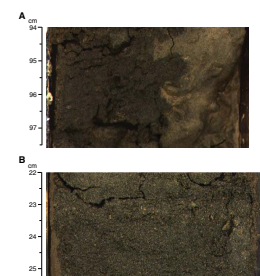
F67. Sediment characterized as volcaniclastic turbidites, p. 120.

F68. Volcaniclastic silt claystone, p. 121.

F69. Tuff layer embedded in volcaniclastic silty claystone classified as altered vitric tuff, p. 122.

F70. Tuff layer embedded in volcaniclastic silty claystone classified as palagonitized crystal vitric tuff, p. 123

in all sediment samples from Hole 1223A down to 5.95 mbsf. The most abundant bacterial community was present in near-surface sediments (Sample 200-1223A-1H-1, 0–5 cm) with at least 2.3×10^{10} cells per gram of wet sediment. Figure **F71** shows an overview of cells and microcolonies stained with the green fluorescent DNA-staining dye SYBR Green I. The inset shows a close up of a bacterial microcolony embedded in extracellular polymeric substances. Microcolonies and microbial aggregates were counted as one cell.

In the sediment layer at 0.95 mbsf (Sample 200-1223A-1H-1, 95–96 cm), the number of total cell counts significantly declined to 1.5×10^8 cells per gram of wet sediment. Population numbers decrease rapidly with increasing depth, confirming the general model for bacterial distributions in marine sediments as previously described by Parkes et al. (1994).

In the sediment layer located at 5.95 mbsf (Sample 200-1223A-1H-4, 145–150 cm), classified as volcaniclastic turbidites, the amount of total cell counts increased again to 3.2×10^9 cells per gram of wet sediment.

To determine the MPN of sulfate-reducing and fermentative bacteria, MPN series were prepared from both sediment samples and vitric tuff. From the altered vitric tuff, additionally 25 distinct microbial colonies could be isolated and further characterized as facultatively anaerobic organisms forming stable cell aggregates under appropriate conditions (Fig. **F72**). Applying DNA-staining fluorescent dyes and FISH with group-specific oligonucleotide probes, it turned out that both the cell morphology and phylogenetic affiliation of all isolates were very similar. All hybridizations were performed at 48°C under stringent conditions using 35% formamide solution in the hybridization buffer and the corresponding sodium chloride concentration in the washing buffer (Manz, 1999). Strong fluorescent signals could be detected using probes EUB338, SRB385Db, and, to a minor extent, with probe LGCa-c. In contrast to this, no hybridization signals could be monitored after hybridizations with probes ARCH915, EUB338-II, EUB338-III, ALF1b, GAM42a, or CF319a.

Discussion and Summary

A common feature shared by all bacteria within the sediment samples was the small average cell size of 1 µm at best, which is in good agreement with the results reported by Torella and Morita (1981). For a comprehensive review on sediment bacteria, see Nealson (1997). In contrast to the widely used acridine orange staining technique, the application of new fluorescent dyes with higher quantum yields (e.g., SYBR Green I and SYTO 9) in combination with objectives of numerical apertures >1.2 enabled the clear visualization of bacterial cells with average cell size of 1 µm or less. Hence, the staining techniques performed in this study led to total cell counts in the sediments that range about one order of magnitude higher than the previously reported bacterial cell counts in sediments from deep marine environments (Parkes et al., 1994; Cragg et al., 1996). One has also to keep in mind that marine bacterial communities might be associated with high numbers of bacteriophages, with average particle sizes ranging up to 0.5 µm. These bacteriophages may significantly contribute to the total cell counts as determined by high-performance nucleic acid stains.

In this study, all colonies obtained from the altered vitric tuff proved to be mixed cultures consisting of at least three different bacterial specimens as revealed by FISH. This is further evidence that the classical ap-

F71. Single nucleic acids containing objects and bacterial microcolonies and a DNA-stained bacterial microcolony, p. 124.
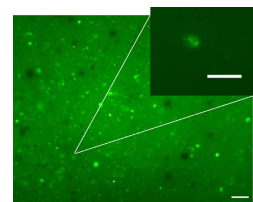
F72. Four distinct colonies obtained from altered vitric tuff cultivated under aerobic and anaerobic conditions, p. 125.
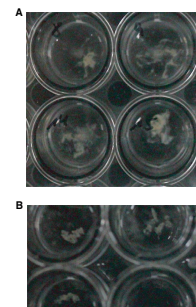
proach to obtaining a pure culture (that is transferring a single colony three times in order to obtain a pure culture) is insufficient to get pure cultures from highly complex, heterogeneous environmental samples. Using FISH, strong fluorescent signals could be detected with the 16S ribosomal ribonucleic acid (rRNA)-targeted oligonucleotide universal probe EUB338 (Amann et al., 1990) specific for Bacteria (Fig. F73). No hybridization signals could be monitored after hybridization with the universal probe ARCH915, specific for the domain Archaea (Burggraf et al., 1994), or the probes EUB338-II and EUB338-III, targeting *Plancto-mycetales* and *Verrucomicrobia* (Daims et al., 1999). As the main phyla of bacteria common in seawater are affiliated within the alpha- and gamma-Proteobacteria (Gauthier et al., 1995; Gonzales and Moran, 1997), the subclass-specific probes ALF42a and GAM1b (Manz et al., 1992) were used to specify the isolated bacteria in terms of potential allochthonous contaminants. Because no fluorescent signals could be detected after application of these probes, it seems very unlikely that the newly isolated bacteria belong to bacterial genera known to be fast-growing heterotrophic contaminants from ambient seawater (e.g., *Pseudoalteromonas* and Zoseobacter group). Positive hybridization signals were also not observed in additional hybridizations performed with probe CF319a/b (Manz et al., 1996), which is specific for the *Cytophaga-Flavobacteria* group, known to be common autochthonous inhabitants within marine microenvironments. The most abundant part of the investigated microcolony, however, showed strong fluorescent signals after hybridization with the probe SRB385dD (Rabus et al., 1996), which was assigned to sulfate-reducing bacteria (Fig. F74). Only a few, but strong, fluorescent signals were achieved by the application of three probes LGCa-c (Meier et al., 1999), initially designed for the specific detection of Gram-positive bacteria with low G+C content of DNA (Fig. F75). Interestingly, the sum of the hybridized cells did not cover all cells visualized by DNA staining. This indicates the presence of further bacterial cells within the microcolony that have not been characterized yet.

Future Work

Besides the onboard investigations performed during Leg 200, additional microbiology data will be generated in shore-based studies. The major effort will be to determine the bacterial composition of the sediments as well as the altered and palagonitized crystal vitric tuff by DNA extraction and subsequent phylogenetic analyses. The characterization of bacteria, isolated from the anaerobic enrichment cultures and from the aerobic colonies grown on solid agar plates containing different levels of substrates, will be continued. Proxies of past microbial activities in the samples will be investigated by extended lipid biomarker analysis for the presence of both bacterial and archaeal traits.

Based on the rRNA sequences of the isolates and clones, additional isolate-specific probes will be developed to recover the cultivated isolates and sequenced clones by FISH. Using these probes, the spatial distribution of the targeted organisms will be studied within the fixed material and within thin sections of both the sediments and the volcaniclastic tuff. Sample material will be embedded in different mounting media, and the spatial bacterial distribution within the thin sections will be investigated by the combination of FISH and wide-field deconvolution epifluorescence microscopy (Manz et al., 2000). To elucidate the nature of the sulfate-reducing bacteria as shown by FISH in the

F73. Single bacterial cells within bacterial colony CFU1 after DAPI staining and hybridization with the Bacteria-specific CY3-labeled probe EUB338, p. 126.
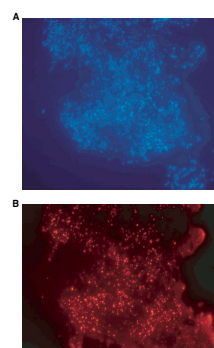
F74. Single bacterial cells within bacterial colony CFU16 after DAPI staining and hybridization with the CY3-labeled probe SRB385Db, p. 127.
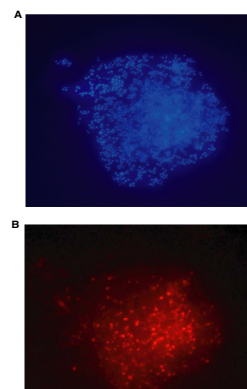
F75. Single bacterial cells of bacterial colony CFU1 after DAPI staining and hybridization with the CY3-labeled probe LGCa-c, p. 128.
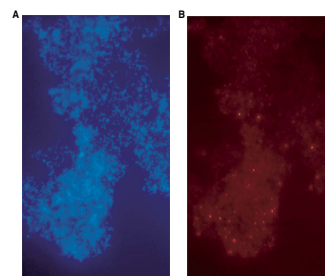
microcolony obtained from altered vitric tuff, further shore-based investigations will be carried out using recently developed genus- to species-specific probes (Manz et al., 1998).

PHYSICAL PROPERTIES

Physical properties in Hole 1223A were measured on whole cores, split cores, and discrete samples. The MST was used to perform nondestructive measurements of bulk density (GRA bulk density), magnetic susceptibility, compressional wave velocity (as measured by the *P*-wave logger [PWL] mounted on the MST), and NGR on whole cores. GRA bulk density and magnetic susceptibility were measured every 2.5 cm. Discrete sample measurements were conducted on sediments and hard rock cores. Compressional wave velocity was measured on split cores using the PWS3 contact probe system in the x-direction for soft sediments and in the x-, y-, and z-directions for hard rock cubes. Moisture and density, such as bulk density, water content, porosity, and grain density, were measured on discrete samples. Thermal conductivity was measured on whole cores for soft sediments and on discrete samples for hard rock cores.

MST Measurements

GRA Density

Lithologic Units 1 and 2 (0 to ~7 mbsf), which are clay and turbidite layers, show a rapid increase of GRA bulk density, ~1.2 to ~2.0 g/cm³ with increasing depth (Fig. F76A). Unit 4 (between ~8 and ~11 mbsf) corresponds to a black sand layer. The bulk densities for this layer also show a rapid increase from ~2.0 to ~2.2 g/cm³ with increasing depth. Unit 5, a crystal vitric tuff, is one of the key horizons in addressing the generation of the section. The bulk densities of Unit 5 (13–15 mbsf) show a gradual increase from ~1.7 to ~2.0 g/cm³. In Units 8 through 10, bulk densities are scattered around 1.8 ± 0.2 g/cm³, suggesting some heterogeneity. Subunit 11B (between 33 and 37 mbsf) is a palagonitized crystal vitric tuff horizon giving fairly constant bulk densities of ~1.9 g/cm³. Bulk densities for Units 13 and 14 (~37 and 38.7 mbsf) show sudden changes from ~1.3 to ~1.9 g/cm³, corresponding to silty claystone and clayey siltstone, respectively.

Magnetic Susceptibility

Magnetic susceptibilities scatter between ~100 and 600 at depths shallower than ~11 mbsf (Fig. F76B) (all susceptibilities reported here are in raw meter units). In Unit 5, which is the crystal vitric tuff layer, they remain approximately constant at 400–500. In Unit 8, the values rapidly increase from ~170 to 400. In Unit 10 (~23–25 mbsf), the values decrease from ~600 to 300. In Subunit 11B, the palagonitized crystal vitric tuff (~33–37 mbsf) has fairly constant susceptibility values of 300–400. Units 12 and 13 show similar trends as seen in the GRA bulk densities.

F76. MST GRA density, magnetic susceptibility, and NGR, p. 129.
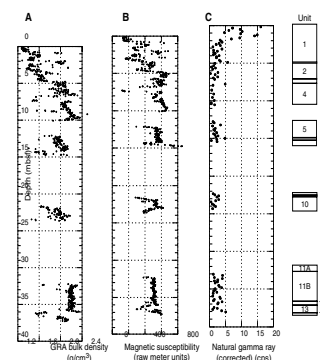
Natural Gamma Radiation

Corrected NGR measurements show a quite simple pattern. Unit 1 (0–5 mbsf) shows a rapid decrease from ~15 to a few counts per second (cps) (Fig. F76C). The rest of the units have quite low values that range between 0 and 4 cps.

Thermal Conductivity

Five measurements of thermal conductivity were made (Fig. F77; Table T17). In the sedimentary sections shallower than ~12 mbsf (Units 1–4), the two measurements are fairly constant at ~0.8 W/(m·K) (Fig. F77; Table T17). In Units 5 and 10, the values are also similar ~1.0 W/(m·K). Subunit 11B is ~1.2 W/(m·K).

Moisture and Density

In Hole 1223A, the upper and lower parts of the cored section contain volcanic turbidites and crystal vitric tuffs, respectively. The PWS velocities and bulk densities show similar tendencies to the PWL velocities and GRA bulk densities, respectively. Individual physical property measurements, however, give more precise values in hard rocks, and insight into the microstructure of the cores is provided by the anisotropy of compressional wave velocities.

In general, bulk densities show similar or higher values than dry densities (Fig. F78; Table T18). Grain densities always give higher values than bulk densities. Porosities at this site vary gradually from 80% to 30%, but the porosities for hard volcanic rocks are unusually high. GRA bulk densities match quite well with bulk densities obtained by individual measurements using cubic samples, except for Unit 5, which corresponds to the crystal vitric tuff.

Above 5 mbsf in Unit 1, bulk densities, dry densities, and porosities remain constant at ~1.3 g/cm^3, ~0.4 g/cm^3, and ~83%, respectively (Fig. F78). In Unit 5, which is the crystal vitric tuff, bulk densities, dry densities, and porosities are ~2.2 g/cm^3, ~1.9 g/cm^3, and ~35%, respectively, based on three samples. Grain densities range from ~3 to ~2.8 g/cm^3. Note that the bulk densities of Unit 5 give significantly larger values (~2.2 g/cm^3) than GRA bulk densities (<1.9 g/cm^3) (Fig. F79). The reason for this is not well understood. In Units 8 and 10, bulk densities for three samples and dry densities range from 1.6 to 1.95 g/cm^3 and from 0.9 to 1.5 g/cm^3, respectively. The porosities range from 66% to 47%. Grain densities, however, are constant near ~2.8 g/cm^3. In Subunit 11B, which is palagonitized crystal vitric tuff, bulk densities, dry densities, grain densities, and porosities show fairly constant values: ~2.1 g/cm^3, ~1.8 g/cm^3, ~2.6 g/cm^3, and 31%, respectively. The bulk densities and porosities of this vitric tuff have values similar to the crystal vitric tuff in Unit 5. In the deepest horizon, Units 12 to 14, bulk densities and dry densities increase with depth from ~1.6 to ~1.7 g/cm^3 and ~1.0 to ~1.2 g/cm^3 and porosities decrease from 60% to 50%.

Compressional Wave Velocities

Compressional wave velocities were measured by the MST PWL on whole APC cores and by the PWS on both split-core sections and discrete samples. PWL velocities above 5 mbsf in Unit 1 stay fairly constant at ~1500 m/s (Fig. F80; Table T19). The PWS velocities for this

F77. Thermal conductivity vs. depth, p. 130.
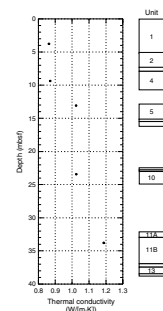
T17. Thermal conductivity measurements, Hole 1223A, p. 156.

F78. Discrete sample bulk density, dry density, grain density, and porosity, p. 131.
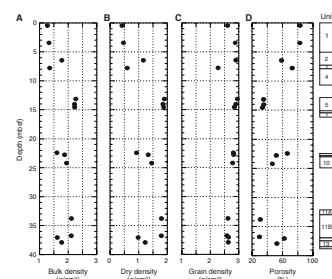
T18. Moisture and density, Hole 1223A, p. 157.

F79. Comparison of GRA density and bulk density, p. 132.
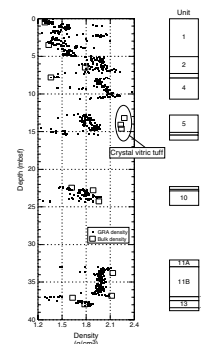
depth range show slightly higher values than PWL velocities. Between 5 and 7 mbsf, the PWL and PWS velocities increase with depth. The values range between 1600 and 1700 m/s. Between 7 and 11 mbsf, only PWL velocities were measured, with values of ~1650 m/s. In Unit 5, the crystal vitric tuff, PWS velocity values are between 3300 and 3400 m/s. Units 8–10 (22 –25 mbsf), which correspond to three different claystones, show quite different velocities ranging from 1900 to 3200 m/s. This suggests a rapid change of petrologic properties among claystones. The velocities for the palagonitized crystal vitric tuff in Subunit 11B are ~4000 m/s and are substantially higher than those for the crystal vitric tuff in Unit 5. This suggests less consolidation in Unit 5 than in Unit 11. PWS velocities in the deepest layer, below 37 mbsf, have values between ~2100 and ~2400 m/s.

Discussion

Figure F81 compares PWS velocity with bulk density and PWS velocity with porosity. There is a general increase of compressional velocity with increasing bulk density except for the crystal vitric tuff in Unit 5. The crystal vitric tuff in Unit 5 shows very different characteristics from the general trend of the PWS vs. bulk density relation. In contrast, the porosities for this crystal vitric tuff are not drastically different from the general trend of PWS velocity vs. porosity. Visual inspection of the texture of the crystal vitric tuff indicates loosely coupled grains. During the PWS velocity measurements, two samples crumbled to black sand similar to unconsolidated black sand of Unit 4. This occurred after the samples were dried by heating to 100°C for many hours. In the petrological description, these samples were identified as hard rocks, but the samples crumbled when the clay minerals lost their moisture.

The palagonitized crystal vitric tuff in Subunit 11B (33–37 mbsf) shows high velocities around ~4000 m/s with ~5% anisotropy.

3.5-kHz SUBSEAFLOOR REFLECTIONS

The 41-m borehole at Site 1223 recovered brown clay and turbidites in the upper 13 m and more consolidated vitric tuffs and claystones below. Based on the physical property measurements, the cored interval represents ~36-ms reflection traveltime, nearly the entire interval during which reflections were visible on the ship's 3.5-kHz echo sounder (Fig. F82).

Reflections from beneath the seafloor are commonly observed in sediments using echo sounders with transducers in the 1- to 5-kHz frequency range. Reflections from continuous interfaces as deep as 100 ms have been observed on traverses of many kilometers in some sediments. A sizable descriptive literature on seafloor sediment deposition has been developed using these reflection profiles. The assumption in these analyses is that the reflections occur at sharp boundaries between thick (in terms of wavelengths) layers. This is not likely the case at Site 1223.

Some of the constraints in correlating the soundings with the cored material are as follows:

1. A large area of the seafloor is insonified because of the wide beam width of the transducer and the 4230-m water depth.
2. The 43-cm wavelength of the sound does not readily discriminate between more closely spaced interfaces.

F80. Comparison of PWL and PWS velocities, p. 133.
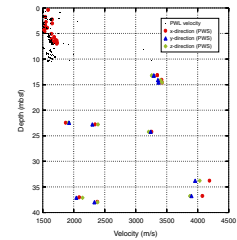
T19. PWS velocity measurements, Hole 1223A, p. 158.

F81. Comparison of PWS velocity to bulk density and porosity, p. 134.
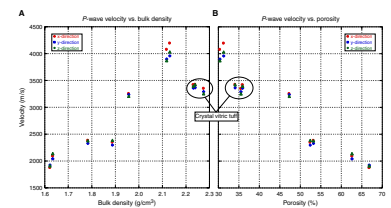
F82. 3.5-kHz echo soundings showing changes in the reflection sequence, p. 135.
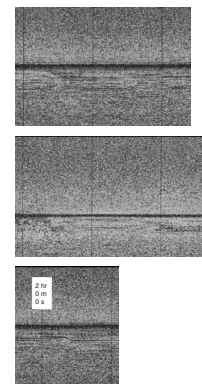
3. The chirp processor of the sounder has anticipatory and trailing side lobes, limiting resolution to ~3 ms.
4. On the 1-s window presented on the EPC graphic recording, the entire echo sequence observed is only about an inch wide.

Observations

Extensive reflecting interfaces were observed as we approached and while we were on the station at Site 1223. We continued to run the echo sounder during drilling operations, and we observed a temporal variability of the reflected returns. The variability of the reflected returns with the time of observation prompted our making a recording for 10 hr.

This variability is somewhat surprising considering the water depth (4235 m), the seafloor's modest slope, and the modest amount of ship movement. A 7-hr-long recording and its navigation files were examined. The time interval was 1258 to 2007 hr on 21 December. These are UTC times. Local time equals UTC time – 10 hr. The ship's position is maintained using a five-element receiving array below the hull and a Datasonics seafloor beacon emitting a stream of 16-kHz pulses. These and the Global Positioning System (GPS) data, taken at 1-min intervals, indicate the ship kept station within 20 m (Fig. F83). The GPS and acoustic positioning systems gave comparably precise measurements for the ship's position.

The Raytheon receiver processor applied a "slow" time-varying gain to the returning signal. The matched filter chirp processor gives rise to the anticipatory precursor to the seafloor reflection. The ship's heading was between 106° and 109° for the duration of these recordings. The periods of the ship's roll, pitch, yaw, reach, sway, and heave are all shorter than the 1- to 4-min changes in the reflection sequences observed.

Core Comparison

Even with the variability observed, some observations common to much of the recording can be matched to the Hole 1223A summary shown in Fig. F2:

1. The seafloor reflection is followed by a relatively "acoustically transparent" interval of ~16 ms. Assuming a velocity of 1.7 km/s, this would be ~12 m thick. This appears to correspond to cored Units 1 to 4, which are volcaniclastic turbidites, dark-brown clay, and black sands. The acoustic impedance contrasts in these units are smaller than the seafloor and other interfaces.
2. Underlying this, there are a variety of reflections in the interval from 16 to 28 ms (~15 m thick). Several of these reflections are strong, but their appearance on the recording comes and goes with observing time. These probably correspond to the more indurated Units 5 through 7. The strength of these reflections suggests a greater impedance contrast, and the variability suggests that the interfaces may be of limited spatial extent.
3. Beneath this interval, there is a 6-ms (~6 m thick) interval in which there are only a few weak reflections.
4. The deepest reflections observed at 36 to 40 ms (32 m and deeper) are weak, and their appearance is discontinuous on the recording. These weaker reflections would correspond to the tuffs and claystones in the lower two cores.

22 December 2001 0200-0259 UTC
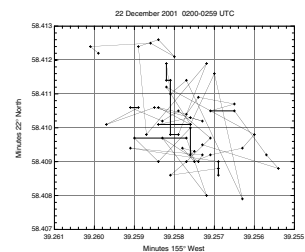
It is possible that Units 8, 9, and 10 may come from the bottom of Core 200-1223A-3X and sit on top of Units 11 to 14. In this case, there may not have been any core recovery for an interval as thick as 13 m between 16 and 29 mbsf.

Variability Analysis

The wavelength in water of 3.5-kHz sound is 43 cm. The reflections seen are presumably from acoustic impedance contrasts comparable or greater in size.

A 212-ms-long traveltime window of the graphic recording, which includes the seafloor and subseafloor reflections, was imaged. Plots were made of the ship's position, and the incremental movement between fixes was calculated. The response time of the ship's dynamic positioning system is comparable to the 1-min fix rate; therefore, applying a smoothing function to the 1-min fixes would probably be inappropriate.

The graphic recording was examined, and the times at which noticeable changes in the reflection sequence occurred were noted and tabulated. The location of these changes were then compared with the positions (Fig. F84) of the ship during the whole period. There were no apparent groupings of the positions at which changes in the recording occurred. The incremental movement of the ship (Fig. F85) (average = 2 m) at these locations was comparable to or less than the incremental movement between successive fixes for the whole survey period.

For a water depth of 4235 m, the 40-ms time period of the seafloor and subseafloor returns could represent scattered returns from a circular area of the seafloor as large as 1400 m in diameter. Table T20 shows the size of the "footprint" from which returns could be received as a function of the length of the echo sequence. From this, the subseafloor volume that could return sound can be estimated using the velocity of sound in the substrate.

Conclusions on Reflection Variability Phenomenon

Preliminary conclusions are as follows:

1. The variability in the seafloor return does not appear to be an artifact of the ship's transducer, heading changes, the chirp correlator processor, or the graphic recording.
2. The seafloor turbidites have an acoustic impedance greater than seawater and less than the underlying tuff and act like a coated lens to increase the amount of sound reaching the deeper interfaces.
3. The seafloor in this area may be acting as a nonspecular reflector as evidenced by the intermittent nature of the reflection that was found in the indurated tuff. Viewing the seafloor and its underlying interfaces as a complex acoustic projector of the dimensions shown above, it would have to have a directivity of 0.2° or greater for the shipboard receiver to observe significant differences with a horizontal movement of a few meters. The diameter of the area that could return sound over the 40-ms interval observed is eight times greater than the minimum required to achieve that degree of directivity.

F84. Navigation plot of a 7-hr recording, p. 137.
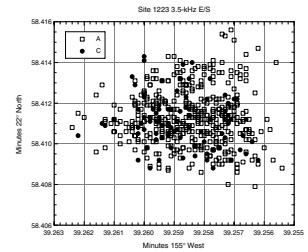
F85. Incremental distance between fixes at which there were noticeable changes in recording, p. 138.
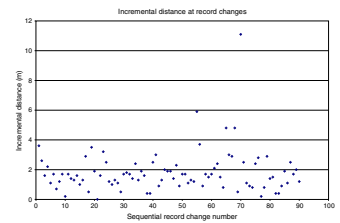
T20. Area insonified, p. 159.

4. The subseafloor reflectors might be an interference from a sequence of reflectors spaced less than a wavelength apart (the dominant wavelength of the sound is 43 cm).

5. Small changes in the 3.5-kHz source frequency content or in the separation of a sequence of layers could make the apparent reflector disappear or move. A mechanism for producing a frequency difference in the source over the periods observed is not apparent. Although the flow of water past the 3.5-kHz transducer pod from thrusters three and four varies, the pod is a massive piece of steel and the surface waters of the ocean here are well mixed to >100 m depth by the recent storm waves.

6. A possible model for these observations might be numerous marbles or prisms disposed on an irregular acoustically transparent substrate. The buried extrusive volcanics found at this site could have such a complex shape. In addition to the dynamics of the tuff deposition, faulting and fracturing give rise to interfaces with varying shapes.

REFERENCES

Alt, J.C., and Teagle, D.A.H., 1998. Probing the TAG hydrothermal mound and stockwork: oxygen-isotopic profiles from deep ocean drilling. *In* Herzig, P.M., Humphris, S.E., Miller, D.J., and Zierenberg, R.A. (Eds.), *Proc. ODP, Sci. Results,* 158: College Station, TX (Ocean Drilling Program), 285–295.

Amann, R.I., Krumholz, L., and Stahl, D.A., 1990. Fluorescent-oligonucleotide probing of whole cells for determinative, phylogenetic, and environmental studies in microbiology. *J. Bacteriol.,* 172:762–770.

Bonatti, E., 1965. Palagonite, hyaloclastites, and alteration of volcanic glass in the ocean. *Bull. Volcanol.,* 28:257–269.

Bouma, A.H., 1962. *Sedimentology of Some Flysch Deposits: A Graphic Approach to Facies Interpretation:* Amsterdam (Elsevier).

Boyd, F.R., 1961. Welded tuff and flows in the rhyolite plateau of Yellowstone Park, Wyoming. *Geol. Soc. Am. Bull.,* 72:387–426.

Burggraf, S., Mayer, T., Amann, R., Schadhauser, S., Woese, C.R., and Stetter, K.O., 1994. Identifying members of the domain Archaea with rRNA-targeted oligonucleotide probes. *Appl. Environ. Microbiol.,* 60:3112–3119.

Carey, S.N., and Sigurdsson, H., 1980. The Roseau ash: deep-sea tephra deposits from a major eruption on Dominica, Lesser Antilles Arc. *J. Volcanol. Geotherm. Res.,* 7:67–86.

Carlisle, D., 1963. Pillow breccias and their aquagene tuffs, Quadra Island, British Columbia. *J. Geol.,* 71:48–71.

Carracedo, J.C., 1999. Growth, structure, instability and collapse of Canarian volcanoes and comparisons with Hawaiian volcanoes. *J. Volcanol. Geotherm. Res.,* 94:1–19.

Chen, C.-Y., Frey, F.A., Garcia, M.O., Dalrymple, G.B., and Hart, S.R., 1991. The tholeiite to alkalic basalt transition at Haleakala Volcano, Maui, Hawaii. *Contrib. Mineral. Petrol.,* 106:183–200.

Clague, D.A., and Dalrymple, G.B., 1987. The Hawaiian-Emperor volcanic chain, Part I. Geologic evolution. *In* Decker, R.W., Wright, T.L., and Stauffer, P.H. (Eds.), *Volcanism in Hawaii*. U.S. Geol. Surv. Prof. Pap., 5–73.

Clague, D.A., and Frey, F.A., 1982. Petrology and trace element geochemistry of the Honolulu volcanics, Oahu: implications for the oceanic mantle below Hawaii. *J. Petrol.,* 23:447–504.

Clague, D.A., Moore, J.G., Dixon, J.E., and Friesen, W.B., 1995. Petrology of submarine lavas from Kilauea's Puna Ridge, Hawaii. *J. Petrol.,* 36:299–349.

Cragg, B.A., Parkes, R.J., Fry, J.C., Weightman, A.J., Rochelle, P.A., and Maxwell, J.R., 1996. Bacterial populations and processes in sediments containing gas hydrates (ODP Leg 146: Cascadia Margin). *Earth Planet. Sci. Lett.,* 139:497–507.

Cronan, D.S., and Toombs, J.S., 1969. The geochemistry of manganese nodules and associated pelagic deposits from the Pacific and Indian Oceans. *Deep-Sea Res.,* 16:335–339.

Daims, H., Bruehl, A., Amann, A., Schleifer, K.-H., and Wagner, M., 1999. The domain-specific probe is insufficient for the detection of all bacteria: development and evaluation of a more comprehensive probe set. *Syst. Appl. Microbiol.,* 22:434–444.

Deer, W.A., Howie, R.A., and Zussman, J., 1992. *An Introduction to the Rock-Forming Minerals:* Essex, United Kingdom (Longman Scientific and Technical).

Dixon, J.E., Clague, D.A., and Stolper, E.M., 1991. Degassing history of water, sulfur, and carbon in submarine lavas from Kilauea Volcano, Hawaii. *J. Geol.,* 99:371–394.

Dixon, J.E., Clague, D.A., Wallace, P., and Poreda, R., 1997. Volatiles in alkalic basalts from the North Arch volcanic field, Hawaii: extensive degassing of deep submarine-erupted alkalic series lavas. *J. Petrol.,* 38:911–939.

Dixon, J.E., Clague, D.A., Wallace, P., and Poreda, R., 1997. Volatiles in alkalic basalts from the North Arch volcanic field, Hawai'i: extensive degassing of deep submarine-erupted alkalic series lavas. *J. Petrol.,* 38:911–939.

Doell, R.R., and Dalrymple, G.B., 1973. Potassium-argon ages and paleomagnetism of the Waianae and Koolau Volcanic Series, Oahu, Hawaii. *Geol. Soc. Am. Bull.,* 84:1217–1242.

Elders, W.A., Hoagland, J.R., McDowell, S.D., 1979. Hydrothermal mineral zones in the geothermal reservoir of Cerro Prieto. *In* Elders, W.A. (Ed.), *Geology and Geothermics of the Salton Trough, (GSA Guidebook):* Riverside, CA (Campus Museum Contrib.), 5:36–43.

Fisher, R.V., and Schmincke, H.-U., 1984. *Pyroclastic Rocks:* New York (Springer-Verlag).

Frey, F.A, Garcia, M.O., and Roden, M., 1994. Geochemical characteristics of Koolau Volcano: implications of intershield geochemical differences among Hawaiian volcanoes. *Geochim. Cosmochim. Acta,* 58:1441–1462.

Furnes, H., 1975. Experimental palagonitization of basaltic glasses of varied composition. *Contrib. Mineral. Petrol.,* 50:105–113.

Garcia, M.O., and Hull, D.M., 1994. Turbidites from giant Hawaiian landslides; results from Ocean Drilling Program Site 842. *Geology,* 22:159–162.

Gauthier, G., Gauthier, M., and Christen, R., 1995. Phylogenetic analysis of the genera *Alteromonas, Shewanella* and *Moritella* using genes coding for small-subunit rRNA sequences and division of the genus *Alteromonas* into two genera, *Alteromonas* (emended) and *Pseudoalteromonas* gen. nov., and proposal of twelve new species combinations. *Int. J. Syst. Bacteriol.,* 45:755–761.

Gonzales, J.M., and Moran, M.A., 1997. Numerical dominance of a group of marine bacteria in the α-subclass of the class Proteobacteria in coastal seawater. *Appl. Environ. Microbiol.,* 63:4237–4242.

Grim, R.E., 1964. *Clay Mineralogy:* New York (McGraw-Hill).

Hay, R.L., and Iijima, A., 1968. Nature and origin of palagonite tuffs of the Honolulu Group on Oahu, Hawaii. *In* Coats, R.R., Hay, R.L., and Anderson, C.A. (Eds.), *Studies in Volcanology.* Mem.—Geol. Soc. Am., 116:331–376.

Herrero-Bervera, E., Cañon-Tapia, E., Walker, G.P.L., and Guerrero-Garcia, J.C., 2002. The Nuuanu and Wailau giant landslides: insights from paleomagnetic and anisotropy of magnetic susceptibility (AMS) studies. *Phys. Earth Planet. Inter.,* 129:83–98.

Honnorez, J., Laverne, C., Hubberten, H.-W., Emmermann, R., and Muehlenbachs, K., 1983. Alteration processes in Layer 2 basalts from Deep Sea Drilling Project Hole 504B, Costa Rica Rift. *In* Cann, J.R., Langseth, M.G., Honnorez, J., Von Herzen, R.P., White, S.M., et al., *Init. Repts. DSDP,* 69: Washington (U.S. Govt. Printing Office), 509–546.

Honnorez, J.J., Alt, J.C., and Humphris, S.E., 1998. Vivisection and autopsy of active and fossil hydrothermal alterations of basalt beneath and within the TAG hydrothermal mound. *In* Herzig, P.M., Humphris, S.E., Miller, D.J., and Zierenberg, R.A. (Eds.), *Proc. ODP, Sci. Results,* 158: College Station, TX (Ocean Drilling Program), 231–254.

Hoppe, H.-G., 1940. Untersuchungen an Palagonittuffen and uber irhe Bildungsbedgungen. *Chem. Erde,* 13:484–514.

Hussong, D.M., Uyeda, S., et al., 1982. *Init. Repts. DSDP,* 60: Washington (U.S. Govt. Printing Office).

Ishii, T., Robinson, P.T., Maekawa, H., and Fiske, R., 1992. Petrological studies of peridotites from diapiric serpentinite seamounts in the Izu-Ogasawara-Mariana forearc, Leg 125. *In* Fryer, P., Pearce, J.A., Stokking, L.B., et al., *Proc. ODP, Sci. Results,* 125: College Station, TX (Ocean Drilling Program), 445–485.

Jackson, E.D., and Wright, T.L., 1970. Xenoliths in the Honolulu Volcanic Series, Hawaii. *J. Petrol.,* 11:405–430.

Johnston, J.E., and Christensen, N.I., 1997. Seismic properties of Layer 2 basalts. *Geophys. J. Intr.,* 128:285–300.

Kato, I., Murai, I., Yamazaki, T., and Abe, M., 1971. Subaqueous pyroclastic flow deposits in the upper Donzurubo Formation, Nijo-san District, Osaka, Japan. *J. Geol. Soc. Jpn.,* 77:193–296.

Kirby, S.H., 1983. Rheology of the lithosphere. *Rev. Geophys.,* 21:1458–1487.

Kirby, S.H., and Green, H.W. II, 1980. Dunite xenoliths from Hualalai Volcano: evidence for mantle diapiric flow beneath the Island of Hawaii. *Am. J. Sci.,* 280A:550–575.

Kirkpatrick, R.J., 1979. Processes of crystallization in pillow basalts, Hole 396B, DSDP Leg 46. *In* Dmitriev, L., Heirtzler, et al., 1979. *Init. Repts. DSDP,* 46: Washington (U.S. Govt. Printing Office), 271–282.

Kirschvink, J.L., 1980. The least-squares line and plane and the analysis of palaeomagnetic data. *Geophys. J. R. Astron. Soc.,* 62:699–718.

Kristmannsdóttir, H., 1976. Types of clay minerals in hydrothermally altered basaltic rocks, Reykjanes, Iceland. *Jokull,* 26:30–39.

Lenat, J.-F., Vincent, P., and Bachelaery, P., 1989. The offshore continuation of an active basaltic volcano: Piton de la Fournaise. *J. Volcanol. Geotherm. Res.,* 36:1–36.

Liou, J.G., 1971. Pressure-temperature stabilities of laumontite, wairakite, lawsonite, and related minerals in the system $CaAl_2Si_2O_8$-H_2O. *J. Petrol.,* 12:379–411.

Macdonald, G.A., and Katsura, T., 1964. Chemical composition of Hawaiian lavas. *J. Petrol.,* 5:82–133.

Manz, W., 1999. In situ analysis of microbial biofilms by rRNA-targeted oligonucleotide probes. *In* Doyle, R.J. (Ed.), *Biofilms.* Meth. Enzymol. Ser.: San Diego (Academic Press), 310:79–91.

Manz, W., Amann, R., Ludwig, W., Vancanneyt, M., and Schleifer, K.-H., 1996. Application of a suite of 16S rRNA-specific oligonucleotide probes designed to investigate bacteria of the phylum cytophaga-flavobacter-bacteroides in the natural environment. *Microbiology,* 142:1097–1106.

Manz, W., Amann, R., Ludwig, W., Wagner, M., and Schleifer, K.-H., 1992. Phylogenetic oligodeoxynucleotide probes for the major subclasses of proteobacteria: problems and solutions. *Syst. Appl. Microbiol.,* 15:593–600.

Manz, W., Arp, G., Schumann-Kindel, G., Szewzyk, U., and Reitner, J., 2000. Widefield deconvolution epifluorescence microscopy combined with fluorescence in situ hybridization reveals the spatial arrangement of bacteria in sponge tissue. *J. Microbiol. Meth.,* 40:125–134.

Manz, W., Eisenbrecher, M., Neu, T.R., and Szewzyk, U., 1998. Abundance and spatial organization of gram-negative sulfate-reducing bacteria in activated sludge investigated by in situ probing with specific 16S rRNA targeted oligonucleotides. *FEMS Microbiol. Ecol.,* 25:43–61.

Masson, D.G., Watts, A.B., Gee, M.J.R., Urgeles, R., Mitchell, N.C., Le Bas, T.P., Canals, M., 2002. Slope failures on the flanks of the western Canary Islands. *Earth-Sci. Rev.,* 57:1–35.

Mazzullo, J.M., Meyer, A., and Kidd, R.B., 1988. New sediment classification scheme for the Ocean Drilling Program. *In* Mazzullo, J., and Graham, A.G. (Eds.), *Handbook for Shipboard Sedimentologists.* ODP Tech. Note, 8:45–67.

Meier, H., Amann, R., Ludwig, W., and Schleifer, K.-H., 1999. Specific oligonucleotide probes for in situ detection of a major group of Gram-positive bacteria with low DNA G+C content. *Syst. Appl. Microbiol.,* 22:186–196.

Miyashiro, A., 1973. *Metamorphism and Metamorphic Belts:* London (George Allen and Unwin).

Moore, G.W., and Moore, J.G., 1988. Large scale bedforms in boulder gravel produced by giant waves in Hawaii. *Spec. Pap.—Geol. Soc. Am.,* 229:101–109.

Moore, J.G., 1964. Giant submarine landslides on the Hawaiian Ridge. *Geological Survey Research 1964.* U.S. Geol. Surv. Prof. Pap., 501-D:95–98.

Moore, J.G., and Albee, W.C., 1981. Topographic and structural changes, March–July 1980; photogrammetric data. *In* Lipman, P.W., and Mullineaux, D.R. (Eds.), *The 1980 Eruptions of Mount St. Helens, Washington.* U.S. Geol. Surv. Prof. Pap., 1250.

Moore, J.G., Clague, D.A., Holcomb, R.T., Lipman, P.W., Normark, W.R., and Torresan, M.E., 1989. Prodigious submarine landslides on the Hawaiian Ridge. *J. Geophys. Res.,* 94:17465–17484.

Moore, J.G., and Fabbi, B.P., 1971. An estimate of the juvenile sulfur content of basalt. *Contrib. Mineral. Petrol.,* 33:118–127.

Moore, J.G., and Melson, W.G., 1969. Nuees ardentes of the 1968 eruption of Mayon Volcano, Philippines. *Bull. Volcanol.,* 33:600–620.

Moore, J.G., Normark, W.R., and Holcomb, R.T., 1994. Giant Hawaiian landslides. *Annu. Rev. Earth Planet. Sci.,* 22:119–144.

Naka, J., Takahashi, E., Clague, D., Garcia, M., Hanyu, T., et al., 2000. Tectonomagmatic processes investigated at deep-water flanks of Hawaiian volcanoes. *Eos, Trans. Am. Geophys. Union.,* 81:227–230.

Natland, J.H., and Hekinian, R., 1982. Hydrothermal alteration of basalts and sediments at Deep Sea Drilling Project Site 456, Mariana Trough. *In* Hussong, D.M., Uyeda, S., et al., *Init. Repts., DSDP,* 60: Washington (U.S. Govt. Printing Office), 759–767.

Nealson, K.H., 1997. Sediment bacteria: who's there, what are they doing, and what's new? *Annu. Rev. Earth. Planet. Sci.,* 25:403–434.

Noack, Y., Emmermann, R., and Hubberten, H.-W., 1983. Alteration in Site 501 (Leg 68) and Site 504 (Leg 69) basalts: preliminary results. *In* Cann, J.R., Langseth, M.G., Honnorez, J., Von Herzen, R.P., White, S.M., et al., *Init. Repts. DSDP,* 69: Washington (U.S. Govt. Printing Office), 497–508.

Normark, W.R., Posamentier, H.W., and Mutti, E., 1993. Submarine turbidite systems: state of the art and future directions. *Rev. Geophys.,* 31:91–116.

Parkes, R.J., Cragg, B.A., Bale, S.J., Getliff, J.M., Goodman, K., Rochelle, P.A., Fry, J.C., Weightman, A.J., and Harvey, S.M., 1994. A deep bacterial biosphere in Pacific Ocean sediments. *Nature,* 371:410–413.

Peacock, M.A., 1926. The petrology of Iceland, Part I. The basic tuffs. *Trans. R. Soc. Edinburgh,* 55:51–76.

Petersen, S., Herzig, P.M., and Hannington, M.D., 1998. Fluid inclusion studies as a guide to the temperature regime within the TAG hydrothermal mound, 26°N, Mid-Atlantic Ridge. *In* Herzig, P.M., Humphris, S.E., Miller, D.J., and Zierenberg, R.A. (Eds.), *Proc. ODP, Sci. Results,* 158: College Station, TX (Ocean Drilling Program), 163–178.

Rabus, R., Fukui, M., Wilkes, H., and Widdel, F., 1996. Degradative capacities and 16S rRNA-targeted whole cell hybridization of sulfate-reducing bacteria in an anaerobic enrichment culture utilizing alkylbenzenes from crude oil. *Appl. Environ. Microbiol.,* 62:3605–3613.

Rees, B.A., Detrick, R.S., and Coakley, B.J., 1993. Seismic stratigraphy of the Hawaiian flexural moat. *Geol. Soc. Am. Bull.,* 105:189–205.

Sanfilippo, A., Westberg-Smith, M.J., and Riedel, W.R., 1985. Cenozoic radiolaria. *In* Bolli, H.M., Saunders, J.B., and Perch-Nielsen, K. (Eds.), *Plankton Stratigraphy:* Cambridge (Cambridge Univ. Press), 631–712.

Seki, Y., 1973. Distribution and modes of occurrence of wairakites in the Japanese island arc. *J. Geol. Soc. Jpn.,* 79:521–527.

Sparks, R.S.J., 1979. Gas release rates from pyroclastic flows: an assessment of the role of fluidization in their emplacement. *Bull. Volcanol.,* 41:1–9.

Surdam, R.C., 1973. Low-grade metamorphism of tuffaceous rocks in the Karmutsen Group, Vancouver Island, British Columbia. *Geol. Soc. Am. Bull.,* 84:1911–1922.

Taylor, B., Fujioka, K., et al., 1990. *Proc. ODP, Init. Repts.,* 126: College Station, TX (Ocean Drilling Program).

Teagle, D.A.H., Alt, J.C., Humphris, S.E., and Halliday, A.N., 1998. Dissecting an active hydrothermal deposit: the strontium and oxygen isotopic anatomy of the TAG hydrothermal mound—whole rock and silicate minerals. *In* Herzig, P.M., Humphris, S.E., Miller, D.J., and Zierenberg, R.A. (Eds.), *Proc. ODP, Sci. Results,* 158: College Station, TX (Ocean Drilling Program), 297–309.

Tomasson and Kristmannsdóttir, 1972. High temperature alteration minerals and thermal brines, Reykjanes, Iceland. *Contrib. Mineral. Petrol.,* 6:123–134.

Torella, F., and Morita, R.Y., 1981. Microcultural study of bacterial size changes and microcolony and ultramicrocolony formation by heterotrophic bacteria in seawater. *Appl. Environ. Microbiol.,* 41:518–527.

Tsuya, H., 1930. The eruption of Komagatake, Hokkaido, in 1929. *Bull. Earthquake Res. Inst., Univ. Tokyo,* 8:238–270.

Yamazaki, T., Kato, I., Muroi, I., and Abe, M., 1973. Textural analysis and flow mechanism of the Donzurubo subaqueous pyroclastic flow deposits. *Bull. Volcanol.,* 37:231–244.

Figure F1. Locations of Site 1223 and the Nuuanu Landslide. Line 12 shows the seismic reflection profile obtained by Rees et al. (1993). Site 1223 is adjacent to a seamount.
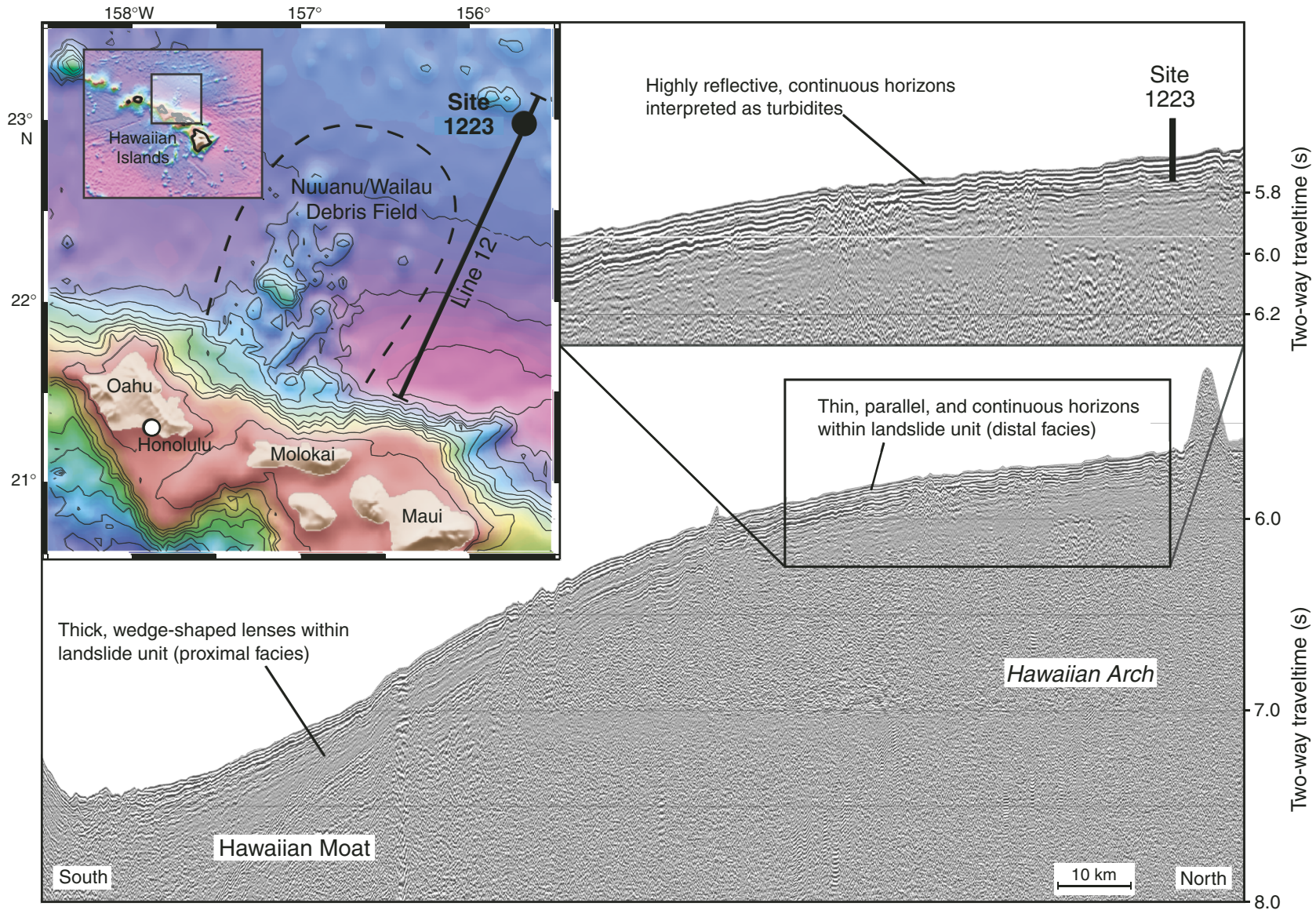
Figure F2. Lithologic units and stratigraphic column of the cores recovered at Site 1223. D ↑ V indicates that rounded cavities increase in size and abundance upward. For detailed unit descriptions, see **"Lithology,"** p. 8.

Lithologic unit descriptions

1. Yellowish brown clay and volcaniclastic turbidites

2. Volcaniclastic turbidites

3. Dark-brown clay

4. Unconsolidated black sand

5. Crystal vitric tuff

6. Bioturbated claystone

7. Volcaniclastic sandy siltstone

8. Volcaniclastic silty claystone with carbonate-filled cavities

9. Volcaniclastic claystone

10. Volcaniclastic silty claystone

11A. Altered palagonitized crystal vitric tuff

11B. Palagonitized crystal vitric tuff

12. Volcaniclastic silty claystone with filled white vugs

13. Volcaniclastic silty claystone

14. Volcaniclastic clayey siltstone

⋋	Sponge spicules	P	Planar laminae
⫽≡	Cross-bedding		Gas pipes
�ら	Bioturbation		Clasts
R	Radiolarians	2	Secondary mineralization
○	Vesicles		
	Interlayered	V	Veins
∧∨	Highly disturbed		

Figure F3. Close-up photograph showing an ~10-cm-thick volcaniclastic turbidite of Unit 1 with yellowish brown clay above and below it (interval 200-1223A-1H-1, 72–120 cm). The turbidite is normally graded from very fine sand to clay. The top contact is gradual and the bottom of the turbidite has a sharp contact.
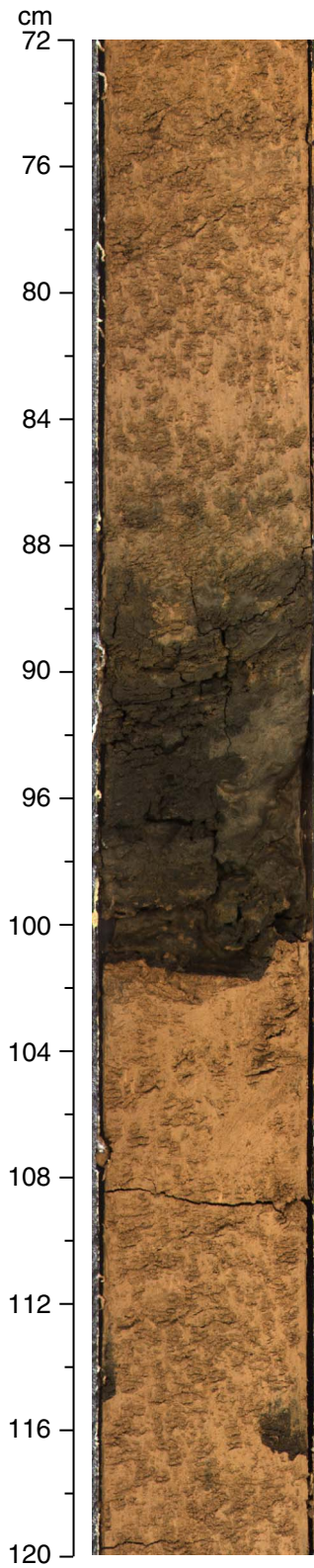
Figure F4. Close-up photograph showing multiple thin turbidite layers in Subunit 1H corresponding to the division D in the Bouma sequence (Bouma, 1962) (interval 200-1223A-1H-4, 40–57 cm). Some beds are bowed downward by the coring process.
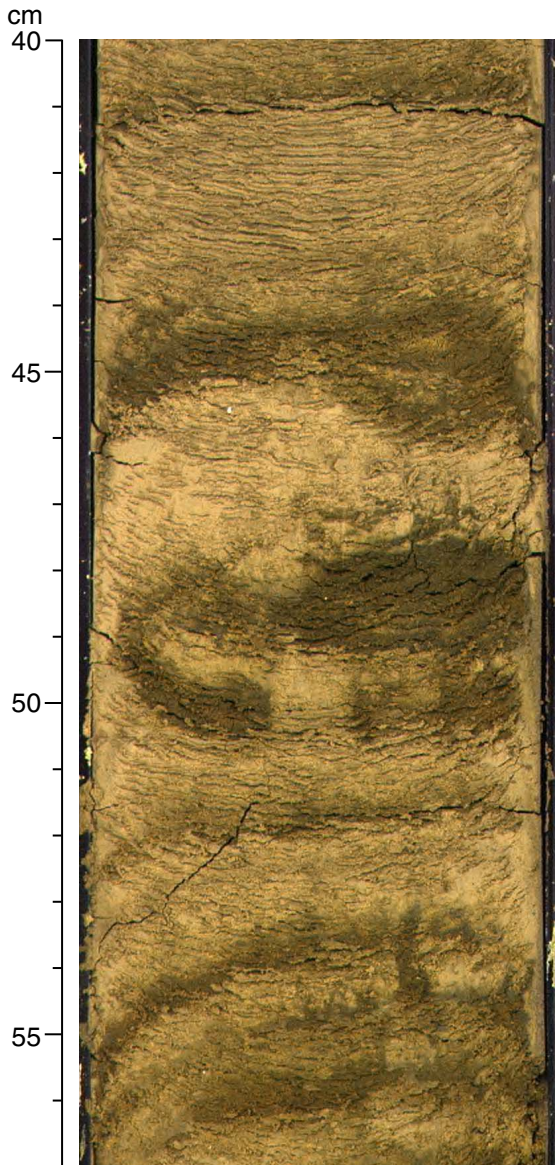
Figure F5. Close-up photograph showing the coarse bottom of a turbidite of Unit 2 directly overlying another turbidite (interval 200-1223A-1H-5, 84–105 cm). The sharp contact between the two turbidites indicates that erosion of the lower turbidite has occurred. The coarse granules are made of phillipsite (XRD determination).
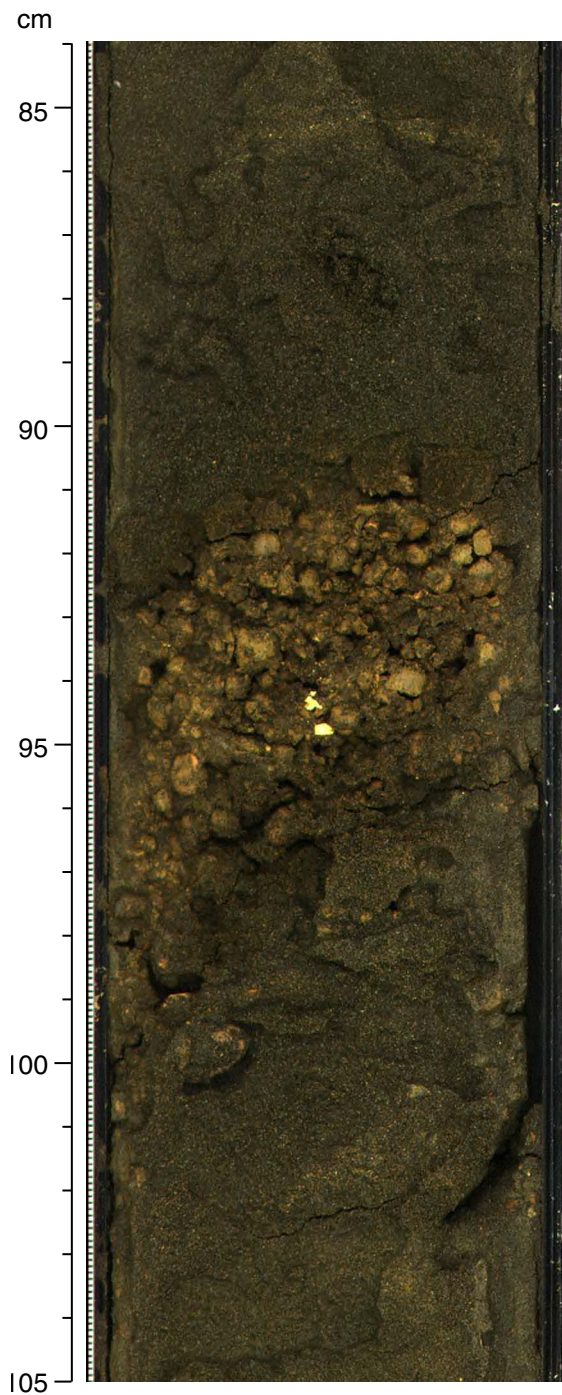
Figure F6. Close-up photograph showing a massive dark-brown clay of Unit 3 underlying the bottom, coarsest part of a turbidite (Section 200-1223A-1H-CC). The granules shown in the turbidite are made of calcite (XRD determination).
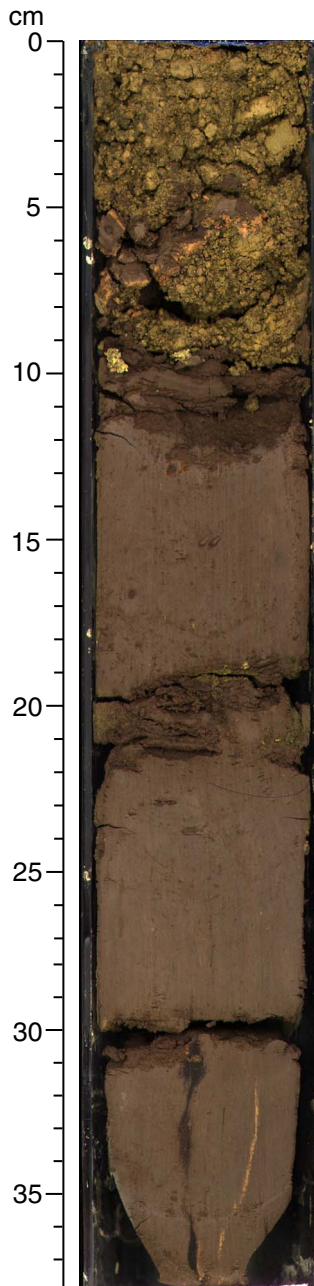
Figure F7. Close-up photograph showing the bottom contact of the dark-brown clay of Unit 3 and the underlying fining-upward black sand of Unit 4 (interval 200-1223A-2H-1, 14–36 cm).
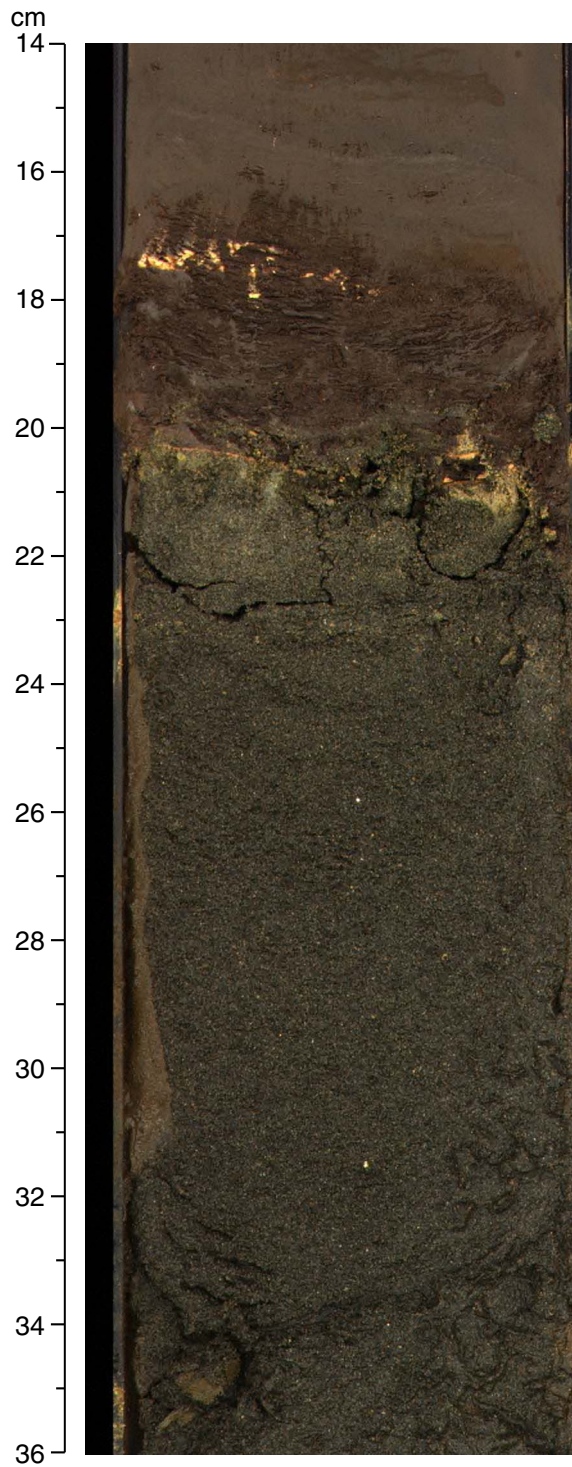
Figure F8. Close-up photograph of the upper portion of a crystal vitric tuff from Unit 5 (interval 200-1223A-3X-1 [Pieces 1 and 2A–2D, 1–40 cm]).
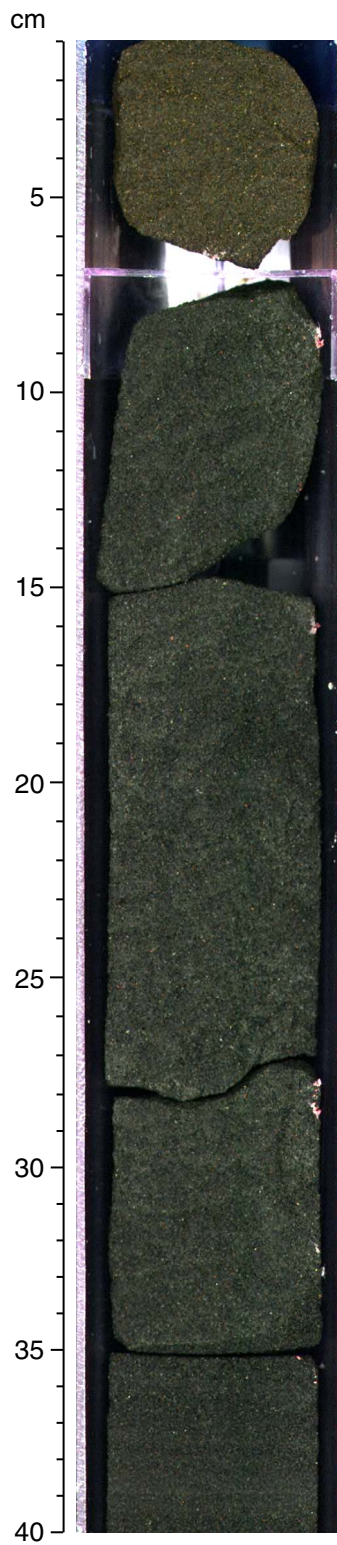
Figure F9. Close-up photograph showing possible gas pipe structures in crystal vitric tuff from Unit 5 (interval 200-1223A-3X-1 [Pieces 3A–3B, 95–114 cm]).
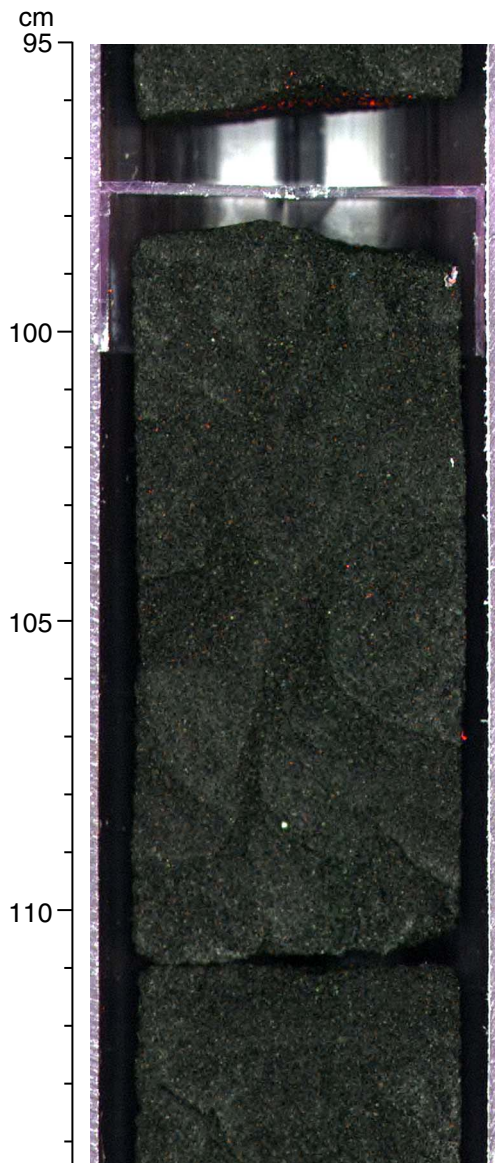
Figure F10. Close-up photograph that shows the bioturbated claystone of Unit 6 separated from the lower part of Unit 5 crystal vitric tuff by a sharp erosional surface (interval 200-1223A-3X-2, 82–107 cm). Bioturbation decreases with depth. The lower half of the unit is intermittently laminated and only slightly bioturbated. Cross-bedding is present at 101 cm.
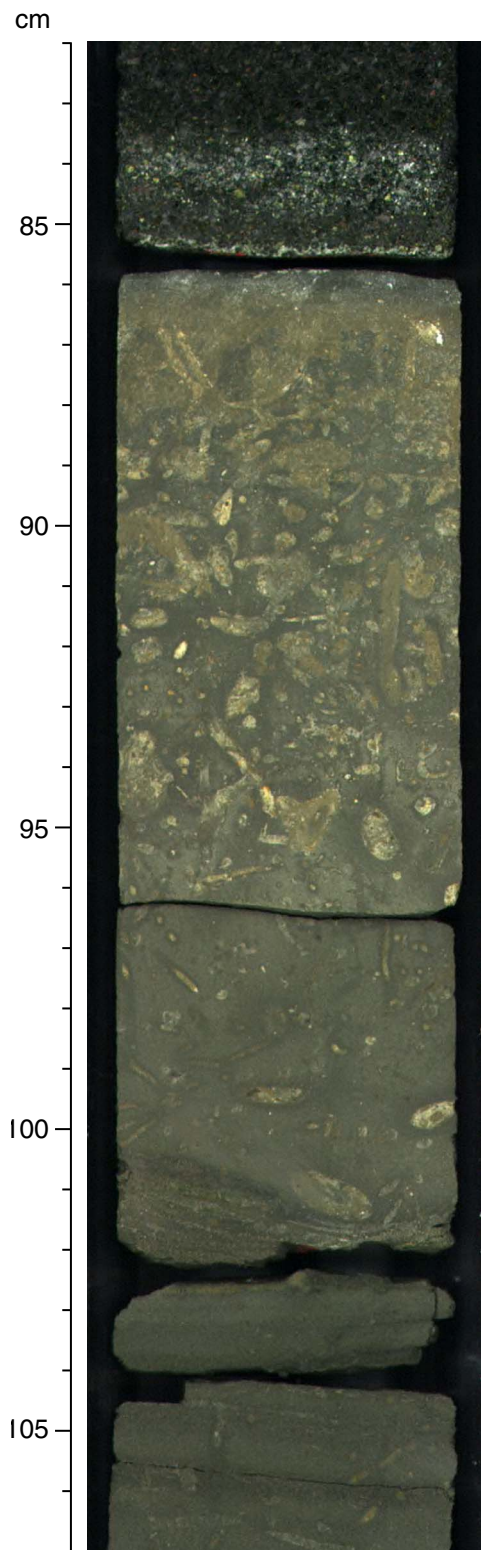
Figure F11. Close-up photograph showing weakly indurated volcaniclastic sandy siltstone from Unit 7 (interval 200-1223A-3X-2, 118–143 cm).
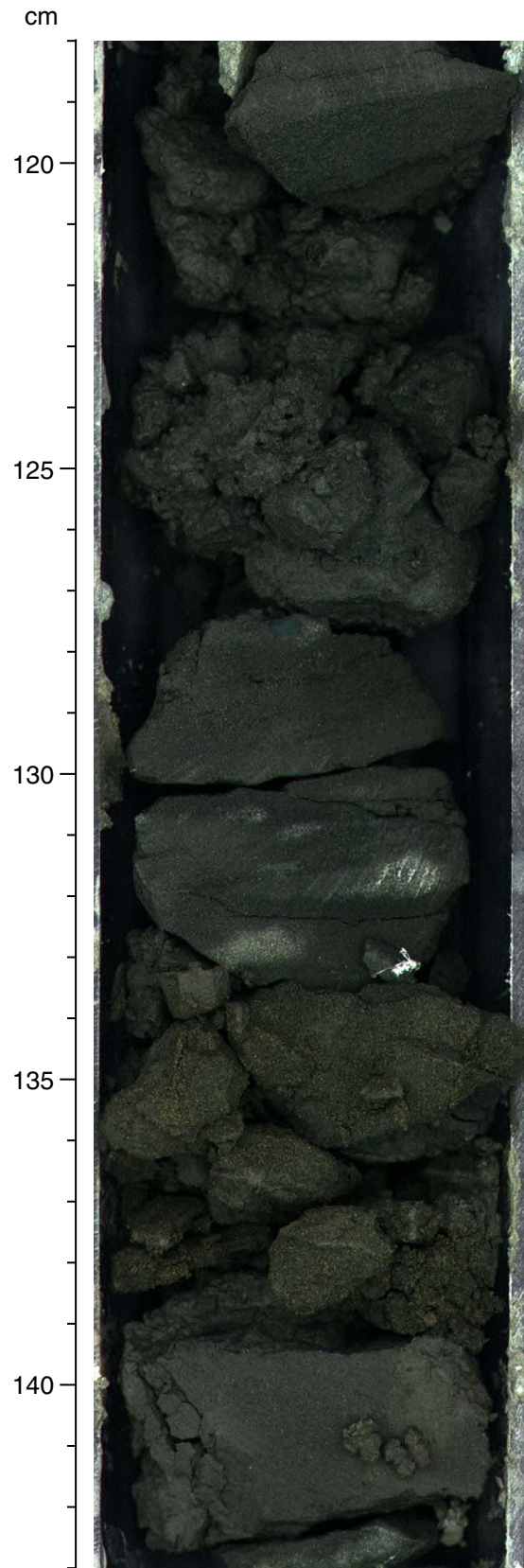
Figure F12. Close-up photograph showing volcaniclastic silty claystone of Unit 8 with carbonate-filled cavities (interval 200-1223A-4X-1, 1–24 cm).
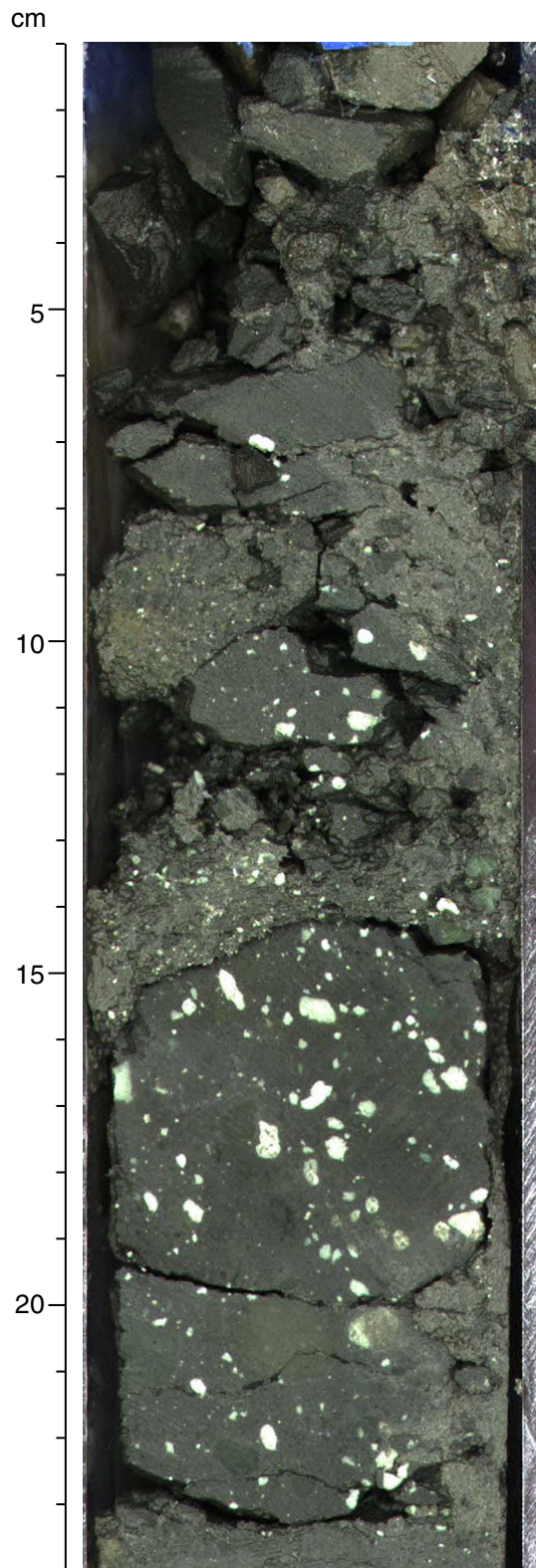
Figure F13. Close-up photograph of volcaniclastic silty claystone from Unit 8 showing a sharp erosional surface and a rip-up clast (interval 200-1223A-4X-1, 46–57 cm).
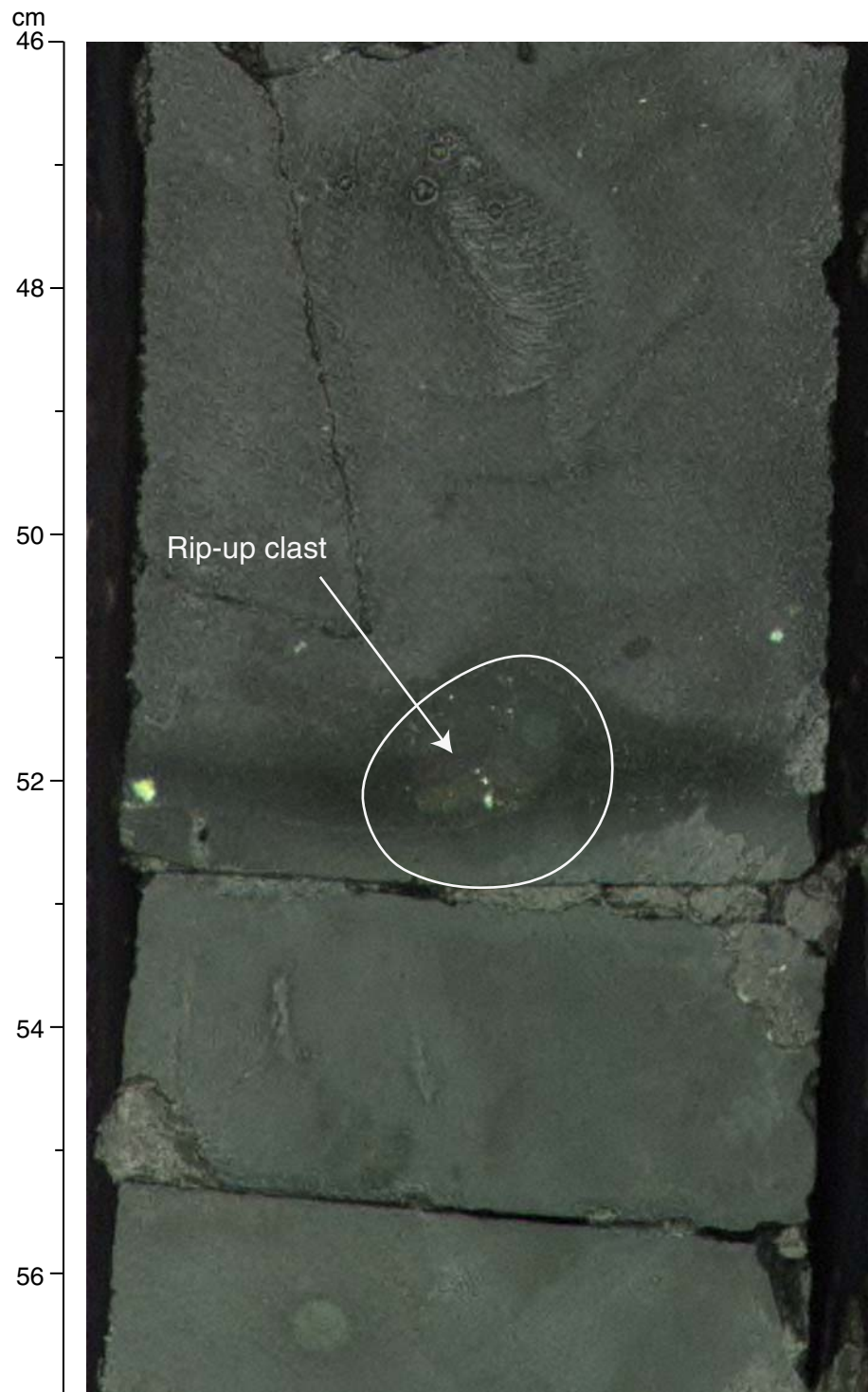
Figure F14. Close-up photograph of volcaniclastic claystone of Unit 9 (interval 200-1223A-4X-1, 50–62 cm). The unit is marked by a sharp erosional contact at the top and a dark gradational layer at the base. A burrow is also indicated on the figure.
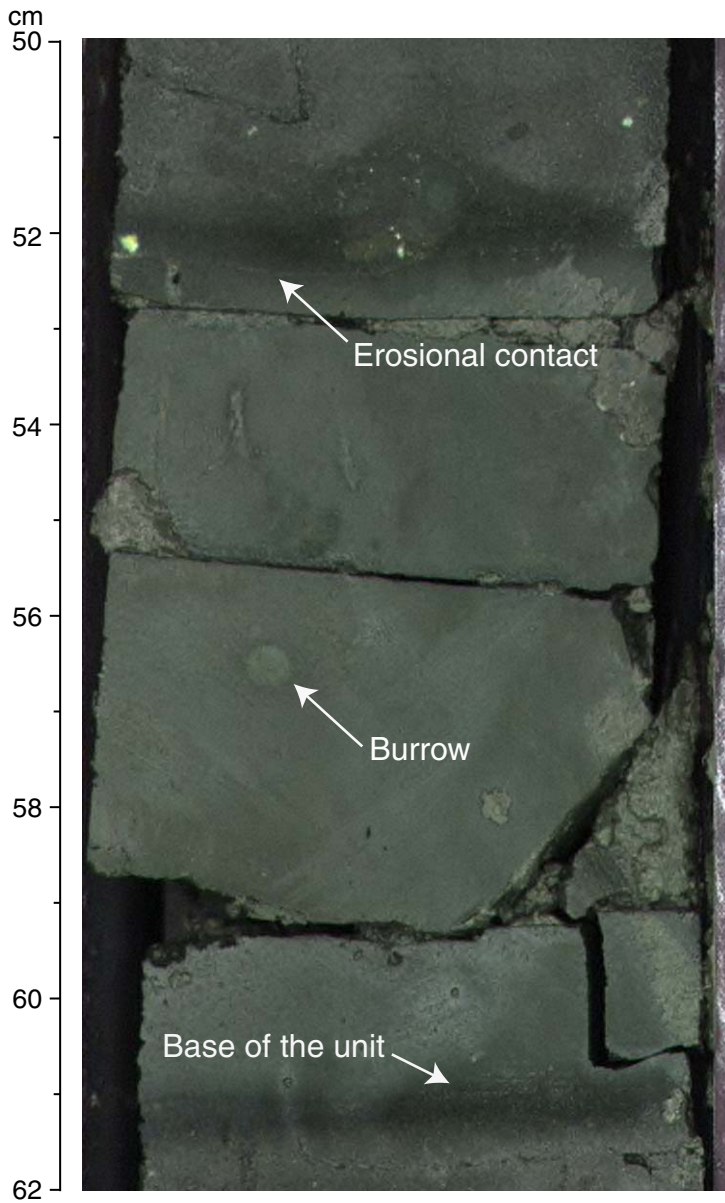
Figure F15. Close-up photograph showing volcaniclastic silty claystone of Unit 10 (interval 200-1223A-4X-2, 50–73 cm).
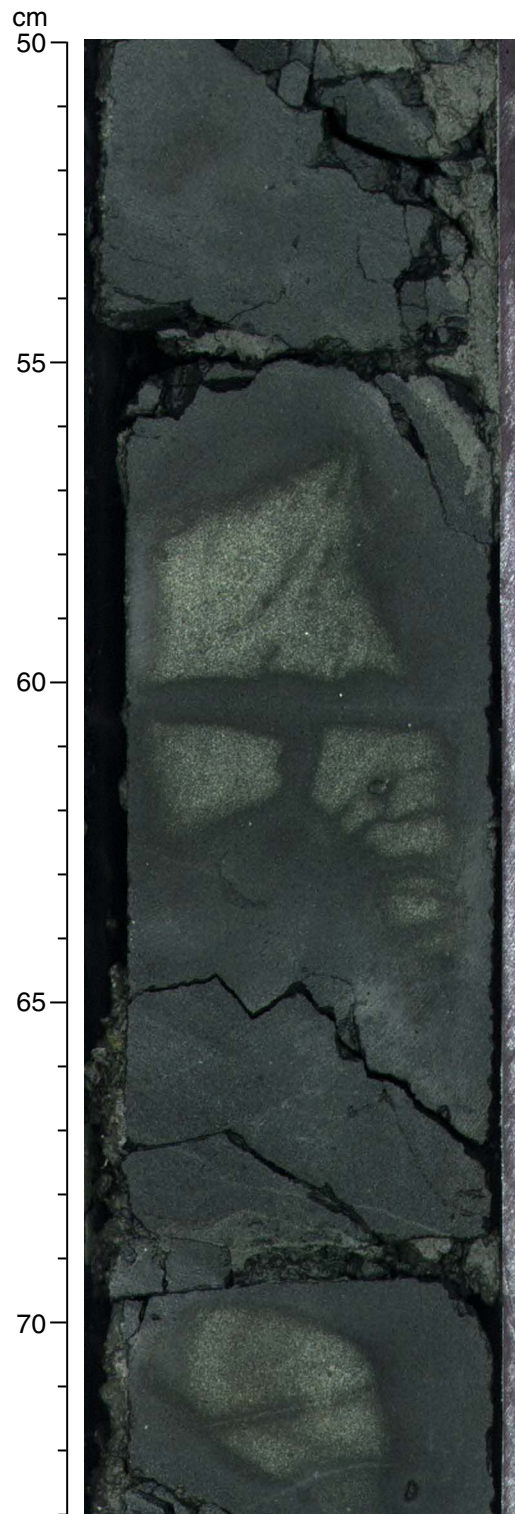
Figure F16. Close-up photograph showing a granule and pebble breccia present in the middle of the volcaniclastic silty claystone of Unit 10 (interval 200-1223A-4X-2, 78–88 cm).
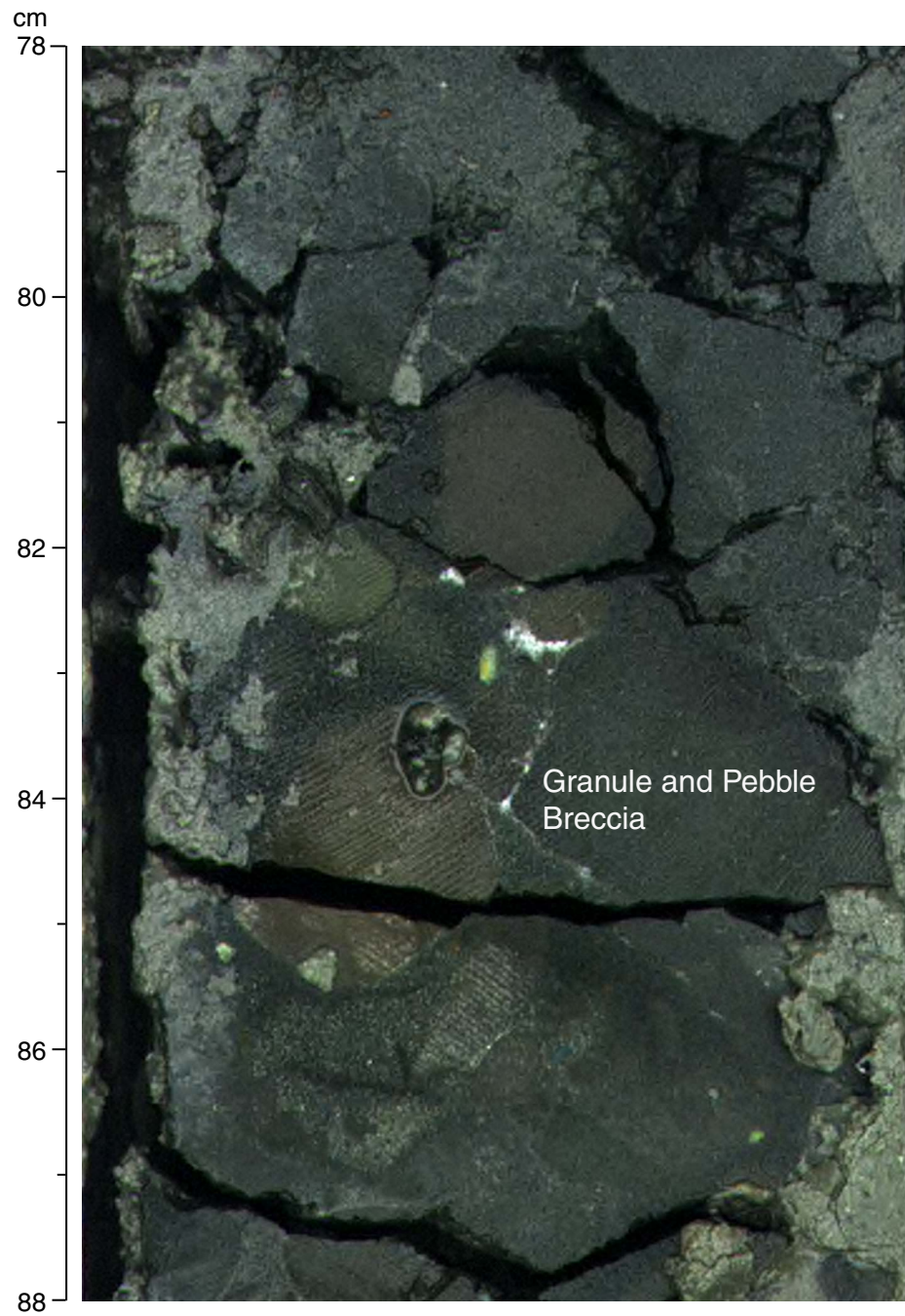
Figure F17. Close-up photograph showing the altered palagonitized crystal vitric tuff of Subunit 11A (interval 200-1223A-5X-1, 25–46 cm). This unit was highly disturbed by drilling.
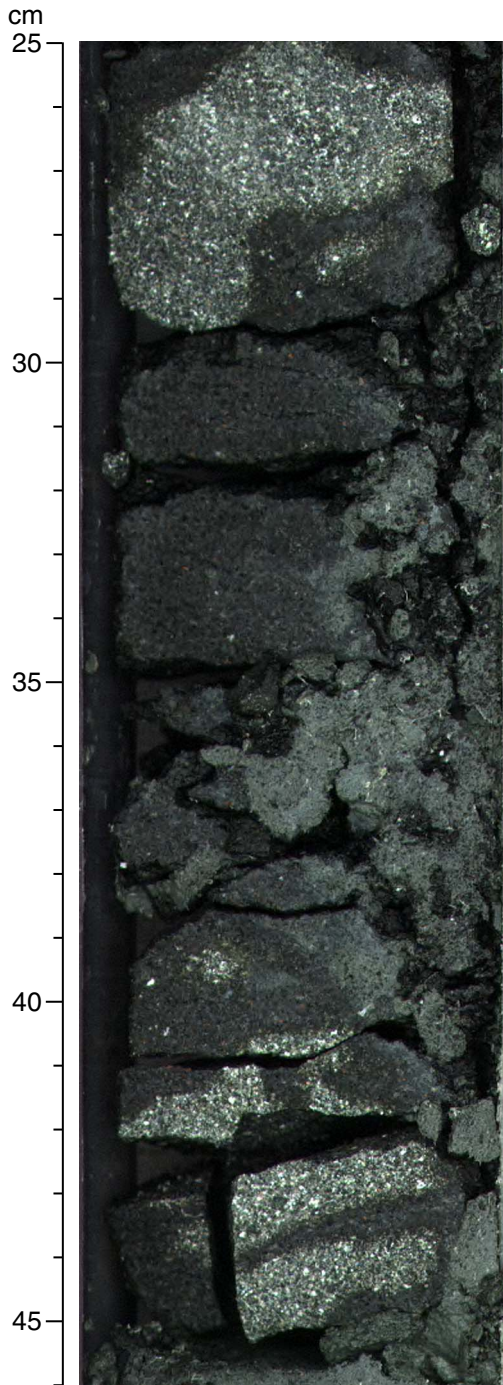
Figure F18. Close-up photograph showing palagonitized crystal vitric tuff of Subunit 11B (interval 200-1223A-6X-1, 34–45 cm).
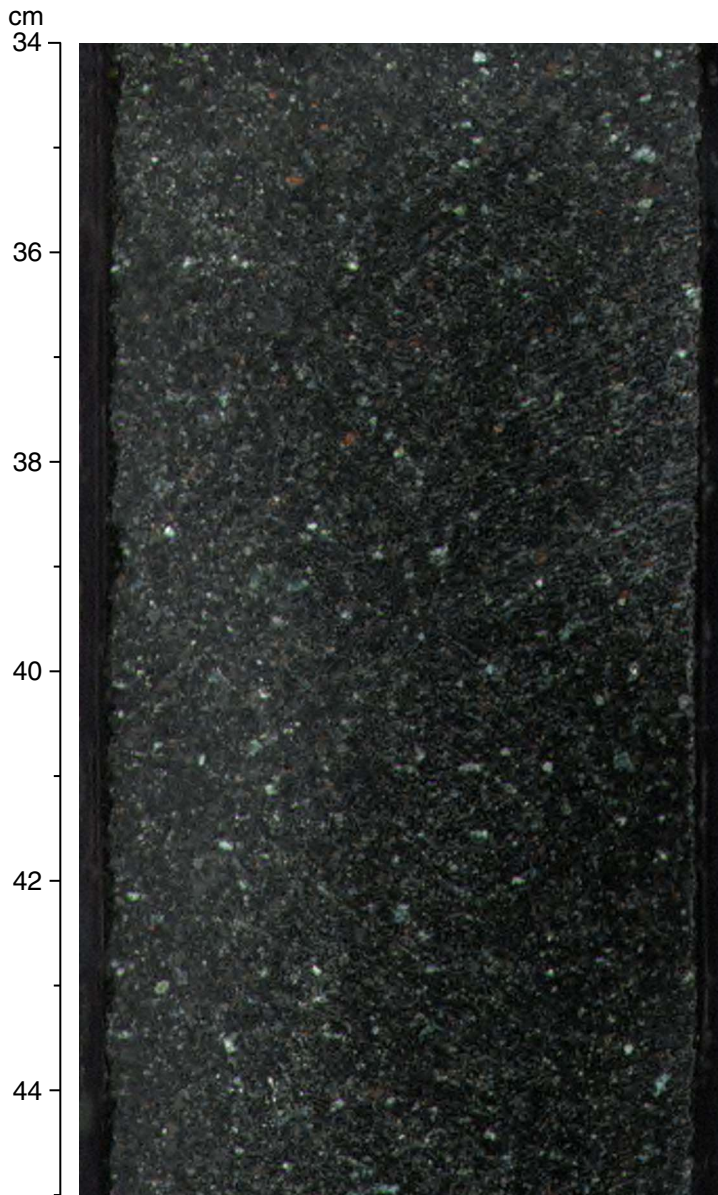
Figure F19. Close-up photograph showing volcaniclastic silty claystone of Unit 12 with anhydrite-filled vugs (interval 200-1223A-6X-3, 95–140 cm). The concentration of filled vugs increases with depth in the unit. There is a sharp contact between Subunit 11B and Unit 12.
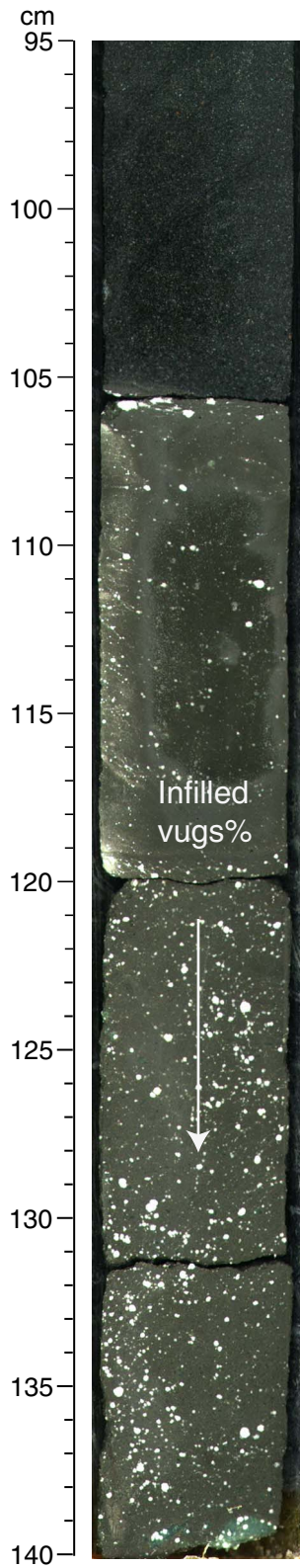
Figure F20. Close-up photograph showing volcaniclastic silty claystone of Unit 13 (interval 200-1223A-6X-4, 38–88 cm). Lithic clasts in the lower half of the unit are indicated.
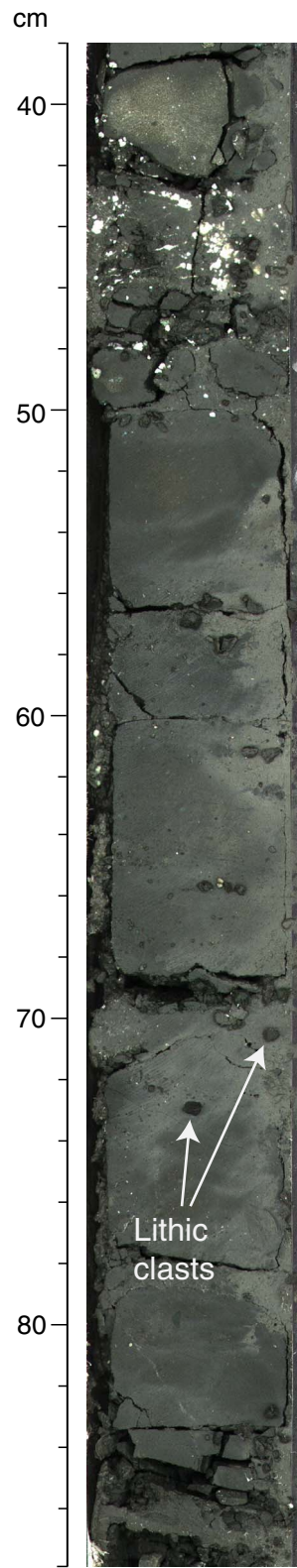
Figure F21. Close-up photograph of the upper half of the volcaniclastic silty claystone of Unit 13, showing the two zones of highly disturbed white material, possibly anhydrite (interval 200-1223A-6X-4, 29–53 cm).
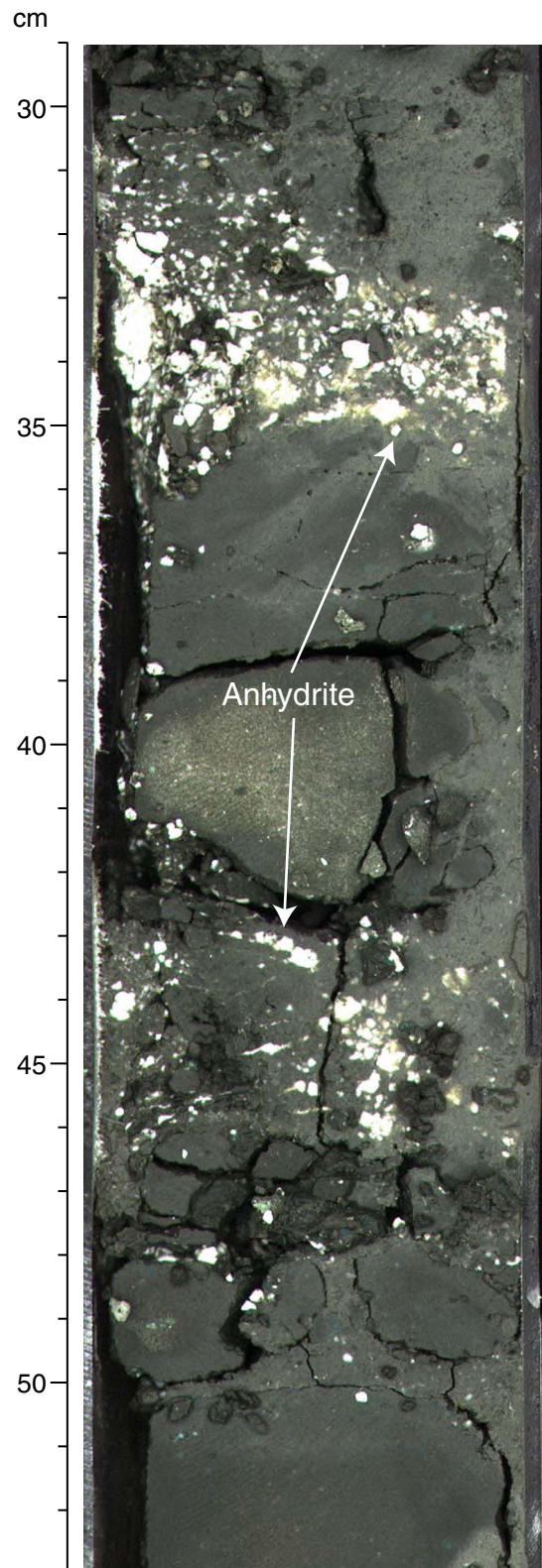
Figure F22. Close-up photograph of the volcaniclastic clayey siltstone of Unit 13 with lithic clasts (circled area) indicated (interval 200-1223A-6X-4, 60–70 cm).

Figure F23. Close-up photograph of Unit 14, showing a weakly indurated, matrix-supported clayey silt-stone (interval 200-1223A-6X-CC, 13–38 cm). The clasts (circled area) at 31 cm are very soft and easily scratched with a fingernail.
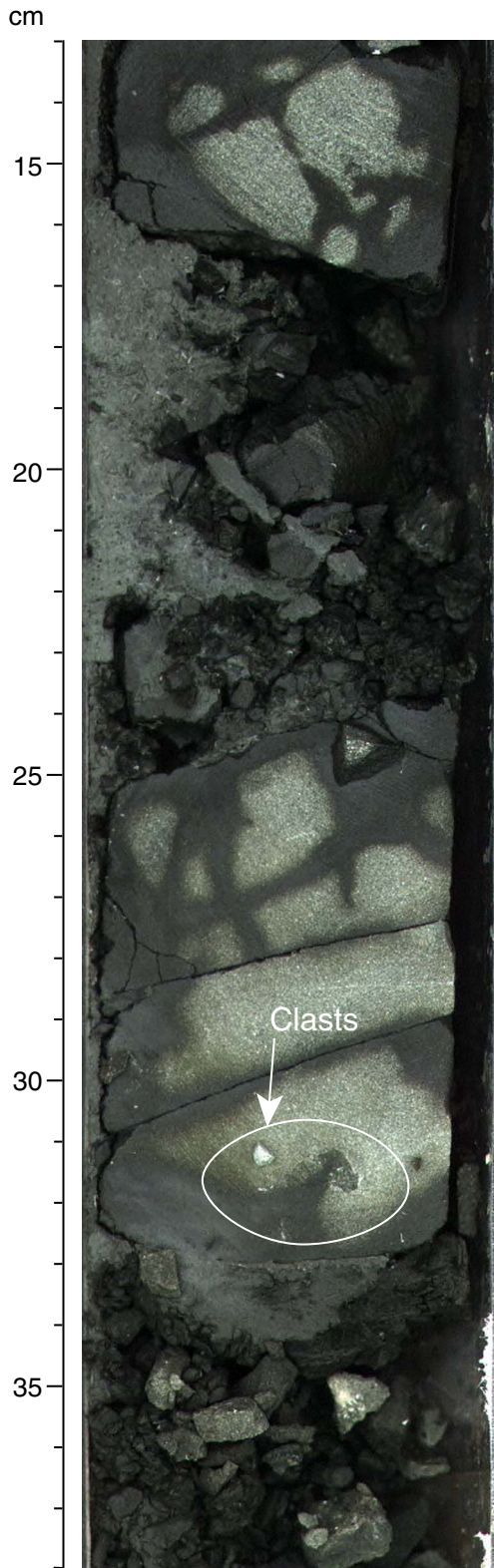
Figure F24. Photomicrograph of (**A**) the sandy fraction of the turbidite levels (**Sample 200-1223A-1H-5, 93–95 cm;** Unit 1; plane-polarized light) and (**B**) the same image embossed.

A

0.5 mm

B
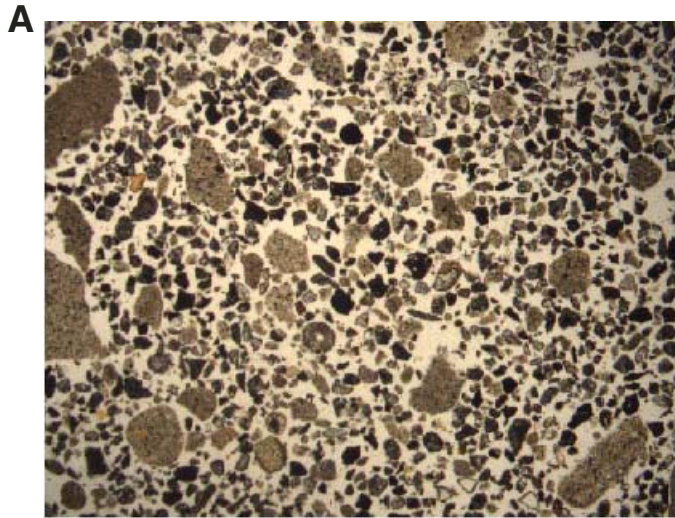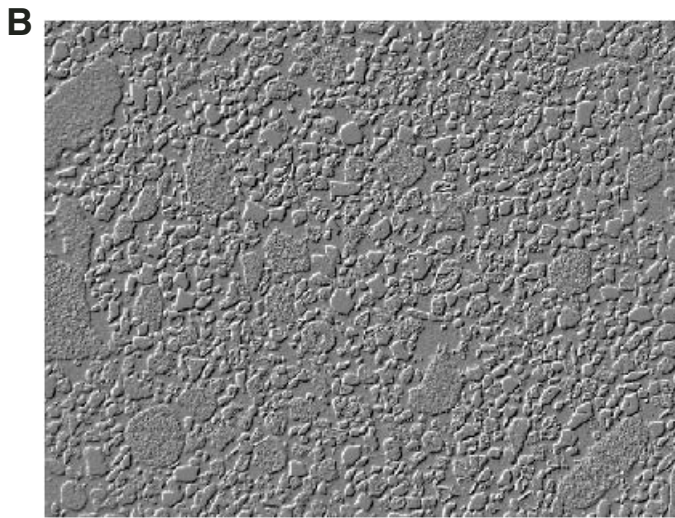
0.5 mm

Figure F25. Photomicrograph of (**A**) the sandy fraction of turbidite layers (**Sample 200-1223A-1H-5, 93–95 cm;** Unit 1; plane-polarized light) and (**B**) a close-up of the same layer.

A

0.5 mm

B
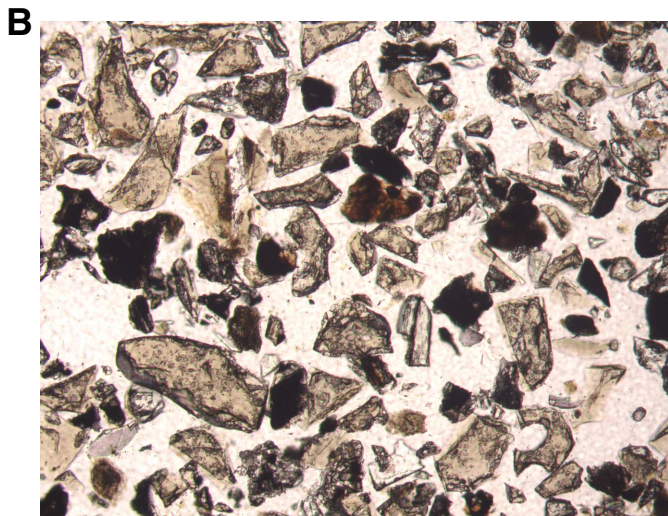
0.2 mm

Figure F26. Photomicrograph of (**A**) claystone granules with volcanic sand in a turbidite layer (**Sample 200-1223A-1H-5, 93–95 cm;** Unit 1; grain-mount, plane-polarized light) and (**B**) the same image embossed.

A
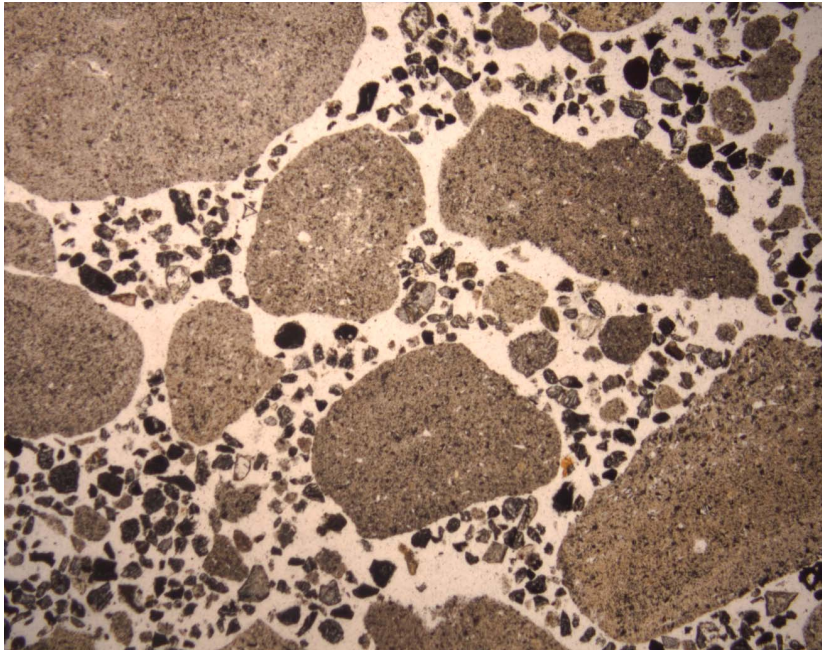
0.5 mm

B
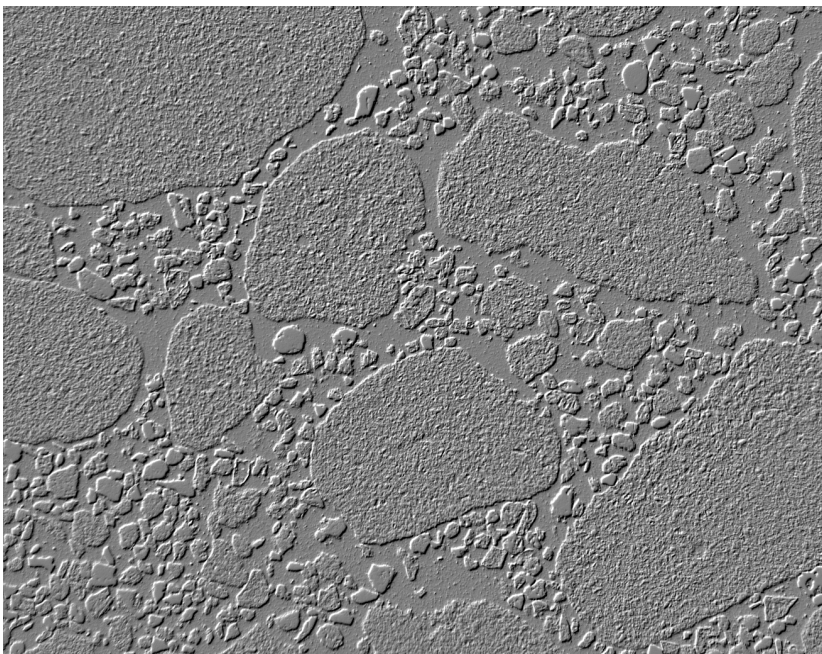
0.5 mm

Figure F27. Photomicrograph of anhydrite-filled vug in volcaniclastic silty claystone (**Sample 200-1223A-6X-3, 113–118 cm;** Unit 12; crossed polars).
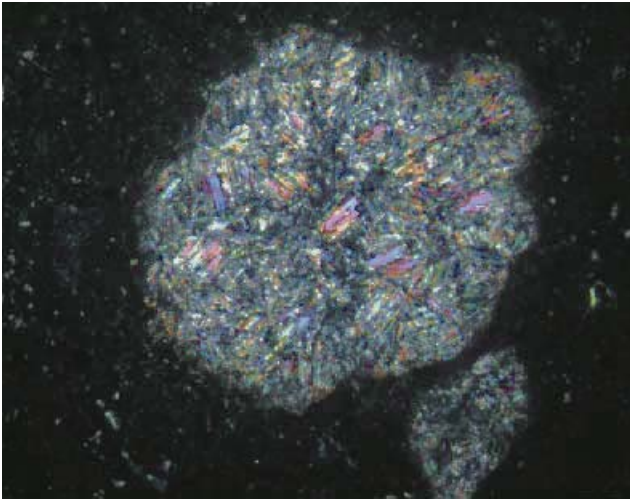
0.2 mm

Figure F28. Photomicrograph of (**A**) the columnar and hexagonal habit of anhydrite in vugs (**Sample 200-1223A-6X-3, 113–118 cm;** Unit 12; plane-polarized light) and (**B**) the same image embossed.

A

0.1 mm

B
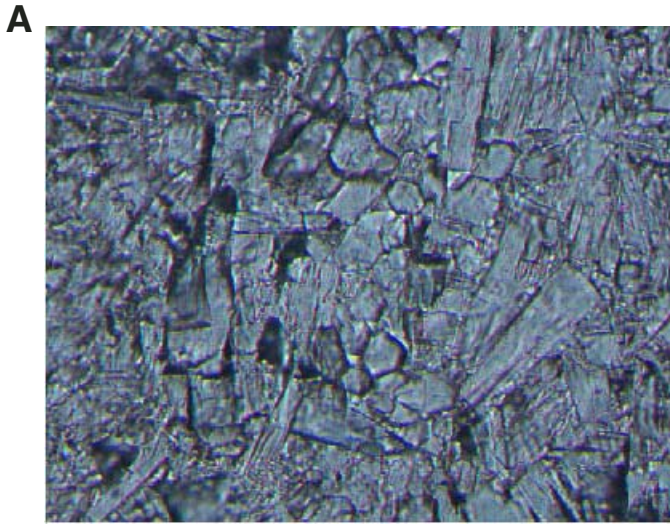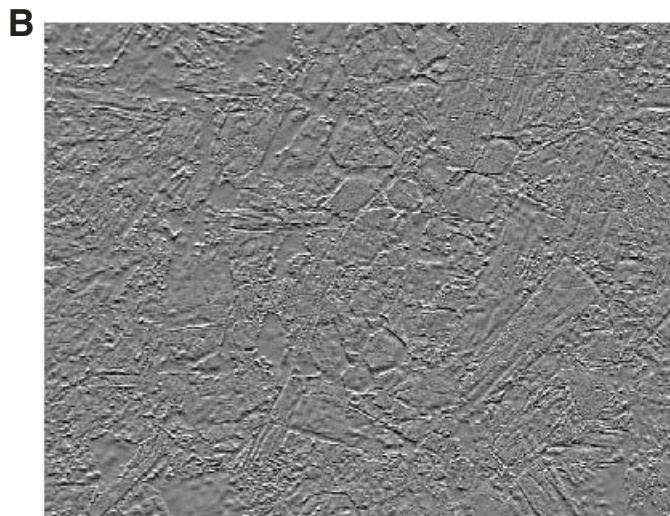
0.1 mm

Figure F29. Photomicrograph of crystal vitric tuff (**Sample 200-1223A-3X-1, 112–114 cm;** Unit 5; plane-polarized light). Pale yellow = glassy shards, colorless minerals = olivine and plagioclase, green granule = chlorite, black to dark brown = vitric fragment, holocrystalline fragments = lithic fragments, brownish rim bordering the glassy shards = clay minerals. Vesicularity = ~20%.
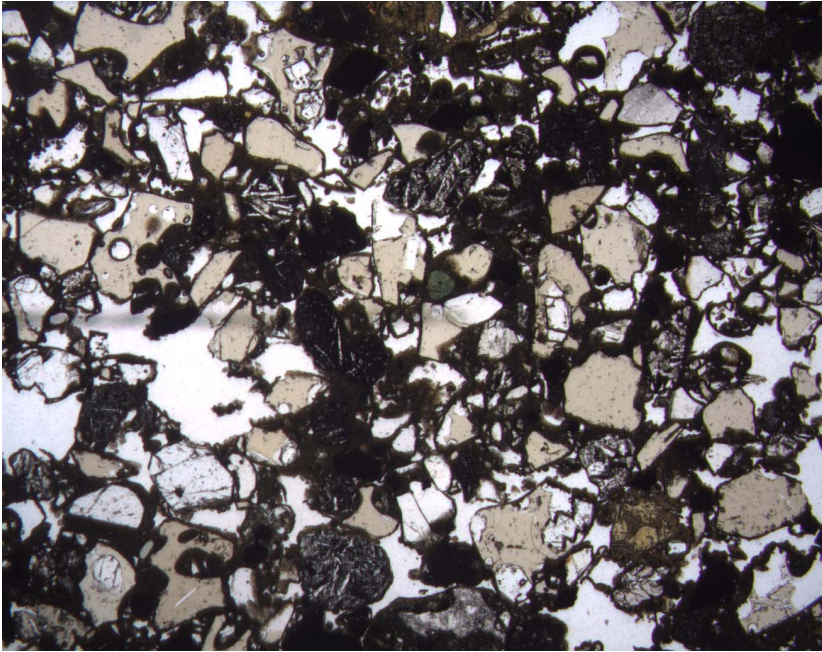
0.5 mm

Figure F30. Photomicrographs of (A) skeletal olivine in a glassy shard (**Sample 200-1223A-3X-1, 112–114 cm;** Unit 5; plane-polarized light) and (B) euhedral olivine in palagonitized glass in crystal vitric tuff (**Sample 200-1223A-3X-2, 71–73 cm;** Unit 5; plane-polarized light).
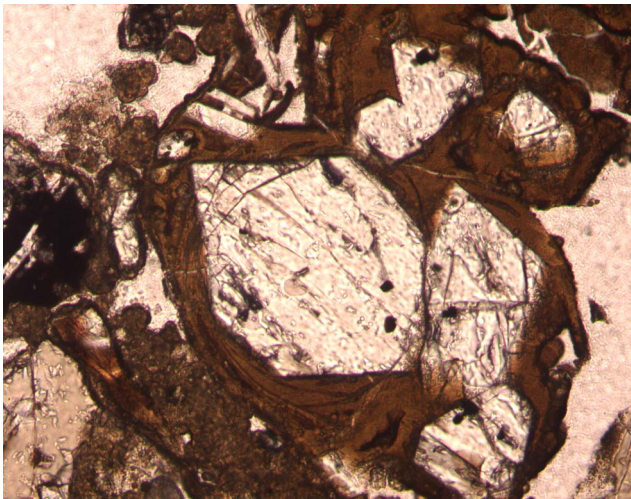
0.1 mm

0.1 mm

Figure F31. Photomicrograph of kink banding in an olivine clast in crystal vitric tuff (**Sample 200-1223A-3X-2, 71–73 cm;** Unit 5; crossed polars).
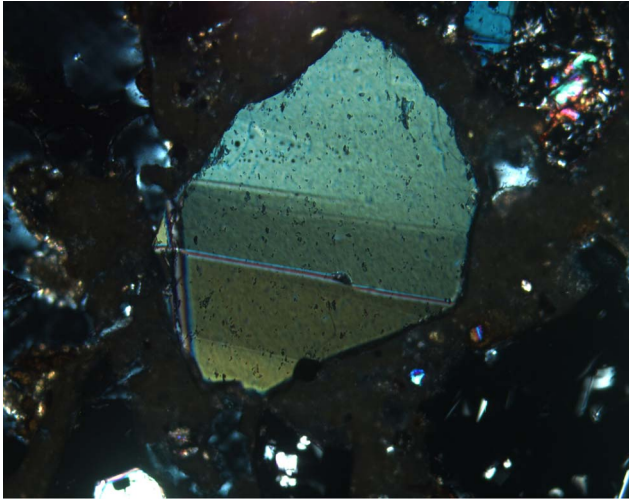
0.2 mm

Figure F32. Photomicrograph of euhedral clinopyroxene in crystal vitric tuff (**Sample 200-1223A-3X-2, 71–73 cm;** Unit 5; crossed polars).
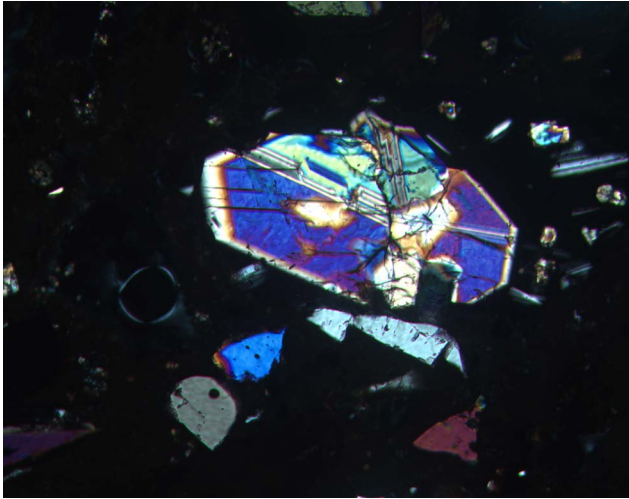
0.1 mm

Figure F33. Photomicrographs of (**A**) vesicle-free, pale-yellow glass shard with thin brownish clay rim (**Sample 200-1223A-3X-1, 112–114 cm;** Unit 5; plane-polarized light) and (**B**) highly vesicular pale-yellow glass shard (**Sample 200-1223A-3X-2, 71–73 cm;** Unit 5; plane-polarized light).

A

0.1 mm

B
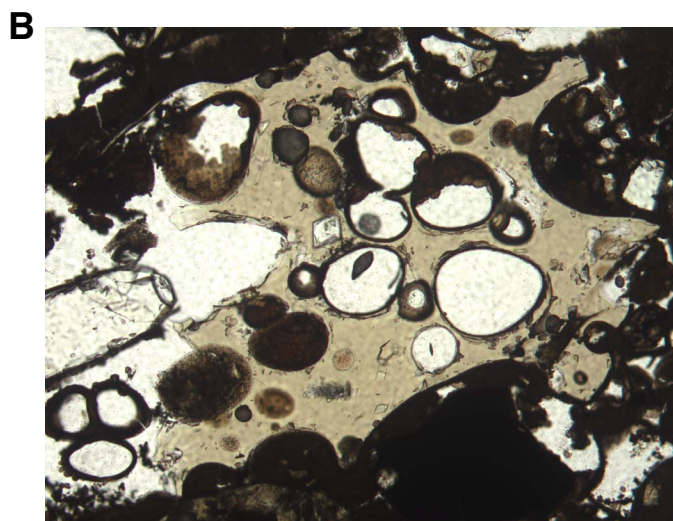
0.2 mm

Figure F34. Photomicrographs of (**A**) "bowtie" plagioclase spherulites in a vitric fragment in crystal vitric tuff and (**B**) skeletal plagioclase in a vitric fragment (**Sample 200-1223A-3X-1, 36–38 cm;** Unit 5; plane-polarized light).

A

0.1 mm

B
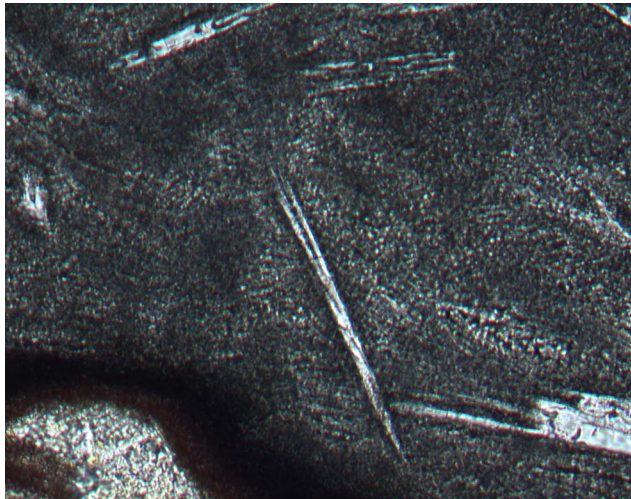
0.1 mm

Figure F35. Photomicrograph of a lithic fragment made up of clinopyroxene, plagioclase, opaque minerals, and possibly glass in crystal vitric tuff (**Sample 200-1223A-3X-1, 112–114 cm;** Unit 5; plane-polarized light).
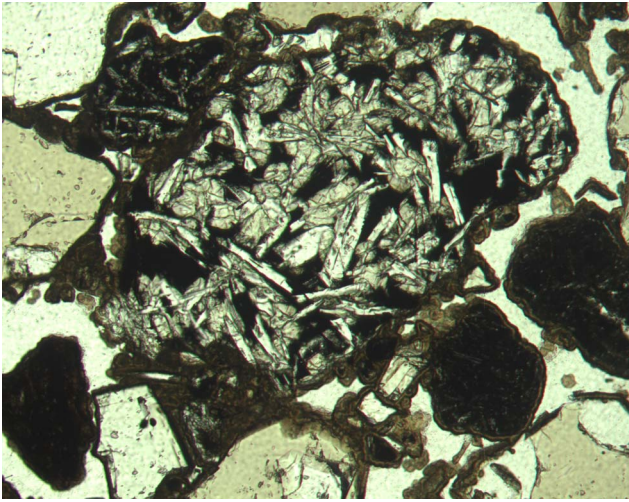
0.2 mm

Figure F36. Photomicrograph of an altered glassy shard with an "atoll-like" structure in crystal vitric tuff (**Sample 200-1223A-5X-1, 12–14 cm;** Subunit 11A; plane-polarized light).

0.1 mm

Figure F37. Photomicrographs of (**A**) a highly vesicular altered glass shard in the altered palagonitized crystal vitric tuff and (**B**) a vesicle-free altered glass shard in the crystal vitric tuff (**Sample 200-1223A-5X-1, 12–14 cm;** Subunit 11A; plane-polarized light).

A

0.2 mm

B

0.2 mm
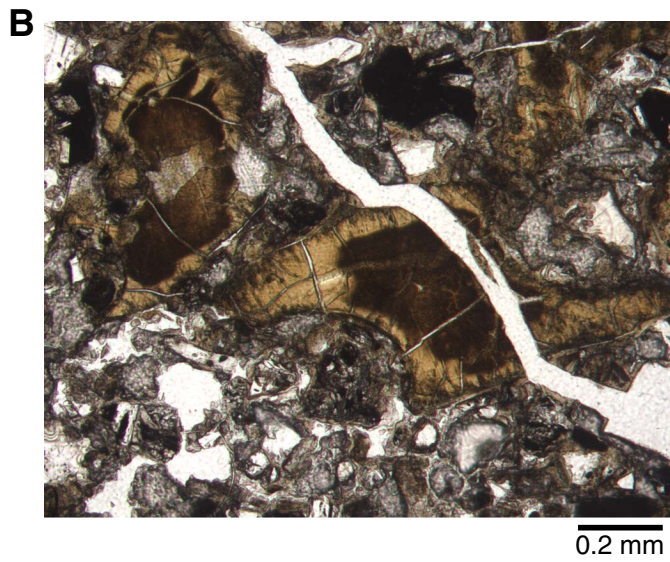
Figure F38. Photomicrograph of palagonitized glass altered to chlorite (**Sample 200-1223A-5X-1, 12–14 cm;** Subunit 11A; plane-polarized light).
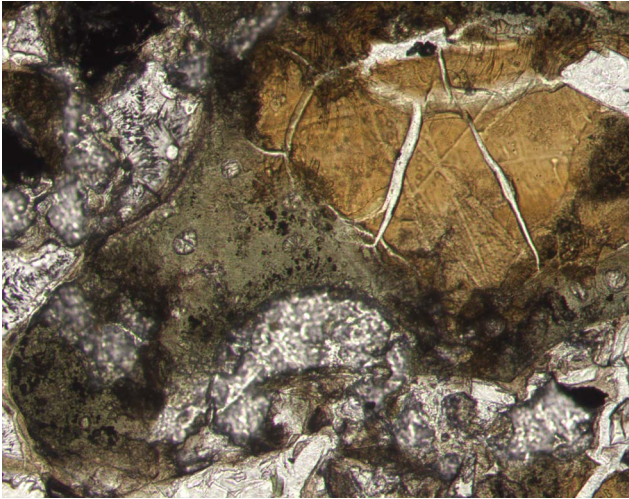
0.1 mm

Figure F39. Photomicrograph of pale-yellow glass shards with orange palagonite rims in the palagonitized crystal vitric tuff (**Sample 200-1223A-6X-2, 79–81 cm;** Subunit 11B; plane-polarized light).
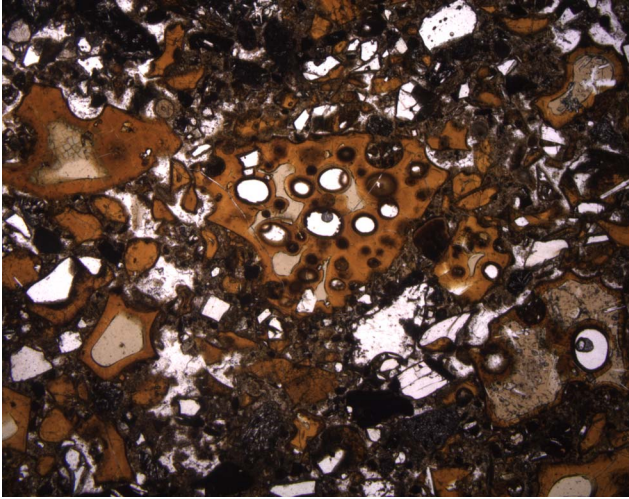
0.5 mm

Figure F40. Photomicrographs of (**A**) anhedral olivine clasts (colorless) and palagonitized glass shards in the palagonitized crystal vitric tuff and (**B**) fresh subhedral olivine in a palagonitized glass shard in the palagonitized crystal vitric tuff (Sample 200-1223A-6X-3, 86–89 cm; Subunit 11B; plane-polarized light).
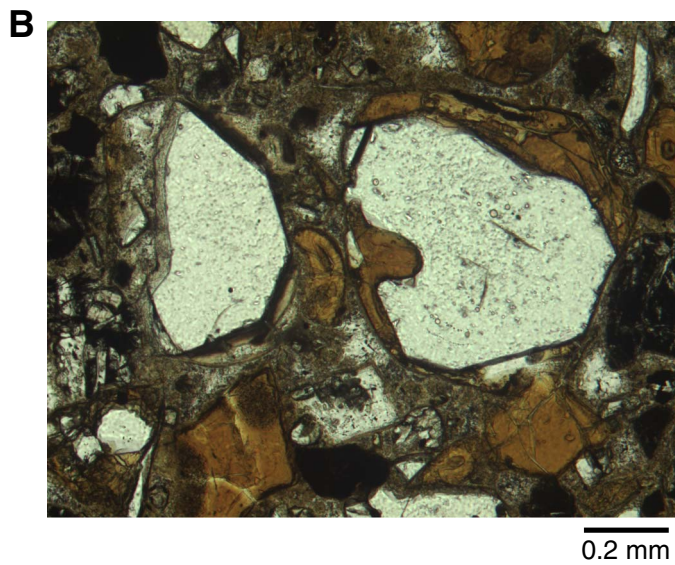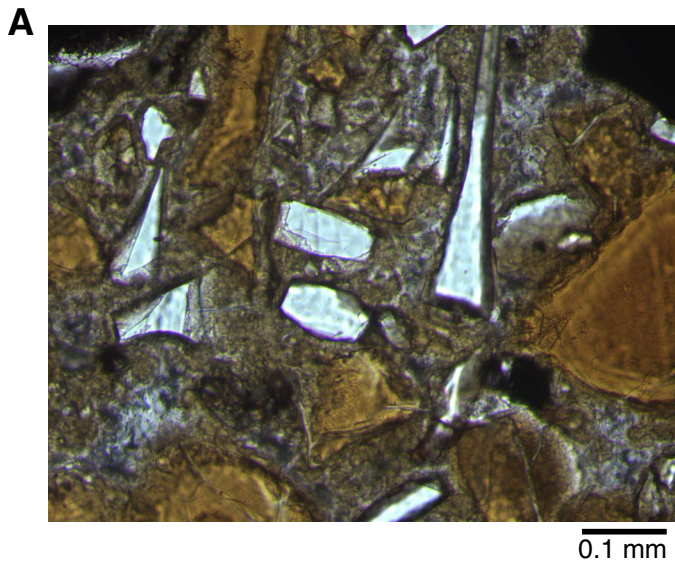
Figure F41. Photomicrographs of (**A**) euhedral skeletal olivine in a partially palagonitized glass shard (**Sample 200-1223A-6X-2, 79–81 cm;** Subunit 11B; plane-polarized light) and (**B**) a glass shard with a single vesicle with a palagonite rim (**Sample 200-1223A-6X-3, 86–89 cm;** Subunit 11B; plane-polarized light).

A

0.2 mm

B
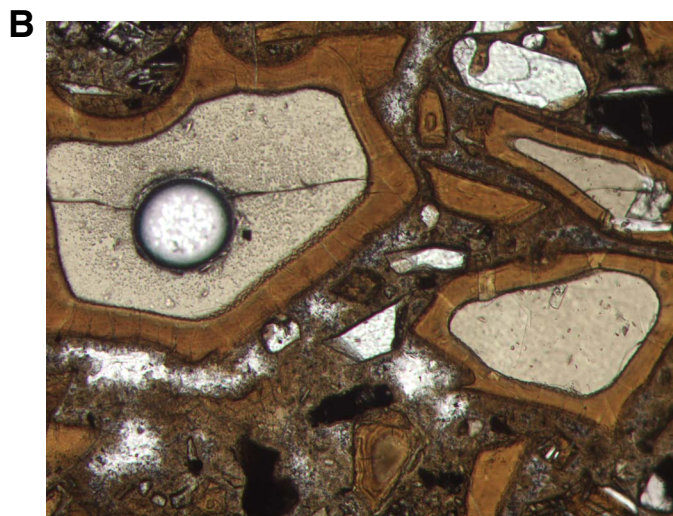
0.2 mm

Figure F42. XRD patterns for brown and yellowish granules from Unit 1 that show peaks that correspond to the minerals (**A**) phillipsite and montmorillonite (Sample 200-1223A-1H-5, 94–95 cm) and (**B**) calcite (Sample 200-1223-1H-5, 114–115 cm). Cps = counts per second.
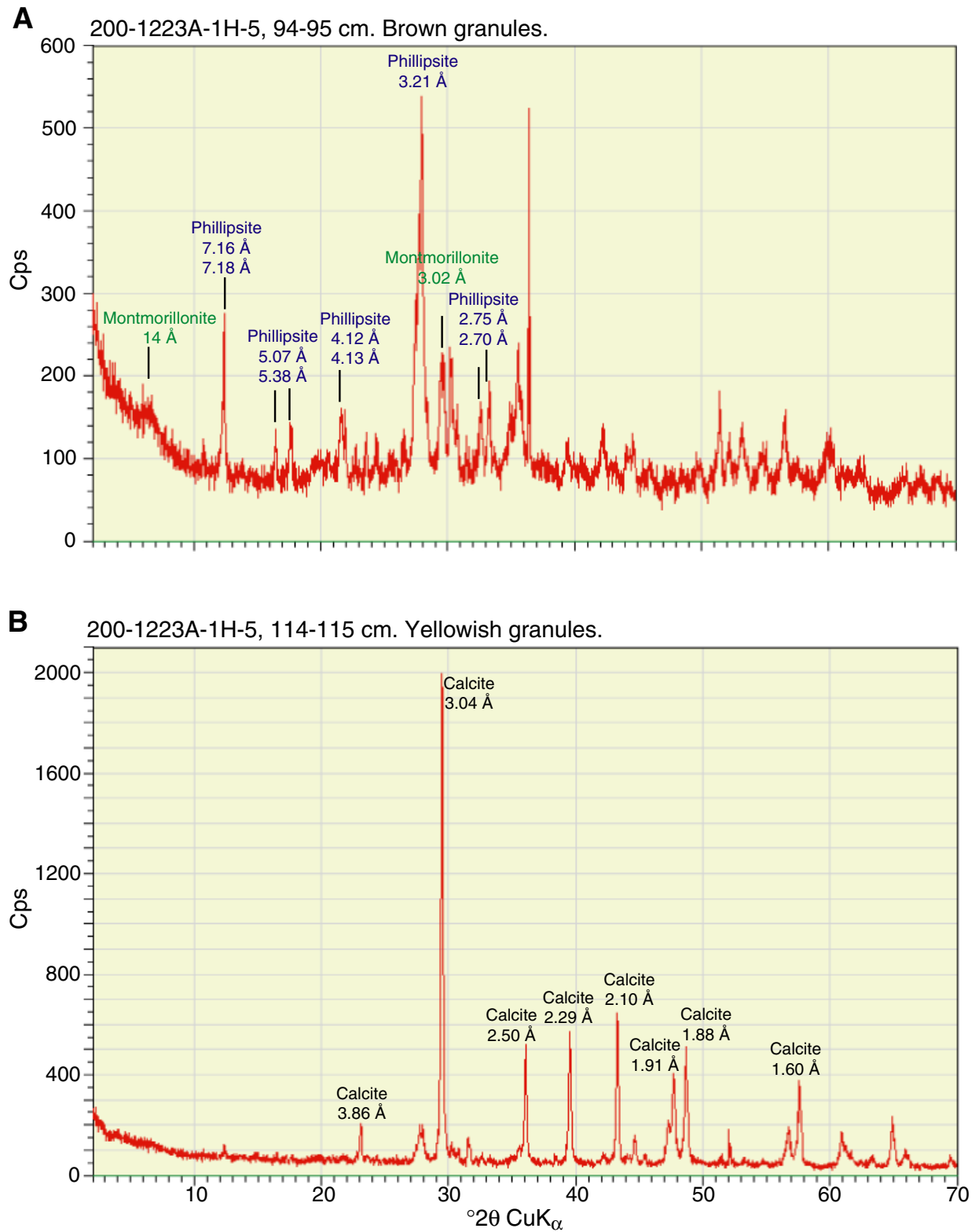
Figure F43. XRD pattern for an inclusion in the palagonitized crystal vitric tuff of Subunit 11A with peaks for saponite and montmorillonite labeled. Cps = counts per second.
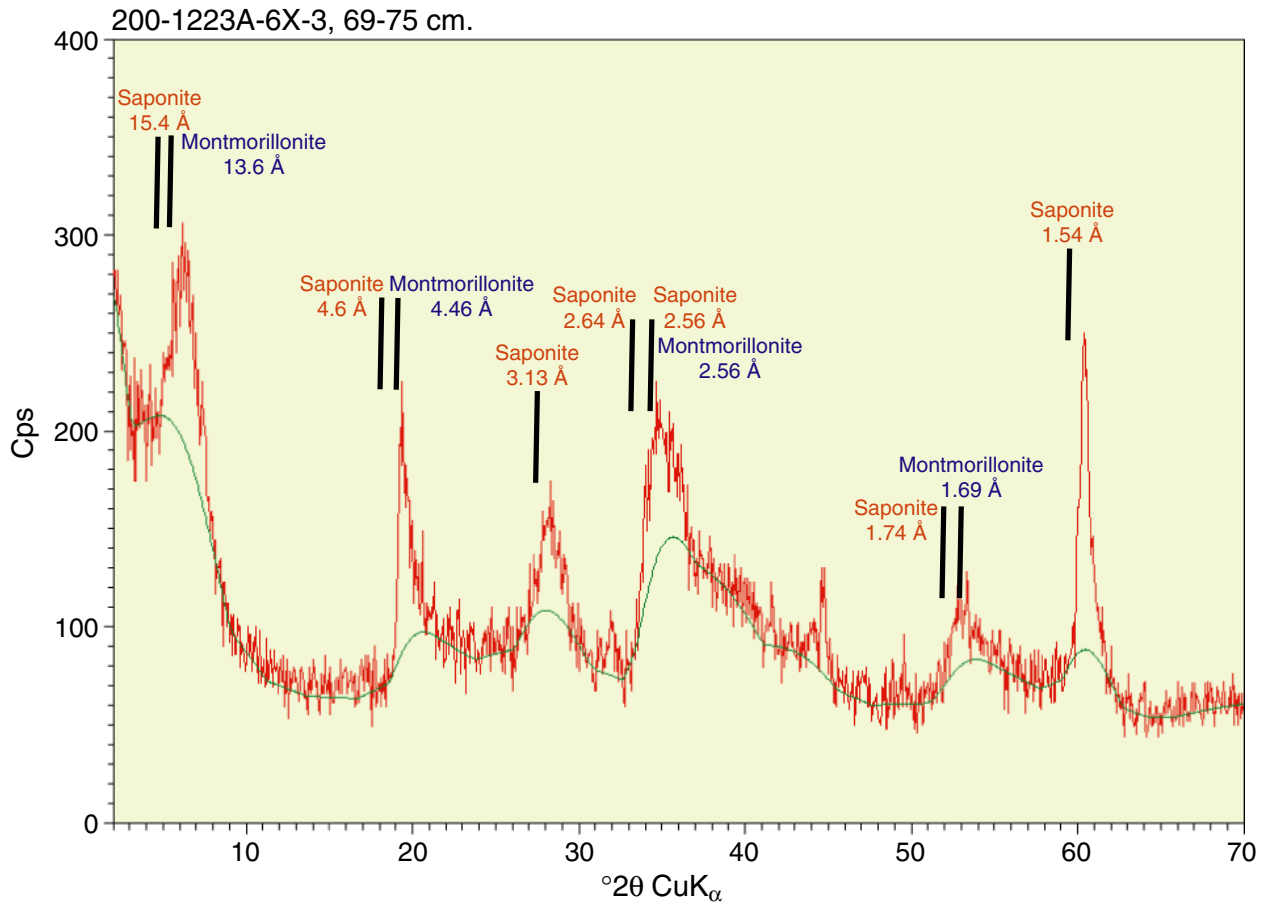
Figure F44. XRD patterns for white vug fillings and white veinlets that show peaks that correspond to the minerals (**A**) paragonite, wairakite, and anhydrite (interval 200-1223A-6X-4, 0–20 cm) and (**B**) thomsonite and phillipsite (interval 200-1223A-6X-3, 117–118 cm). Cps = counts per second.
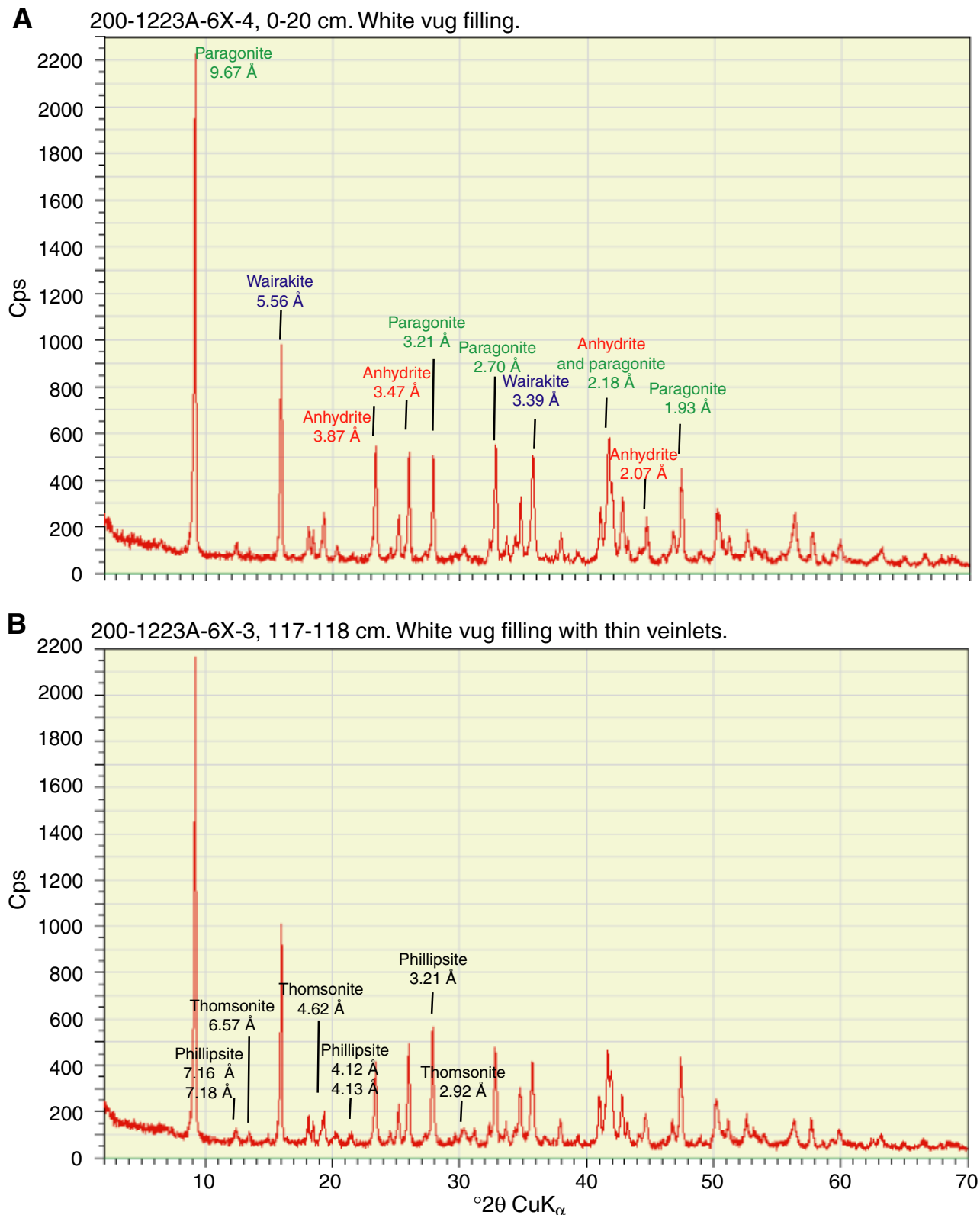
Figure F45. Photomicrographs of palagonitic basaltic glass shards in the palagonitized crystal vitric tuff (**Sample 200-200-1223A-6X-3 [Piece 1C, 86–89 cm];** plane-polarized light). **A.** Palagonitized crystal vitric tuff texture. **B.** Glass fragments with palagonitic rims. **C.** Completely palagonitized vesicular glass shard with matrix material in vesicles. **D.** Palagonitized glass shard containing spherulites and filled vesicles. Individual vesicles are rimmed with palagonite (Subunit 11B).
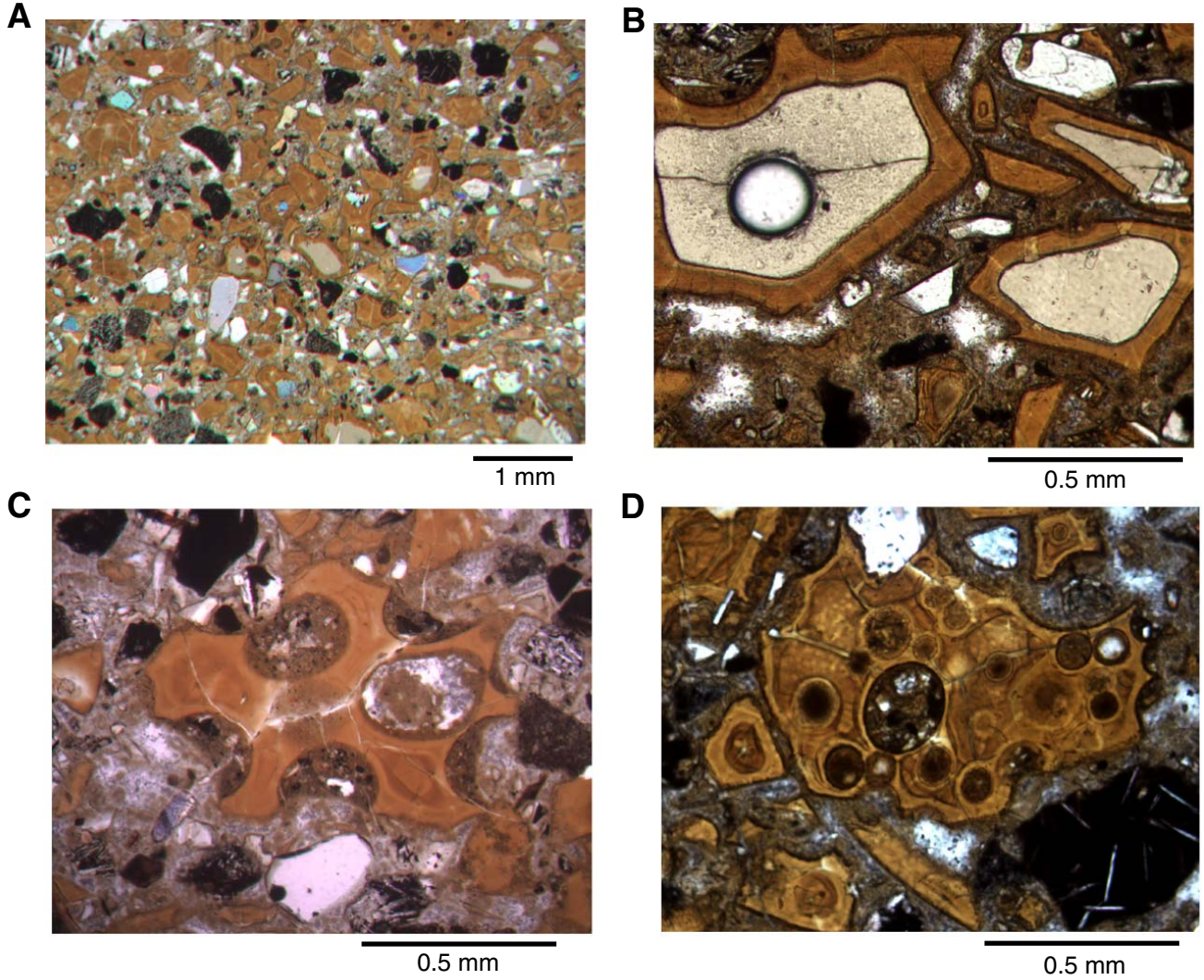
Figure F46. Photomicrographs of alteration in the altered palagonitized crystal vitric tuff (**Sample 200-1223A-5X-CC, 16–19 cm**). **A.** Glass core replaced by clays in a shard with a palagonitized rim (plane-polarized light). **B.** Palagonitized shard with its rim replaced by clays (plane-polarized light). **C.** Zeolites in a matrix (plane-polarized light). **D.** Matrix zeolites (crossed polars). **E.** Enlarged portion of C, showing zeolite intergrowths. **F.** Zeolites in matrix (plane-polarized light).

A

Glass in palagonite replaced by clays; plane-polarized light
0.5 mm

B

Palagonite with rim replaced by clays; plane-polarized light
0.1 mm

C

Zeolites in matrix; plane-polarized light
0.1 mm

D

Matrix zeolites; crossed polars
0.1 mm

E

Zeolites in matrix; plane-polarized light
0.1 mm

F

Enlarged, contrast enhanced; crossed polars
0.1 mm
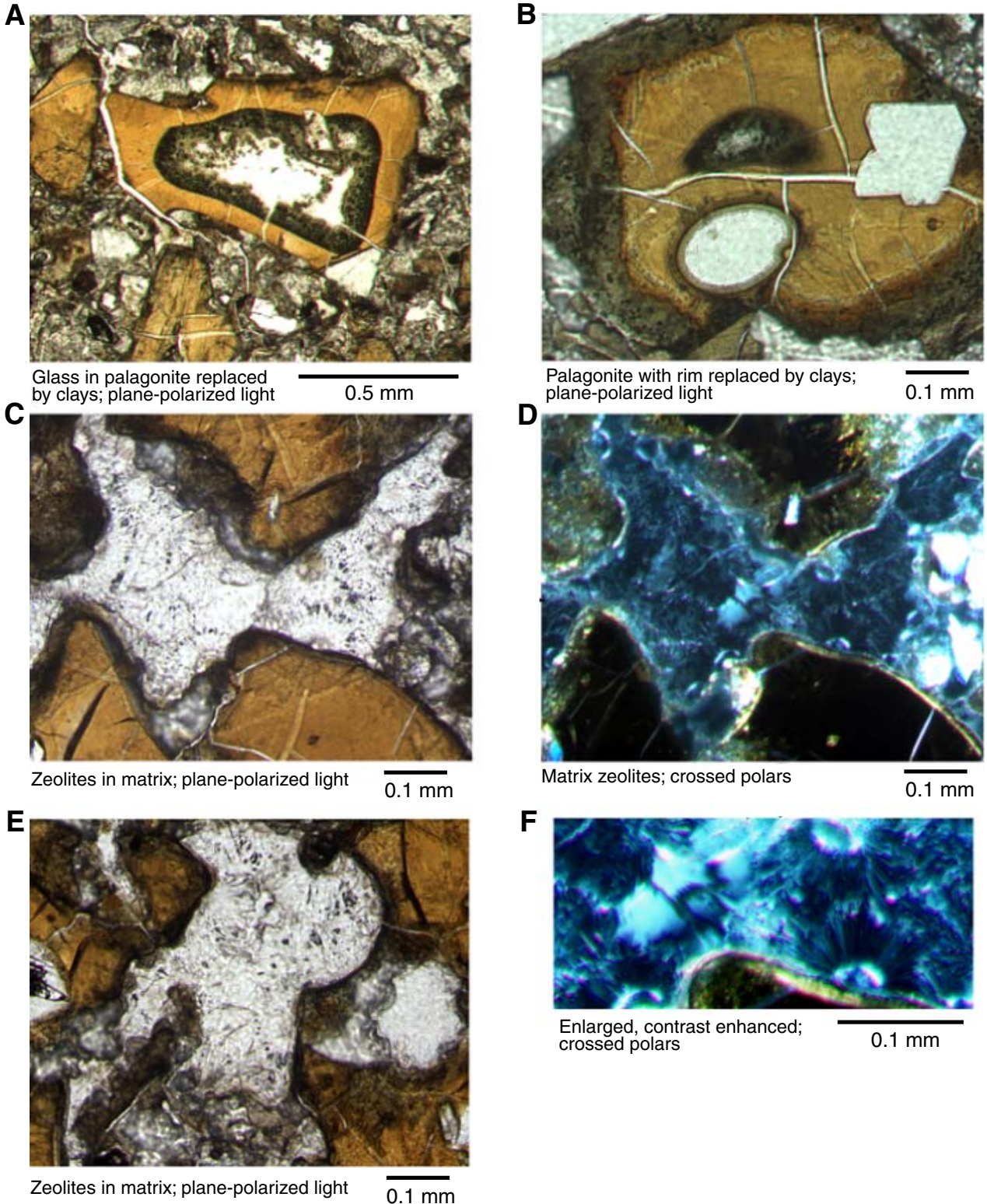
Figure F47. Photomicrographs of cementation and alteration in the upper crystal vitric tuff (Unit 5). **A.** Matrix clays (**Sample 200-1223A-3X-2, 71–73;** plane-polarized light). **B.** Clays lining altered olivine (same sample as A). **C.** Green chloritized glass shard (same sample as A). **D.** Zeolite in a vesicle (**Sample 200-1223A-3X-2, 82–84 cm**).

Matrix clays

0.1 mm

Clays lining olivine and glass

0.1 mm

Chloritized glass

0.1 mm

Zeolite in a vesicle

0.1 mm
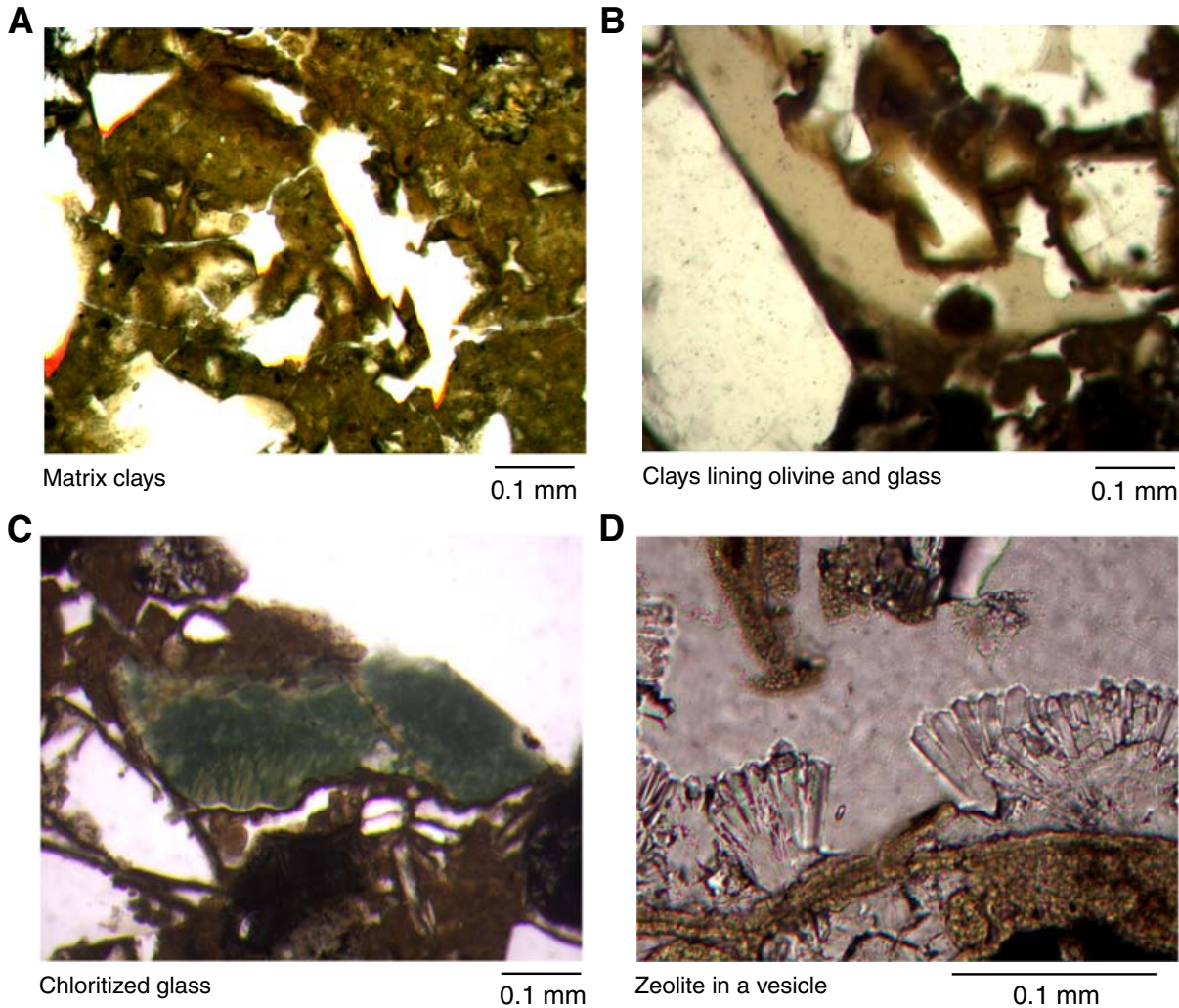
Figure F48. Photomicrographs of deformed and decorated olivine crystals in the upper crystal vitric tuff (Unit 5). **A.** Olivine decorated with exsolved swirls of iron oxide (**Sample 200-1223A-3X-1, 112–114 cm;** plane-polarized light). **B.** Kink-banded olivine fragments (**Sample 200-1223A-3X-2, 71–73 cm;** crossed polars). **C, D.** Olivine decorated with swirls of iron oxides divided into parallel bands with differential staining (**Sample 200-1223A-3X-2, 71–73 cm;** plane-polarized light and crossed polars, respectively). The stain bands are not kink bands because they have uniform birefringence, as seen in D. **E, F.** Another olivine decorated with swirls of iron oxides divided into parallel bands with differential staining (**Sample 200-1223A-3X-2, 71–73 cm;** plane-polarized light and crossed polars, respectively). In this olivine, the cuspate stacking of the swirls coincides with the bands. In F, the bands also have uniform birefringence.
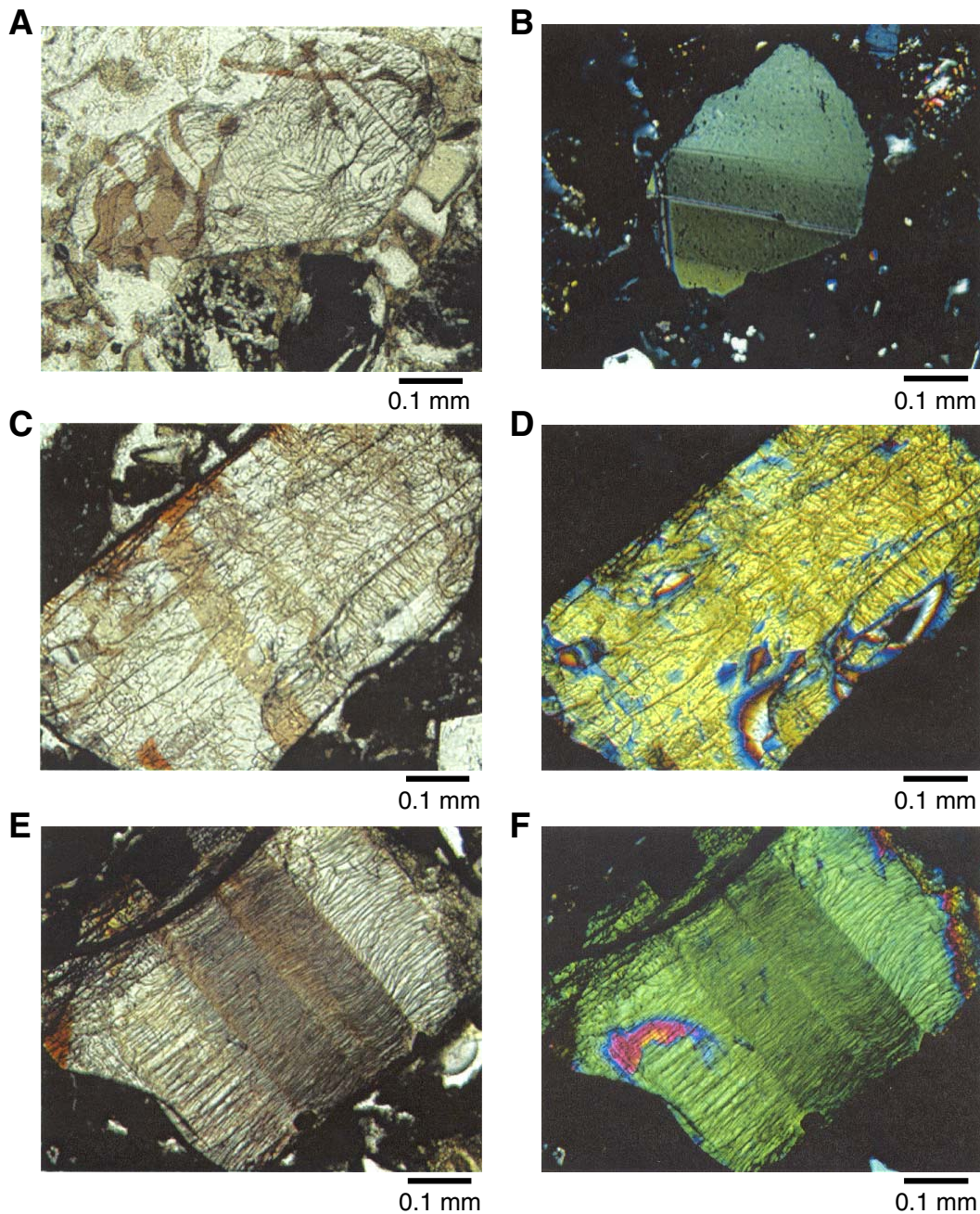
Figure F49. Features of indurated volcaniclastic silty claystone (Unit 12) at the basal contact of the lower palagonitized crystal vitric tuff (Sample 200-1223A-6X-3, 100–117 cm). **A.** Scanned image of the contact. **B.** Close up of white vugs just beneath the tuff. **C.** Detail of the vein network linking the vugs near the base of the lower piece. **D.** Photomicrograph of anhydrite in a vug (crossed polars). **E.** Embossed image, lighted from the top, showing grains of minerals in a vug. Note grains with pseudohexagonal cross sections. **F.** Bladelike mineral in rosettes in a space along a vein (crossed polars). **G.** Recrystallized matrix of the claystone (plane-polarized light). **H.** Zeolite filling a circular center of a former radiolarian test. **I.** Tiny rosette of a secondary mineral (cristobalite?) in the recrystallized matrix of the claystone.
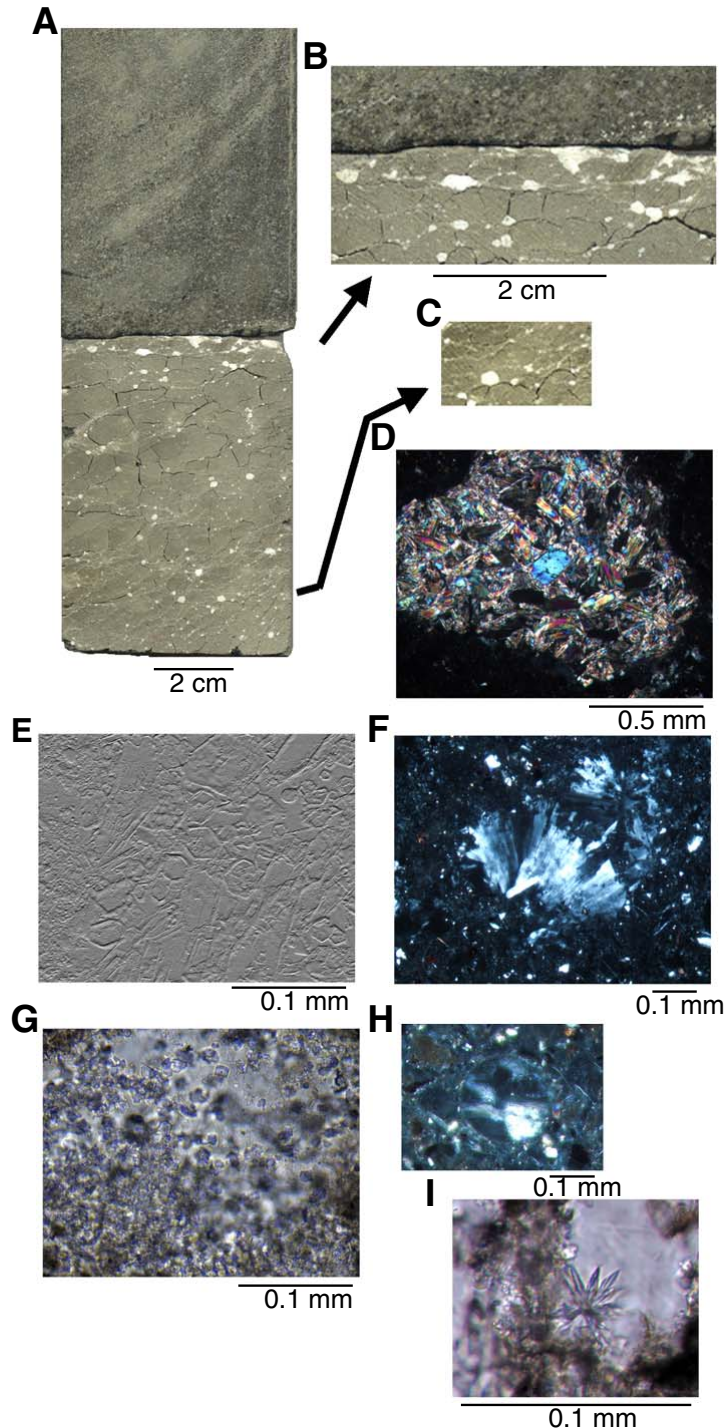
Figure F50. Photomicrographs of vein and radiolarian fillings in volcaniclastic silty claystone (**Sample 200-1223A-6X-3, 113–116 cm;** crossed polars). **A.** Zeolite, either wairakite or analcime, in a vein. **B.** Nearby silicate mineral (pumpellyite?). **C–E.** Zeolites in variably preserved radiolarian tests.
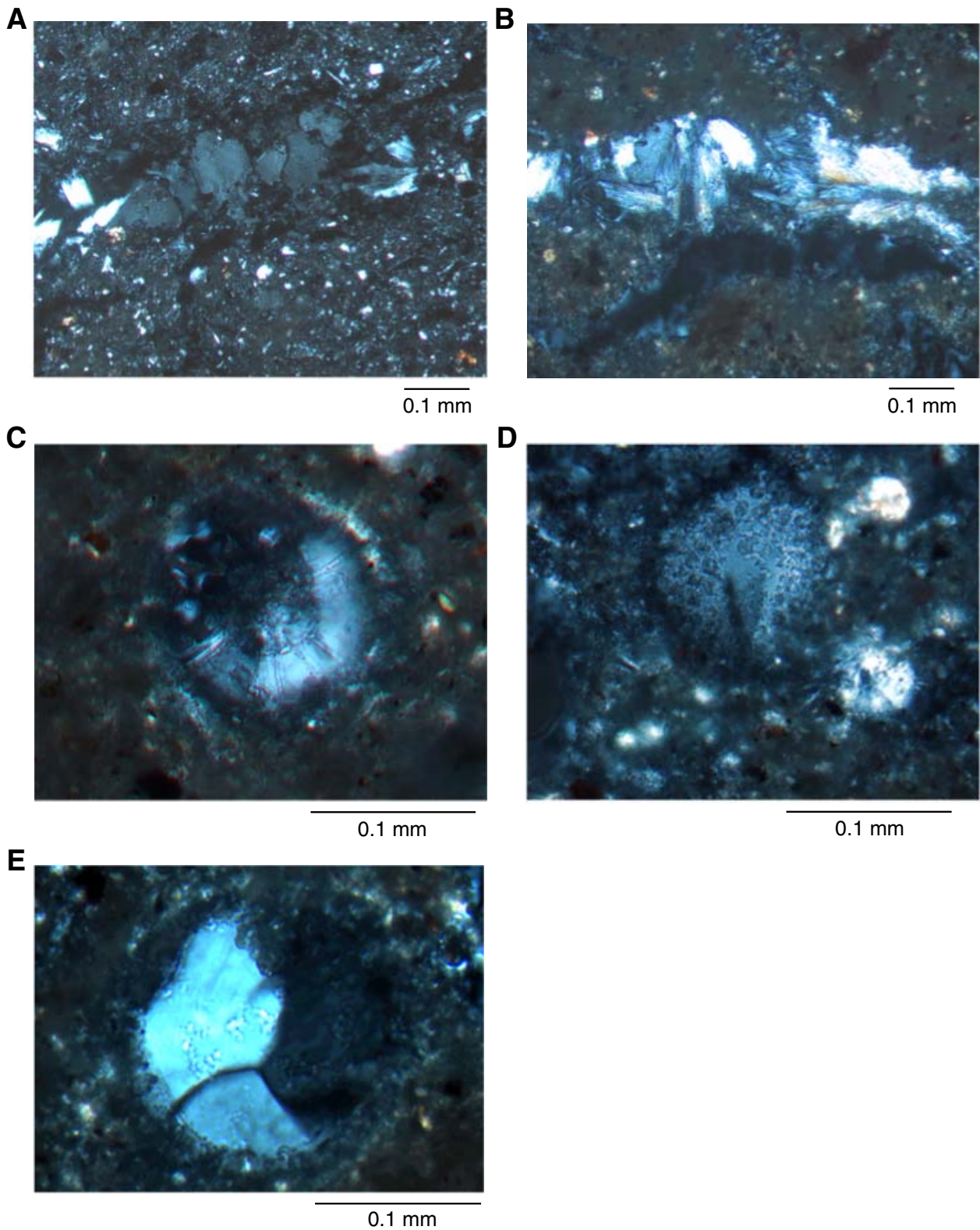
Figure F51. Schematic drawing of a landslide and the resulting directed blast eruption of the 1980 eruption of Mount Saint Helens (after Moore and Albee, 1981).
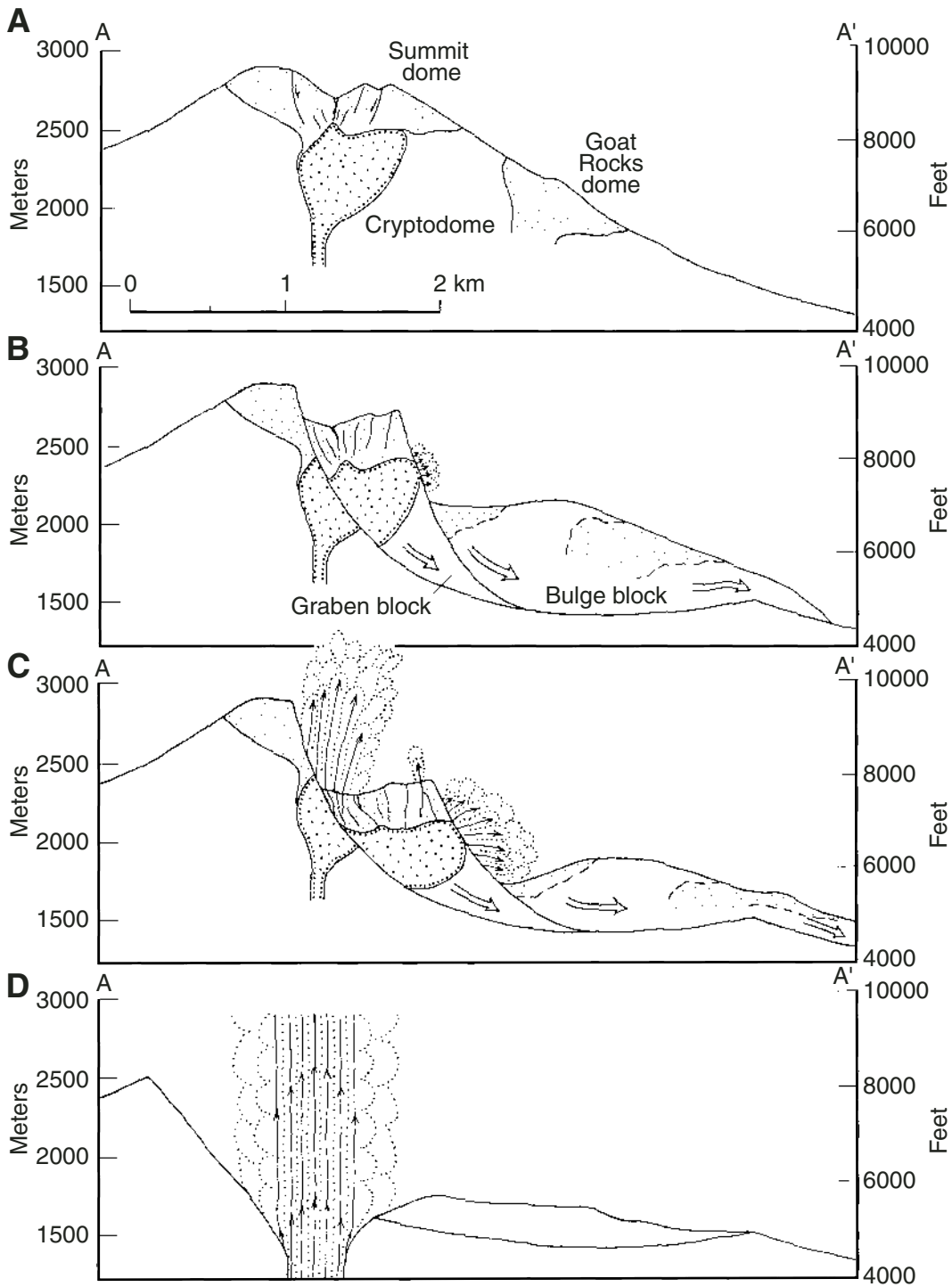
Figure F52. Loss on ignition (LOI) vs. K_2O for crystal vitric tuffs (red left-pointing triangles) and siltstones (gray triangles) analyzed from Hole 1223A. See "Geochemistry," p. 15, in the "Explanatory Notes" chapter for a discussion on error.
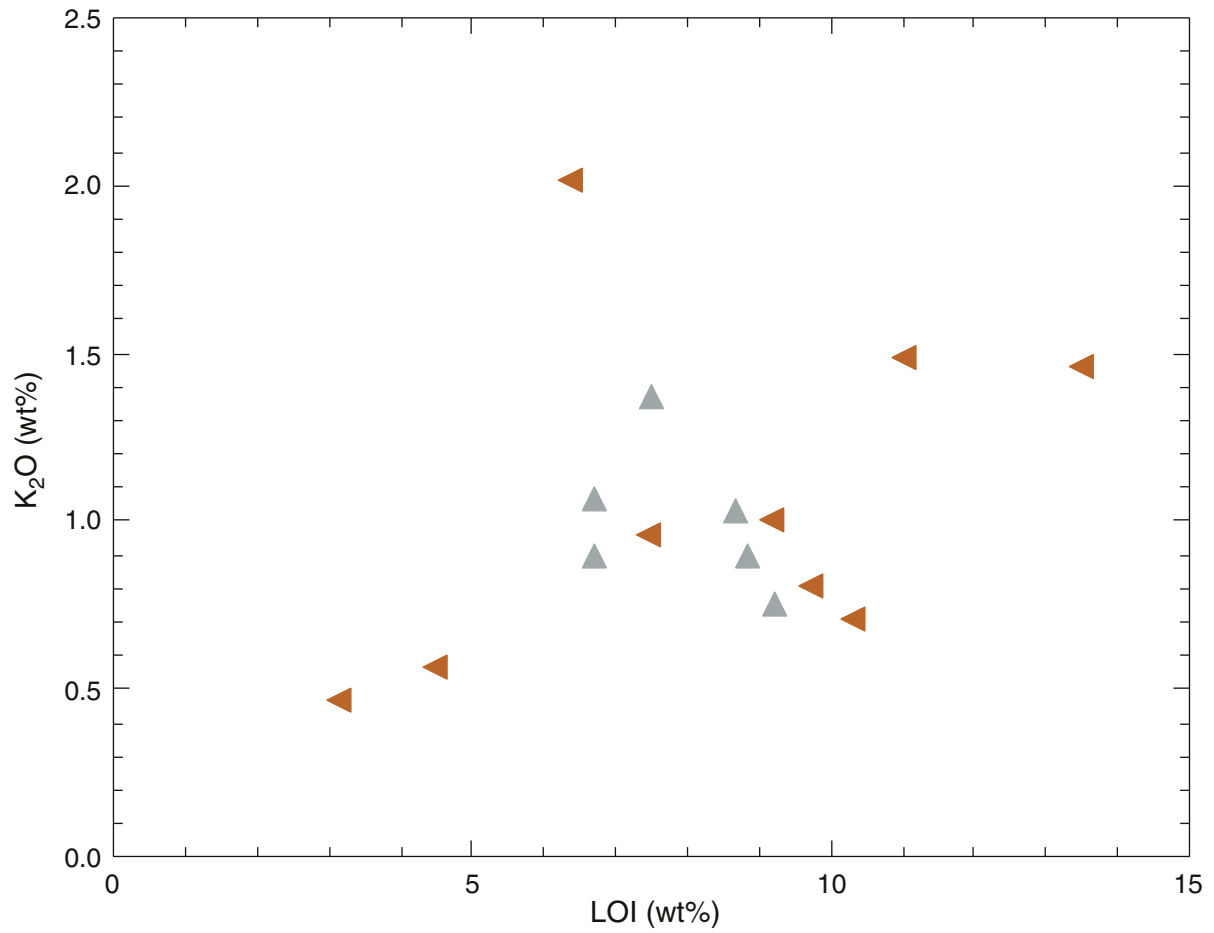
Figure F53. Ternary diagrams showing effects of addition of detrital and authigenic clays to basaltic volcaniclastic material. Inset diagrams show placement of enlarged portions of ternary diagrams on which data are plotted. **A.** CaO-Al$_2$O$_3$-K$_2$O (CAK) diagram. **B.** MgO-Al$_2$O$_3$-Fe$_2$O$_3$(T) (MAF) diagram; total iron as Fe$_2$O$_3^T$. Symbols distinguish vitric tuffs (red left-pointing triangles) and siltstones (gray triangles). Groups 1 and 2 distinguish samples having, respectively, higher proportions of detrital clay, inferred from their proportionate increase in Al$_2$O$_3$. (See **"Diagenesis and Alteration vs. a Detrital Component,"** p. 30, and **"Provenance,"** p. 32). Additional symbols are as follows: small open triangles = glasses from Kilauea and Puna Ridge (Clague et al., 1995); small dots = normal mid-ocean-ridge basalt (N-MORB) glasses from the Pacific-Antarctic East Pacific Rise; large purple dots = N-MORB glass from DSDP Site 501 and three portions of its palagonitized rim (Noack et al., 1983). Fields for kaolinite (K), illite (I), and continental montmorillonite (M) are from Grim (1964). Average pelagic clay (PC) is from Cronan and Toombs (1969). The saponite-nontronite (sap and non) fields (inset diagrams only) are for vein and replacement clays in basalts of DSDP Hole 504B (Honnorez et al., 1983). See **"Geochemistry,"** p. 15, in the "Explanatory Notes" chapter for a discussion on error.
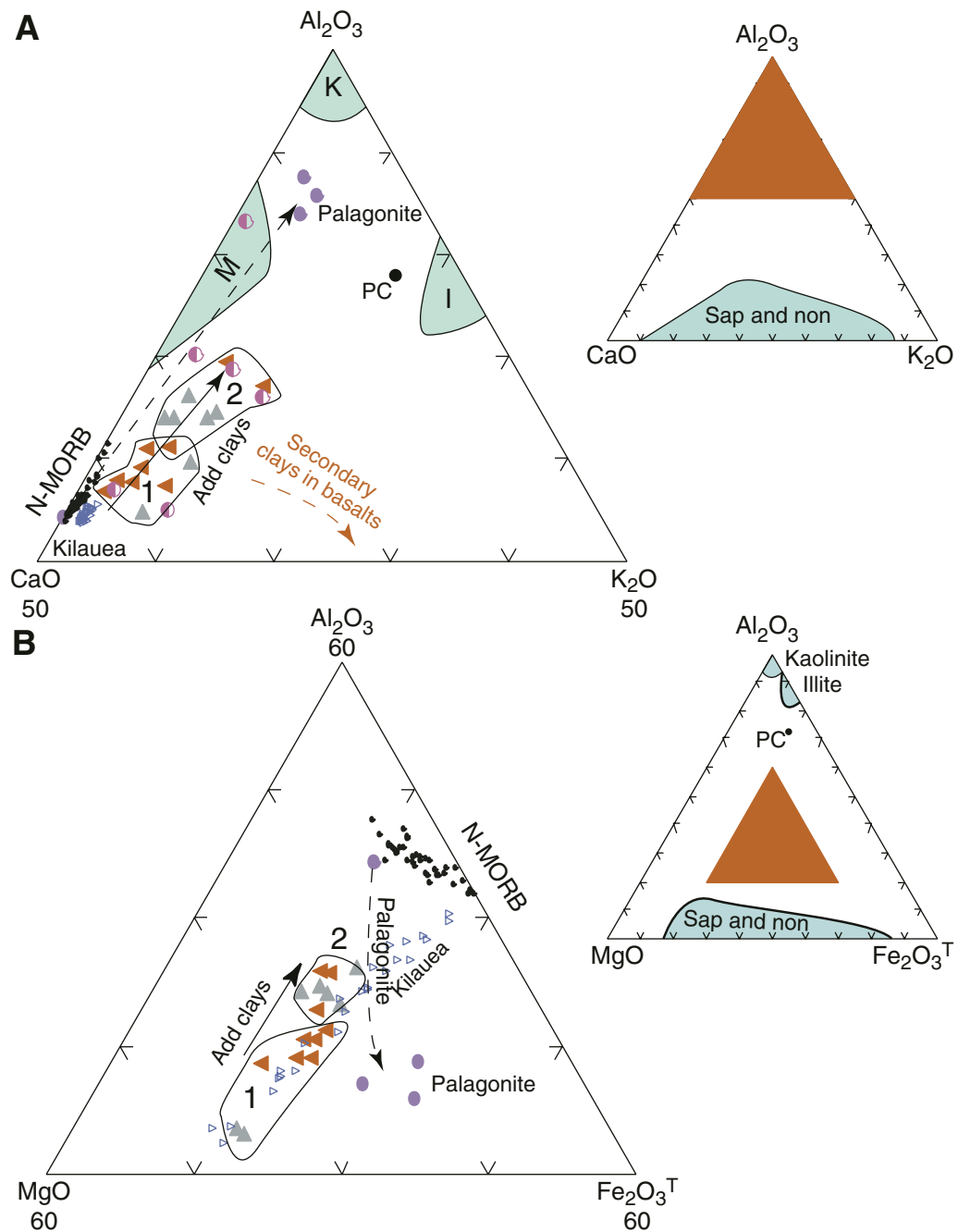
Figure F54. Major oxide discriminant diagrams. **A, C.** Al_2O_3 vs. FeO^T as Fe_2O_3. **B, D.** SiO_2 vs. Al_2O_3. Symbols distinguish vitric tuffs (red left-pointing triangles) and siltstones (gray triangles). Arrows in A and B indicate the effects of subtraction of 13 wt% olivine = Fo_{85} from a representative tuff composition. (See **"Diagenesis and Alteration vs. a Detrital Component,"** p. 30, and **"Provenance,"** p. 32). Additional symbols in A and B are as follows: large open triangles = basaltic glasses from Kilauea and Puna Ridge (Clague et al., 1995); half-filled squares = Honolulu Volcanic Series (Jackson and Wright, 1970; Clague and Frey, 1982); downward-pointing triangles = North Arch Volcanic Series (Dixon et al., 1997); blue diamonds = Hana Volcanic Series, Haleakala Volcano, Maui (Chen et al., 1991). Additional symbols in C and D are as follows: dark-green squares = high-MgO basalts from Koolau Volcano, Oahu (Frey et al., 1994); light-green right-pointing triangles = E-MORB (data compilation from Lamont-Doherty Earth Observatory Petrologic Database at **www.ldeo.columbia.edu/datarep/index.html** and J. Natland, P. Castillo, and Y.-L. Niu, unpubl. data). See **"Geochemistry,"** p. 15, in the "Explanatory Notes" chapter.
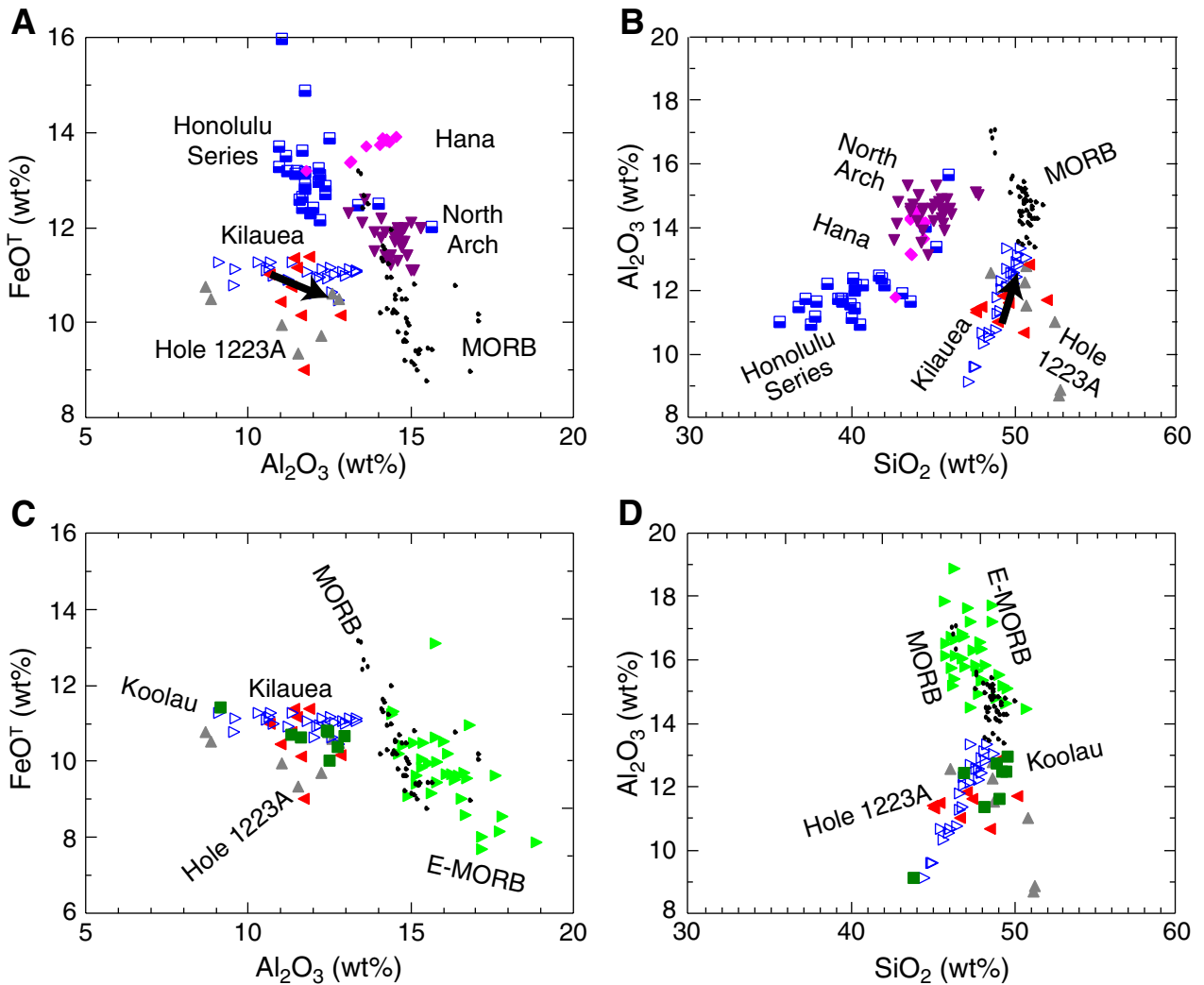
Figure F55. Comparison of analyses of samples from Hole 1223A with Kilauea-Puna Ridge and Koolau tholeiites, plus normal and enriched mid-ocean-ridge basalt (MORB and E-MORB, respectively). **A.** MgO vs. SiO_2. **B.** MgO vs. Ba. **C.** MgO vs. Zr. The general effect of subtraction of olivine with 45 wt% MgO is indicated by the arrow in C. Symbols distinguish vitric tuffs (red left-pointing triangles) and siltstones (gray triangles). Large open triangles = basaltic glasses from Kilauea and Puna Ridge (Clague et al., 1995); dark-green squares = high-MgO basalts from Koolau Volcano, Oahu (Frey et al., 1994); light-green right-pointing triangles = E-MORB (data compilation from Lamont-Doherty Earth Observatory Petrologic Database at **www.ldeo.columbia.edu/datarep/index.html** and J. Natland, P. Castillo, and Y.-L. Niu, unpubl. data); small dots = normal mid-ocean-ridge basalt (N-MORB) glasses from the Pacific-Antarctic East Pacific Rise. See **"Geochemistry,"** p. 15, in the "Explanatory Notes" chapter.
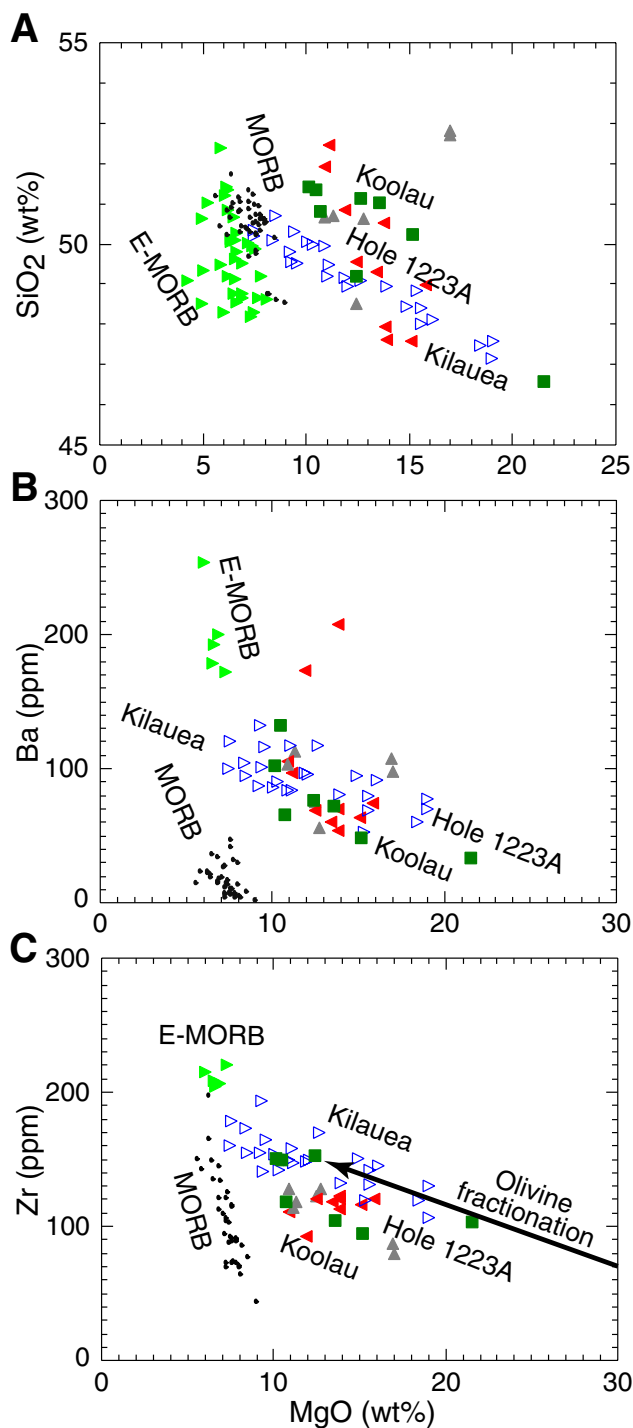
Figure F56. Inclination, declination, and intensity from archive-half split-core sections prior to AF demagnetization are plotted vs. depth downhole for Hole 1223A. Also shown are the whole-core susceptibility results (in raw meter units).
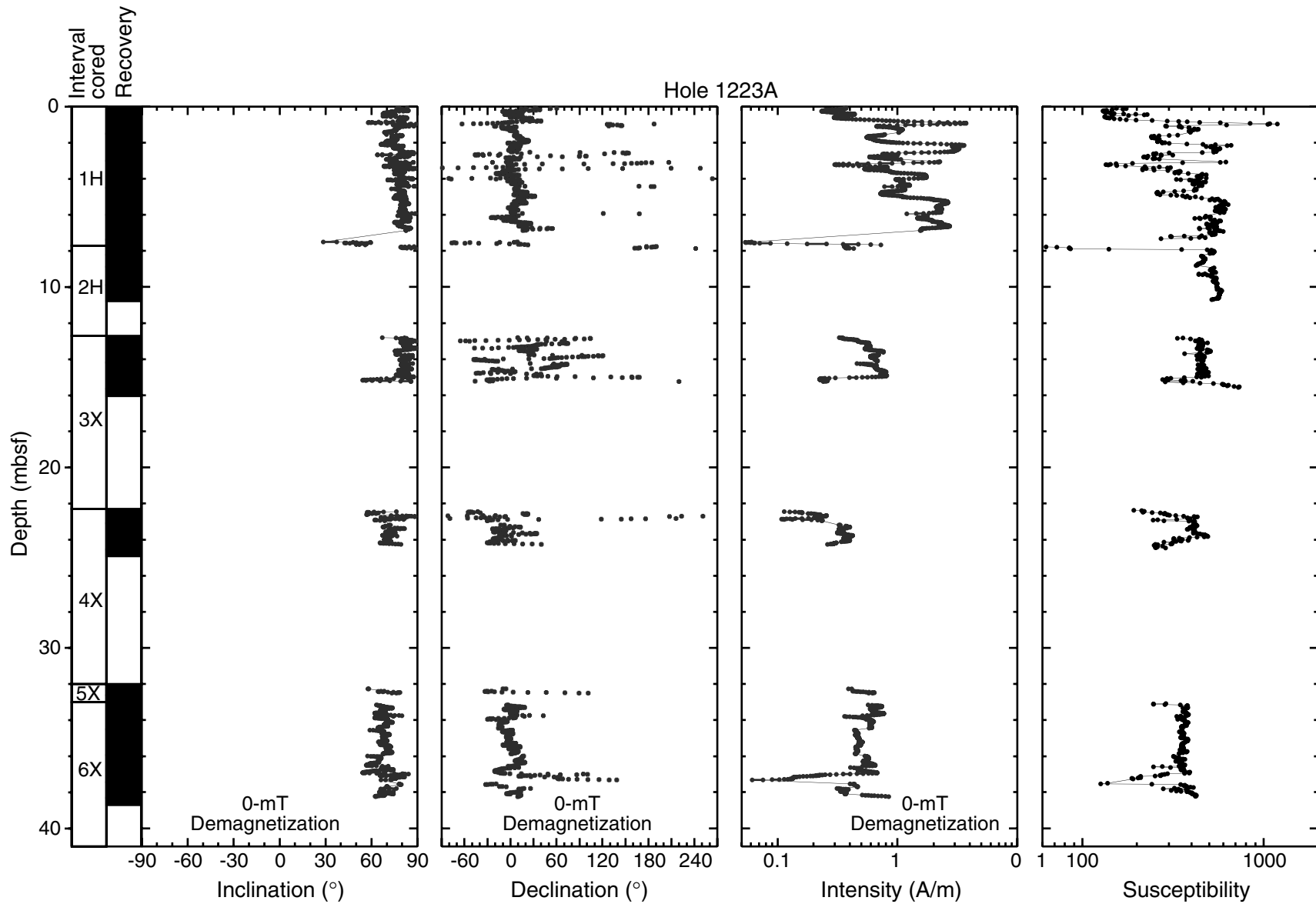
Figure F57. AF demagnetization results from split-core interval 200-1223A-1H-1, 65 cm. The top left diagram shows the intensity variation with progressive demagnetization; the top right diagram shows vector endpoints on a vector demagnetization diagram (orthogonal projections, where open squares are inclination, and solid squares are declination); the middle right diagram is an enlargement of the region near the origin of the above diagram; the bottom left area shows the data; and the bottom right diagram shows the magnetization directions on an equal-area projection (open squares are directions with negative inclinations).

Split-core interval 200-1223A-1H-1, 65 cm, 0.65 mbsf

J/J_{max}

J_{max} = 3.24E-01 A/m

Demagnetization (mT)

Demag (mT)	Dec (°)	Inc (°)	Intensity
0.0	25.2	83.1	3.24E-01
2.0	23.2	81.2	2.45E-01
4.0	21.4	78.5	1.53E-01
6.0	19.8	72.6	7.29E-02
8.0	14.9	59.0	2.91E-02
10.0	7.6	28.8	1.34E-02
12.0	3.4	3.6	1.13E-02
14.0	1.0	-12.0	1.09E-02
16.0	359.6	-19.2	1.18E-02
18.0	358.1	-23.6	1.19E-02
20.0	352.7	-25.8	1.20E-02
25.0	355.0	-28.9	1.14E-02
30.0	350.9	-30.5	1.04E-02
35.0	348.0	-31.6	9.53E-03
35.0	353.3	-30.2	8.91E-03
40.0	351.8	-29.5	8.45E-03
45.0	348.4	-29.0	8.00E-03
50.0	346.0	-28.5	7.24E-03

N, Up

N, E

E, H

6 mT

Removal of drilling overprint

N, Up

NRM

ChRM

20 mT

50 mT

E, H

N

W

E

S

Equal area

Figure F58. AF demagnetization results from split-core interval 200-1223A-6X-3, 90 cm. The top left diagram shows the intensity variation with progressive demagnetization; the top right diagram shows vector endpoints on a vector demagnetization diagram (orthogonal projections, where open squares are inclination and solid squares are declination); the middle right diagram is an enlargement of the region near the origin of the above diagram; the bottom left area shows the data; and the bottom right diagram shows the magnetization directions on an equal-area projection (open squares are directions with negative inclinations). A great circle is plotted on the stereonet to illustrate the migration of the remanence vector during progressive AF demagnetization.

Split-core interval 200-1223A-6X-3, 90 cm, 36.83 mbsf

J_{max} = 5.45E-01 A/m

Demag (mT)	Dec (°)	Inc (°)	Intensity
0.0	339.3	60.6	5.45E-01
4.0	336.6	50.3	3.43E-01
8.0	331.4	42.9	2.01E-01
12.0	323.2	36.9	1.12E-01
16.0	314.3	30.3	6.96E-02
20.0	304.4	21.1	4.55E-02
25.0	291.4	8.4	3.10E-02
30.0	280.5	-4.7	2.45E-02
35.0	272.7	-12.6	2.12E-02
40.0	269.0	-16.8	2.03E-02
40.0	268.5	-17.1	1.97E-02
45.0	265.3	-18.4	1.86E-02
50.0	263.0	-20.1	1.76E-02
50.0	263.6	-25.8	1.76E-02
55.0	263.5	-25.9	1.73E-02
60.0	261.9	-26.5	1.69E-02
60.0	261.4	-25.4	1.61E-02
65.0	262.4	-28.2	1.61E-02
70.0	262.4	-27.1	1.52E-02

Figure F59. Magnetostratigraphy and comparison of inclinations from split cores and discrete samples for the upper 9 m of the lithologic section. The inclinations are computed using principal component analysis (PCA) and stable endpoints.
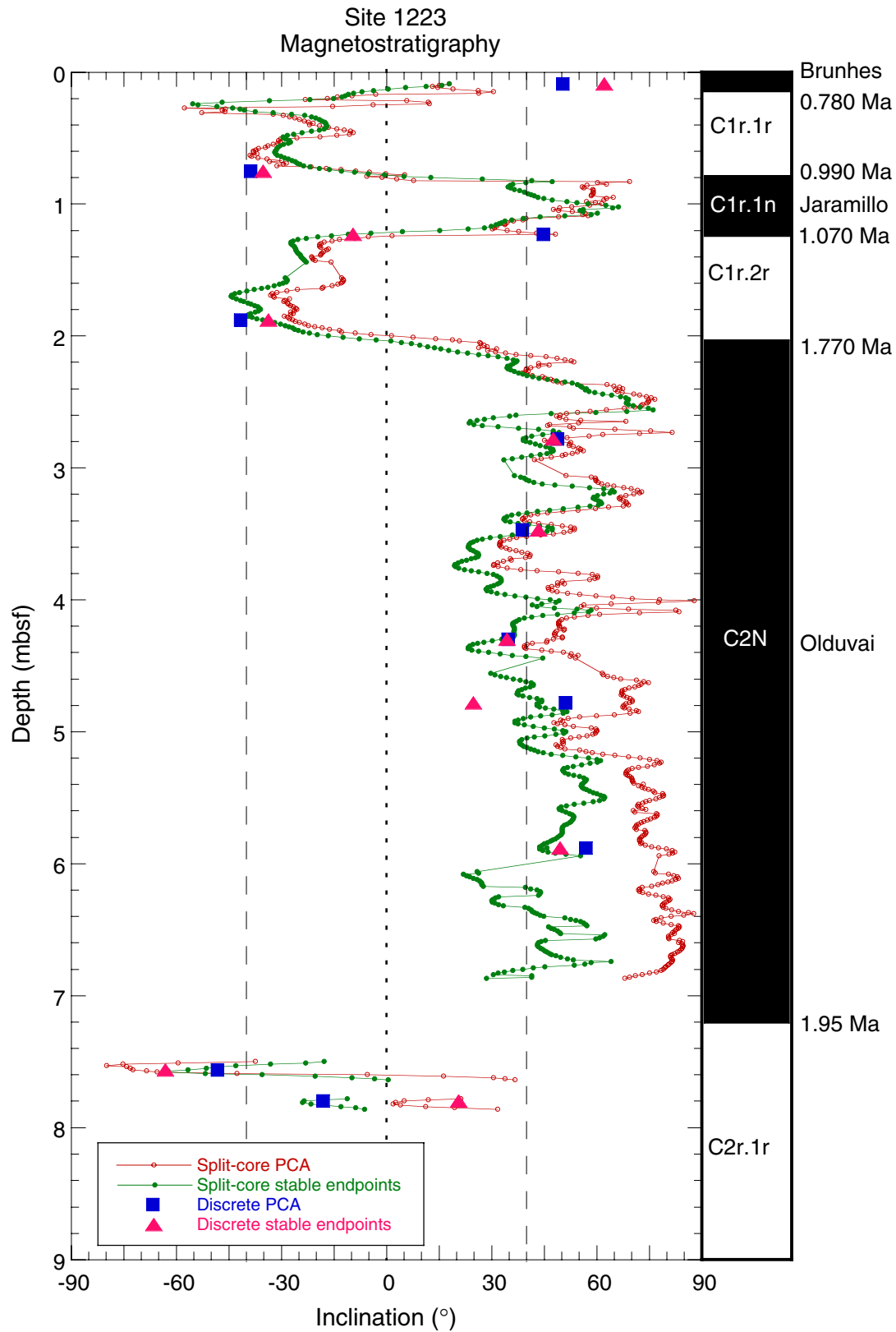
Figure F60. AF demagnetization results from split-core interval 200-1223A-1H-2, 38 cm. The top left diagram shows the intensity variation with progressive demagnetization; the top right diagram shows vector endpoints on a vector demagnetization diagram (orthogonal projections, where open squares are inclination and solid squares are declination); the bottom left area shows the data; and the bottom right diagram shows the magnetization directions on an equal-area projection (open squares are directions with negative inclinations).

Discrete Sample 200-1223A-1H-2, 38 cm, 1.88 mbsf

J_{max} = 1.93E-01 A/m
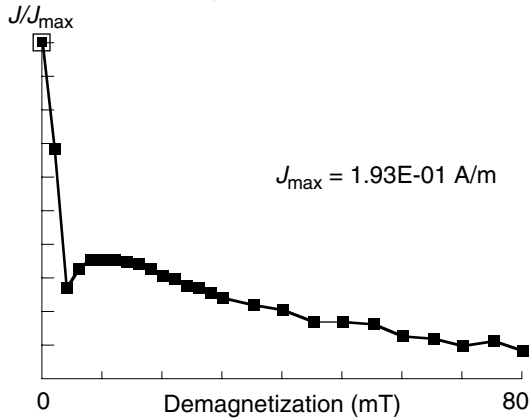
Demag (mT)	Dec (°)	Inc (°)	Intensity
0.0	31.5	79.9	1.93E-01
2.0	19.3	72.7	1.33E-01
4.0	11.7	9.2	5.27E-02
6.0	9.4	-25.1	6.40E-02
8.0	9.2	-30.2	6.84E-02
10.0	9.1	-32.3	6.95E-02
12.0	9.2	-33.5	6.91E-02
14.0	8.9	-33.7	6.78E-02
16.0	9.1	-33.9	6.59E-02
18.0	8.7	-34.4	6.34E-02
20.0	8.9	-34.9	5.99E-02
22.0	9.0	-35.3	5.76E-02
24.0	8.3	-34.5	5.42E-02
26.0	8.3	-35.1	5.23E-02
28.0	8.5	-35.2	4.91E-02
30.0	8.9	-36.0	4.64E-02
35.0	8.9	-36.7	4.22E-02
40.0	8.6	-35.6	4.06E-02
45.0	10.8	-36.2	3.32E-02
50.0	9.5	-33.9	3.30E-02
55.0	8.2	-33.8	3.17E-02
60.0	7.9	-33.0	2.53E-02
65.0	10.3	-36.2	2.42E-02
70.0	13.4	-35.6	2.00E-02
75.0	9.6	-24.9	2.25E-02
80.0	7.9	-30.3	1.65E-02
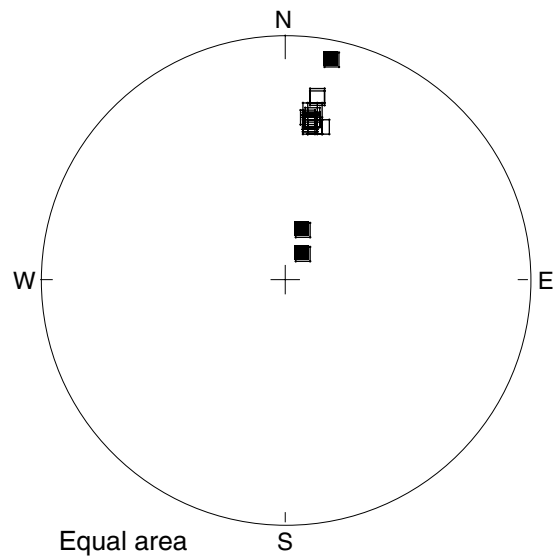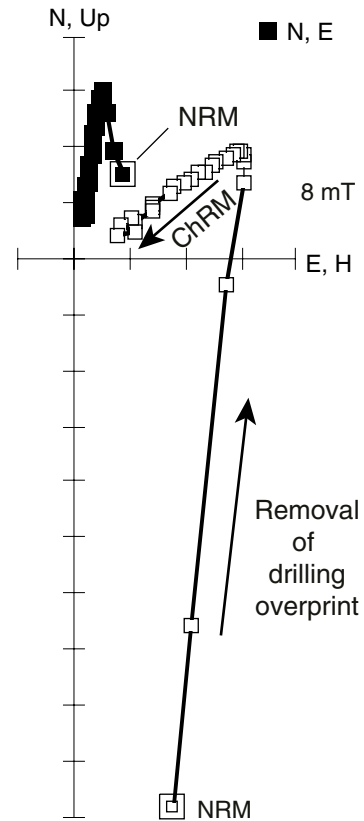
Figure F61. AF demagnetization results from split-core interval 200-1223A-1H-3, 47 cm. The top left diagram shows the intensity variation with progressive demagnetization; the top right diagram shows vector endpoints on a vector demagnetization diagram (orthogonal projections, where open squares are inclination and solid squares are declination); the bottom left area shows the data; and the bottom right diagram shows the magnetization directions on an equal-area projection (open squares are directions with negative inclinations).

Discrete Sample 200-1223A-1H-3, 47 cm, 3.47 mbsf

J/J_{max}

J_{max} = 2.36E-01 A/m

Demagnetization level (mT)

Demag (mT)	Dec (°)	Inc (°)	Intensity
0.0	195.4	74.3	2.36E-01
2.0	200.2	71.5	1.94E-01
4.0	205.6	60.5	1.18E-01
6.0	209.7	46.4	7.94E-02
8.0	210.3	43.7	7.26E-02
10.0	210.6	42.4	6.71E-02
12.0	210.4	41.6	6.36E-02
14.0	210.5	41.3	6.06E-02
16.0	210.1	41.2	5.72E-02
18.0	209.6	41.2	5.45E-02
20.0	209.6	41.4	5.23E-02
22.0	209.2	41.5	4.96E-02
24.0	209.5	41.5	4.68E-02
26.0	208.8	40.9	4.45E-02
28.0	209.0	41.2	4.18E-02
30.0	207.9	40.6	3.93E-02
35.0	207.9	40.8	3.48E-02
40.0	207.6	41.6	3.10E-02
45.0	205.8	40.8	2.85E-02
50.0	205.4	40.9	2.43E-02
55.0	205.3	41.3	2.23E-02
60.0	206.0	42.0	1.96E-02
65.0	205.9	43.6	1.78E-02
70.0	204.8	42.9	1.68E-02
75.0	204.8	42.7	1.41E-02
80.0	205.0	44.9	1.46E-02

N, Up

■ N, E

E, H

ChRM

ChRM

10 mT

Removal of drilling overprint

4 mT

Removal of drilling overprint

NRM

N

W

E

S

Equal area
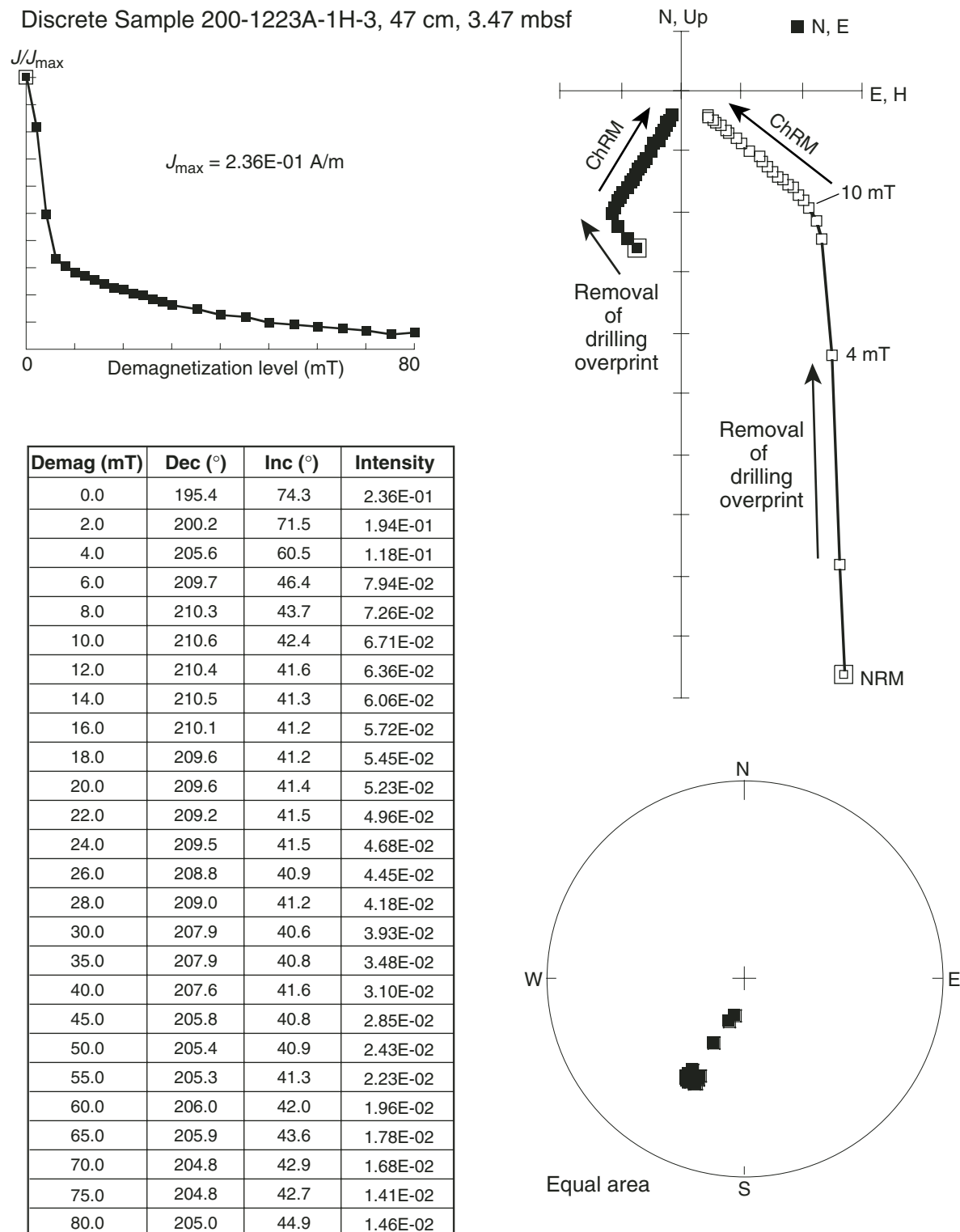
Figure F62. Orthogonal vector demagnetization plots for 11 samples taken from a 1-cm-thick slice of vitric tuff. The <1-cm³ pieces from near the periphery differ from those near the center in the degree of drilling overprint. For example, Pieces 3 and 4 are the least overprinted, and they are nearest the center of the core. They also have a steeper overprint than those samples near the periphery. The drilling overprint deflects the declination of all samples toward the center of the core as shown by the arrows on each diagram.

Discrete samples from interval 200-1223A-6X-3, 90 cm, 36-83 mbsf

Figure F63. IRM acquisition results for subsamples from two intervals in the vitric tuff in Core 200-1223A-6X. The piece number is given in parentheses in the key.
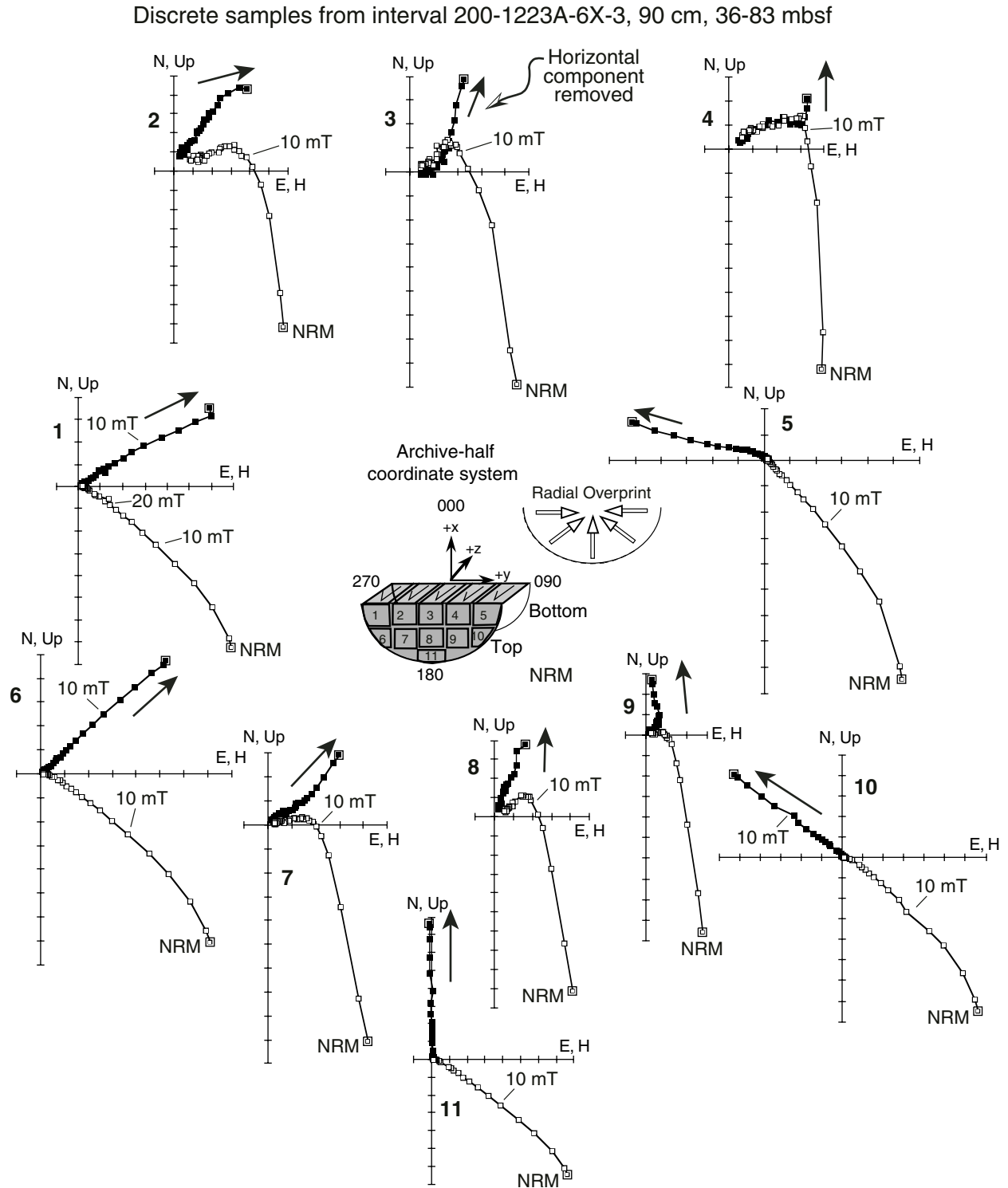
Figure F64. Magnetostratigraphy, inclination, and declination of the cored interval as computed using principal component analysis (PCA) and stable endpoints (SEP) for both split cores and discrete samples. The intensity of magnetization following 50-mT AF demagnetization is also shown.
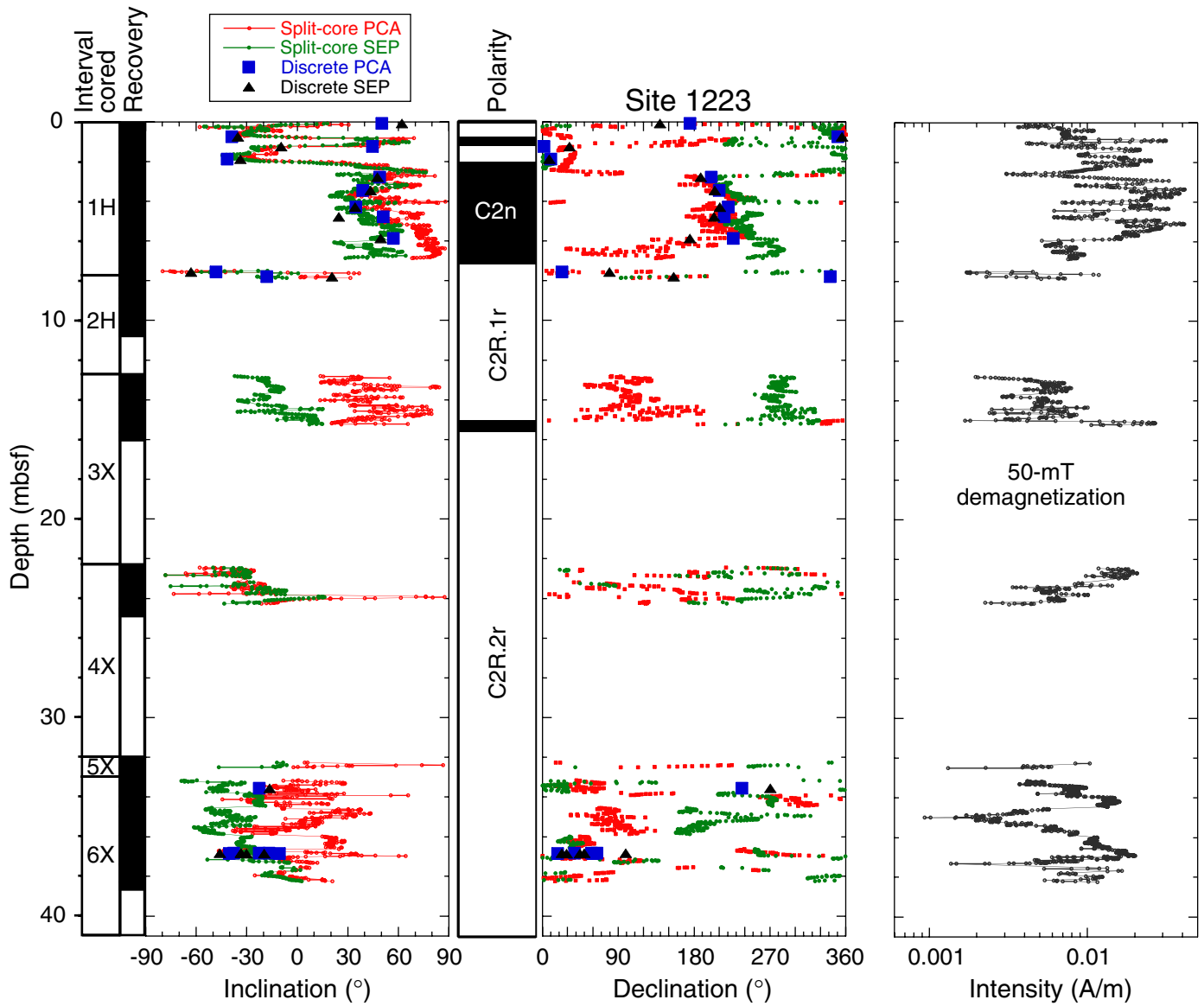
Figure F65. Close-up photograph of sediment from just below the whole-round interval we sampled illustrating the uppermost yellowish brown clay (Section 200-1223A-1H-1).

Figure F66. Close-up photographs of black sand layers. We took partial samples of black sands from depths of (**A**) 0.95 mbsf (Sample 200-1223A-1H-1, 95–96 cm [photographic interval 94–97.5 cm]) and (**B**) 7.90 mbsf (Sample 200-1223A-2H-1, 20–25 cm [photographic interval 22–25 cm]).

Figure F67. Close-up photograph of a sediment section characterized by volcaniclastic turbidites, taken at a depth of 6 mbsf (Section 200-1223A-1H-4). A whole-round sample was taken from just below the photographed interval.

Figure F68. Close-up photograph of volcaniclastic silt claystone, taken from a depth of 23.9 mbsf (Sample 200-1223A-4X-2, 85–87 cm).

Figure F69. Close-up photograph of a tuff layer embedded in volcaniclastic silty claystone that is classified as altered vitric tuff, taken at a depth of 32.2 mbsf (Section 200-1223A-5X-1). The corresponding half-round sample was collected from the working half.
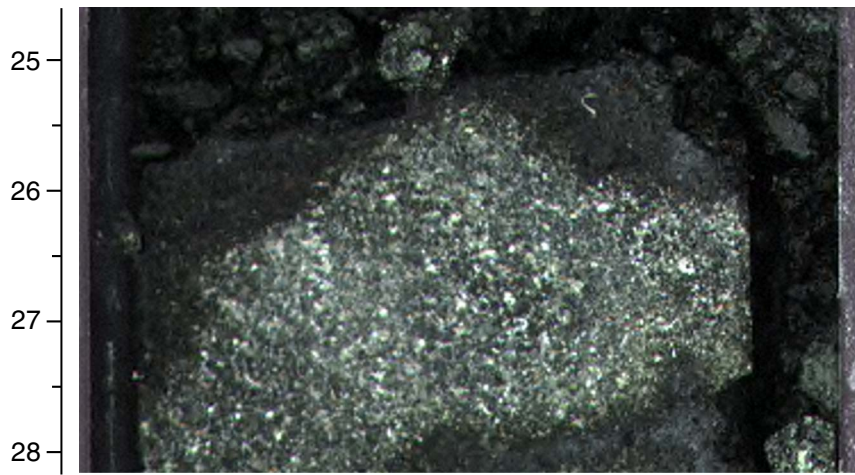
Figure F70. Close-up photograph of a tuff layer embedded in volcaniclastic silty claystone that is classified as palagonitized crystal vitric tuff, taken at a depth of 37.3 mbsf (Section 200-1223A-6X-3). A sample was collected from this section directly above the photographed interval.
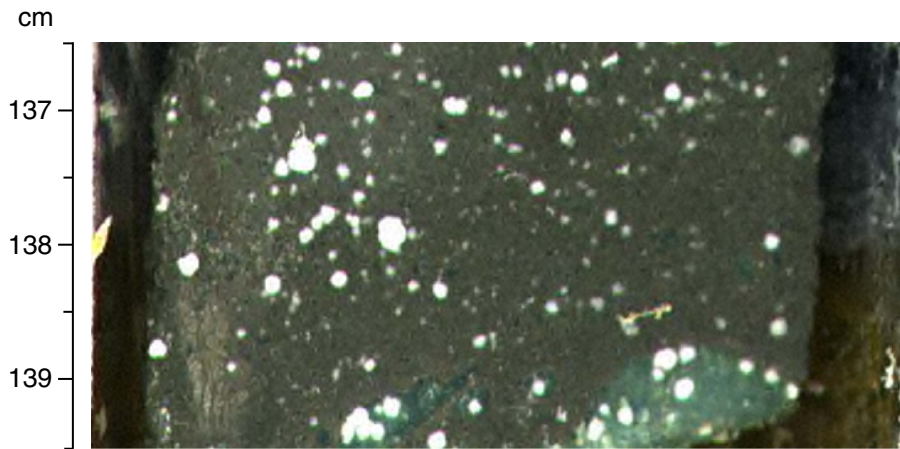
Figure F71. Photomicrograph of sediment showing distinct single small nucleic acids containing objects and bacterial microcolonies after staining with SYBR Green I (Sample 200-1223-1H-1, 0–5 cm). The inset shows a DNA-stained bacterial microcolony at higher magnification. Note the single cells embedded in extracellular polymeric substances. Scale bars for both figures represent 10 µm.
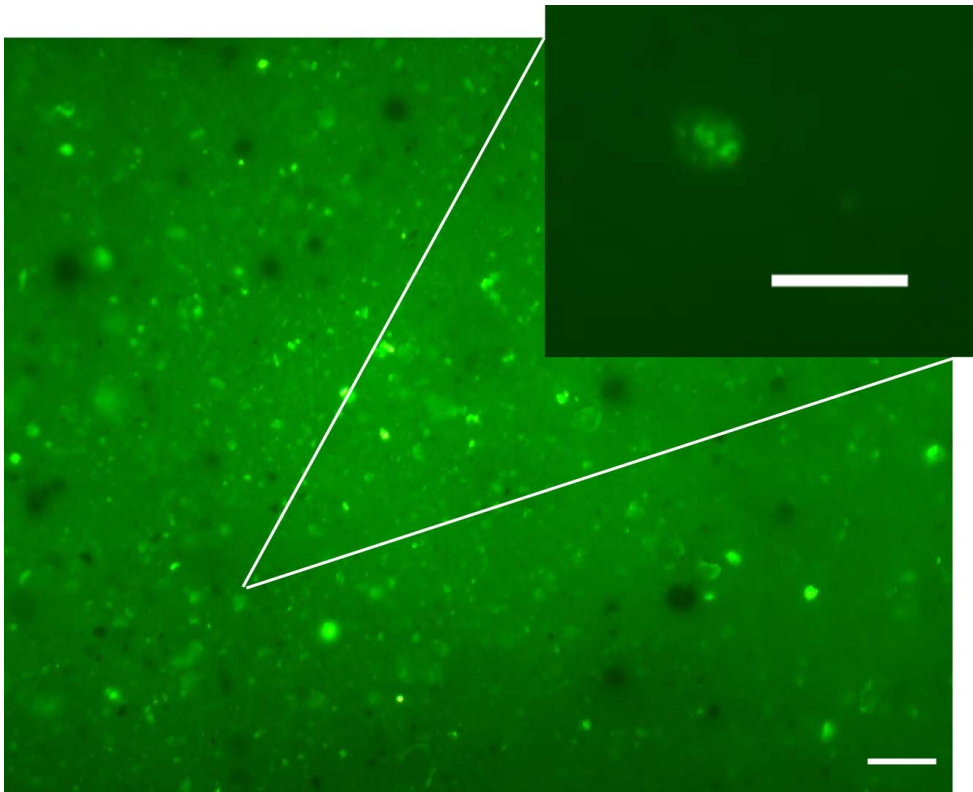
Figure F72. Liquid cultures of four distinct colonies obtained from altered vitric tuff that are cultivated under (**A**) aerobic and (**B**) anaerobic conditions. Note the visible large cell aggregates (Sample 200-1223A-5X-1, 24–26 cm).
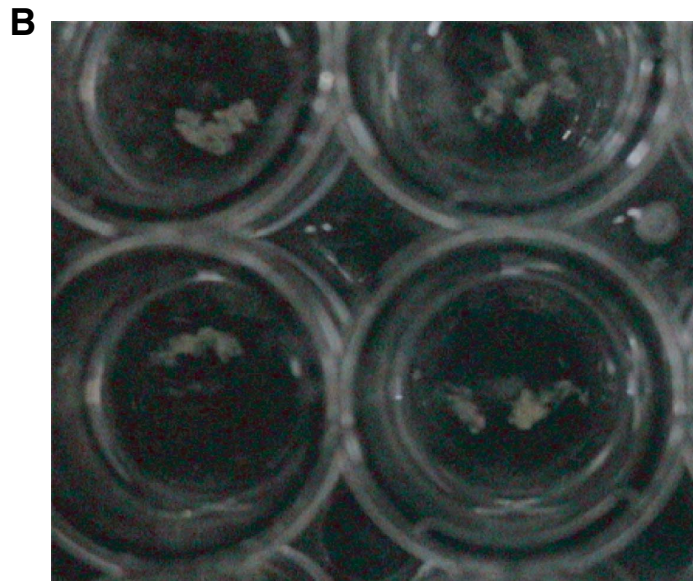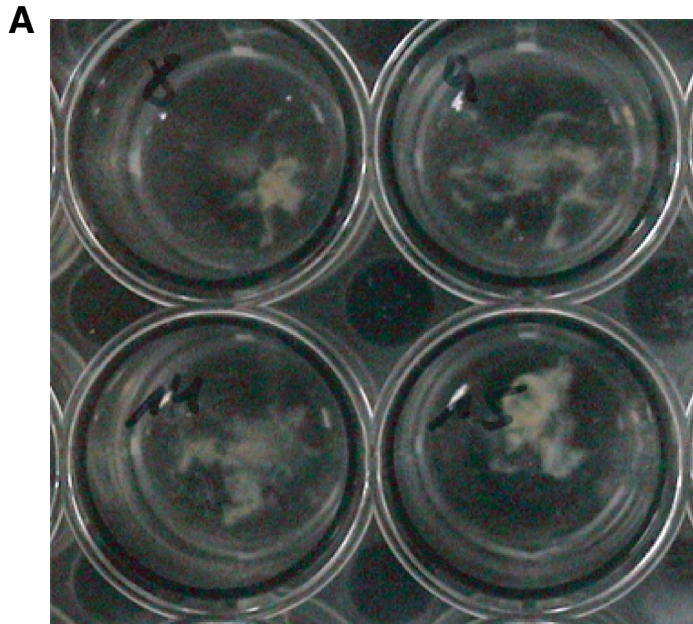
Figure F73. Photomicrograph showing single bacterial cells within bacterial colony CFU1, cultured from altered vitric tuff, after (**A**) simultaneously staining with the DNA-binding fluorochrome DAPI and (**B**) hybridization with the Bacteria-specific CY3-labeled probe EUB338. Note the numerous bacteria responding to the specific hybridization shown in B, indicating the high amount of metabolically active bacteria within the bacterial colony.
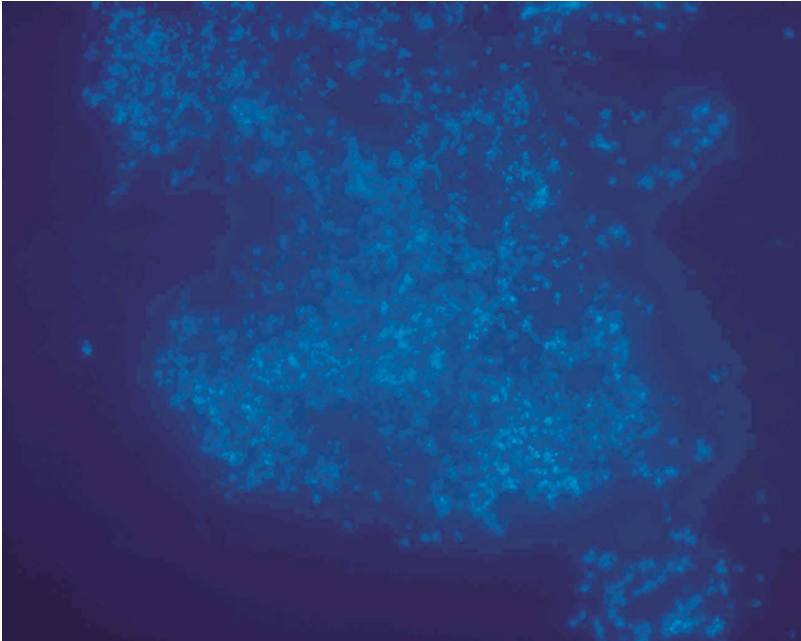
Figure F74. Photomicrograph showing single bacterial cells within bacterial colony CFU16, cultured from altered vitric tuff, after (**A**) simultaneously staining with the DNA-binding fluorochrome DAPI and (**B**) hybridization with the CY3-labeled probe SRB385Db, specific for sulfate-reducing bacteria. Note that not all cells given in A did respond to the specific hybridization shown, indicating at least two different bacterial specimens exist within the bacterial colony.
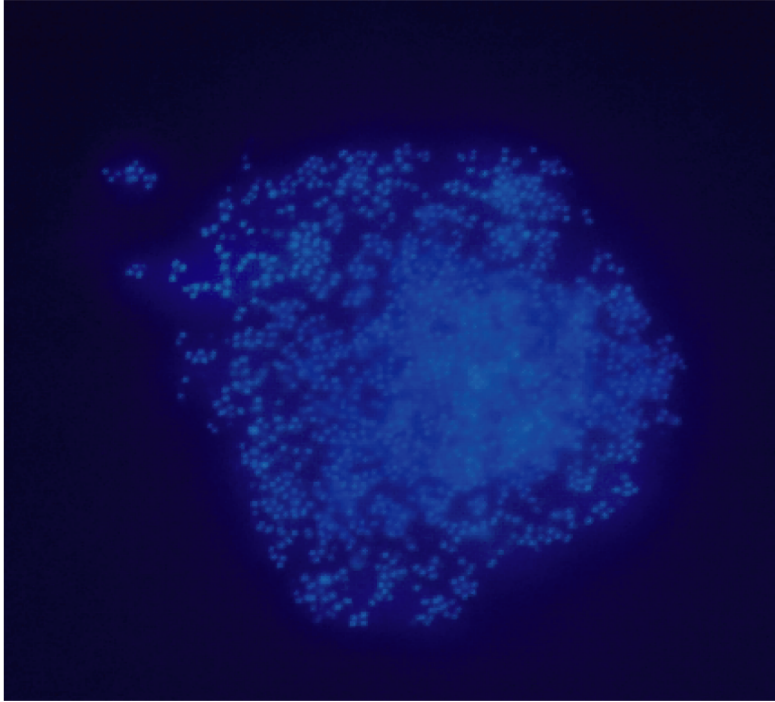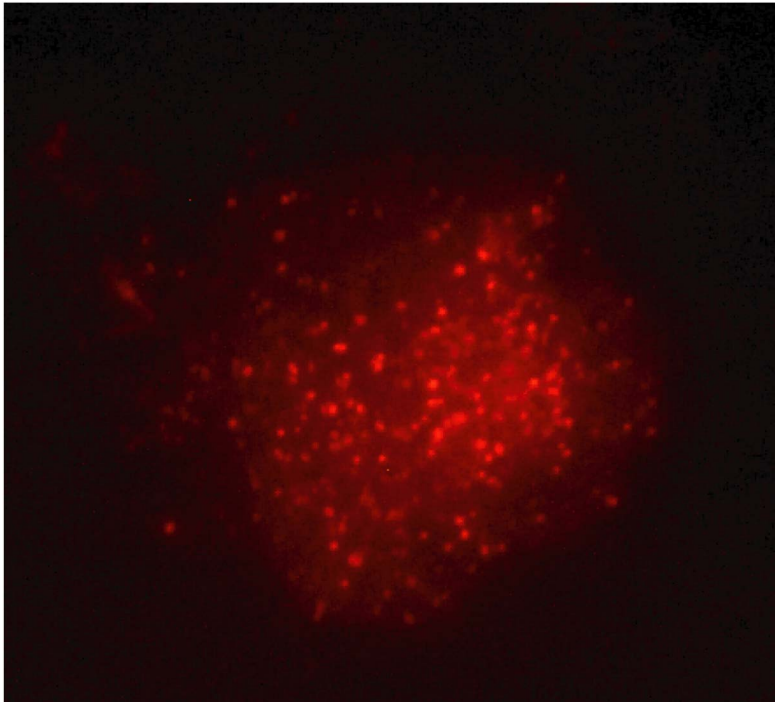
Figure F75. Photomicrograph showing single bacterial cells of bacterial colony CFU1, obtained from altered vitric tuff, after (**A**) simultaneously staining with the DNA-binding fluorochrome DAPI and (**B**) hybridization with the CY3-labeled probe LGCa-c, specific for Gram-positive bacteria with low G+C content of DNA.
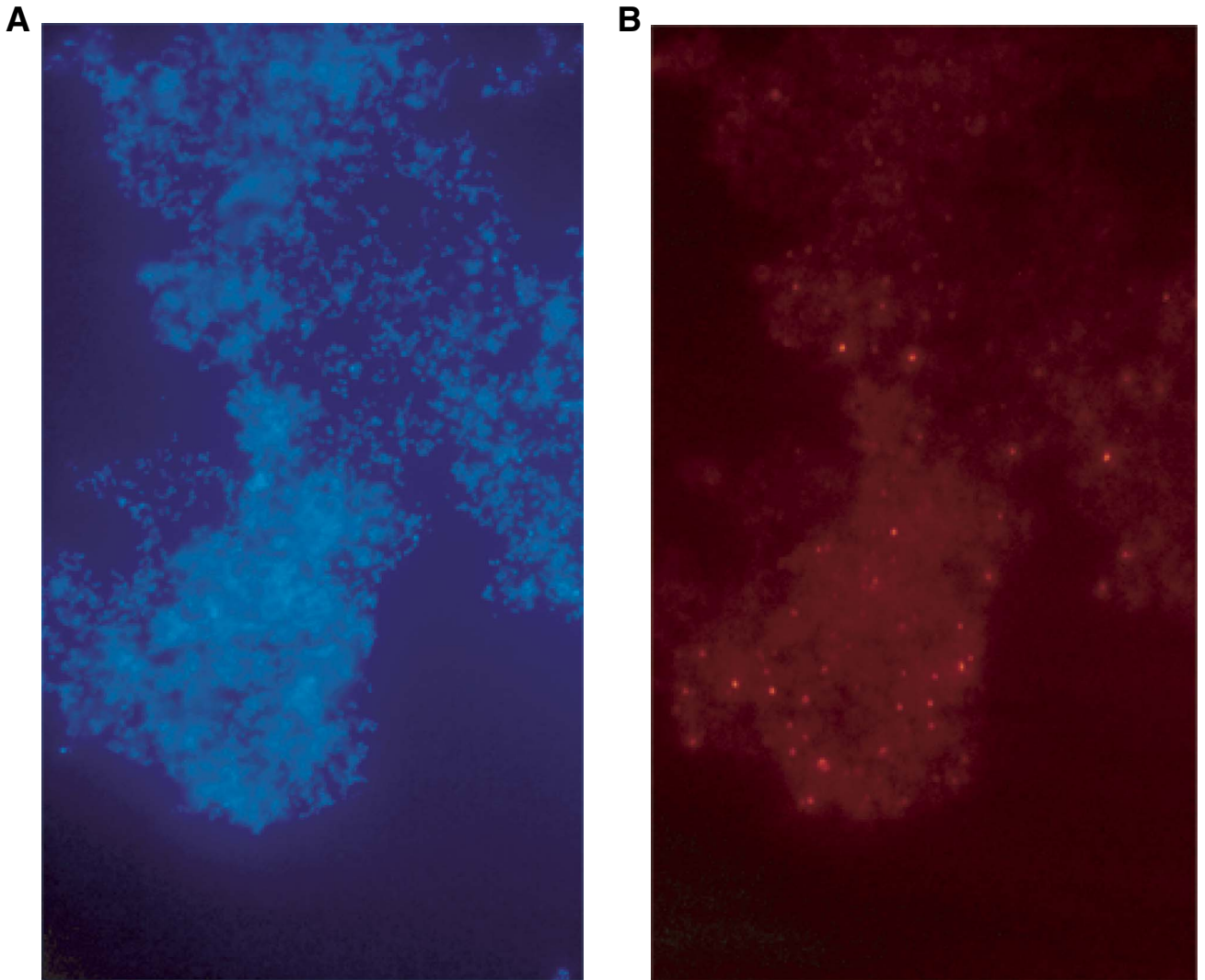
Figure F76. GRA (bulk) density, magnetic susceptibility, and natural gamma ray intensity from the MST are shown vs. depth. Lithologic units are shown on the far right. cps = counts per second.
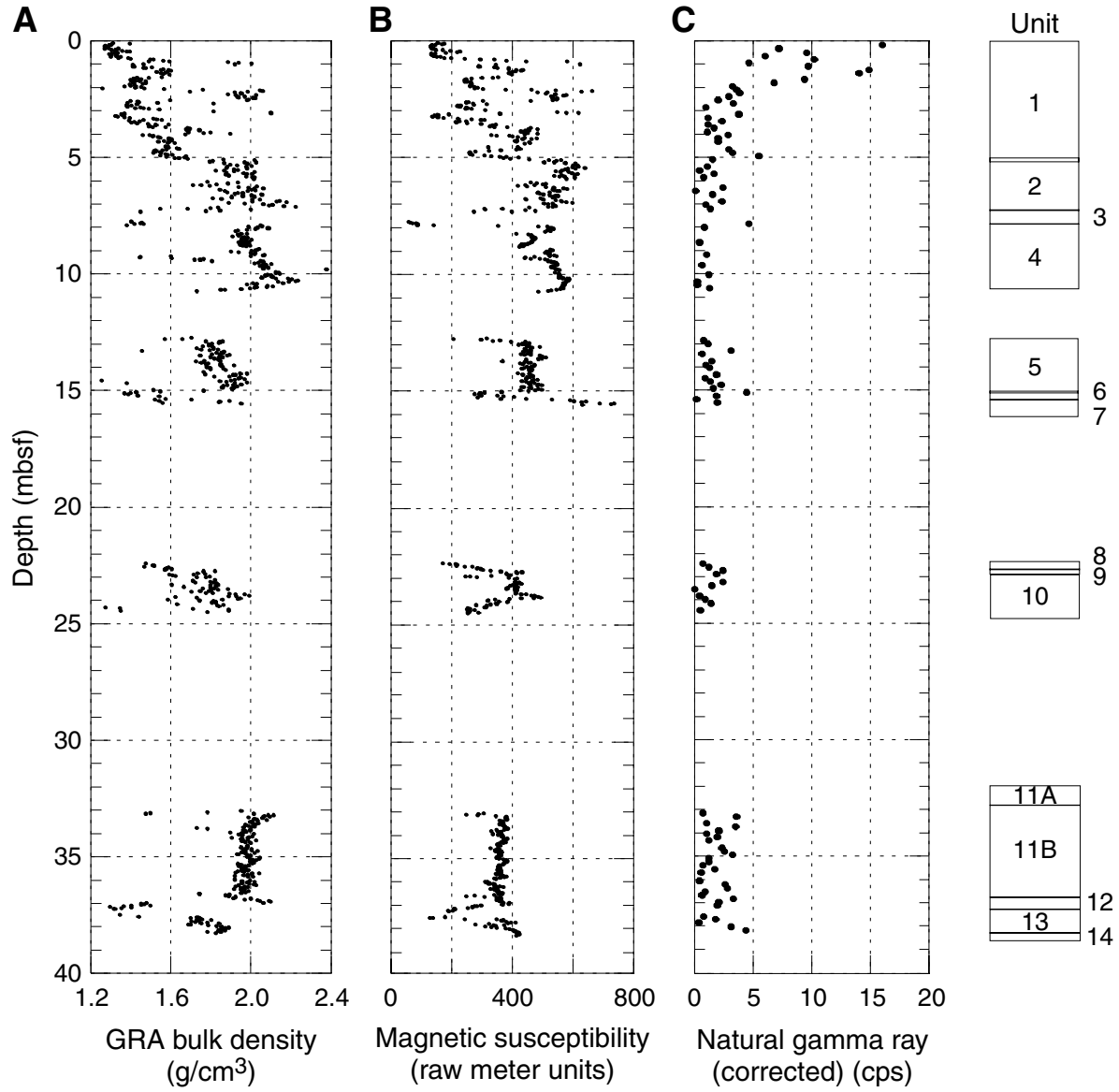
Figure F77. Thermal conductivity vs. depth. Lithologic units are shown on the far right.
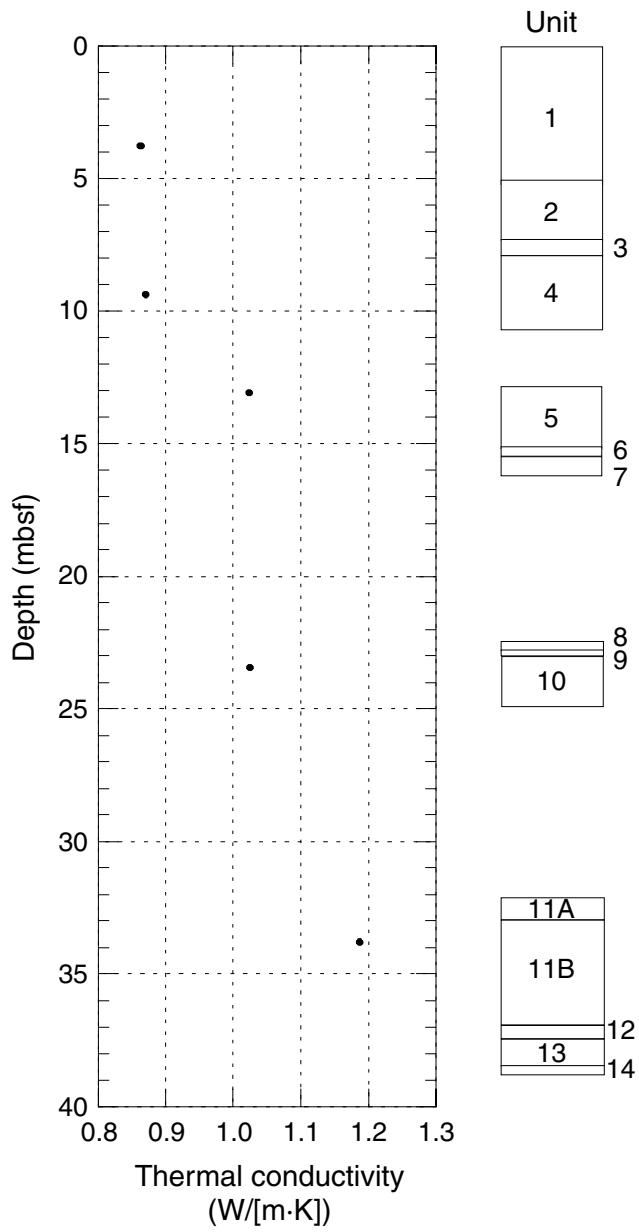
Figure F78. Bulk density, dry density, grain density, and porosity from discrete samples are shown vs. depth. Lithologic units are shown on the far right.
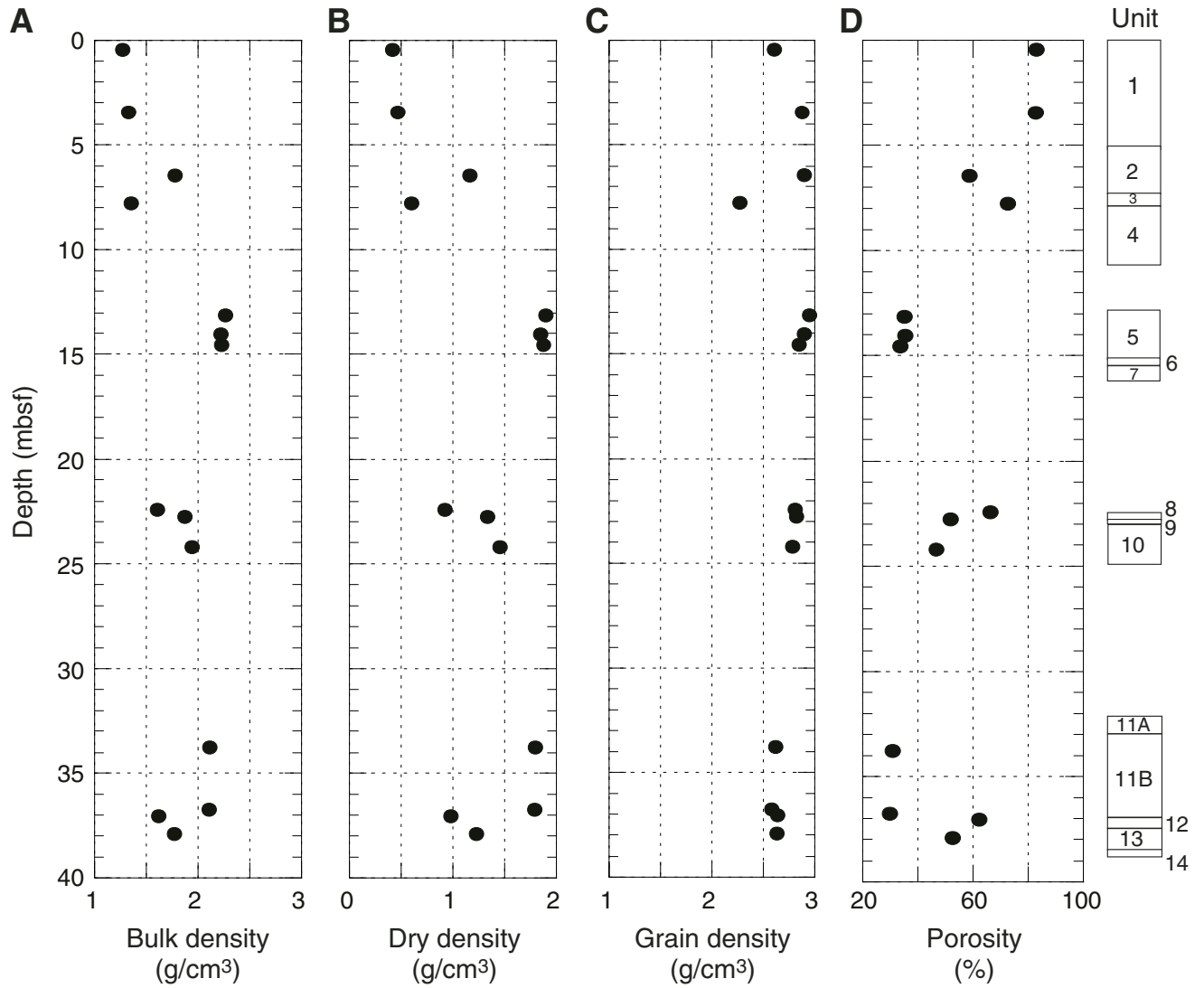
Figure F79. Comparison of GRA density (dots) and bulk density (open squares). Most of the measurements agree, except in Unit 5. The GRA densities are slightly smaller than the bulk densities of individual measurements in Units 5 to 14 and are slightly higher in Units 1 to 4.
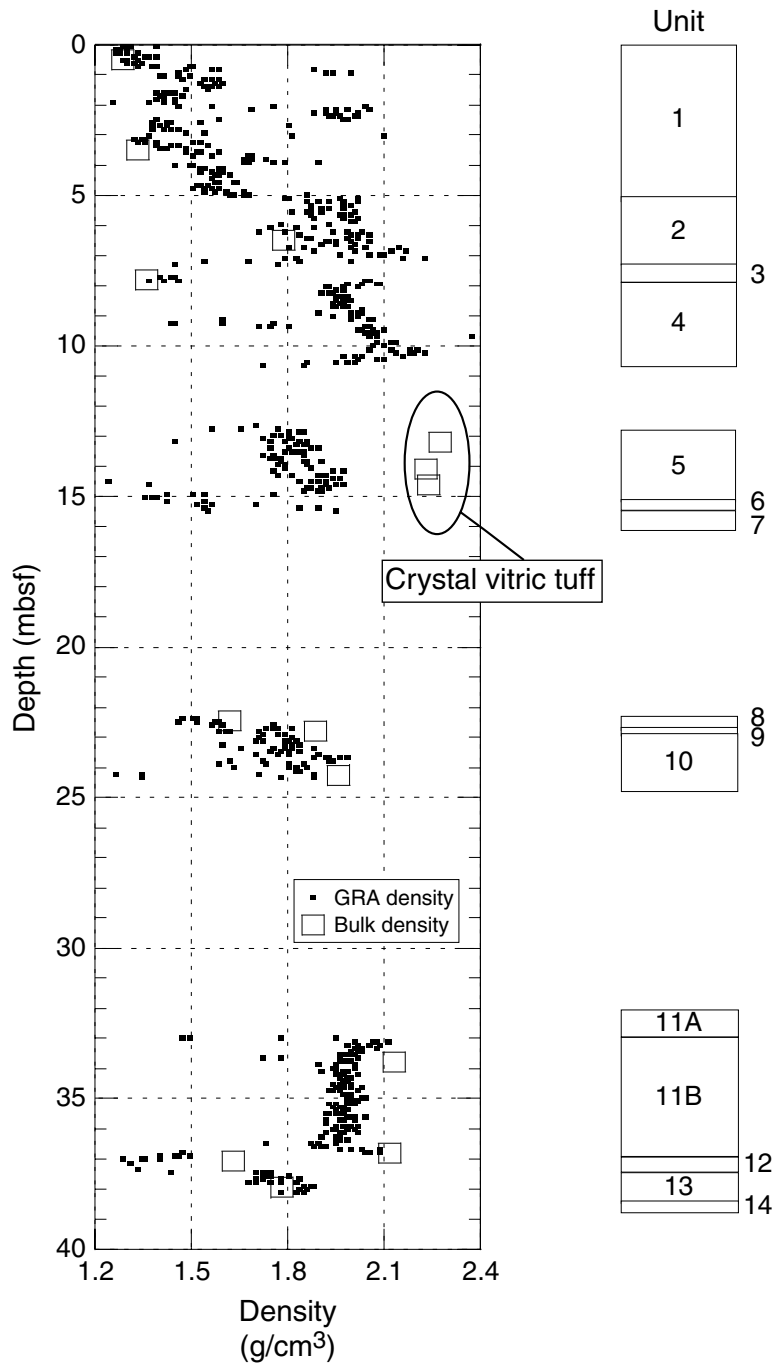
Figure F80. Comparison of PWL and PWS velocities. At depths shallower than 10 mbsf for the stacks of turbidite layers, PWL velocities are ~1500 m/s, corresponding to typical values for unconsolidated sediments. Between ~13 and ~15 mbsf, PWS velocities jump to ~3350 m/s. Between 22 and 25 mbsf, PWS velocities range from 1900 to 3200 m/s, suggesting slightly consolidated to highly consolidated sediments. The velocities between 34 and 37 mbsf correspond to palagonitized crystal vitric tuff. Below this layer, velocity values are small.
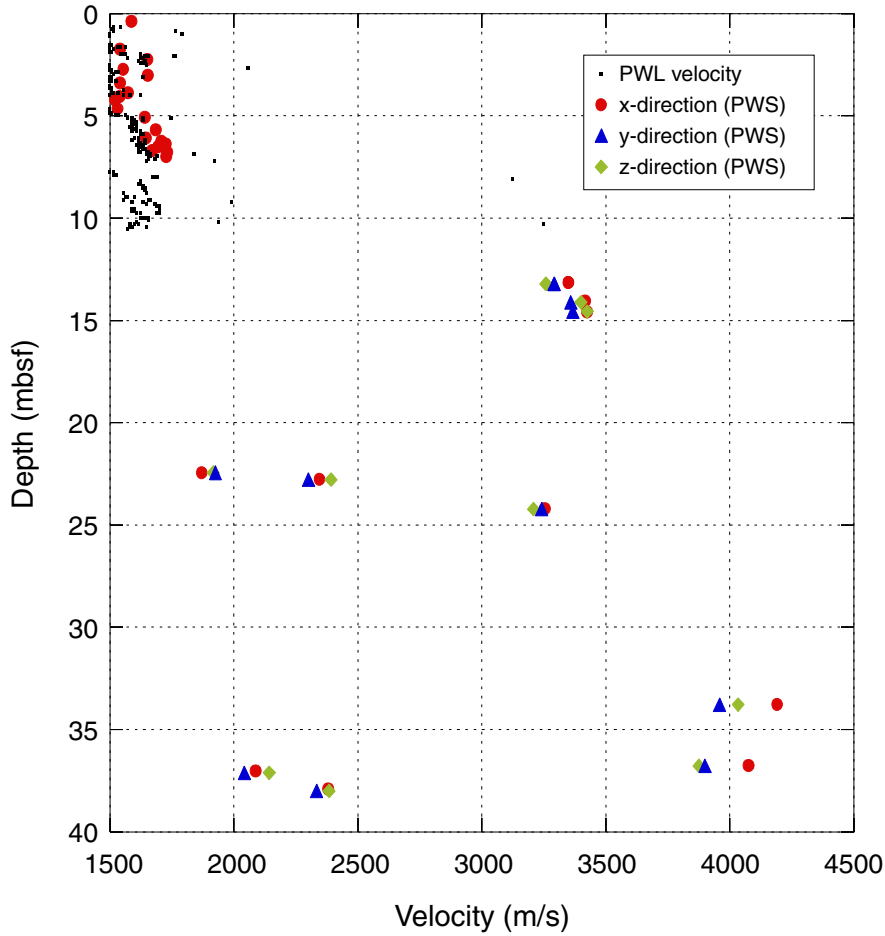
Figure F81. Comparison of PWS velocity with bulk density and porosity. Note that the crystal vitric tuff shows exceptional tendencies from the general trend, especially in PWS velocity vs. bulk density.
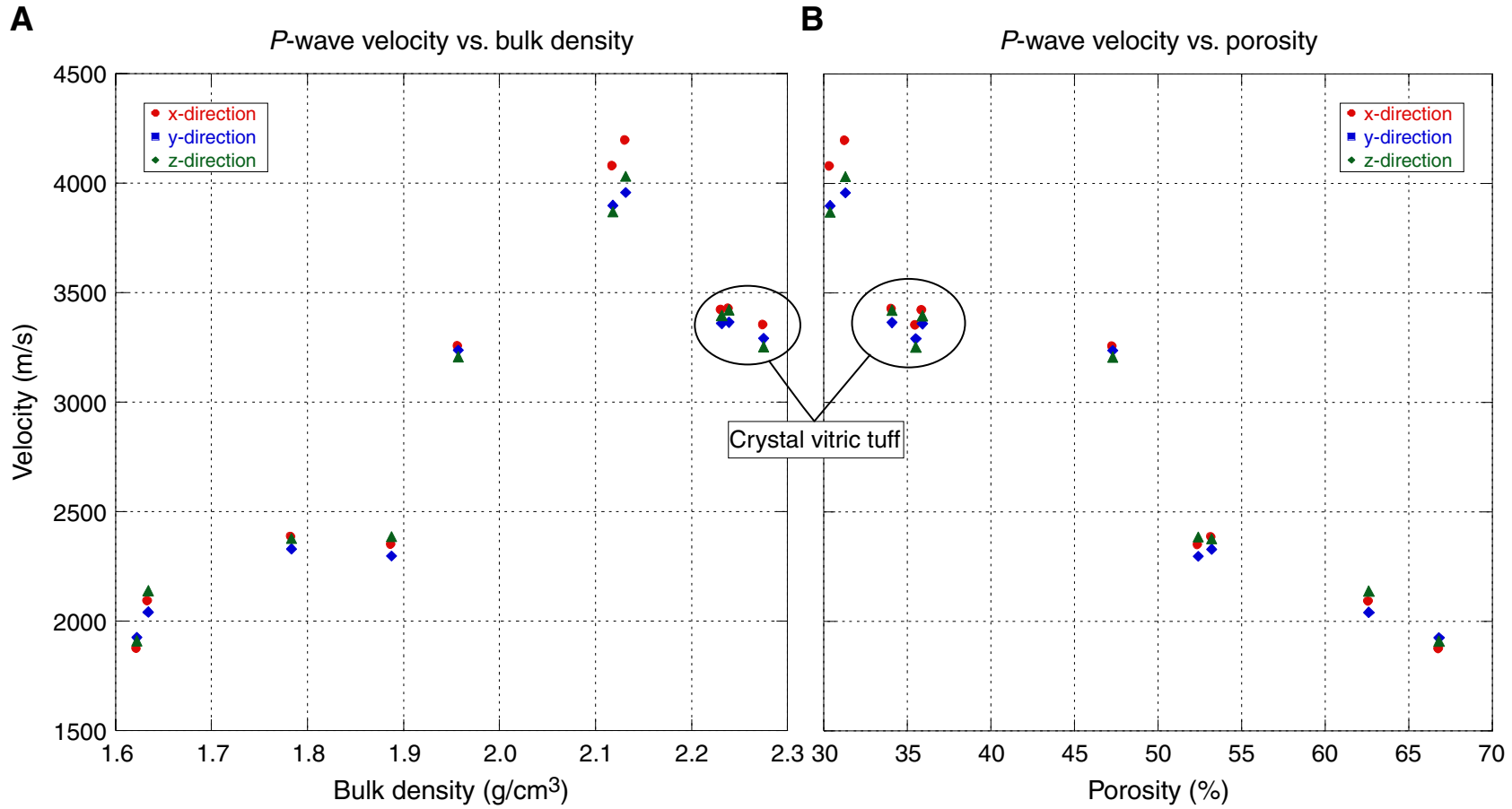
Figure F82. Three examples of 3.5-kHz echo soundings showing changes in the reflection sequence. Vertical traveltime interval from top to bottom is 212 ms. The vertical lines are 5-min recording marks. There are 30 traces per minute. The dark horizontal line is the seafloor reflection. Note the discontinuous nature of several of the subseafloor reflectors and, for some, an apparent change in traveltime.

2 hr
0 m
0 s
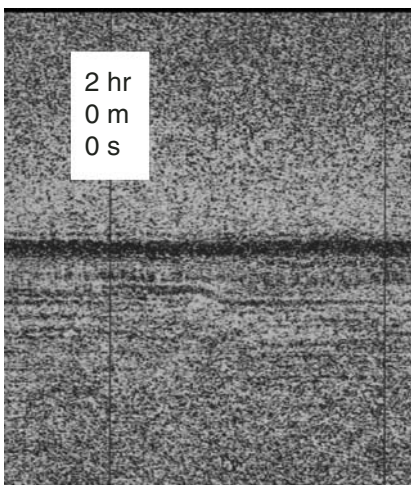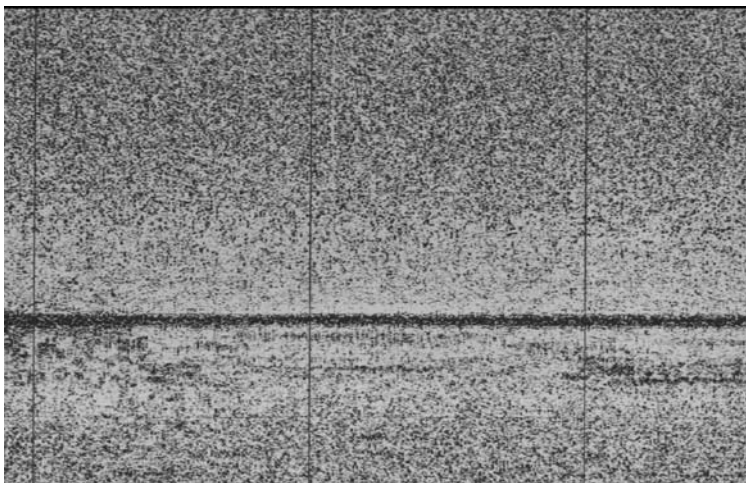
Figure F83. Navigation plot using GPS fixes at 1-min intervals. Crosses = fixes, grid spacing = ~1.8 m.

22 December 2001 0200-0259 UTC
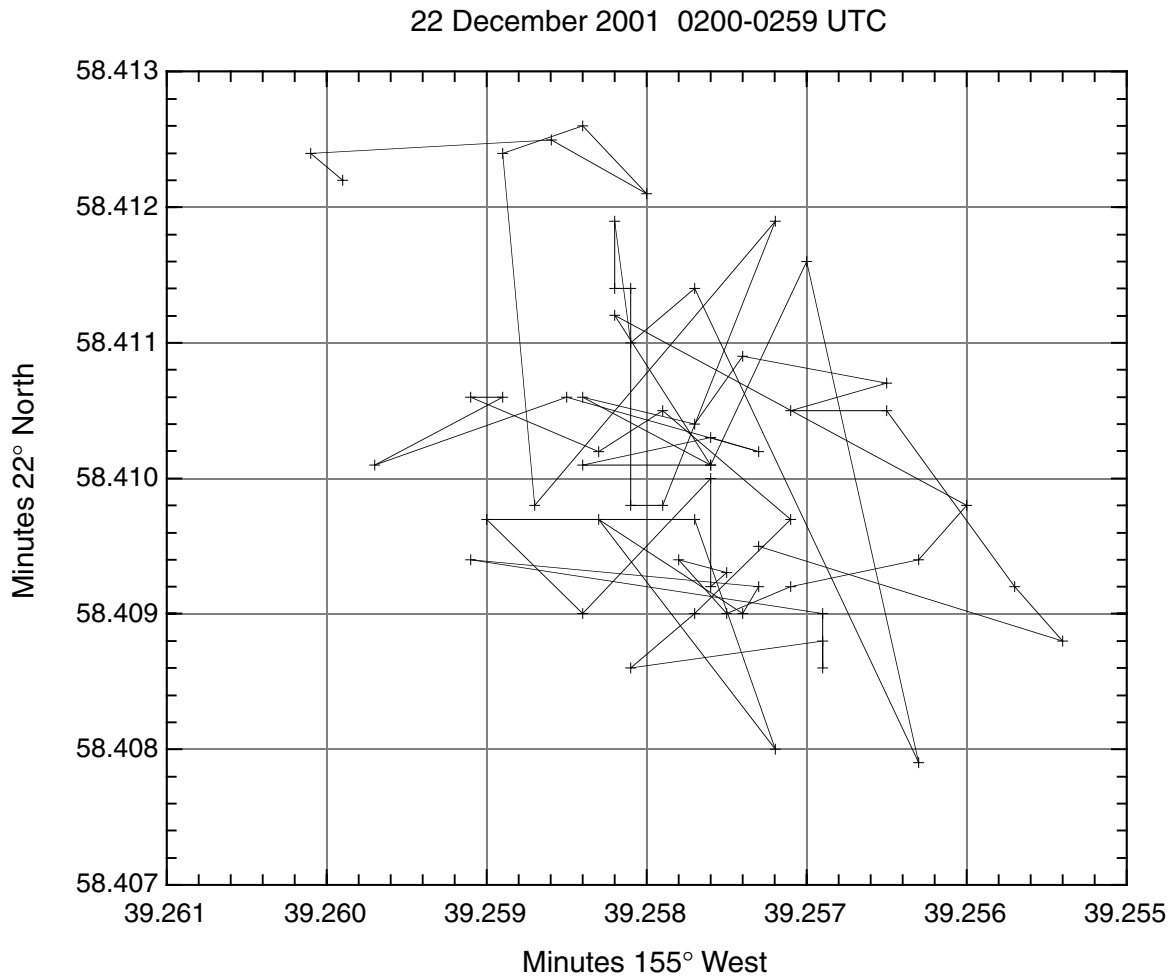
Figure F84. Navigation plot of a 7-hr recording. The 424 squares are fixes at 1-min intervals. The 90 black dots are the locations of noticeable changes in recording.

Site 1223 3.5-kHz E/S
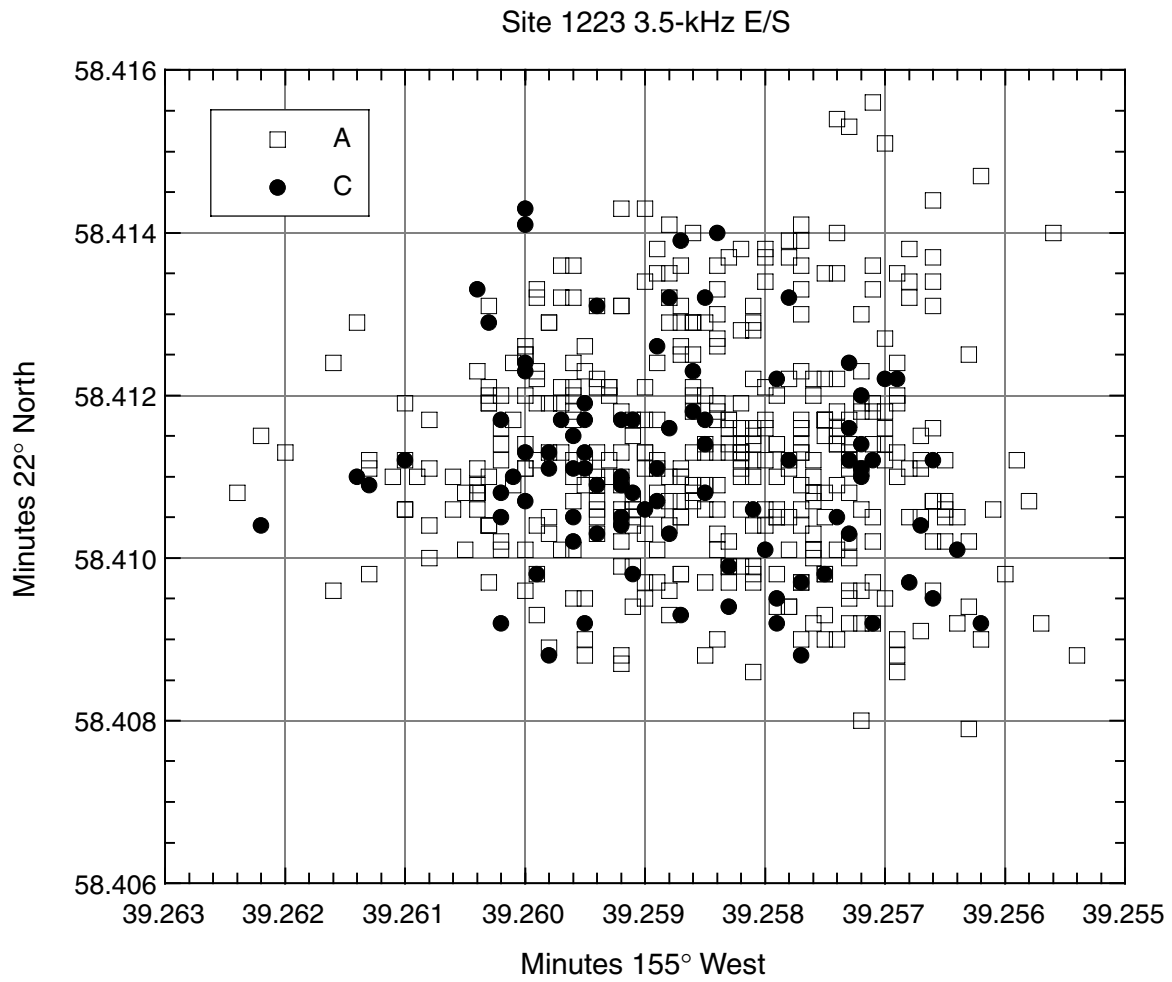
Figure F85. Incremental distance between fixes at which there were noticeable changes in recording.

Incremental distance at record changes
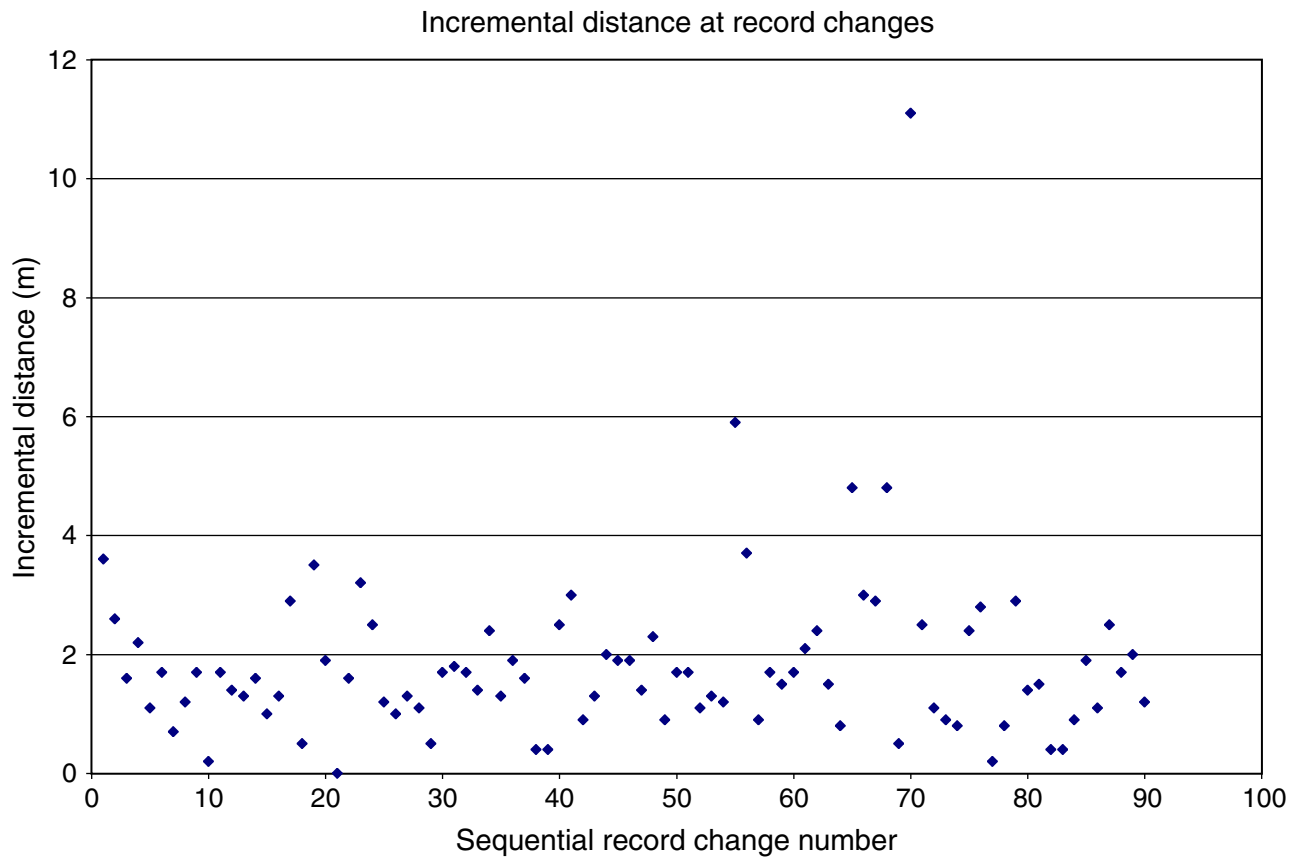
Table T1. Coring summary, Site 1223.

Hole 1223A
Latitude: 22°58.4095′N
Longitude: 155°39.2590′W
Time on site (hr): 42 (0730 hr, 21 December–0130 hr, 23 December 2001)
Time on hole (hr): 29 (2030 hr, 21 December–0130 hr, 23 December, 2001)
Seafloor (drill pipe measurement from rig floor, mbrf): 4245.8
Distance between rig floor and sea level (m): 10.7
Water depth (drill pipe measurement from sea level, m): 4235.1
Total depth (drill pipe measurement from rig floor, mbrf): 4286.8
Total penetration (meters below seafloor, mbsf): 41
Total length of cored section (m): 41.0
Total core recovered (m): 23.54
Core recovery (%): 57.4
Total number of cores: 6

Core	Date (Dec 2001)	Local time (hr)	Depth (mbsf)		Length (m)		Recovered (%)
			Top	Bottom	Cored	Recovered	
200-1223A-							
1H	21	2055	0.0	7.7	7.7	7.79	101.2
2H	21	2225	7.7	12.7	5.0	3.08	61.6
3X	22	0515	12.7	22.3	9.6	3.34	34.8
4X	22	0915	22.3	32.0	9.7	2.62	27.0
5X	22	1115	32.0	33.0	1.0	1.01	101.0
6X	22	1700	33.0	41.0	8.0	5.70	71.2
				Cored totals:	41.0	23.54	57.4

Table T2. Expanded coring summary, Site 1223.

Position: 22°58.4095′N, 155°39.2590′W
Water depth from sea surface = 4235.1 m

Leg	Site	Hole	Core	Type	Date (Dec 2001)	Local time (hr)	Depth (mbsf) Top	Depth (mbsf) Bottom	Length (m) Cored	Length (m) Recovered	Recovery (%)	Section	Length (m) Liner	Length (m) Curated	Section depth (mbsf) Top	Section depth (mbsf) Bottom	Catwalk samples	Comment
200	1223	A	1	H	21	2055	0.0	7.7	7.7	7.79	101.2							
												1	1.50	1.50	0.00	1.50	MBIO, MBIO	
												2	1.50	1.50	1.50	3.00		
												3	1.50	1.50	3.00	4.50	IW	
												4	1.50	1.50	4.50	6.00	MBIO, HS	
												5	1.38	1.38	6.00	7.38		
												CC (w/CC)	0.41	0.41	7.38	7.79		
												Totals:	7.79	7.79				
200	1223	A	2	H	21	2225	7.7	12.7	5.0	3.08	61.6							Nonmag core barrel
												1	0.51	0.51	7.70	8.21		20-min downtime
												2	0.67	0.67	8.21	8.88		120-min downtime for rathole
												3	1.00	1.00	8.88	9.88		
												4	0.90	0.90	9.88	10.78		
												Totals:	3.08	3.08				
200	1223	A	3	X	22	0515	12.7	22.3	9.6	3.34	34.8							
												1	1.48	1.48	12.70	14.18		
												2	1.45	1.45	14.18	15.63		Changed length
												CC (w/CC)	0.41	0.41	15.63	16.04		
												Totals:	3.34	3.34				
200	1223	A	4	X	22	0915	22.3	32.0	9.7	2.62	27.0							Shattered liner
												1	0.79	0.79	22.30	23.09		
												2	1.45	1.45	23.09	24.54		
												CC (w/2)	0.38	0.38	24.54	24.92		
												Totals:	2.62	2.62				
200	1223	A	5	X	22	1115	32.0	33.0	1.0	1.01	101.0							Shattered liner
												1	0.61	0.61	32.00	32.61	MBIO	
												CC (w/1)	0.40	0.40	32.61	33.01		
												Totals:	1.01	1.01				
200	1223	A	6	X	22	1700	33.0	41.0	8.0	5.70	71.3							Sinker bars out
												1	1.50	1.50	33.00	34.50		
												2	1.43	1.43	34.50	35.93		
												3	1.50	1.50	35.93	37.43	MBIO	
												4	0.88	0.88	37.43	38.31		
												CC (w/4)	0.39	0.39	38.31	38.70		
												Totals:	5.70	5.70				
								Totals:	41.0	23.54	57.4							

Notes: CC = core catcher (number in parenthesis indicates which section the core catcher is stored with). MBIO = microbiology sample, IW = interstitial water sample, HS = headspace sample. Nonmag = nonmagnetic. This table is also available in **ASCII.**

Table T3. Lithologic unit descriptions, Hole 1223A. (**See table notes.** Continued on next page.)

Lithologic unit	Depth (mbsf)	Unit interval	Thickness (m)	Unit name	Shipboard laboratory information
1	Seafloor–5.11	200-1223A-1H-1, 0 cm, to 1H-4, 67 cm	5.11	Yellowish brown clay and volcaniclastic turbidites	TSB: 1H-1, 98–100 cm; 1H-2, 100–102 cm; 1H-3, 8–10 cm; 1H-3, 97–99 cm MBIO: 1H-1, 0–5 cm; 1H-1, 95–96 cm PMAG: 1H-1, 8–10cm; 1H-1, 74–76 cm; 1H-1, 122–124 cm; 1H-2, 37–39 cm; 1H-2, 127–129 cm; 1H-3, 46–48 cm; 1H-3, 129–131 cm; 1H-4, 27–29 cm PP: 1H-1, 50–52 cm; 1H-3, 50–52 cm IW: 1H-3, 145–150 cm
2	5.11–7.32	1H-4, 67 cm, to 1H-CC, 9 cm	2.21	Volcaniclastic turbidites	TSB: 1H-4, 134–136 cm; 1H-5, 88–90 cm; 1H-5, 93–95 cm; 1H-5, 118–120 cm; 1H-CC, 35 cm MBIO: 1H-4, 145–150 cm PMAG: 1H-4, 137–139 cm PP: 1H-5, 50–52 cm XRD: 1H-5, 94–95 cm; 1H-5, 114–115 cm
3	7.32–7.90	1H-CC, 9 cm, to 2H-1, 20 cm	0.58	Dark-brown clay	PMAG: 2H-1, 9–11 cm PP: 2H-1, 11–13 cm
4	7.90–10.78	2H-1, 20 cm, to 2H-4, 90 cm	2.88	Unconsolidated black sand	TSB: 2H-1, 24–26 cm
5	12.70–15.06	3X-1, 0 cm, to 3X-2, 86 cm	2.36	Crystal vitric tuff	TSB: 3X-1, 36–38 cm; 3X-1, 112–114 cm; 3X-2, 71–73 cm; 3X-2, 82–84 cm PP: 3X-1, 49–51 cm; 3X-1, 139–141 cm; 3X-2, 44–46 cm ICP: 3X-1, 49–51 cm; 3X-2, 71–73 cm
6	15.06–15.29	3X-2, 86 cm, to 3X-2, 109 cm	0.23	Bioturbated claystone	TSB: 3X-2, 92–95 cm; 3X-2, 106–109 cm ICP: 3X-2, 93–95 cm
7	15.29–16.10	3X-2, 109 cm, to 3X-CC, 40 cm (base)	0.81	Volcaniclastic sandy siltstone	TSB: 3X-2, 129–132 cm ICP: 3X-2, 130–132 cm
8	22.30–22.80	4X-1, 0 cm, to 4X-1, 50 cm	0.50	Volcaniclastic silty claystone with carbonate-filled cavities	TSB: 4X-1, 13–15 cm ICP: 4X-1, 13–15 cm PP: 4X-1, 16–18 cm
9	22.80–22.91	4X-1, 50 cm, to 4X-1, 61 cm	0.11	Volcaniclastic claystone	ICP: 4X-1, 53–55 cm; 4X-2, 58–60 cm PP: 4X-1, 51–53 cm; 4X-1, 58–60 cm TSB: 4X-2, 58–60 cm
10	22.91–24.92	4X-1, 61 cm, to 4X-CC, 37 cm (base)	2.01	Volcaniclastic silty claystone	TSB: 4X-2, 83–85 cm; 4X-2, 140–142 cm PP: 4X-2, 117–119 cm ICP: 4X-2, 140–142 cm
11A	32.0–33.0	5X-1, 0 cm, to 5X-CC, 39 cm (base)	1.00	Altered palagonitized crystal vitric tuff	TSB: 5X-1, 12–14 cm; 5X-CC, 16–19 cm ICP: 5X-CC, 16–19 cm
11B	33.0–36.99	6X-1, 0 cm, to 6X-3, 105 cm	3.99	Palagonitized crystal vitric tuff	TSB: 6X-1, 73–75 cm; 6X-2, 79–81 cm; 6X-3, 86–89 cm ICP: 6X-1, 73–75 cm; 6X-2, 79–81 cm; 6X-3, 87–89 cm PP: 6X-1, 80–82 cm; 6X-3, 88–90 cm XRD: 6X-3, 69–75 cm; 6X-3, 69–75 cm
12	36.99–37.47	6X-3, 105 cm, to 6X-4, 8 cm	0.48	Volcaniclastic silty claystone with filled white vugs	TSB: 6X-3, 113–116 cm; 6X-4, 4–6 cm PP: 6X-3, 114–116 cm ICP: 6X-3, 114–116 cm MBIO: 6X-3, 140–150 cm XRD: 6X-4, 0–20 cm
13	37.47–38.31	6X-4, 8 cm, to 6X-4, 89 cm (base)	0.84	Volcaniclastic silty claystone	TSB: 6X-4, 62–64 cm PP: 6X-4, 52–54 cm ICP: 6X-4, 63–65 cm

Table T3 (continued).

Lithologic unit	Depth (mbsf)	Unit interval	Thickness (m)	Unit name	Shipboard laboratory information
14	38.31–38.70	6X-CC, 0 cm, to 6X-CC, 39 cm (base)	0.39	Volcaniclastic clayey siltstone	TSB: 6X-CC, 27–29 cm ICP: 6X-CC, 29–31 cm

Notes: Units as described in "Unit Descriptions," p. 8, in "Lithology." TSB = thin section billet, MBIO = microbiology, XRD = X-ray diffraction, ICP = inductively coupled plasma spectroscopy, PP = physical properties, PMAG = paleomagnetism.

Table T4. General review of the most important petrographic features of the different units of Site 1223.

Lithologic unit	Unit name	Thin section type	Thin sections examined	Average dimension of the clasts (mm)	Main constituents
1	Yellowish brown clay and volcaniclastic turbidites	Volcaniclastic sand	4	0.1–0.2	Unaltered glass shards, olivine, vitric fragments, plagioclase, lithic fragments, palagonitized glass, clinopyroxene, and radiolarians
2	Volcaniclastic turbidite	Volcaniclastic sand	3	0.1 to 1.8	Claystone and carbonate (micrite) clasts plus volcanic sand (plagioclase, clinopyroxene, olivine, opaques, and glass)
3	Dark-brown clay	Volcaniclastic sand	1	0.3–1.5	Claystone fragments plus volcanic sand (plagioclase, clinopyroxene, olivine, opaques, and glass)
4	Unconsolidated black sand	Volcaniclastic sand	1	0.1–0.3	Unaltered glass shards, olivine, vitric fragments, plagioclase, lithic fragments, palagonitized glass, and clinopyroxene
5	Crystal vitric tuff	Tuff	4	0.1–1.1	Olivine and plagioclase clasts plus lithic and vitric fragments and glass shards; chlorite, palagonite, and zeolite
6	Bioturbated claystone	Claystone	1		
7	Volcaniclastic sandy siltstone	Clay with volcanic ash layers	1	<0.2	Olivine and plagioclase clasts plus lithic and vitric fragments and glass shards; chlorite, zeolite, clay clasts, and palagonite
8	Volcaniclastic silty claystone with carbonate-filled cavities	Volcaniclastic silty claystone with carbonate granules	1	2.5*	Carbonate, glass shards, olivine, vitric fragments, plagioclase, lithic fragments, palagonitized glass, clinopyroxene, and radiolarians
10	Volcaniclastic silty claystone	Volcaniclastic sandy claystone	2	0.1–0.2	Olivine and plagioclase clasts plus lithic and vitric fragments and glass shards; chlorite, zeolite, and palagonite
11	Altered palagonitized crystal vitric tuff	Altered crystal vitric tuff	4	0.2–1	Olivine, plagioclase and clinopyroxene clasts, plus lithic and vitric fragments; palagonite, serpentine, and zeolites
12	Volcaniclastic silty claystone with white vugs	Claystone with paragonite granules(?)	2	0.2–0.7	Anhydrite-filled vugs (maximum size 3.5 mm) and zeolites
13	Volcaniclastic silty claystone	Volcaniclastic silty claystone	1	0.06–0.4[†]	Olivine, vitric and lithic fragments, and zeolite
14	Volcaniclastic clayey siltstone	Volcaniclastic clayey siltstone	1	0.06–0.4[†]	Olivine, vitric and lithic fragments, zeolite, and chlorite

Note: * = carbonate granules; † = silty fraction.

Table T5. Results of XRD analyses for samples, Site 1223.

Core, section, interval (cm)	Depth (mbsf)	Unit	Comments	Main minerals	Accessory minerals
200-1223A-					
1H-5, 94–95	6.94	2C	Brown granule in turbidite	Phillipsite	Montmorillonite, illite, plagioclase
1H-5, 114–115	7.14	2D	Yellow granule in turbidite	Calcite	Plagioclase
6X-3, 69–75	36.62	11B	White vein	Montmorillonite, saponite	
6X-3, 69–75	36.62	11B	Green vein	Montmorillonite, saponite	
6X-3, 117–118	37.10	12	Thin white vein	Phillipsite, natrolite, thomsonite	
6X-3, 129–130	37.22	12	White vug filling	Paragonite, wairakite, anhydrite	Pumpellyite, kaolinite, montmorillonite
6X-4, 0–20	37.43	12	White vug filling	Paragonite, wairakite, anhydrite	Pumpellyite, kaolinite, montmorillonite
6X-4, 34–35	37.77	13	White vug filling	Paragonite, wairakite, anhydrite	Pumpellyite, kaolinite, montmorillonite

Table T6. Principal wavelengths and corresponding
°2θ of the mineral peaks identified.

d (Å)	CuK$_\alpha$ (°2θ)
Paragonite:	
9.67	9.14
3.21	27.72
2.7	33.14
2.18	41.38
1.93	47.02
Wairakite:	
5.56	15.96
3.39	26.32
Scapolite:	
3.87	23.02
3.47	25.68
2.07	43.72
Montmorillonite:	
13.6	6.48
4.46	19.88
2.56	35.06
1.69	54.24
Saponite:	
15.4	5.76
4.6	19.3
3.13	28.5
2.64	33.96
2.56	35.06
1.74	52.58
1.54	60.08

Note: d = spacing between principal crystallographic planes in Å.

Table T7. ICP-AES analyses, Hole 1223A.

Core, section, interval (cm)	Unit	Depth (mbsf)	Type	SiO$_2$ (wt%)	TiO$_2$ (wt%)	Al$_2$O$_3$ (wt%)	Fe$_2$O$_3$ (wt%)	MnO (wt%)	MgO (wt%)	CaO (wt%)	Na$_2$O (wt%)	K$_2$O (wt%)	P$_2$O$_5$ (wt%)	Total
200-1223A-														
3X-1, 49	5	13.19	Tuff	47.62	2.12	11.33	11.96	0.20	13.86	8.17	2.19	0.47	0.23	98.15
3X-2, 71	5	14.89	Tuff	47.60	2.03	11.39	12.63	0.19	15.06	7.74	2.27	0.57	0.21	99.69
3X-2, 93	5	15.11	Tuff	50.53	1.62	10.67	12.22	0.16	13.78	5.81	3.21	0.96	0.40	99.36
3X-2, 130	5	15.48	Tuff	50.84	1.55	12.83	11.29	0.15	11.86	4.26	3.88	2.02	0.11	98.79
4X-1, 13	8	22.43	Claystone	50.69	2.05	11.55	10.39	0.20	11.33	8.13	3.63	1.37	0.22	99.56
4X-1, 53	8	22.83	Claystone	52.83	1.39	8.85	11.68	0.14	16.98	3.93	2.97	1.03	0.41	100.21
4X-1, 58	8	22.88	Claystone	52.71	1.34	8.69	11.96	0.14	16.94	3.69	2.96	1.07	0.41	99.91
4X-2, 58	10	23.67	Claystone	48.50	2.19	12.57	11.78	0.22	12.46	6.17	3.38	0.90	0.17	98.34
4X-2, 140	10	24.49	Claystone	50.62	2.23	12.25	10.79	0.20	12.76	6.15	3.14	0.75	0.22	99.11
5X-CC, 16	11A	32.77	Tuff	48.97	2.00	11.00	11.59	0.19	15.81	3.85	3.15	1.00	0.18	97.74
6X-1, 73	11B	33.73	Tuff	47.94	2.06	11.51	12.40	0.19	13.80	7.11	3.07	0.81	0.17	99.06
6X-2, 79	11B	35.29	Tuff	49.31	2.02	11.85	12.65	0.19	13.44	7.82	2.97	0.83	0.16	101.24
6X-3, 87	11B	36.80	Tuff	49.57	2.10	11.61	11.27	0.19	12.44	6.74	3.09	0.71	0.18	97.90
6X-3, 114	11B	37.07	Tuff	51.93	1.87	11.69	10.02	0.18	10.92	7.20	4.93	1.46	0.16	100.36
6X-4, 63	13	38.06	Claystone	52.45	1.98	11.03	11.07	0.19	11.11	5.94	4.75	1.49	0.18	100.19
6X-CC, 29	14	38.60	Claystone	50.67	2.18	12.79	11.66	0.21	10.90	5.61	4.68	0.90	0.19	99.79

Core, section, interval (cm)	Unit	Depth (mbsf)	Type	LOI (wt%)	Mg#	Ba (ppm)	Sr (ppm)	Y (ppm)	Zr (ppm)	Ni (ppm)	V (ppm)	Cr (ppm)	Sc (ppm)
200-1223A-													
3X-1, 49	5	13.19	Tuff	3.12	0.699	54	239	23	121	466	266	703	27
3X-2, 71	5	14.89	Tuff	4.47	0.707	64	222	22	116	584	267	770	27
3X-2, 93	5	15.11	Tuff	7.44	0.694	208	185	23	113	331	207	487	20
3X-2, 130	5	15.48	Tuff	6.35	0.677	173	128	21	93	251	230	468	24
4X-1, 13	8	22.43	Claystone	7.48	0.682	113	207	25	118	325	241	665	26
4X-1, 53	8	22.83	Claystone	8.67	0.744	98	108	14	80	356	151	487	25
4X-1, 58	8	22.88	Claystone	6.69	0.740	108	101	14	87	250	146	498	17
4X-2, 58	10	23.67	Claystone	8.84	0.679	75	175	23	123	325	257	709	28
4X-2, 140	10	24.49	Claystone	9.21	0.700	56	214	25	128	316	248	666	29
5X-CC, 16	11A	32.77	Tuff	9.17	0.732	74	117	22	120	448	257	756	27
6X-1, 73	11B	33.73	Tuff	9.72	0.692	70	284	24	123	503	285	788	26
6X-2, 79	11B	35.29	Tuff	8.51	0.682	60	265	22	118	471	255	740	26
6X-3, 87	11B	36.80	Tuff	10.30	0.687	69	328	23	121	434	259	718	27
6X-3, 114	11B	37.07	Tuff	13.48	0.681	106	174	22	111	333	198	566	21
6X-4, 63	13	38.06	Claystone	11.03	0.666	97	178	25	114	330	237	704	25
6X-CC, 29	14	38.60	Claystone	6.69	0.652	103	260	27	128	328	269	752	30

Note: LOI = loss on ignition.

Table T8. Drilling disturbed intervals and gaps that affect paleomagnetic results, Hole 1223A.

Leg	Site	Hole	Core	Type	Section	Interval (cm)	Comment
200	1223	A	1	H	1	0–5	Microbiology whole-round sample
200	1223	A	1	H	1	5–8	Avoid end of section
200	1223	A	1	H	5	88–138	Drilling disturbance
200	1223	A	1	H	CC	0–11	Drilling disturbance
200	1223	A	1	H	CC	29–41	Drilling disturbance
200	1223	A	2	H	1	17–51	Unconsolidated sand
200	1223	A	2	H	2	0–67	Unconsolidated sand
200	1223	A	2	H	3	0–100	Unconsolidated sand
200	1223	A	2	H	4	0–90	Unconsolidated sand
200	1223	A	3	X	1	0–10	Unoriented piece + edge of next piece
200	1223	A	3	X	1	92–102	Edges of adjacent pieces
200	1223	A	3	X	2	107–141	Edges of piece with broken pieces below
200	1223	A	4	X	1	0–14	XCB slurry
200	1223	A	4	X	1	23–25	XCB slurry
200	1223	A	4	X	1	32–35	XCB slurry
200	1223	A	4	X	1	66–79	XCB slurry
200	1223	A	4	X	2	0–9	XCB slurry
200	1223	A	4	X	2	12–16	XCB slurry
200	1223	A	4	X	2	23–25	XCB slurry
200	1223	A	4	X	2	73–81	XCB slurry
200	1223	A	4	X	2	104–107	XCB slurry
200	1223	A	4	X	2	118–145	XCB slurry and end of section
200	1223	A	4	X	CC	0–38	XCB slurry and possibly unoriented pieces
200	1223	A	5	X	1	0–26	XCB slurry
200	1223	A	5	X	1	29–38	XCB slurry
200	1223	A	5	X	1	52–61	XCB slurry
200	1223	A	5	X	CC	0–40	XCB slurry and possibly unoriented pieces
200	1223	A	6	X	1	0–16	Small pieces and edge of long piece
200	1223	A	6	X	1	76–79	Edges of adjacent pieces
200	1223	A	6	X	3	64–70	Edges of adjacent pieces
200	1223	A	6	X	4	0–10	XCB slurry and possibly unoriented pieces
200	1223	A	6	X	4	16–24	XCB slurry
200	1223	A	6	X	4	28–35	XCB slurry
200	1223	A	6	X	4	43–51	XCB slurry
200	1223	A	6	X	4	68–72	XCB slurry
200	1223	A	6	X	4	82–88	XCB slurry
200	1223	A	6	X	CC	0–40	XCB slurry and possibly unoriented pieces

Notes: XCB = extended core barrel. This table is also available in **ASCII.**

Table T9. Paleomagnetic data from archive-half sections, Hole 1223A.

Leg	Site	Hole	Core	Type	Section	Interval (cm)	Depth (mbsf)	Demagnetization step (mT)	Declination (°)	Inclination (°)	Intensity (A/m)
200	1223	A	1	H	1	9	0.09	0	31.98	83.31	3.73E–01
200	1223	A	1	H	1	9	0.09	2	22.40	84.70	3.35E–01
200	1223	A	1	H	1	9	0.09	4	77.24	87.62	2.50E–01
200	1223	A	1	H	1	9	0.09	6	109.63	84.96	1.49E–01
200	1223	A	1	H	1	9	0.09	8	125.00	84.72	7.52E–02
200	1223	A	1	H	1	9	0.09	10	192.53	79.62	3.54E–02
200	1223	A	1	H	1	9	0.09	12	211.16	64.17	2.18E–02
200	1223	A	1	H	1	9	0.09	14	210.25	46.93	1.69E–02
200	1223	A	1	H	1	9	0.09	16	210.19	38.53	1.43E–02
200	1223	A	1	H	1	9	0.09	18	208.55	34.06	1.32E–02
200	1223	A	1	H	1	9	0.09	20	213.51	28.57	1.31E–02
200	1223	A	1	H	1	9	0.09	25	207.82	26.74	1.14E–02
200	1223	A	1	H	1	9	0.09	30	210.39	23.64	1.03E–02
200	1223	A	1	H	1	9	0.09	35	213.62	20.68	9.23E–03
200	1223	A	1	H	1	9	0.09	35	233.51	19.66	6.47E–03
200	1223	A	1	H	1	9	0.09	40	234.88	19.21	6.41E–03
200	1223	A	1	H	1	9	0.09	45	236.01	18.21	6.12E–03
200	1223	A	1	H	1	9	0.09	50	238.19	16.12	6.08E–03
200	1223	A	1	H	1	10	0.10	0	60.34	78.38	3.71E–01
200	1223	A	1	H	1	10	0.10	2	65.38	78.51	3.31E–01
200	1223	A	1	H	1	10	0.10	4	87.11	76.81	2.42E–01
200	1223	A	1	H	1	10	0.10	6	94.41	72.74	1.42E–01
200	1223	A	1	H	1	10	0.10	8	94.95	72.46	7.04E–02
200	1223	A	1	H	1	10	0.10	10	114.14	78.13	3.16E–02
200	1223	A	1	H	1	10	0.10	12	193.79	77.15	1.80E–02
200	1223	A	1	H	1	10	0.10	14	210.94	59.65	1.29E–02
200	1223	A	1	H	1	10	0.10	16	215.49	49.38	1.05E–02
200	1223	A	1	H	1	10	0.10	18	213.51	42.40	9.65E–03
200	1223	A	1	H	1	10	0.10	20	220.40	33.71	9.70E–03
200	1223	A	1	H	1	10	0.10	25	211.83	30.30	8.43E–03
200	1223	A	1	H	1	10	0.10	30	214.94	25.05	7.76E–03
200	1223	A	1	H	1	10	0.10	35	219.26	20.51	7.06E–03
200	1223	A	1	H	1	10	0.10	35	252.23	18.90	4.86E–03
200	1223	A	1	H	1	10	0.10	40	252.96	17.94	4.84E–03
200	1223	A	1	H	1	10	0.10	45	254.54	16.27	4.73E–03
200	1223	A	1	H	1	10	0.10	50	255.00	13.50	4.69E–03
200	1223	A	1	H	1	11	0.11	0	52.55	76.67	3.66E–01
200	1223	A	1	H	1	11	0.11	2	59.42	75.53	3.25E–01
200	1223	A	1	H	1	11	0.11	4	74.25	73.21	2.33E–01
200	1223	A	1	H	1	11	0.11	6	79.03	69.31	1.33E–01
200	1223	A	1	H	1	11	0.11	8	74.06	68.08	6.44E–02
200	1223	A	1	H	1	11	0.11	10	59.14	74.57	2.83E–02
200	1223	A	1	H	1	11	0.11	12	347.69	82.79	1.58E–02
200	1223	A	1	H	1	11	0.11	14	267.04	72.66	1.05E–02
200	1223	A	1	H	1	11	0.11	16	260.26	61.05	8.11E–03
200	1223	A	1	H	1	11	0.11	18	249.47	54.50	7.02E–03
200	1223	A	1	H	1	11	0.11	20	248.09	39.46	7.29E–03
200	1223	A	1	H	1	11	0.11	25	234.28	36.85	5.82E–03
200	1223	A	1	H	1	11	0.11	30	234.74	27.84	5.46E–03
200	1223	A	1	H	1	11	0.11	35	238.07	20.54	5.09E–03
200	1223	A	1	H	1	11	0.11	35	283.29	14.66	4.29E–03
200	1223	A	1	H	1	11	0.11	40	281.77	14.01	4.19E–03
200	1223	A	1	H	1	11	0.11	45	283.63	11.74	4.16E–03
200	1223	A	1	H	1	11	0.11	50	281.45	8.57	4.14E–03
200	1223	A	1	H	1	12	0.12	0	34.00	76.66	3.59E–01
200	1223	A	1	H	1	12	0.12	2	39.28	75.44	3.17E–01
200	1223	A	1	H	1	12	0.12	4	48.46	73.75	2.23E–01
200	1223	A	1	H	1	12	0.12	6	49.37	70.42	1.24E–01
200	1223	A	1	H	1	12	0.12	8	38.08	67.16	5.93E–02
200	1223	A	1	H	1	12	0.12	10	10.36	64.49	2.73E–02
200	1223	A	1	H	1	12	0.12	12	342.62	59.32	1.66E–02
200	1223	A	1	H	1	12	0.12	14	319.58	54.73	1.13E–02
200	1223	A	1	H	1	12	0.12	16	310.17	46.90	8.95E–03
200	1223	A	1	H	1	12	0.12	18	301.06	45.00	7.36E–03
200	1223	A	1	H	1	12	0.12	20	287.25	34.21	7.31E–03

Note: Only a portion of this table appears here. The complete table is available in **ASCII.**

Table T10. Principal component analysis results from paleomagnetic data from archive-half sections, Hole 1223A.

| | | | | | | | | Principal component analysis | | | | | | | | Stable endpoint | | | | Angular |
Leg	Site	Hole	Core	Type	Section	Interval (cm)	Depth (mbsf)	Inclination (°)	Declination (°)	MAD (°)	Length (A/m)	Deviation angle (°)	Number of steps	Lowest step (mT)	Highest step (mT)	Inclination (°)	Declination (°)	k	N	distance (°)
200	1223	A	1	H	1	9	0.09	17.9	178.5	2.38	4.16E–02	46.71	4	35	45	17.9	236.4	1298.5	3	54.9
200	1223	A	1	H	1	10	0.10	15.0	176.9	2.34	4.08E–02	62.31	4	35	45	15.9	254.2	1079.3	3	74.0
200	1223	A	1	H	1	11	0.11	13.2	180.9	3.32	3.61E–02	86.13	4	35	45	11.4	282.3	746.5	3	98.2
200	1223	A	1	H	1	12	0.12	14.6	192.7	4.64	2.79E–02	103.35	4	35	45	5.4	306.6	922.9	3	111.5
200	1223	A	1	H	1	13	0.13	19.0	211.4	6.25	2.05E–02	104.37	4	35	45	0.6	322.6	1381.3	3	109.8
200	1223	A	1	H	1	14	0.14	26.1	231.7	7.66	1.58E–02	97.86	4	35	45	–3.6	333.2	2021.8	3	101.8
200	1223	A	1	H	1	15	0.15	30.5	249.5	8.9	1.25E–02	91.65	4	35	45	–7.0	340.7	3109.2	3	94.6
200	1223	A	1	H	1	16	0.16	26.4	267.9	9.13	1.04E–02	83.03	4	35	45	–9.4	347.5	4194.3	3	85.0
200	1223	A	1	H	1	17	0.17	–3.0	64.6	7.56	5.49E–03	68.01	4	35	50	–10.9	355.5	2048.5	3	69.0
200	1223	A	1	H	1	18	0.18	–9.8	64.1	8.26	6.79E–03	56.37	4	35	50	–11.8	5.5	1423.7	3	57.5
200	1223	A	1	H	1	19	0.19	–14.0	67.0	3.42	8.63E–03	47.37	4	35	50	–12.6	16.9	815.3	3	48.7
200	1223	A	1	H	1	20	0.20	–16.9	68.7	5.42	9.93E–03	38.4	4	35	50	–15.1	27.2	652.2	3	39.8
200	1223	A	1	H	1	21	0.21	–23.2	68.1	6.09	1.03E–02	31.45	4	35	50	–21.8	32.6	730.9	3	32.8
200	1223	A	1	H	1	22	0.22	5.8	60.0	7.56	2.95E–02	37.52	4	30	50	–33.3	31.5	647.2	3	47.5
200	1223	A	1	H	1	23	0.23	12.0	69.2	6.82	2.98E–02	57.67	4	30	45	–46.9	22.0	788.6	3	72.4
200	1223	A	1	H	1	24	0.24	12.2	81.2	6.57	2.76E–02	78.37	4	30	40	–55.3	0.4	974.6	3	94.9
200	1223	A	1	H	1	25	0.25	–3.8	86.0	8.15	3.02E–02	84.31	4	30	45	–53.8	334.9	1481.8	3	99.1
200	1223	A	1	H	1	26	0.26	–15.4	95.2	12.2	2.46E–02	91.81	4	30	45	–48.3	324.7	1489.5	3	102.6
200	1223	A	1	H	1	27	0.27	–57.7	86.7	17.11	2.07E–02	62.03	4	30	50	–43.9	324.2	1808.7	3	67.7
200	1223	A	1	H	1	28	0.28	–45.9	357.1	3.88	1.75E–02	19.06	4	35	50	–41.8	329.9	2569.3	3	19.9
200	1223	A	1	H	1	29	0.29	–46.9	295.2	12.95	3.09E–02	26.9	4	30	50	–40.6	340.2	1648.4	3	32.7
200	1223	A	1	H	1	30	0.30	–46.1	303.0	11.67	3.42E–02	28.21	4	30	50	–37.4	348.6	3440.8	3	34.6
200	1223	A	1	H	1	31	0.31	–52.8	322.5	11.97	3.31E–02	24.44	4	30	50	–32.4	352.5	4655.2	3	29.6
200	1223	A	1	H	1	32	0.32	–32.4	14.4	3.02	2.00E–02	19.65	4	35	50	–27.1	351.6	1294.9	3	20.5
200	1223	A	1	H	1	33	0.33	–29.4	14.9	2.26	2.02E–02	23.01	4	35	50	–23.3	348.9	1234.3	3	24.1
200	1223	A	1	H	1	34	0.34	–27.7	12.5	2.05	2.06E–02	24.67	4	35	50	–21.3	345.0	1070.2	3	25.8
200	1223	A	1	H	1	35	0.35	–26.2	10.6	1.43	2.14E–02	27.95	4	35	50	–20.2	339.5	904.5	3	29.2
200	1223	A	1	H	1	36	0.36	–24.9	5.8	3.36	2.20E–02	29.41	4	35	50	–19.2	333.3	888.0	3	30.6
200	1223	A	1	H	1	37	0.37	–23.5	0.8	3.49	2.31E–02	28.37	4	35	50	–18.3	329.8	935.3	3	29.4
200	1223	A	1	H	1	38	0.38	–22.2	1.0	3.9	2.47E–02	29.23	4	35	50	–17.6	329.2	936.4	3	30.3
200	1223	A	1	H	1	39	0.39	–21.0	2.8	5.8	2.61E–02	30.04	4	35	50	–17.3	330.1	804.3	3	31.1

Notes: The mean paleomagnetic direction is estimated from the demagnetization data using the principal component analysis (PCA) method of Kirschvink (1980). The best-fit line that passes through the vector demagnetization data is not forced to be anchored to the origin of vector demagnetization space, but is allowed to freely fit the data. To avoid data possibly contaminated by the drilling overprint, we do not use demagnetization steps <30 mT for Core 200-1223A-1H, or <40 mT for all other cores. We use an iterative search program to find and delete demagnetization steps in any interval that gives directions that are outliers relative to directions from other demagnetization steps from that interval. PCA parameters, in addition to the direction (inclination and declination), are MAD = maximum angular deviation; length = distance from origin of the vector demagnetization space to the centroid of the data used to find the best-fit line; deviation angle = the angle between the best-fit line and a line that passes through the origin and centroid; number of steps = number of demagnetization steps used in finding the best-fit line; lowest step = the lowest demagnetization step used in finding the best-fit line; highest step = the highest demagnetization step used in finding the best-fit line. For comparison, we also compute a Fisherian mean of the highest three or four demagnetization steps for each interval. This is referred to as the stable endpoint direction. Typically, only the highest three demagnetization steps are used in the average, unless the mean of these three directions has a dispersion parameter <200, in which case the fourth highest demagnetization step is included. When the dispersion parameter is <200, we also use an iterative search to find and remove the direction that is the largest outlier. Stable endpoint parameters, in addition to the mean direction (inclination and declination), are k = the Fisherian dispersion parameter and N = the number of directions from the three highest demagnetization steps that were averaged. Angular distance = the angular distance between the PCA direction and the stable endpoint direction. Only a portion of this table appears here. The complete table is available in **ASCII.**

Table T11. Paleomagnetic data from discrete samples, Hole 1223A.

Leg	Site	Hole	Core	Type	Section	Interval (cm)	Depth (mbsf)	Demagnetization step (mT)	Declination (°)	Inclination (°)	Intensity (A/m)
200	1223	A	1	H	1	9	0.09	0	156.9	83.1	1.37E–01
200	1223	A	1	H	1	9	0.09	2	163.2	81.2	1.00E–01
200	1223	A	1	H	1	9	0.09	4	169.8	74.8	4.56E–02
200	1223	A	1	H	1	9	0.09	6	173.9	63.7	2.16E–02
200	1223	A	1	H	1	9	0.09	8	176.8	58.1	1.62E–02
200	1223	A	1	H	1	9	0.09	10	174.8	53.2	1.26E–02
200	1223	A	1	H	1	9	0.09	12	175.3	52.8	1.09E–02
200	1223	A	1	H	1	9	0.09	14	174.1	48.8	9.26E–03
200	1223	A	1	H	1	9	0.09	16	176.6	47.6	8.63E–03
200	1223	A	1	H	1	9	0.09	18	172.2	49.6	8.05E–03
200	1223	A	1	H	1	9	0.09	20	165.6	55.6	6.27E–03
200	1223	A	1	H	1	9	0.09	22	161.6	60.4	5.46E–03
200	1223	A	1	H	1	9	0.09	24	165.3	53.8	4.47E–03
200	1223	A	1	H	1	9	0.09	26	171.7	52.2	4.62E–03
200	1223	A	1	H	1	9	0.09	28	159.3	47.3	3.91E–03
200	1223	A	1	H	1	9	0.09	30	167.1	43.2	3.89E–03
200	1223	A	1	H	1	9	0.09	35	174.5	46.5	5.09E–03
200	1223	A	1	H	1	9	0.09	40	149.9	62.6	2.82E–03
200	1223	A	1	H	1	9	0.09	45	141.5	60.2	2.41E–03
200	1223	A	1	H	1	9	0.09	50	137.2	64.2	1.96E–03
200	1223	A	1	H	1	9	0.09	50	145.1	31.2	2.25E–03
200	1223	A	1	H	1	9	0.09	55	47.4	3.3	2.39E–03
200	1223	A	1	H	1	9	0.09	55	21.2	12.9	1.62E–03
200	1223	A	1	H	1	9	0.09	60	180.7	36.0	6.54E–03
200	1223	A	1	H	1	9	0.09	60	69.1	66.6	1.57E–03
200	1223	A	1	H	1	9	0.09	65	101.5	74.6	1.49E–03
200	1223	A	1	H	1	9	0.09	65	173.1	42.4	4.31E–03
200	1223	A	1	H	1	9	0.09	70	358.8	–8.1	2.05E–03
200	1223	A	1	H	1	9	0.09	70	186.6	54.5	3.50E–03
200	1223	A	1	H	1	9	0.09	75	25.8	15.4	8.97E–04
200	1223	A	1	H	1	9	0.09	75	9.6	12.1	3.39E–03
200	1223	A	1	H	1	9	0.09	80	164.0	43.7	2.26E–03
200	1223	A	1	H	1	9	0.09	80	164.6	43.3	1.82E–03
200	1223	A	1	H	1	75	0.75	0	170.1	87.5	2.20E–01
200	1223	A	1	H	1	75	0.75	2	163.9	88.0	1.63E–01
200	1223	A	1	H	1	75	0.75	4	333.7	83.2	4.60E–02
200	1223	A	1	H	1	75	0.75	6	339.3	33.3	1.32E–02
200	1223	A	1	H	1	75	0.75	8	341.5	–2.8	1.31E–02
200	1223	A	1	H	1	75	0.75	10	341.3	–18.1	1.48E–02
200	1223	A	1	H	1	75	0.75	12	342.4	–24.1	1.54E–02
200	1223	A	1	H	1	75	0.75	14	345.1	–28.5	1.62E–02
200	1223	A	1	H	1	75	0.75	16	346.1	–30.6	1.59E–02
200	1223	A	1	H	1	75	0.75	18	346.8	–33.0	1.58E–02
200	1223	A	1	H	1	75	0.75	20	348.0	–34.3	1.47E–02
200	1223	A	1	H	1	75	0.75	22	349.9	–32.9	1.59E–02
200	1223	A	1	H	1	75	0.75	24	349.0	–33.5	1.46E–02
200	1223	A	1	H	1	75	0.75	26	353.0	–34.1	1.37E–02
200	1223	A	1	H	1	75	0.75	28	353.3	–36.8	1.34E–02
200	1223	A	1	H	1	75	0.75	30	354.9	–36.2	1.37E–02
200	1223	A	1	H	1	75	0.75	35	354.5	–36.0	1.12E–02
200	1223	A	1	H	1	75	0.75	40	352.1	–36.4	1.02E–02
200	1223	A	1	H	1	75	0.75	45	357.0	–34.6	1.02E–02
200	1223	A	1	H	1	75	0.75	50	357.7	–34.2	7.43E–03
200	1223	A	1	H	1	75	0.75	55	356.7	–38.8	9.71E–03
200	1223	A	1	H	1	75	0.75	60	12.7	–54.0	2.71E–03
200	1223	A	1	H	1	75	0.75	65	349.4	–30.3	7.08E–03
200	1223	A	1	H	1	75	0.75	70	21.0	–39.0	1.38E–03
200	1223	A	1	H	1	75	0.75	75	356.1	–35.9	5.04E–03
200	1223	A	1	H	1	75	0.75	80	353.1	–31.9	7.12E–03

Notes: The samples from intervals 200-1223A-6X-1, 55–56 cm, and 6X-3, 90–91 cm, were cut into multiple pieces. The piece number was divided by ten and added to the top interval in order to keep track of the pieces. Thus, Piece 1 from interval 200-1223A-6X-3, 90–91 cm, is listed in the table as 6X-3, 90.1 cm, and Piece 11 as 6X-3, 91.1 cm. Only a portion of this table appears here. The complete table is available in **ASCII.**

Table T12. Anhysteretic remanent magnetization (ARM) data from discrete samples, Hole 1223A.

Leg	Site	Hole	Core	Type	Section	Interval (cm)	Depth (mbsf)	Run number	Demagnetization level (mT)	Declination (°)	Inclination (°)	Intensity (A/m)	J_x (A/m)	J_y (A/m)	J_z (A/m)
200	1223	A	1	H	1	9	0.09	2132	0	171.21	–89.71	4.70E–01	–2.37E–03	3.66E–04	–4.70E–01
200	1223	A	1	H	1	9	0.09	2134	5	122.63	–89.74	4.48E–01	–1.10E–03	1.72E–03	–4.48E–01
200	1223	A	1	H	1	9	0.09	2136	10	111.89	–89.80	4.00E–01	–5.12E–04	1.27E–03	–4.00E–01
200	1223	A	1	H	1	9	0.09	2138	15	94.24	–89.80	3.42E–01	–9.00E–05	1.21E–03	–3.42E–01
200	1223	A	1	H	1	9	0.09	2140	20	110.69	–89.77	2.81E–01	–3.90E–04	1.03E–03	–2.81E–01
200	1223	A	1	H	1	9	0.09	2142	25	106.20	–89.82	2.26E–01	–2.00E–04	6.87E–04	–2.26E–01
200	1223	A	1	H	1	9	0.09	2144	30	53.11	–89.74	1.71E–01	4.58E–04	6.10E–04	–1.71E–01
200	1223	A	1	H	1	9	0.09	2146	35	37.29	–89.62	1.29E–01	6.72E–04	5.11E–04	–1.29E–01
200	1223	A	1	H	1	9	0.09	2148	40	346.36	–89.71	1.01E–01	5.02E–04	–1.22E–04	–1.01E–01
200	1223	A	1	H	1	9	0.09	2150	45	348.09	–89.01	7.47E–02	1.26E–03	–2.67E–04	–7.47E–02
200	1223	A	1	H	1	9	0.09	2152	50	359.98	–88.83	5.46E–02	1.11E–03	–4.58E–07	–5.46E–02
200	1223	A	1	H	1	9	0.09	2154	55	6.69	–89.16	4.14E–02	5.99E–04	7.02E–05	–4.14E–02
200	1223	A	1	H	1	9	0.09	2156	60	326.85	–88.22	3.11E–02	8.08E–04	–5.28E–04	–3.11E–02
200	1223	A	1	H	1	9	0.09	2158	65	330.77	–88.15	2.36E–02	6.63E–04	–3.71E–04	–2.36E–02
200	1223	A	1	H	1	9	0.09	2160	70	340.53	–83.26	1.73E–02	1.92E–03	–6.78E–04	–1.72E–02
200	1223	A	1	H	1	9	0.09	2162	75	0.58	–85.54	1.31E–02	1.02E–03	1.02E–05	–1.31E–02
200	1223	A	1	H	1	9	0.09	2164	80	347.11	–80.24	1.07E–02	1.77E–03	–4.04E–04	–1.05E–02
200	1223	A	1	H	1	75	0.75	2133	0	323.20	–89.57	6.72E–01	4.07E–03	–3.04E–03	–6.72E–01
200	1223	A	1	H	1	75	0.75	2135	5	345.76	–89.46	6.41E–01	5.80E–03	–1.47E–03	–6.41E–01
200	1223	A	1	H	1	75	0.75	2137	10	349.28	–89.29	5.74E–01	6.93E–03	–1.31E–03	–5.74E–01
200	1223	A	1	H	1	75	0.75	2139	15	350.53	–89.37	4.90E–01	5.34E–03	–8.92E–04	–4.90E–01
200	1223	A	1	H	1	75	0.75	2141	20	352.20	–89.36	4.01E–01	4.45E–03	–6.10E–04	–4.01E–01
200	1223	A	1	H	1	75	0.75	2143	25	353.89	–89.10	3.20E–01	5.00E–03	–5.35E–04	–3.20E–01
200	1223	A	1	H	1	75	0.75	2145	30	347.89	–88.94	2.39E–01	4.30E–03	–9.23E–04	–2.39E–01
200	1223	A	1	H	1	75	0.75	2147	35	342.79	–88.63	1.77E–01	4.04E–03	–1.25E–03	–1.77E–01
200	1223	A	1	H	1	75	0.75	2149	40	346.19	–88.42	1.38E–01	3.68E–03	–9.05E–04	–1.38E–01
200	1223	A	1	H	1	75	0.75	2151	45	351.00	–87.69	1.01E–01	4.01E–03	–6.36E–04	–1.01E–01
200	1223	A	1	H	1	75	0.75	2153	50	352.97	–86.79	7.26E–02	4.04E–03	–4.99E–04	–7.25E–02
200	1223	A	1	H	1	75	0.75	2155	55	343.33	–87.19	5.40E–02	2.54E–03	–7.60E–04	–5.39E–02
200	1223	A	1	H	1	75	0.75	2157	60	1.14	–83.76	4.29E–02	4.66E–03	9.28E–05	–4.26E–02
200	1223	A	1	H	1	75	0.75	2159	65	352.39	–83.24	3.19E–02	3.72E–03	–4.98E–04	–3.17E–02
200	1223	A	1	H	1	75	0.75	2161	70	352.62	–82.17	2.41E–02	3.25E–03	–4.21E–04	–2.39E–02
200	1223	A	1	H	1	75	0.75	2163	75	358.05	–79.62	1.88E–02	3.39E–03	–1.16E–04	–1.85E–02
200	1223	A	1	H	1	75	0.75	2165	80	352.62	–79.51	1.55E–02	2.79E–03	–3.62E–04	–1.52E–02
200	1223	A	1	H	1	123	1.23	2174	0	204.30	–89.16	9.83E–01	–1.31E–02	–5.90E–03	–9.83E–01
200	1223	A	1	H	1	123	1.23	2176	5	192.67	–89.32	9.42E–01	–1.09E–02	–2.45E–03	–9.41E–01
200	1223	A	1	H	1	123	1.23	2178	10	191.76	–89.37	8.39E–01	–9.01E–03	–1.88E–03	–8.39E–01
200	1223	A	1	H	1	123	1.23	2180	15	194.76	–89.44	7.17E–01	–6.74E–03	–1.78E–03	–7.17E–01
200	1223	A	1	H	1	123	1.23	2182	20	187.86	–89.54	5.79E–01	–4.64E–03	–6.40E–04	–5.79E–01
200	1223	A	1	H	1	123	1.23	2184	25	119.57	–89.28	4.53E–01	–2.81E–03	4.95E–03	–4.53E–01
200	1223	A	1	H	1	123	1.23	2186	30	244.57	–89.63	3.32E–01	–9.09E–04	–1.91E–03	–3.32E–01
200	1223	A	1	H	1	123	1.23	2188	35	273.80	–88.52	2.43E–01	4.15E–04	–6.26E–03	–2.43E–01
200	1223	A	1	H	1	123	1.23	2190	40	323.31	–89.69	1.86E–01	8.01E–04	–5.97E–04	–1.86E–01

Notes: An ARM was applied with a 50-µT biasing field and a 100-mT demagnetizing field. The samples were then AF demagnetized. J_x, J_y, and J_z are the x-, y-, and z-components of the intensity of magnetization. Run number is a sequential measurement number used for tracking the order of measurements. Only a portion of this table appears here. The complete table is available in ASCII.

Table T13. Isothermal remanent magnetization (IRM) data from discrete samples, Hole 1223A.

Leg	Site	Hole	Core	Type	Section	Interval (cm)	Depth (mbsf)	Run number	Applied IRM (mT)	Demagnetization level (mT)	Declination (°)	Inclination (°)	Intensity (A/m)	J_x (A/m)	J_y (A/m)	J_z (A/m)
200	1223	A	1	H	1	9	0.09	2662	–1000	0	186.49	–86.83	2.01E+01	–1.10E+00	–1.26E–01	–2.00E+01
200	1223	A	1	H	1	9	0.09	2666	100	0	81.65	88.61	1.51E+01	5.34E–02	3.64E–01	1.51E+01
200	1223	A	1	H	1	9	0.09	2670	300	0	12.42	87.28	1.83E+01	8.45E–01	1.86E–01	1.82E+01
200	1223	A	1	H	1	9	0.09	2674	1000	0	345.74	86.30	1.87E+01	1.17E+00	–2.98E–01	1.87E+01
200	1223	A	1	H	1	9	0.09	2678	1000	5	290.39	89.01	1.80E+01	1.08E–01	–2.91E–01	1.80E+01
200	1223	A	1	H	1	9	0.09	2682	1000	10	245.56	89.05	1.64E+01	–1.13E–01	–2.49E–01	1.64E+01
200	1223	A	1	H	1	9	0.09	2686	1000	15	243.24	89.17	1.65E+01	–1.07E–01	–2.12E–01	1.65E+01
200	1223	A	1	H	1	9	0.09	2690	1000	20	243.00	89.18	1.44E+01	–9.32E–02	–1.83E–01	1.44E+01
200	1223	A	1	H	1	9	0.09	2694	1000	25	243.10	89.10	1.11E+01	–7.87E–02	–1.55E–01	1.11E+01
200	1223	A	1	H	1	9	0.09	2698	1000	30	245.31	89.11	9.31E+00	–6.05E–02	–1.32E–01	9.31E+00
200	1223	A	1	H	1	9	0.09	2702	1000	35	246.40	89.21	8.96E+00	–4.94E–02	–1.13E–01	8.96E+00
200	1223	A	1	H	1	9	0.09	2706	1000	40	246.85	89.24	8.27E+00	–4.31E–02	–1.01E–01	8.27E+00
200	1223	A	1	H	1	9	0.09	2710	1000	45	247.04	89.18	6.85E+00	–3.81E–02	–9.00E–02	6.85E+00
200	1223	A	1	H	1	9	0.09	2714	1000	50	247.78	89.27	6.82E+00	–3.28E–02	–8.02E–02	6.82E+00
200	1223	A	1	H	1	9	0.09	2718	1000	55	247.72	89.32	6.60E+00	–2.96E–02	–7.23E–02	6.60E+00
200	1223	A	1	H	1	9	0.09	2722	1000	60	247.50	89.33	6.04E+00	–2.71E–02	–6.55E–02	6.04E+00
200	1223	A	1	H	1	9	0.09	2726	1000	65	248.07	89.33	5.47E+00	–2.40E–02	–5.96E–02	5.47E+00
200	1223	A	1	H	1	9	0.09	2730	1000	70	248.66	89.32	4.99E+00	–2.16E–02	–5.54E–02	4.99E+00
200	1223	A	1	H	1	9	0.09	2734	1000	75	249.54	89.31	4.57E+00	–1.92E–02	–5.16E–02	4.57E+00
200	1223	A	1	H	1	9	0.09	2738	1000	80	249.46	89.30	4.26E+00	–1.82E–02	–4.86E–02	4.26E+00
200	1223	A	1	H	1	75	0.75	2663	–1000	0	24.91	–88.26	2.82E+01	7.79E–01	3.62E–01	–2.82E+01
200	1223	A	1	H	1	75	0.75	2667	100	0	192.03	88.18	1.99E+01	–6.19E–01	–1.32E–01	1.99E+01
200	1223	A	1	H	1	75	0.75	2671	300	0	319.33	88.65	2.56E+01	4.60E–01	–3.95E–01	2.56E+01
200	1223	A	1	H	1	75	0.75	2675	1000	0	263.70	87.72	2.65E+01	–1.16E–01	–1.05E+00	2.65E+01
200	1223	A	1	H	1	75	0.75	2679	1000	5	228.64	86.92	2.43E+01	–8.64E–01	–9.82E–01	2.43E+01
200	1223	A	1	H	1	75	0.75	2683	1000	10	222.19	86.58	2.08E+01	–9.17E–01	–8.31E–01	2.07E+01
200	1223	A	1	H	1	75	0.75	2687	1000	15	221.54	86.93	1.98E+01	–7.94E–01	–7.03E–01	1.97E+01
200	1223	A	1	H	1	75	0.75	2691	1000	20	221.87	87.24	1.86E+01	–6.67E–01	–5.98E–01	1.86E+01
200	1223	A	1	H	1	75	0.75	2695	1000	25	221.49	87.49	1.72E+01	–5.66E–01	–5.01E–01	1.72E+01
200	1223	A	1	H	1	75	0.75	2699	1000	30	220.91	87.73	1.62E+01	–4.83E–01	–4.19E–01	1.62E+01
200	1223	A	1	H	1	75	0.75	2703	1000	35	220.77	87.82	1.45E+01	–4.18E–01	–3.60E–01	1.45E+01
200	1223	A	1	H	1	75	0.75	2707	1000	40	221.14	87.91	1.32E+01	–3.63E–01	–3.17E–01	1.32E+01
200	1223	A	1	H	1	75	0.75	2711	1000	45	220.99	87.79	1.10E+01	–3.18E–01	–2.77E–01	1.09E+01
200	1223	A	1	H	1	75	0.75	2715	1000	50	221.56	87.90	9.83E+00	–2.69E–01	–2.39E–01	9.82E+00
200	1223	A	1	H	1	75	0.75	2719	1000	55	221.82	87.97	8.96E+00	–2.37E–01	–2.12E–01	8.95E+00
200	1223	A	1	H	1	75	0.75	2723	1000	60	221.72	87.99	8.02E+00	–2.10E–01	–1.87E–01	8.01E+00
200	1223	A	1	H	1	75	0.75	2727	1000	65	222.40	88.00	7.11E+00	–1.83E–01	–1.67E–01	7.11E+00
200	1223	A	1	H	1	75	0.75	2731	1000	70	222.22	88.00	6.35E+00	–1.64E–01	–1.49E–01	6.34E+00
200	1223	A	1	H	1	75	0.75	2735	1000	75	222.55	87.96	5.69E+00	–1.49E–01	–1.37E–01	5.69E+00
200	1223	A	1	H	1	75	0.75	2739	1000	80	222.60	87.97	5.20E+00	–1.36E–01	–1.25E–01	5.20E+00
200	1223	A	1	H	1	123	1.23	2664	–1000	0	77.14	–87.52	3.46E+01	3.33E–01	1.46E+00	–3.46E+01
200	1223	A	1	H	1	123	1.23	2668	100	0	7.18	86.06	2.54E+01	1.73E+00	2.18E–01	2.53E+01
200	1223	A	1	H	1	123	1.23	2672	300	0	330.07	86.38	3.16E+01	1.72E+00	–9.93E–01	3.15E+01
200	1223	A	1	H	1	123	1.23	2676	1000	0	295.57	87.68	3.26E+01	5.68E–01	–1.19E+00	3.25E+01
200	1223	A	1	H	1	123	1.23	2680	1000	5	272.35	87.92	3.08E+01	4.61E–02	–1.12E+00	3.08E+01

Notes: Applied IRM gives the direct-current field applied to the sample (see the "Explanatory Notes" chapter for details). J_x, J_y, and J_z are the x-, y-, and z-components of the intensity of magnetization. Run number is a sequential measurement number used for tracking the order of measurements. Only a portion of this table appears here. The complete table is available in ASCII.

Table T14. Principal component analysis results from paleomagnetic data from discrete samples, Hole 1223A.

								Principal component analysis								Stable endpoint				Angular
Leg	Site	Hole	Core	Type	Section	Interval (cm)	Depth (mbsf)	Inclination (°)	Declination (°)	MAD (°)	Length (A/m)	Deviation angle (°)	Number of steps	Lowest step (mT)	Highest step (mT)	Inclination (°)	Declination (°)	k	N	distance (°)
200	1223	A	1	H	1	9	0.09	50.3	174.9	2.24	4.42E–02	14.65	4	20	50	62.2	139.5	662	2	22.6
200	1223	A	1	H	1	75	0.75	–38.8	350.8	3.43	6.27E–02	5.24	4	30	50	–35.1	355.7	877.9	3	5.4
200	1223	A	1	H	1	123	1.23	44.7	1.8	18.75	3.17E–03	66.83	4	50	65	–9.5	32.1	1733.9	2	60.7
200	1223	A	1	H	2	38	1.88	–41.6	10.2	2.59	1.71E–01	6.67	4	35	60	–33.6	8.5	9372.7	3	8.1
200	1223	A	1	H	2	128	2.78	48.9	200.3	0.88	1.41E–01	5.19	4	28	80	47.7	187.9	227.9	3	8.3
200	1223	A	1	H	3	47	3.47	38.8	209.8	1.28	2.48E–01	3.89	8	30	80	43.5	204.9	4459.7	3	6
200	1223	A	1	H	3	130	4.3	34.8	220.4	3.55	8.59E–02	7.65	4	26	40	34.5	210.8	1029.9	3	7.8
200	1223	A	1	H	4	28	4.78	51.1	216.0	4.35	4.06E–02	19.22	4	26	45	24.8	203.8	81.2	3	28
200	1223	A	1	H	4	138	5.88	57.0	226.4	4.67	1.58E–01	13.27	4	24	45	49.6	175.2	261.2	2	30.7
200	1223	A	1	H	CC	18	7.56	–48.2	23.5	12.49	1.15E–02	32.77	4	24	30	–63.0	79.7	123.7	4	33.7
200	1223	A	2	H	1	10	7.8	–18.0	341.4	8.75	3.50E–02	165.36	4	40	50	20.7	155.9	156.4	2	174.2
200	1223	A	6	X	1	55.1	33.55								75	–47.3	287.2	170.7	3	
200	1223	A	6	X	1	55.2	33.55								80	–26.9	279.7	18.8	2	
200	1223	A	6	X	1	55.3	33.55	–22.4	236.6	3.21	1.21E–01	24.06	4	40	75	–16.2	270.7	126.2	4	32.6
200	1223	A	6	X	3	90.1	36.83								80	–13.5	59.0	323.2	2	
200	1223	A	6	X	3	90.2	36.83	–22.4	38.4	10.81	4.15E–01	10.69	19	22	80	–33.5	23.6	148.9	4	17.12
200	1223	A	6	X	3	90.3	36.83	–37.6	58.4	17.59	3.01E–01	18.16	20	22	80	–33.2	99.1	143.6	3	33.2
200	1223	A	6	X	3	90.4	36.83	–16.8	64.9	9.46	5.59E–01	18.83	19	22	80	–45.7	49.8	156.1	4	31.6
200	1223	A	6	X	3	90.5	36.83								80	–42.1	10.0	95.5	2	
200	1223	A	6	X	3	90.6	36.83								80	–3.7	55.4	192.1	2	
200	1223	A	6	X	3	90.7	36.83	–10.5	60.4	14.65	5.65E–02	13.84	18	26	80	–19.6	44.9	92.5	3	17.5
200	1223	A	6	X	3	90.8	36.83	–40.2	18.4	24.22	6.09E–02	6.11	21	20	80	–29.9	28.9	467.7	3	13.4
200	1223	A	6	X	3	90.9	36.83								80	–21.3	38.3	68.7	2	
200	1223	A	6	X	3	91.0	36.83								80	–4.4	336.1	88.2	2	
200	1223	A	6	X	3	91.1	36.83								80	–14.1	28.5	651.3	2	

Notes: The mean paleomagnetic direction is estimated from the demagnetization data using the principal component analysis (PCA) method of Kirschvink (1980). The best-fit line that passes through the vector demagnetization data is not forced to be anchored to the origin of vector demagnetization space, but is allowed to freely fit the data. To avoid data possibly contaminated by the drilling overprint, we do not use demagnetization steps <30 mT for Core 200-1223A-1H, or <40 mT for all other cores. We use an iterative search program to find and delete demagnetization steps in any interval that gives directions that are outliers relative to directions from other demagnetization steps from that interval. PCA parameters, in addition to the direction (inclination and declination), are MAD = maximum angular deviation; length = distance from origin of the vector demagnetization space to the centroid of the data used to find the best-fit line; deviation angle = the angle between the best-fit line and a line that passes through the origin and centroid; number of steps = number of demagnetization steps used in finding the best-fit line; lowest step = the lowest demagnetization step used in finding the best-fit line; highest step = the highest demagnetization step used in finding the best-fit line. For comparison, we also compute a Fisherian mean of the highest three or four demagnetization steps for each interval. This is referred to as the stable endpoint direction. Typically, only the highest three demagnetization steps are used in the average, unless the mean of these three directions has a dispersion parameter <200, in which case the fourth highest demagnetization step is included. When the dispersion parameter is <200, we also use an iterative search to find and remove the direction that is the largest outlier. Stable endpoint parameters, in addition to the mean direction (inclination and declination), are k = the Fisherian dispersion parameter; N = the number of directions from the three highest demagnetization steps that were averaged; and angular distance = the angular distance between the PCA direction and the stable endpoint direction. The samples from intervals 200-1223A-6X-1, 55–56 cm, and 6X-3, 90–91 cm, were cut into multiple pieces. The piece number was divided by ten and added to the top interval in order to keep track of the pieces. Thus, Piece 1 from interval 200-1223A-6X-3, 90–91 cm, is listed in the table as 6X-3, 90.1 cm, and Piece 11 as 6X-3, 91.1 cm. This table is also available in **ASCII.**

Table T15. Magnetostratigraphy, Site 1223.

Polarity chron	Reversal type	Age (Ma)	Depth (mbsf)	Best estimate (mbsf)	Best estimate (Core, section, interval)	Sedimentation rate (m/m.y.)	Comment
0	N	0.000	0.00–0.00	0.00	Top of Core 200-1223A-1H or higher		*
C1n(o)	R→N	0.780	0.11–0.17	0.14	200-1223A-1H-1, 14 cm	0.18	
C1r.1n(t)	N→R	0.990	0.77–0.81	0.79	200-1223A-1H-1, 79 cm	3.10	
C1r.1n(o)	R→N	1.070	1.20–1.26	1.23	200-1223A-1H-1, 123 cm	5.50	
C2n(t)	N→R	1.770	1.99–2.05	2.02	200-1223A-1H-2, 52 cm	1.13	
C2n(o)	R→N	1.950	6.87–7.50	7.19	200-1223A-1H-5, 119 cm	28.69	†
C2r.1n(t)	N→R	2.140	15.02–15.04	15.03	200-1223A-3X-2, 85 cm	41.29	‡
C2r.1n(o)	R→N	2.150	15.24–22.30	15.63	200-1223A-3X-2, 145 cm	60.00	‡
C2An.1n(t)	N→R	2.581			Not observed		**

Notes: Ages for chrons are from Cande and Kent (1995). The suffixes (o) and (t) that are used for the chron names refer to the onset and termination of a polarity chron, respectively. N→R: a reversal where the polarity of the field changed from normal to reversed. R→N a reversal where the polarity of the field changed from reversed to normal. * = the mudline and possibly several centimeters of sediment may not have been recovered (see **"Paleomagnetism,"** p. 34). † = the reversal is not observed as it occurs within a turbidite near the bottom of Section 200-1223A-1H-5, which is disturbed by drilling. ‡ = the short polarity interval is restricted to the bioturbated unit directly below the vitric tuff in Section 200-1223A-3X-2. A clear normal polarity direction is recorded after removal of the drilling overprint, but the direction trends toward a shallow or possibly negative inclination. This could indicate that a reversed component exists but is poorly resolved. The normal component would then be an overprint, perhaps of Brunhes age. Alternatively, the normal component is real, in which case the normal polarity subzone would likely be Chron C2r.1n. The base of this normal polarity subzone occurs somewhere between the base of the bioturbated sediment unit and the top of Core 200-1223A-4X. We have placed it arbitrarily at the base of Section 200-1223A-3X-2, which results in sedimentation rates consistent with the overlying interval. ** = the rocks from Cores 200-1223A-4X, 5X, and 6X all have reversed polarities, which are interpreted to be within Chron C2r.

Table T16. Ages of lithologic units, Hole 1223A.

Lithologic unit	Boundary depth (mbsf)		Age (Ma)	
	Top	Bottom	Top	Bottom
1	0.00	5.11	0.00	1.88
2	5.11	7.32	1.88	1.95
3	7.32	7.90	1.95	1.97
4	7.90	10.78	1.97	2.04
5	12.70	15.06	2.08	2.14
6	15.06	15.29	2.14	2.14
7	15.29	16.10	2.14	>2.15
8	22.30	22.80		
9	22.80	22.91		
10	22.91	24.92		
11A	32.00	33.00		
11B	33.00	36.99		
12	36.99	37.47		
13	37.47	38.31		
14	38.31	38.70		<2.58

Notes: Ages are calculated by linear interpolation between identified polarity reversals. This table is also available in **ASCII.**

Table T17. Thermal conductivity measurements, Hole 1223A.

Leg	Site	Hole	Core	Type	Section	Interval (cm)		Depth (mbsf)	Type	Thermal conductivity (W/[m·K])
						Top	Bottom			
200	1223	A	1	H	3	75	75	3.75	Full	0.862
200	1223	A	2	H	3	50	50	9.38	Full	0.874
200	1223	A	3	X	1	36	46	13.06	Half	1.024
200	1223	A	4	X	2	35	42	23.44	Half	1.023
200	1223	A	6	X	1	77	93	33.77	Half	1.187

This table is also available in **ASCII.**

Table T18. Moisture and density, Hole 1223A.

Leg	Site	Hole	Core	Type	Section	Interval (cm) Top	Bottom	Depth (mbsf)	Water Content (%) Bulk	Dry	Density (g/cm³) Bulk	Dry	Grain	Porosity (%)	Comments
200	1223	A	1	H	1	50	52	0.50	66.4	198.0*	1.287	0.432	2.621	83.5	
200	1223	A	1	H	3	50	52	3.50	63.8	176.2*	1.336	0.484	2.889	83.3	
200	1223	A	1	H	5	50	52	6.50	34.0	51.4	1.790	1.182	2.908	59.3	
200	1223	A	2	H	1	11	13	7.81	55.1	122.7*	1.361	0.611	2.283	73.2	
200	1223	A	3	X	1	23	25	12.93	13.5	15.7	2.307	1.994	2.870	30.5	
200	1223	A	3	X	1	24	26	12.94	13.3	15.4	2.324	2.015	2.888	30.2	Freeze-dried
200	1223	A	3	X	1	49	51	13.19	16.0	19.0	2.275	1.911	2.963	35.5	
200	1223	A	3	X	1	104	106	13.74	14.3	16.7	2.340	2.006	2.98	32.7	
200	1223	A	3	X	1	105	107	13.75	15.2	18.0	2.286	1.938	2.936	34.0	Freeze-dried
200	1223	A	3	X	1	139	141	14.09	16.5	19.7	2.231	1.864	2.907	35.9	
200	1223	A	3	X	2	11	13	14.29	12.8	14.7	2.346	2.045	2.894	29.3	
200	1223	A	3	X	2	12	14	14.30	15.6	18.5	2.238	1.889	2.867	34.1	Freeze-dried
200	1223	A	3	X	2	44	46	14.62	15.6	18.5	2.239	1.890	2.867	34.1	
200	1223	A	3	X	2	76	78	14.94	12.6	14.4	2.397	2.095	2.970	29.5	
200	1223	A	3	X	2	77	79	14.95	12.8	14.6	2.391	2.085	2.971	29.8	Freeze-dried
200	1223	A	4	X	1	16	18	22.46	42.2	73.0	1.622	0.937	2.825	66.8	
200	1223	A	4	X	1	51	53	22.81	28.4	39.7	1.887	1.350	2.836	52.4	
200	1223	A	4	X	2	117	119	24.26	24.8	32.9	1.957	1.472	2.795	47.3	
200	1223	A	6	X	1	80	82	33.80	15.0	17.7	2.131	1.811	2.635	31.3	
200	1223	A	6	X	3	88	90	36.81	14.7	17.2	2.118	1.807	2.595	30.4	
200	1223	A	6	X	3	114	116	37.07	39.2	64.5	1.634	0.993	2.654	62.6	
200	1223	A	6	X	4	52	54	37.95	30.6	44.0	1.783	1.238	2.645	53.2	

Notes: * = large error included due to large porosities. This table is also available in **ASCII.**

Table T19. *P*-wave velocity sensor (PWS) measurements, Hole 1223A.

Leg	Site	Hole	Core	Type	Section	Interval (cm) Top	Bottom	Depth (mbsf)	Direction	Velocity (m/s)
200	1223	A	1	H	1	41.6	41.6	0.42	x	1590.7
200	1223	A	1	H	2	28.6	28.6	1.79	x	1543.4
200	1223	A	1	H	2	78.3	78.3	2.28	x	1654.8
200	1223	A	1	H	2	123.9	123.9	2.74	x	1556.9
200	1223	A	1	H	3	6.1	6.1	3.06	x	1656.2
200	1223	A	1	H	3	43.1	43.1	3.43	x	1544.3
200	1223	A	1	H	3	90.8	90.8	3.91	x	1575.5
200	1223	A	1	H	3	108.2	108.2	4.08	x	1542.1
200	1223	A	1	H	3	124.9	124.9	4.25	x	1523.9
200	1223	A	1	H	4	19.0	19.0	4.69	x	1533.0
200	1223	A	1	H	4	61.5	61.5	5.11	x	1645.2
200	1223	A	1	H	4	122.1	122.1	5.72	x	1687.9
200	1223	A	1	H	5	13.1	13.1	6.13	x	1649.0
200	1223	A	1	H	5	27.7	27.7	6.28	x	1711.4
200	1223	A	1	H	5	41.9	41.9	6.42	x	1727.2
200	1223	A	1	H	5	54.5	54.5	6.55	x	1698.0
200	1223	A	1	H	5	73.0	73.0	6.73	x	1672.3
200	1223	A	1	H	5	81.2	81.2	6.81	x	1733.4
200	1223	A	1	H	5	103.2	103.2	7.03	x	1729.0
200	1223	A	3	X	1	23.0	25.0	12.93	x	3267.0
200	1223	A	3	X	1	23.0	25.0	12.93	y	3264.7
200	1223	A	3	X	1	23.0	25.0	12.93	z	3283.1
200	1223	A	3	X	1	49.0	51.0	13.19	x	3353.2
200	1223	A	3	X	1	49.0	51.0	13.19	y	3254.6
200	1223	A	3	X	1	49.0	51.0	13.19	z	3292.9
200	1223	A	3	X	1	104.0	106.0	13.74	x	3023.7
200	1223	A	3	X	1	104.0	106.0	13.74	y	2949.5
200	1223	A	3	X	1	104.0	106.0	13.74	z	2955.9
200	1223	A	3	X	1	139.0	141.0	14.09	x	3419.8
200	1223	A	3	X	1	139.0	141.0	14.09	y	3397.5
200	1223	A	3	X	1	139.0	141.0	14.09	z	3361.5
200	1223	A	3	X	2	11.0	13.0	14.29	x	3082.2
200	1223	A	3	X	2	11.0	13.0	14.29	y	3170.4
200	1223	A	3	X	2	11.0	13.0	14.29	z	2832.5
200	1223	A	3	X	2	43.0	45.0	14.61	x	3428.2
200	1223	A	3	X	2	43.0	45.0	14.61	y	3423.9
200	1223	A	3	X	2	43.0	45.0	14.61	z	3368.5
200	1223	A	3	X	2	76.0	78.0	14.94	x	3102.1
200	1223	A	3	X	2	76.0	78.0	14.94	y	2982.5
200	1223	A	3	X	2	76.0	78.0	14.94	z	2900.1
200	1223	A	4	X	1	16.5	18.5	22.47	x	1872.9
200	1223	A	4	X	1	16.5	18.5	22.47	y	1913.4
200	1223	A	4	X	1	16.5	18.5	22.47	z	1926.6
200	1223	A	4	X	1	51.0	53.0	22.81	x	2349.0
200	1223	A	4	X	1	51.0	53.0	22.81	y	2388.5
200	1223	A	4	X	1	51.0	53.0	22.81	z	2298.3
200	1223	A	4	X	2	117.0	119.0	24.26	x	3255.8
200	1223	A	4	X	2	117.0	119.0	24.26	y	3210.2
200	1223	A	4	X	2	117.0	119.0	24.26	z	3239.0
200	1223	A	6	X	1	80.0	82.0	33.80	x	4195.3
200	1223	A	6	X	1	80.0	82.0	33.80	y	4035.2
200	1223	A	6	X	1	80.0	82.0	33.80	z	3960.0
200	1223	A	6	X	3	88.0	90.0	36.81	x	4080.1
200	1223	A	6	X	3	88.0	90.0	36.81	y	3871.3
200	1223	A	6	X	3	88.0	90.0	36.81	z	3901.3
200	1223	A	6	X	3	114.0	116.0	37.07	x	2089.9
200	1223	A	6	X	3	114.0	116.0	37.07	y	2141.0
200	1223	A	6	X	3	114.0	116.0	37.07	z	2044.0
200	1223	A	6	X	4	52.0	54.0	37.95	x	2384.6
200	1223	A	6	X	4	52.0	54.0	37.95	y	2379.7
200	1223	A	6	X	4	52.0	54.0	37.95	z	2332.9

Note: This table is also available in **ASCII.**

Table T20. Area insonified.

Traveltime increment (ms)	Distance increment (m)	Angular deviation (°)	Diameter of return area (m)	Area of return (m²)
5	3.75	7.1	1,074	905,782
10	7.50	7.5	1,132	1,005,989
15	11.25	7.9	1,187	1,106,109
20	15.00	8.3	1,240	1,206,141
25	18.75	8.6	1,290	1,306,087
30	22.50	8.9	1,338	1,405,946
35	26.25	9.2	1,385	1,505,717
40	30.00	9.5	1,430	1,605,401
45	33.75	9.8	1,474	1,704,999
50	37.50	10.1	1,516	1,804,509